



# Kent Academic Repository

**Kinnear, Timothy Michael (2016) *Investigation into Triggered Star Formation by Radiative Driven Implosion*. Doctor of Philosophy (PhD) thesis, University of Kent,.**

## Downloaded from

<https://kar.kent.ac.uk/52436/> The University of Kent's Academic Repository KAR

## The version of record is available from

## This document version

UNSPECIFIED

## DOI for this version

## Licence for this version

UNSPECIFIED

## Additional information

## Versions of research works

### Versions of Record

If this version is the version of record, it is the same as the published version available on the publisher's web site. Cite as the published version.

### Author Accepted Manuscripts

If this document is identified as the Author Accepted Manuscript it is the version after peer review but before type setting, copy editing or publisher branding. Cite as Surname, Initial. (Year) 'Title of article'. To be published in *Title of Journal*, Volume and issue numbers [peer-reviewed accepted version]. Available at: DOI or URL (Accessed: date).

## Enquiries

If you have questions about this document contact [ResearchSupport@kent.ac.uk](mailto:ResearchSupport@kent.ac.uk). Please include the URL of the record in KAR. If you believe that your, or a third party's rights have been compromised through this document please see our [Take Down policy](https://www.kent.ac.uk/guides/kar-the-kent-academic-repository#policies) (available from <https://www.kent.ac.uk/guides/kar-the-kent-academic-repository#policies>).

**Investigation into Triggered Star  
Formation by Radiative Driven Implosion**

by

**Timothy Michael Kinnear**

**Thesis**

Submitted to the University of Kent

for the degree of

**Doctor of Philosophy**

**School of Physical Sciences**

June 2016

**University of  
Kent**

---

# CONTENTS

---

<b>List of Tables</b>	<b>v</b>
<b>List of Figures</b>	<b>viii</b>
<b>Acknowledgments</b>	<b>xix</b>
<b>Declarations</b>	<b>xxi</b>
<b>Abstract</b>	<b>xxii</b>
<b>Chapter 1 Introduction</b>	<b>1</b>
1.1 Molecular Clouds and the Interstellar Medium . . . . .	3
1.2 Star Formation in Molecular Clouds . . . . .	4
1.2.1 Gravitational Collapse . . . . .	4
1.2.2 Triggered Star Formation . . . . .	6
1.3 HII Regions . . . . .	7
1.4 Bright Rimmed Clouds . . . . .	10
1.4.1 Regular Structures . . . . .	10
1.4.2 Asymmetric Structures . . . . .	10
1.5 Theoretical Models of RDI . . . . .	14
1.5.1 Semi-Analytical . . . . .	14
1.5.2 Numerical Models Without Gravity . . . . .	14
1.5.3 Improved Numerical Models . . . . .	15
1.6 Limitations of Existing Numerical Investigations . . . . .	15
1.7 An Updated Model . . . . .	16
1.8 Thesis Structure . . . . .	16

<b>Chapter 2</b>	<b>Smoothed Particle Hydrodynamics Code</b>	<b>19</b>
2.1	Properties of the ISM . . . . .	20
2.2	Hydrodynamic Equations . . . . .	21
2.3	Forces and Physical Processes . . . . .	23
2.3.1	Gravity and the Barnes-Hut Oct Tree . . . . .	23
2.3.2	Artificial Viscosity . . . . .	25
2.3.3	The FUV and EUV Radiation Fields . . . . .	27
2.3.4	Chemical Processes . . . . .	28
2.3.5	Thermodynamic Processes . . . . .	30
2.3.6	Turbulence and Magnetic Fields . . . . .	31
2.4	Computational Approaches . . . . .	32
2.5	Smoothed Particle Hydrodynamics . . . . .	33
2.5.1	Basic SPH Theory . . . . .	33
2.5.2	The Smoothing Kernel Function $W$ . . . . .	35
2.6	Integration Schemes . . . . .	37
2.6.1	Leap Frog Algorithm . . . . .	37
2.6.2	Courant-Friedrichs-Lewy Condition . . . . .	38
2.7	Initial Distribution of SPH Particles . . . . .	41
2.7.1	Particle Distribution Methods . . . . .	41
2.7.2	Particle Distribution Effectiveness . . . . .	43
2.7.3	Edge Effect . . . . .	46
2.8	Code Background . . . . .	48
<b>Chapter 3</b>	<b>Ionising Radiation and Code Implementation</b>	<b>50</b>
3.1	Algorithm Implementation and Integration into SPH Code . . . . .	52
3.1.1	Mathematical Formulation . . . . .	53
3.1.2	Ray Tracing . . . . .	56
3.1.3	Optical Path Evaluation . . . . .	59
3.1.4	Timestep modification . . . . .	60
3.2	Ionising Radiation Testing . . . . .	61
3.2.1	Ionisation Without Hydrodynamics . . . . .	61
3.2.2	Ionisation Including Hydrodynamics - Hydrodynamic Implosion	72
3.3	Convergence Testing . . . . .	75
3.3.1	Mass Resolution . . . . .	75
3.3.2	Spherical Cloud Uniformity . . . . .	80
3.3.3	Inclined Ellipsoidal Cloud . . . . .	86
3.3.4	Summary . . . . .	96
3.4	The EUV Radiation Penetration Depth Parameter . . . . .	96

3.4.1	Clouds with $\varphi = 0^\circ$ Inclination . . . . .	97
3.4.2	Clouds with $\varphi \neq 0^\circ$ Inclinations . . . . .	98
3.4.3	Effective Initial Geometry . . . . .	100
3.5	Setting initial conditions . . . . .	105

**Chapter 4 The evolution of normal prolate molecular clouds at H II boundaries 107**

4.1	Introduction . . . . .	108
4.1.1	Background . . . . .	108
4.1.2	Initial Stability of a Prolate Cloud . . . . .	109
4.1.3	Initial Conditions of Prolate Clouds . . . . .	110
4.2	Core finding . . . . .	110
4.2.1	The Algorithm . . . . .	113
4.2.2	Code Testing . . . . .	115
4.3	Axial Density Profile . . . . .	118
4.3.1	Bin Resolution . . . . .	120
4.4	Evolution of High Mass Prolate Clouds . . . . .	124
4.4.1	Basic Evolutionary Features . . . . .	126
4.4.2	Common and Dissimilar Evolutionary Features . . . . .	129
4.4.3	Effects of Varied Initial Density and EUV Flux . . . . .	129
4.5	Evolution of $30 M_\odot$ Prolate Clouds . . . . .	133
4.5.1	Effects of Varied Axial Ratio at $1\,200\text{ cm}^{-3}$ . . . . .	133
4.5.2	Effects of Varied Axial Ratio at $600\text{ cm}^{-3}$ . . . . .	140
4.5.3	Effects of Varied Axial Ratio at lower densities . . . . .	141
4.5.4	Location and Distribution of Cores . . . . .	141
4.5.5	Total Mass and Formation Times of Cores . . . . .	143
4.6	Correlation with Observations . . . . .	147
4.7	Link with Other Modelling Work . . . . .	147
4.8	Conclusions . . . . .	149

**Chapter 5 The evolution of inclined prolate molecular clouds at H II boundaries 151**

5.1	Introduction . . . . .	151
5.1.1	Background . . . . .	153
5.1.2	Initial Conditions . . . . .	154
5.1.3	Ionisation penetration depth parameter $d_{\text{EUV}}$ . . . . .	155
5.1.4	Investigated Parameter Space . . . . .	155
5.2	Evolution of cloud G1200(5) with $\varphi = 45^\circ$ . . . . .	156

5.3	Evolution of cloud G1200(5) with $0^\circ \leq \varphi \leq 90^\circ$ . . . . .	158
5.3.1	Morphological variation with $\varphi$ . . . . .	158
5.3.2	The location of high density cores . . . . .	162
5.3.3	The early triggered core masses and formation timescales . . . . .	166
5.3.4	Projected Views . . . . .	168
5.3.5	Shock Front Convergence Analysis . . . . .	168
5.4	Evolution of G1200 cloud series at $1 \leq \gamma \leq 8$ . . . . .	175
5.4.1	Morphology of final structures . . . . .	175
5.4.2	Displacement of the high density cores . . . . .	177
5.4.3	The total core mass . . . . .	180
5.5	Evolution of clouds with varied density and ionising flux . . . . .	180
5.5.1	An overview of the final morphological structures . . . . .	183
5.5.2	Growing from ‘nose’ to ‘horse-head’ structure . . . . .	187
5.5.3	Development of other irregular morphologies . . . . .	190
5.6	Conclusions . . . . .	191
<b>Chapter 6 Conclusions and Future Work</b>		<b>195</b>
6.1	Conclusions . . . . .	195
6.2	Future Work . . . . .	196
6.2.1	Synthetic Observations . . . . .	196
6.2.2	Sequential Star Formation in BRC Associations . . . . .	197
6.2.3	Semi-analytical Model . . . . .	198
6.2.4	Non-uniform Initial Conditions . . . . .	198
6.2.5	Alternative Geometries . . . . .	199
<b>Bibliography</b>		<b>200</b>
<b>About the Author</b>		<b>216</b>

---

# LIST OF TABLES

---

1.1	ISM elemental abundances relative to total hydrogen number density ( $\mathcal{A}_i = n_i/n$ , where $n = n_{\text{HII}} + n_{\text{HI}} + n_{\text{H}_2}$ ) from Wolfire et al. (1995). . .	3
2.1	Chemical Reaction Table. Elements and molecules presented in default notation, superscript ‘+’ indicates singly ionised. ‘M’ indicates the category for all metals, dealt with in abstract only. ‘cr’ indicates cosmic ray presence in the reaction. $h\nu$ indicates a photon contributing to, or resulting from, the reaction. Data table is essentially the same as that shown in, for example, Nelson and Langer (1999), one of the original descriptions of the chemistry in the code. Values for rate coefficients, unless stated otherwise, are based on the UMIST catalogue data (Bergin et al., 1995). † Rate and equation from Bergin et al. (1995), developed from the work of van Dishoeck and Black (1988). $\Theta$ indicates the CO self-shielding function. . . . .	29
2.2	Statistical properties for the densities of particles produced through different distributions intended to represent the same simulated object. All values are in $\text{cm}^{-3}$ . The target density was $144.80 \text{ cm}^{-3}$ . . . . .	43
3.1	Table of the particle counts and mass resolutions for the mass resolution convergence testing simulations. Each of the ‘particles/ $M_\odot$ ’ mass resolutions are rounded to the nearest particle. . . . .	76

3.2	Statistical properties for two sets of 32 simulations, one a spherical cloud and one an ellipsoidal cloud with axial ratio $\gamma = 2$ and inclination $\varphi = 45^\circ$ . The other initial conditions of both cloud types were identical, with $n = 1\,200\text{ cm}^{-3}$ , $M = 30 M_\odot$ and $F = 10^9\text{ cm}^{-2}\text{ s}^{-1}$ . Each of the 64 clouds had different particles distributions, obtained randomly using the glass-like method described in Section 2.7.1. $t_{\text{final}}$ are the times at which the simulations ended due to timestep contraction as a result of high-density core formation. $t_{\text{common}}$ indicates the final time of the earliest simulation to finish, in other words the final time at which all simulations have data. The masses indicated are the mass for all material $n > 10^8\text{ cm}^{-3}$ . . . . .	92
4.1	Summary of the parameters of all tests examined. After the name of the test series, the next four columns (Mass, Density, Ratio & EUV Flux) are the defining parameters of each simulation set. For all series, three of the four are fixed values, and the remaining parameter is represented by a variable, whose range is described in the Varied Parameter column. The final column indicates the main Section/Subsection in which the test series is discussed. . . . .	111
4.2	Summary of test conditions for evaluation of the corefinding algorithm parameters. To the left are the parameters as set, to the right are the results for several properties of obtained from running the algorithm on identical sample simulations. . . . .	118
4.3	The parameters of the three prolate clouds of similar initial uniform density of $100\text{ cm}^{-3}$ and axial ratio $\gamma = 2$ . They have particle mass resolution of $10^{-3} M_\odot$ per SPH particle (the resolution requirement determined in Section 3.3.1). The columns, from left to right, are the name, mass, major axis length $a$ , the critical major axis length and the ionising radiation penetration depth parameter (calculated with Equations 4.2 and 3.36). . . . .	125
4.4	The parameters of the further exploration high mass prolate clouds. The columns, from left to right, are the name, density, major axis length $a$ , incident EUV flux and the ionising radiation penetration depth parameter. Time indicates the final simulation time. Clouds D1-3 are the additional density-varied tests, and clouds E1-3 are the additional incident flux-varied tests. . . . .	130

4.5	Parameters of two groups of molecular clouds of same mass but different initial densities of $600$ and $1\,200\text{ cm}^{-3}$ . From left to right, columns 1-3 are the number identity, axial ratio and the critical semi major axis defined by Equation 4.2 for both G1 and G2 clouds. Columns 4-5 are the major axis and $d_{\text{EUV}}$ defined by Equation 3.36 for the G1 clouds, and columns 6-7 are the same parameters for the G2 clouds. All of the semi-major axes and critical semi-major axes are in units of pc and $d_{\text{EUV}}$ values as percentages. . . . .	134
4.6	A summary of the evolutionary destiny of the molecular clouds of mass $30 M_{\odot}$ . . . . .	141
5.1	Summary of the parameter spaces investigated for the separate series of cloud groups. $n$ is initial density, $\gamma$ the axial ratio, $\varphi$ the inclination angle and $F_0$ the incident flux. . . . .	156
5.2	Values for $d_{\text{EUV}}$ of molecular cloud G1200(5) with $0^{\circ} \leq \varphi \leq 90^{\circ}$ for the cloud G1200(5). $d_{\text{EUV}}$ defined by Equation (3.38). . . . .	158
5.3	Parameters of molecular clouds of G1200 series with an inclination angle $\varphi = 45^{\circ}$ . From left to right, columns 1-3 are the number identity, axial ratio and the critical semi major axis defined by Section 4.1.2. Columns 4-5 are the major axis and $d_{\text{EUV}}$ defined by Equation (3.38). All of the semi-major axes and critical semi-major axes are in units of pc and the penetration depth is in %. . . . .	176
5.4	Parameters of molecular clouds of mass $30 M_{\odot}$ , inclination angle $\varphi = 60^{\circ}$ , $\gamma = 2$ , and $a_{\text{crit}} = 0.079\text{ pc}$ . From left to right, columns are the cloud index, initial number density, the major axis and $d_{\text{EUV}}$ defined by Section 4.1.2, with different ionization fluxes $F_1$ and $F_2$ being $1 \times 10^9$ and $2 \times 10^9\text{ cm}^{-2}\text{ s}^{-1}$ respectively. . . . .	182

---

# LIST OF FIGURES

---

1.1	View of the entire M16 <i>Eagle Nebula</i> region. Taken by the National Science Foundation’s telescope on Kitt Peak, it is a false colour image with red, green and blue corresponding to narrow-band observation in SII, H $\alpha$ and OIII respectively. Image credit: T.A.Rector (NRAO/AUI/NSF and NOAO/AURA/NSF) and B.A.Wolpa (NOAO/AURA/NSF). . . .	9
1.2	View of the ‘ <i>Pillars of Creation</i> ’ in the M16 <i>Eagle Nebula</i> . As with Figure 1.1, the colours red, green and blue map to observations in SII, H $\alpha$ and OIII respectively. Image taken by the Hubble Space Telescope (HST), image credit: NASA, ESA, and the Hubble Heritage Team (STScI/AURA). This image in particular is a repeat observation (Jan, 2015) of a commonly used image taken by the HST in 1995. . . . .	11
1.3	Diagrammatic representation of standard type A, B and C bright rimmed clouds, along with the type ‘M’ extension (Miao et al., 2010), and asymmetric morphologies. All are presented relative to the illuminating source as indicated. . . . .	12
1.4	Images of BRCs and a MC illustrating the basic variation in morphology for the A/B/C/M type classifications of surface curvature, as well as two examples of irregular morphology (B33 being non-BRC). Images via Wenger et al. (2000) of DSS-2-Red data. All are presented as 15’ by 15’ in the ICRS frame. * Copyright © 1993-2000 by AAO and AURA ** Copyright © 1992-2000, Caltech and AURA . . . . .	13

2.1	Diagrammatic illustration of the leap frog integration scheme with the inclusion of $\mathbf{a}$ dependence on $\mathbf{v}$ due to artificial viscosity. $\hat{\mathbf{v}}$ is the additional ‘timestep centred’ velocity. Each circular node represents a calculated value for the property notated on the left. Lines from one node to a second node represent the use of the first value in calculating the second. Of interest is that the value for a parameter based on the same one full timestep ago, is calculated using another quantity mid-way between, representing the best available value for the continuous time between the steps. The spontaneously calculated property, acceleration $\mathbf{a}$ is calculated using other properties which are only timestep-synchronised.	39
2.2	Radially binned density for uniform random, glass-like and BCC crystalline particle distributions, intended to represent a homogeneous density of $144.80 \text{ cm}^{-3}$ . The crystalline distribution is partially obscured by the glass-like distribution for much of the inner portion of the cloud, as the mean values are more similar than can be easily distinguished. . . .	44
2.3	Log of the cross-sectional number density difference rendered images of: (top) uniform random number generated distribution (middle) glass-like distribution (bottom) BCC crystalline distribution. Note the improvement in homogeneity from top to bottom, as well as the edge feature in the glass-like and crystalline distribution. . . . .	45
3.1	One-dimensional grid-based implementation of the algorithm for radiation propagation. . . . .	55
3.2	Illustration of the building and creation of the evaluation point and evaluation intervals, in the ray tracing algorithm for radiation transfer. In sequence, (a) to (e), the construction of the evaluation points used to determine the flux reaching the focus particle (red, at the foot of each panel) and therefore its own optical depth and change in ionisation fraction. Also (f), the conversion of the evaluation point positions into 1D evaluation intervals. See text for a full description of the process. .	58
3.3	50 000 particle simulation for 1D, non-hydrodynamic ionisation front propagation test at $24.82 \text{ kyr}$ ( $\approx 2.1 t_{\text{rec}}$ ). Shown are the particle ionisation fractions with depth; the red horizontal line is at $X_{\text{thresh}} = 0.734 299$ , the red vertical blue line is the Gaussian-based fit to the weighted-mean position of the particles at the same $X_{\text{thresh}}$ , the blue vertical line is the analytical solution position based on Equation (3.15); and the green vertical line is given by the particle ionisation fraction integral described in Equation (3.31). . . . .	67

3.4	Results for 50 000 particles for static medium ionisation front propagation tests. Illustrated by a solid red line is the position with time of the ionisation front using the $X_{\text{thresh}} = 0.734\,299$ criteria, and the solid green line the direct summation/integral method given by Equation (3.31); as well as the analytical solutions of Equation (3.15) for $X_0 = 1$ and $X_0 = 0.990\,586$ . . . . .	68
3.5	Profiles of ionisation front position with time for varied particle number of the static medium ionisation front propagation tests. Illustrated are the positions with time of the ionisation front using the integral method described in the text, for 50 000, 100 000 and 250 000 particles in a glass-like structure, and 125 000 particles in a cubic grid structure. The dashed line indicates the analytical solution for the propagation of a discontinuous front through the same medium. . . . .	69
3.6	Results for varied particle number for the ionisation fraction profile at equilibrium. Illustrated are the Gaussian-smoothed fits to the particle distributions of ionisation fraction with depth at $t \approx 5t_{\text{rec}}$ . Shown are lines for 50 000, 100 000 and 250 000 particles in a glass-like structure, and 125 000 particles in a cubic grid structure. Solid lines are the ionised fraction, dashed lines are the neutral fraction. The grey line represents the analytical solution based on Equation (3.28) for the boundary condition $X_0 = X_0^{\text{calc}}$ , and the black line that but with the boundary condition $X_0 = 0.990\,591$ . . . . .	71
3.7	Profile of initial density with radius for hydrodynamic implosion test. All SPH particles at $r \leq 0.75$ pc (black dots) are the ‘cold’ sphere at $T_c = 100$ K, and all SPH particles $r > 0.75$ pc (red dots) are the ‘hot’ medium at $T_h = 20\,000$ K. . . . .	73
3.8	Profile of boundary radius between the cold and hot material of the hydrodynamical implosion with time. The red and blue dots indicate the radius and time of maximum compression for this simulation and Lefloch and Lazareff (1994) respectively. The horizontal red and blue dashed lines indicate the values of $R_{\text{eq}}$ for this simulation and Lefloch and Lazareff (1994), respectively. . . . .	74
3.9	Snapshots of the cross-sectional density through the $x$ - $z$ plane of the collapsing sphere during the early shock (left hand frame, $t = 0.045$ Myr) and at approximately maximum compression (right hand frame, $t = 0.219$ Myr). . . . .	75

3.10	Times in the resolution convergence testing simulations at which an all-simulation mean density of $\langle n \rangle = 10^8 \text{ cm}^{-3}$ is reached (interpolated between output snapshots), across several of the resolutions examined. Black crosses are simulation results, red pluses with error bars are the means and $\pm 2\sigma$ . . . . .	77
3.11	Column density renders of one of each of the particle resolution simulations for particle numbers of 10 000, 20 000, 50 000 and 75 000 (indicated in upper left corner of each panel; column density is in $\text{cm}^{-2}$ ). . . . .	78
3.12	Column density renders of one of each of the particle resolution simulations for particle numbers of 100 000, 150 000, 200 000 and 300 000 (indicated in upper left corner of each panel; column density is in $\text{cm}^{-2}$ ). . . . .	78
3.13	Column density renders at $t = 0.120 \text{ Myr}$ of one of each of the particle resolution simulations for particle numbers of 50 000, 100 000 and 300 000 (indicated in upper left corner of each panel; column density is in $\text{cm}^{-2}$ ). . . . .	79
3.14	Percentage of particles exceeding the strict Jeans critical density threshold for artificial fragmentation at $t = 0.120 \text{ Myr}$ , versus particle resolution. Black crosses are from individual simulations, red pluses with error bars are the means and $\pm 2\sigma$ . . . . .	81
3.15	Distribution of the time of the final timestep for 32 simulations with identical initial conditions but varied particle distributions. The mean is $0.133 \text{ Myr}$ , the standard deviation $0.002 \text{ Myr}$ . . . . .	82
3.16	Distribution of the masses above a density threshold of $10^8 \text{ cm}^{-3}$ at the final timestep for 32 simulations with identical initial conditions but varied particle distributions. The mean is $3.07 M_{\odot}$ , the standard deviation $0.46 M_{\odot}$ . . . . .	83
3.17	Distribution of the maximum density at the final timestep for 32 simulations with identical initial conditions but varied particle distributions. The mean is $3.18 \times 10^{11} \text{ cm}^{-3}$ , the standard deviation $0.73 \times 10^{11} \text{ cm}^{-3}$ . . . . .	83
3.18	Distribution of the masses above a density threshold of $10^8 \text{ cm}^{-3}$ at the common time of $t = 0.1275(1) \text{ Myr}$ for 32 simulations with identical initial conditions but varied particle distributions. The mean is $1.96 M_{\odot}$ , the standard deviation $0.20 M_{\odot}$ . . . . .	84
3.19	Distribution of the maximum density at the common time of $t = 0.1275(1) \text{ Myr}$ for 32 simulations with identical initial conditions but varied particle distributions. The mean is $2.12 \times 10^{11} \text{ cm}^{-3}$ , the standard deviation $1.30 \times 10^{11} \text{ cm}^{-3}$ . . . . .	85

3.20	Snapshots of rendered column density at $t = 0.1275(1)$ Myr for 9 simulations with identical initial conditions but varied particle distributions. Column density is in $\text{cm}^{-2}$ . . . . .	86
3.21	Snapshots of rendered column density at $t = 0.1275(1)$ Myr for 9 simulations with identical initial conditions but varied particle distributions. Detail of the high density spike structure at the apex of the cloud. Column density is in $\text{cm}^{-2}$ . . . . .	87
3.22	Snapshots of rendered column density at the final timestep for each of 9 simulations with identical initial conditions but varied particle distributions. Detail of the high density spike structure at the apex of the cloud. Column density is in $\text{cm}^{-2}$ . . . . .	88
3.23	Time evolution of the mean (lower, black lines) and maximum (upper, red lines) densities. Presented as solid, smooth lines in contrasting colours and in front of each of the data sets is a spline-based best fit for each parameter. . . . .	89
3.24	Time evolution of the fractional differences between the density of each of the 32 simulations to the spline-based best fit line. Two horizontal dashed lines indicate 100% and 1% difference. . . . .	90
3.25	Distribution of the time of the final timestep for 32 simulations with identical initial conditions but varied particle distributions. The black line is the histogram for the angled ellipsoid initial conditions, with a mean of 0.147 Myr, and standard deviation 0.009 Myr. The red line is a re-plot of the data presented in Figure 3.15, presented for comparison. .	91
3.26	Rendered column density at $t = 0.3$ Myr for one of the ellipsoidal test clouds, taken as a representative sample case. Column density is in $\text{cm}^{-2}$ . . . . .	93
3.27	Snapshots of rendered column density at $t = 0.1300(1)$ Myr for nine inclined ellipsoidal simulations with identical initial conditions but varied particle distributions. Detail of the high density spike structure at the apex of the cloud. Column density is in $\text{cm}^{-2}$ . . . . .	94
3.28	Snapshots of rendered column density at the final timestep for each of nine inclined ellipsoidal simulations with identical initial conditions but varied particle distributions. Detail of the high density spike structure at the apex of the cloud. Column density is in $\text{cm}^{-2}$ . . . . .	95

3.29	An overall illustration of the geometry and parameters relevant for inclined clouds. On the left is a cross-section through the $x - z$ plane at $y = 0$ , and on the right is a cross-section through the $y - z$ plane at $x = 0$ . The parameters and lines in orange are the geometric definitions of the cloud, semi-major axis $a$ , semi-minor axis $a/\gamma$ (expressed as a function of the axial ratio $\gamma$ ) and the cloud inclination $\varphi$ . The curved black line ellipse arc is the initially unaffected surface of the cloud; the upper blue ellipse arc is the original upper surface; and the upper red ellipse arc is the modified upper surface, after penetration of the ionising radiation to the equilibrium depth $d$ . That equilibrium depth is shown throughout as the short, green, vertical lines. The half-depth of the longest vertical path through the ellipsoid at $(y = 0, x = 0)$ is $d_0$ , where $d_{\text{EUV}} = d/d_0$ . In addition, the vertical, grey, dashed lines are labelled for parameters used for identification of features in other sections. $x_{\text{max}}$ is the farthest distance along the $x$ -axis that any part of the cloud extends to, $x_{\text{peak}}$ is the location of the $x$ -axis of the peak or apex of the cloud (the $x$ position for maximum $y$ ), and $x_a$ is the projected distance $x_a = a \cos \varphi$ of the semi-major axis. . . . .	98
3.30	Profiles of initially neutral material after one equilibrium depth of ionising radiation (at a flux of $2 \times 10^9 \text{ cm}^{-2} \text{ s}^{-1}$ ) is applied to initial clouds of $M = 30 M_{\odot}$ and $\varphi = 0^\circ$ at the indicated densities. . . . .	101
3.31	Effective initial mass profiles as a function of the cloud ratio, for $30 M_{\odot}$ , $100 \text{ cm}^{-3}$ clouds at the indicated inclinations. . . . .	101
3.32	Effective initial mass profiles for $30 M_{\odot}$ clouds. Numerical results as data points for 50, 100 and $600 \text{ cm}^{-3}$ clouds at inclination ranges of 0 to $90^\circ$ in steps of $15^\circ$ and axial ratios of 1 to 8 in steps of 1. Each are plotted as a function of the cloud's value of $d_{\text{EUV}}$ . The solid line indicates the analytical profile. . . . .	102
3.33	Geometric illustration of the displaced cloud surface by the ionisation depth as cross-sections of the original ellipsoids (a), and the corresponding geometry with the transforms applied to simplify to unit spheres (b). . . . .	102
3.34	Profiles with stellar luminosities of the distances required for each specified flux of $1 \times 10^8$ , $10^9$ and $10^{10} \text{ cm}^{-2} \text{ s}^{-1}$ . (a) the distances themselves in parsec, (b) as a fraction of the Strömgen radius. . . . .	106

4.1	Annotated illustration of the geometry of the clouds investigated in this section; an isotropic interstellar background radiation field is also included, but not presented in the diagram. . . . .	108
4.2	The distribution of molecular clumps over the semi-major to minor axial ratios $\gamma$ . Statistics based on the data in a survey for 6 124 single molecular clumps (Rathborne et al., 2009). . . . .	109
4.3	Illustration of the corefinding process. . . . .	116
4.4	Each of three axial projections for a cloud with initial conditions $\gamma = 2$ , $n = 1\,200\text{ cm}^{-3}$ and $M = 30\text{ M}_{\odot}$ . Column density is in $\text{cm}^{-2}$ . . . . .	119
4.5	Raw particle density properties with position along $x$ -axis for the cloud of $\gamma = 2$ , $n = 1\,200\text{ cm}^{-3}$ and $M = 30\text{ M}_{\odot}$ . . . . .	121
4.6	Comparison of varied bin resolution for axial density plots, the minimum, mean, median and maximum smoothing lengths for the cloud were: $1.87 \times 10^{-5}$ , 0.060 1, 0.002 7 and 0.741 6 pc; where bin widths are $\approx 0.016$ , 0.005, 0.001 and 0.000 2 pc for 50, 150, 600 and 4 000 respectively. Compare with column density plots for the same cloud in Figure 4.4. . . . .	122
4.7	Equivalent of Figure 4.6 with a filter to only sample those SPH particles with $h < x_{\text{bin}}$ . Problematic zero-weighted bins only occur at the high resolution configuration, the other profiles are qualitatively identical to those without the filter. See Figure 4.8 for a direct comparison. . . . .	123
4.8	Direct comparison of the 150 bin resolution plots without and with the $h < x_{\text{bin}}$ SPH particle filter applied. . . . .	124
4.9	Comparison of the mean SPH particle density for each bin (red) and the maximum SPH particle density per bin (green) for the 150 bin resolution plots. . . . .	125
4.10	Sequence of the evolution of the mid-plane cross-sectional number density for Cloud C, of initial density $100\text{ cm}^{-3}$ and $\gamma = 2.0$ ; subject to an isotropic interstellar background radiation and ionising radiation. Time sequence is top to bottom then left to right. . . . .	126
4.11	Mean hydrogen number density along the semi-major axis of three prolate clouds of initial density $100\text{ cm}^{-3}$ and varying masses. The upper panel displays the three clouds subject to an isotropic FUV radiation only; the lower panel shows the same three clouds subject to both FUV and EUV radiation fields. The time scales for the clouds in frame (a) are 3.10, 3.02 and 3.03 Myr for the clouds of 100, 150 and $200\text{ M}_{\odot}$ respectively; and 0.33 Myr for <i>all</i> of the clouds in frame (b). . . . .	128

4.12	The axial mean number density profile at the final timesteps in four molecular clouds of same mass of $200 M_{\odot}$ , and $\gamma = 2$ , but different initial densities as shown in the top-left corner in each panel. The densities are in units of $\text{cm}^{-3}$ . The times at which the simulations ended are shown in Table 4.4. . . . . .	131
4.13	The axial mean number density profile at the final timesteps in four molecular clouds of same mass of $200 M_{\odot}$ , $\gamma = 2$ and initial density of $100 \text{ cm}^{-3}$ , but under the effect of different EUV radiation fluxes as shown in the top-left corner in each panel. The fluxes are in units of $\text{cm}^{-2} \text{ s}^{-1}$ . The times at which the simulations ended are shown in Table 4.4. . . .	132
4.14	Evolution of the cross-sectional density in the mid-plane for the prolate cloud G2(5) over 0.19 Myr. Time is displayed in the upper right of each panel. The order of time evolution is top to bottom and then left to right.	135
4.15	Evolution in the $xy$ -plane projection (column density) of the prolate cloud G2(5). Time is displayed in the upper right of each panel. The development of a linear filament-like structure along the ‘spine’ of the cloud can be seen to have occurred by 0.11 Myr; its fragmentation into zig-zagging, thinner filaments visible at the final time, 0.19 Myr. Column density is in $\text{cm}^{-2}$ . . . . .	136
4.16	The axial mean number density profile for clouds G1(5) ( $600 \text{ cm}^{-3}$ , $\gamma = 2$ ) in solid black and G2(5) ( $1200 \text{ cm}^{-3}$ , $\gamma = 2$ ) in dashed red. G1(5) is at $t = 0.22 \text{ Myr}$ and G2(5) at $t = 0.19 \text{ Myr}$ . . . . .	137
4.17	The cross-sectional density in the mid-plane for the 9 representative prolate clouds in the G2 series at their final time step. The number in the upper-left of each panel is the axial ratio $\gamma$ , and the number in the upper right is the evolutionary time. . . . .	138
4.18	The axial mean density over $x$ -axis (normalised to the initial cloud semi-major axis) for nine of the G1 (black solid line) and G2 (red dashed line) series clouds (indices 1, 3, 5, 7, 9, 13, 15, 17 and 19). The number in the upper left of each panel is the $\gamma$ value of the clouds. . . . .	139
4.19	The axial mean number density distribution for molecular clouds of $30 M_{\odot}$ and $\gamma = 2$ but different initial densities. The legend boxes describe the line styles and colours for the densities of the featured clouds, G0 ( $100 \text{ cm}^{-3}$ ), G1(5) ( $600 \text{ cm}^{-3}$ ) and G2(5) ( $1200 \text{ cm}^{-3}$ ). The evolutionary times of the clouds featured are 0.25, 0.22 and 0.19 Myr for G0, G1(5) and G2(5), respectively. . . . .	142

4.20	$x$ -displacement locations ( $ x_c $ ) of condensed cores formed in the G1 and G2 cloud series with different criteria on the threshold of core mass $m_c$ . $n$ is the initial density of the clouds whose cores are sampled in the corresponding panel. The short horizontal line for each $\gamma$ examined denotes the initial semi-major axis of the cloud. The white circles indicate cores of density $10^8 \leq n_c \leq 10^{12} \text{ cm}^{-3}$ and the black circles core densities of $n_c \geq 10^{12} \text{ cm}^{-3}$ . . . . .	144
4.21	The total mass $m_{\text{tot}}$ of all cores with selection criteria of $n_c \geq 10^6 \text{ cm}^{-3}$ and $m_c = 0.06 M_\odot$ at the end of the simulated evolution for all G1 and G2 clouds. . . . .	145
4.22	The earliest core formation time for all clouds in the G1 and G2 series.	146
4.23	Fragment-core structures taken from various sources. On the left is the segment of the Herschel image of M16 at $60 \mu\text{m}$ . In the upper right panel is a section of a Spitzer pseudo-colour image of part of IC1848E (Chauhan et al., 2011). The lower right panel shows a segment of a fragment-core structure in a Hubble image of Carina Nebula in neutral hydrogen, taken from the Hubble website. . . . .	148
5.1	Annotated illustration of the geometry of the clouds investigated in this Chapter. . . . .	152
5.2	The distribution of the inclination angle $\varphi$ , which is defined as the angle between the major axis and the $x$ axis as shown in Figure 5.1, of the BRCs in about 10 emission nebulae (Osterbrock, 1957). . . . .	154
5.3	Sequential evolution of the column number density for Cloud G1200(5) with the incline angle $\varphi = 45^\circ$ . Time sequence is left to right, then top to bottom then left to right. Column density is in $\text{cm}^{-2}$ . . . . .	159
5.4	Axial mean density distribution along the $x$ axis of the cloud G1200(5) corresponding to the column density evolutionary snapshots in Figure 5.3.	160
5.5	Magnification of the column density profiles time $t = 0.11$ (left) and $0.13 \text{ Myr}$ (right) at the head of the cloud G1200(5) with $\varphi = 45^\circ$ . Column density is in $\text{cm}^{-2}$ . . . . .	161
5.6	The final snapshot of the column density from six simulations of G1200(5) with different initial inclination angles; left to right, top row then bottom row are: $0, 15, 30, 60, 75$ and $90^\circ$ . Column density is in $\text{cm}^{-2}$ . . . . .	163
5.7	The $x$ displacement of the cores formed in G1200(5) with different initial inclination angles. The short ‘-’ indicates $x_{\text{max}}$ , ‘+’ $x_p$ , ‘o’ for the cores with $10^8 \leq n_{\text{peak}} \leq 10^{12} \text{ cm}^{-3}$ , and ‘•’ for the extremely high density cores with $n_{\text{peak}} > 10^{12} \text{ cm}^{-3}$ . . . . .	164

5.8	The evolution of maximum density of the core(s) in the cloud G1200(5) with different initial inclination angles. . . . .	165
5.9	The variation of the total core mass of the cloud G1200(5) over different initial inclination angles. The symbols and their represented properties of cores are shown in the legend box. . . . .	167
5.10	$x - z$ (top) and $x - y$ (bottom) column density projections for the cloud of $n = 1\,200\text{ cm}^{-3}$ , $\gamma = 2$ and $\phi = 15^\circ$ . Column density is in $\text{cm}^{-2}$ . . . .	169
5.11	$x - z$ (top) and $x - y$ (bottom) column density projections for the cloud of $n = 1\,200\text{ cm}^{-3}$ , $\gamma = 2$ and $\phi = 60^\circ$ . Column density is in $\text{cm}^{-2}$ . . . .	170
5.12	$x - z$ (top) and $x - y$ (bottom) column density projections for the cloud of $n = 600\text{ cm}^{-3}$ , $\gamma = 2$ and $\phi = 15^\circ$ . Column density is in $\text{cm}^{-2}$ . . . .	171
5.13	$x - z$ (top) and $x - y$ (bottom) column density projections for the cloud of $n = 600\text{ cm}^{-3}$ , $\gamma = 2$ and $\phi = 60^\circ$ . Column density is in $\text{cm}^{-2}$ . . . .	172
5.14	Diagrammatic illustration of the observed front convergence and density enhancement. Time advances from left to right, with the blue and red lines representing the initial positive and negative axis surface material (respectively). Yellow circle indicates a position of core formation. . . .	173
5.15	Simplistic representation of motion of the shock front normal to positions along the upper surface of a $\gamma = 2$ cloud for several inclinations. Red dots represent initial surface elements, with blue lines indicating normals to those elements with a length proportional to the square root of the flux at each element ( $\propto v$ ) and the solid green line connecting the final positions after the pseudo-motion. . . . .	174
5.16	The final snapshots of the column density from six simulations of G1200 with $\gamma$ equal to the values shown in the top-left corner of each panel. The inclination angle is $45^\circ$ for all of the initial clouds. Column density is in $\text{cm}^{-2}$ . . . . .	178
5.17	The $x$ displacement of condensed core in G1200 series with an inclination of $\varphi = 45^\circ$ for varied $\gamma$ . The short ‘-’ indicates $x_{\text{max}}$ , ‘+’ $x_{\text{p}}$ , ‘o’ for the cores with $10^8 \leq n_{\text{peak}} \leq 10^{12}\text{ cm}^{-3}$ , and ‘●’ for the extremely high density cores with $n_{\text{peak}} > 10^{12}\text{ cm}^{-3}$ . . . . .	179
5.18	The $x$ displacements of the cores formed in G1200 for each of multiple inclinations and axial ratios, the same for $\varphi = 45^\circ$ can be found as Figure 5.17. The short ‘-’ indicates $x_{\text{max}}$ , ‘+’ $x_{\text{p}}$ , ‘o’ for the cores with $10^8 \leq n_{\text{peak}} \leq 10^{12}\text{ cm}^{-3}$ , and ‘●’ for the extremely high density cores with $n_{\text{peak}} > 10^{12}\text{ cm}^{-3}$ . . . . .	181

5.19	Total mass of condensed cores in cloud G1200 series at an inclination of $45^\circ$ for varied axial ratio $\gamma$ . . . . .	182
5.20	The final snapshot of the column density of clouds of initial mass of $30 M_\odot$ , $\gamma = 2.0$ and $\varphi = 60^\circ$ but different initial densities as shown in the top-left corner of each panel. The ionization flux $F_1 = 1 \times 10^9 \text{ cm}^{-2} \text{ s}^{-1}$ . Column density is in $\text{cm}^{-2}$ . . . . .	184
5.21	The final snapshot of the column density of the same 8 clouds as in Figure 5.20 (initial mass of $30 M_\odot$ , $\gamma = 2.0$ and $\varphi = 60^\circ$ ) but with increased incident flux of $F_2 = 2 \times 10^9 \text{ cm}^{-2} \text{ s}^{-1}$ . Column density is in $\text{cm}^{-2}$ . . . . .	185
5.22	The core formation time of the $F_1$ and $F_2$ group clouds vs. their initial densities. . . . .	186
5.23	The total mass of the cores formed in $F_1$ and $F_2$ group clouds vs. their initial densities. . . . .	186
5.24	The column density evolution of a cloud G400( $F_2$ ), with an inclination angle of $60^\circ$ . This Figure pairs with Figure 5.25, with the same frame times per panel, though note that the colour scale in this figure is specifically column density, whilst the other is cross-sectional density. Column density is in $\text{cm}^{-2}$ . . . . .	188
5.25	The evolution of the RDI induced shock velocity of cloud G400( $F_2$ ) overlapped in the corresponding cross-section density snapshot. The magnitude of the velocity is between 2 and $12 \text{ km s}^{-1}$ . This Figure pairs with Figure 5.24, with the same frame times per panel, though note that the colour scale in this figure is specifically cross-sectional density, whilst the other is column density. . . . .	189
5.26	The final morphologies of the clouds G400( $F_2$ ) of different initial geometry and inclination angle. The axis scales vary between panels, because of the different initial scale of the major- and minor axes for the clouds depicted. . . . .	192

---

# ACKNOWLEDGMENTS

---

For my academic acknowledgements, first must be my supervisor, Dr. Jingqi Miao, who has provided the foundation and support of my research for this PhD. Second would have to be the University itself, which funded the majority of my time spent on this research both directly (my initial studentship) and indirectly (employment first as a demonstrator and later as an hourly lecturer/part-time staff). This thanks extends to the School of Physical Sciences as a whole, and the Centre for Astrophysics and Planetary Science in particular. The staff of the school have been supportive throughout, importantly the postgraduate administrators, initially Sarah Saunders later Sophie Godfrey, as well as recently Helen West.

By far my most important personal acknowledgement is for my parents, Michael and Natalie Kinnear. I owe the extent of my achievements and progress to their unwavering and immense support in all forms they could provide. Ignoring, briefly, the literal interpretation that without them I would not exist; without their personalities, attitudes and care in particular I would not have had a hope of being where I am today, in a position to submit this Philosophical Doctoral thesis.

My thanks extend, also, to my sisters (Sophie, Amy and Hayley), my family's dogs (Rocky, Sally, Ollie and Jack; whose thoughtful contributions of barks, grumbles and tail wags have especially benefited the scientific content), and the friends I have made before and during the (now, many) years of doing my PhD. Your support has succeeded in bouying my spirit throughout. To list every one of your names would be too time (and paper/ink) consuming for this limited acknowledgement. I hope that you each

know who you are.

During my earlier education, I am indebted to the assistance and guidance of those at The Link at Hazelwick, especially Kay and Jane.

Many people have contributed both as friends but also assisting with progress on the work itself. I would like to thank Michael Knight especially amongst these people, with whom I had many discussions of the concepts I have worked with, and whose assistance has helped me work out many tricky aspects of an assortment of topics for the entire duration of my work here.

This thesis was typeset with L<sup>A</sup>T<sub>E</sub>X 2<sub>ε</sub><sup>1</sup> by the author.

---

<sup>1</sup>L<sup>A</sup>T<sub>E</sub>X 2<sub>ε</sub> is an extension of L<sup>A</sup>T<sub>E</sub>X. L<sup>A</sup>T<sub>E</sub>X is a collection of macros for T<sub>E</sub>X. T<sub>E</sub>X is a trademark of the American Mathematical Society. The style package *warwickthesis* was used in an adapted format for the University of Kent thesis guidelines.

---

# DECLARATIONS

---

The content herein was composed by the author, and has not been submitted for the purposes of a qualification at any other institution or for any other degree.

The content comprising Chapter 4 was adapted and extended from work which has been published as Kinnear et al. (2014).

The content comprising Chapter 5 was adapted and extended from work which has been published as Kinnear et al. (2015).

All data is the author's own, unless explicitly stated otherwise. All instances where use has been made of other work has been cited.

---

# ABSTRACT

---

When massive stars form, they emit strong, hydrogen ionising radiation fields into their molecular cloud environment, forming HII regions. This is believed to be capable of inducing effects which can trigger further star formation through a process known as Radiative Driven Implosion. Hydrodynamic shock fronts are generated at the interface between ionised and un-ionised material. These shocks propagate into the clouds, and their motion and increase in density can result in the conditions required for star formation.

Using the method of Smoothed Particle Hydrodynamics, the effect of varied initial geometrical and physical properties of a molecular cloud on the prospect of radiation triggered star formation is investigated over a large parameter space. The physical processes of the model include a detailed ray-tracing implementation of the ionising radiation, along with a thermodynamic model and chemical evolution for multiple species of atoms.

A parameter  $d_{\text{EUV}}$ , defined as the ratio of the initial ionising penetration depth to the scale length of the cloud along the radiation axis, was found to be an effective indicator of the final evolutionary prospects of the molecular clouds investigated. Low  $d_{\text{EUV}}$  clouds typically exhibit shock front motion which converges on a focus or foci, and form symmetric or asymmetric B or C type Bright Rimmed Clouds depending on orientation. At medium  $d_{\text{EUV}}$  there is a mixture of focus/foci convergent and linear or filamentary structure formation with cores formed indirectly, after disruption of material by the shock fronts. At high  $d_{\text{EUV}}$  only fragment-core and irregular structures form, with the clouds being increasingly dominated by photoevaporation. At extremely high  $d_{\text{EUV}}$  cores cannot form and the cloud will photoevaporate.

In addition, qualitative impressions of the scope of structure morphologies, especially those for irregular morphologies, is compiled. Of note, it is found that the simple initial conditions of a uniform prolate cloud at inclinations to incident radiation are capable of producing a wide variety of the structures observed at HII boundaries.

# CHAPTER 1

---

## INTRODUCTION

---

An initial narrative overview to the processes being investigated is presented here, with all elements expanded upon later in the text.

The cycles of stellar evolution permitted the existence of a small bluey-green planet, third out from a G2V class star in an outer spiral arm of an SBb galaxy and, as a result of that, this very document. Much of those same cycles which resulted in this confluence of circumstances, remains something of a mystery. It is, then, of great interest to determine and understand the processes involved in stellar evolution. Importantly, an understanding of stellar evolution is one of (admittedly several) lynch-pins in the understanding of the whole chain of astrophysical interactions which link everything from cosmological scales down to planetary formation and solar system dynamics.

One process involved in the formation of stars also presents a peculiar dichotomy of destruction and creation, feedback. The result of this process can be examined on various scales, from the modification of the immediate environment around a protostar, to stellar winds and radiation across star forming regions, up to supernovæ, releasing enormous quantities of energy on timescales which would be short to us, let alone astrophysically. The topic of interest for this thesis is ionising radiation feedback, such as found in HII regions.

When a massive star forms (though, how it does that is another major question in itself), it will reach a point at which its radiation output increases substantially. This occurs on relatively short timescales, and results in an expanding spherical front

(subject to surroundings), propagating and ionising the region around the star. For the first period of the ionising radiation's expansion, it does so as an R-type front ('R' being 'rarefaction', indicating the low densities involved), with the nature of the expansion being supersonic relative to the material upon which the radiation is incident. The ionisation front fans out, ionising material faster than the material is able to react hydrodynamically, creating a diffuse, but high temperature and pressure, region, referred to as an HII region.

As the radiation fans out further, a combination of the increasing area over which it is incident (going as  $r^2$ ) and the attenuation in the inner material, means that the flux decreases to a point at which the ionisation front transitions from a supersonic R-type to a subsonic D-type ('D' being 'dense'). At this stage, the ionisation front advances more slowly than the hydrodynamic shock wave produced by the pressure discontinuity between ionised and non-ionised material.

It is of interest to us to examine the interaction of the ionising radiation with a dense (relative to ISM) cloud structure. Specifically, in sequence, the formation of an ionised region of the cloud, followed by the shock front generated at the interface between the ionised and neutral material when the ionisation front becomes D-type, then the motion of that shock front into the cloud.

The dichotomy previously mentioned is this: such effects can very easily eliminate all chances of a cloud undergoing gravitational collapse and star formation. Material is swept up, ionised and dissipated, easily winning out against the relatively weak binding force of gravity. However, the ionisation heating induced shock propagates into the neutral material of the cloud, creating high density structures, which enhance self-gravity. When this effect is strong enough, the high density structures can form cores, further collapsing to create a protostar. This process is Radiative Driven Implosion (RDI). This permits, through RDI, stars to form in neutral clouds which otherwise could not collapse to form a star (or stars) with their own initially weak self-gravity.

Full analytical treatment of this problem is beset by the difficulties in solving the highly non-linear astrophysical fluid dynamics equations for a non-isotropic environment, with infeasibly large systems of interconnected variables required to fully describe the scenario. Whilst analytical solutions to some of the simpler configurations of a particular scenario can be constructed, arbitrary geometries and complex density structures cannot be described. It is the aim here to provide an insight, using the computational method of Smoothed Particle Hydrodynamics (SPH), into the effect of varied cloud properties, especially geometry, on the evolution and potential for such clouds to be hosts of triggered star formation.

Element	$\log_{10} \mathcal{A}_i$	Element	$\log_{10} \mathcal{A}_i$
He	-1.00	C	-3.44
O	-3.34	Si	-4.45
Mg	-4.41	Fe	-4.49
S	-4.73	N	-3.95

Table 1.1: ISM elemental abundances relative to total hydrogen number density ( $\mathcal{A}_i = n_i/n$ , where  $n = n_{\text{HII}} + n_{\text{HI}} + n_{\text{H}_2}$ ) from Wolfire et al. (1995).

## 1.1 MOLECULAR CLOUDS AND THE INTERSTELLAR MEDIUM

---

Current generation star formation predominantly takes place inside Giant Molecular Clouds (GMC) (Blitz, 1993; Williams and McKee, 1997; Wong and Blitz, 2002). They possess the largest localised reservoirs of molecular hydrogen available to fuel the star formation process, by whichever actual star forming mechanism (Burton, 1976; Williams and McKee, 1997; Wong and Blitz, 2002). This makes the molecular cloud environment and the Interstellar Medium (ISM) important to understand in order to provide the circumstances and initial conditions required for star formation itself.

GMCs are typically regions of the order of  $10^5 M_{\odot}$ , tens of Parsecs in linear dimension, and average densities of tens of particles per cubic centimetre (Stark and Blitz, 1978; Blitz, 1993). However, their exact definition, and specific ranges of properties are difficult to delimit to agreement. They are also known to be ‘clumpy’ on a wide variety of length scales (Larson, 1981; Shu et al., 1987; Williams et al., 1994, 2000) that is, that they are composed of substructure rather than purely uniform. Part of the difficulty in their analysis and categorisation is their composition: cold (10 K) molecular hydrogen -  $\text{H}_2$ .  $\text{H}_2$  at this temperature is not directly observable, lacking excited states. Several methods exist for measuring it indirectly using various ‘tracers’, molecular lines and other signs which are expected to have a relation to the abundance of  $\text{H}_2$ , especially extinction and line emission from several isotopic forms of carbon-monoxide CO (Tan et al. (2013) includes a good summary).

The average ISM composition which will prove a good basis for the initial chemistry conditions is shown in Table 1.1.

## 1.2 STAR FORMATION IN MOLECULAR CLOUDS

---

Because molecular clouds provide the raw material in the quantities required for the mechanisms of star formation to take place, it is a common phrase that ‘star formation occurs in molecular clouds’ (Blitz, 1993). Whilst isolated star formation may occur, for instance in Bok Globules (Bok and Reilly, 1947; Yun and Clemens, 1990), by pure weight of matter it is bound to be substantially rarer, making star formation in the more common molecular clouds more likely to be important in overall stellar statistics and population evolution.

### 1.2.1 GRAVITATIONAL COLLAPSE

Gravitational collapse is generally described in the context (for non-massive star formation) of the local medium exceeding some critical mass for its density and scale (McKee and Ostriker, 2007). Once the point of criticality is passed, the balance of gravitational potential against thermal and net-kinetic energies falls in favour of gravity and the structure constricts.

Massive stars are thought to require more complex conditions, or conditions which are at least not fully elaborated. ‘Massive’ can constitute a range of masses from  $8 M_{\odot}$  and above, up to over  $100 M_{\odot}$ . Stars of this mass range are small in number, being  $< 1\%$  of all stars or  $\approx 10\%$  of the number of stars of masses 1 to  $2 M_{\odot}$  (using the modified Salpeter Initial Mass Function (IMF) of Kroupa (2001)), but are of considerable importance; not least due to the substantial effect they can have on their surroundings, as will become evident.

The peculiarities in the formation of massive stars are due to several features of known processes preventing accumulation of such mass via the same mechanisms as lower mass stars. For instance, the luminosity of the protostar becomes sufficiently large as to prevent further accretion before high stellar masses can be reached (Larson and Starrfield, 1971); i.e. the so-called Eddington luminosity (beginning with Eddington (1916) for ‘classical’ Eddington luminosity). More recent work has expanded the description, with better understanding of physical processes within stars, see for example Hennebelle and Commerçon (2012) (published in Stamatellos et al. (2014)). Massive star formation is therefore believed to necessitate a different manner of collapse, requiring turbulent cores within a large cluster, for instance (McKee and Tan, 2002); or a multi-stage process (Zinnecker and Yorke, 2007) in order to result in the quantity and size of massive stars known to exist through observation.

The exact details of massive star formation are incidental to the effect they have on their environment, forming HII regions, as outlined in Section 1.3.

Low-mass star formation retains mysteries of its own, but a general picture is available describing the expected path.

A key reference point for the collapse of gas is that of the Jeans parameters. Tracing roots back to Jeans (1902), these parameters describe analytical conditions of, and behaviour of, collapse of a symmetric, isothermal cloud of gas. These descriptions have been updated with time, as more has come to light regarding expected factors contributing to collapse, but the underlying concept remains as a basis for comparison with any subsequent description. The Jeans' mass and Jeans' length can be given as,

$$M_{\text{Jeans}'} = \frac{4 \pi}{3} \frac{c_s^3}{\sqrt{G^3 \rho}}, \quad (1.1)$$

$$R_{\text{Jeans}'} = \frac{c_s}{\sqrt{G \rho}}, \quad (1.2)$$

where  $c_s$  is the characteristic sound speed,  $G$  the gravitational constant and  $\rho$  the characteristic density. The nature of what constitutes 'characteristic' is circumstance dependent (McKee and Ostriker, 2007).

A more comprehensive description of the critical mass is that of the Bonner-Ebert mass (Bonnor, 1956; Ebert, 1957). In this, self-collapse accounts for conditions of the Virial theorem applied to the gravitational energy along with multiple supporting kinetic energies. The results here are obtained independently from the assumptions regarding density used for the Jeans' Criteria, instead, they are from modified descriptions of gas properties from Boyles' law. An equation with very similar form to that of Jeans' mass is obtained (as would be expected). Similarly to Equations (1.1) and (1.2) the Bonner-Ebert mass and length can be given as,

$$M_{\text{Bonner-Ebert}} = 1.182 \frac{\sigma^3}{\sqrt{G^3 \rho_0}}, \quad (1.3)$$

$$R_{\text{Bonner-Ebert}} = A \frac{\sigma}{\sqrt{G \rho_0}}, \quad (1.4)$$

where  $\rho_0$  is the surface/boundary density of the cloud and  $\sigma$  is the mean-square gas velocity;  $A$  is a density profile factor which is frequently given as either  $A \approx 0.66$  for a simple mean density sphere (Krumholz, 2011); or  $A \approx 0.486$  for a Bonnor-Ebert profile (McKee and Ostriker, 2007).

Collapse of these idealised spheres occurs on timescales of the order of the freefall time (Spitzer, 1978; Dyson and Williams, 1997),  $t_{ff}$ , the time taken for the cloud to fall in to a point from pure gravity (excluding hydrodynamic effects of pressure preventing

collapse). The potential at a point location within a cloud at any time is a function of the radial position from the centre of mass of that point and the total mass enclosed at all smaller radii (with spherical symmetry assumed). Integrating the equations of motion with this in mind provides the gravitational free-fall time as,

$$t_{ff} = \sqrt{\frac{3 \pi}{32 G \rho}}, \quad (1.5)$$

with  $\rho$  in this case being the initial mean density of the cloud (i.e., that which can be defined as  $\rho = M/(\frac{4}{3}\pi R^3)$ , with  $M$  the total mass and  $R$  the outer radius).

This gives an impression of the required timescales, but represents only a bound on the realistic collapse times, as it does not account for any of the thermodynamic changes undergone by the core during its collapse. In particular, it describes neither the pressure gradient forces, nor the change from isothermal to adiabatic as the core reaches densities at which it becomes opaque to emission from excited molecules deeper within.

Once the opacity changes in this way, energy is ‘trapped’ in the core and, with the existing inertia of the collapse to that time, continues to compress whilst increasing in temperature. Collapse soon becomes inhibited by the increasing pressure which results, but at the same time, chemical changes (specifically dissociation of molecular hydrogen) uses more energy from the system and results in a further pseudo-isothermal collapse and increase in core mass. This continues until energy ceases to be used in dissociation, and the temperature and pressure rise to produce a supported central core; the protostar proper. This pattern is described, and evaluated numerically, as early as Larson (1969).

The basic premise of the pattern remains broadly similar today, with the gradual evaluation and inclusion of other expected physical effects and processes; along with values being refined as better data became (and continues to become) available for the assumptions. The range of alterations to the basic model is extensive. One can consider rotation (Norman et al., 1980; Terebey et al., 1984), micro- and macro-scopic turbulence (Lizano and Shu, 1989) and magnetic fields (McKee et al. (1993) for an early review of several magnetic effects) to name a few key developments. It is not the intention here to describe the full process of the formation of core and star in much detail, as it is almost tangential to the topic of the environment in which the process is permitted, which is the key interest of this thesis. A far more adept description of the process can be found in, for example, Shu et al. (1987); McKee and Ostriker (2007).

### 1.2.2 TRIGGERED STAR FORMATION

Whilst star formation via gravitational collapse is fairly well understood and categorised for non-massive stars (at least, as far as any topic in star formation goes), a greater unknown is that of other mechanisms of star formation. Triggered star formation is the process in which the behaviour of some factor external to a region, drives circumstances for star formation where otherwise closed internal behaviour of that region may not. This can be accomplished by any external factor capable of either directly altering the density profile within a molecular cloud, or driving a shock into the cloud which reaches sufficient densities for material to begin collapsing into a protostellar core.

Amongst these triggering processes are compression by stellar wind (Foster and Boss, 1996), driven turbulent motion (Elmegreen, 2002), or even potentially supernovæ, either directly, or as a driver of turbulence (Cameron and Truran, 1977; Elmegreen, 2002; Gritschneider et al., 2012; Li et al., 2014). The last-most of these is also of interest due to the possibility for it to have been the formation mechanism for the solar system (Cameron and Truran, 1977; Gritschneider et al., 2012).

The focus of the understanding of triggered star formation in this context is Radiative Driven Implosion. In this mechanism, the formation of HII regions results in the expansion of an ionisation front up to the surfaces of pre-existing clumps / overdensities within the overall cloud (Reipurth, 1983; Bertoldi, 1989; Lefloch and Lazareff, 1995). Shock waves formed at the surfaces of these objects propagate inwards, and the density increase from this effect is thought to be capable of triggering star formation. This differs from other descriptions such as ‘Collect & Collapse’ (C&C), in which expansion of the ionisation front is through a sufficiently uniform medium that triggering is due to the fragmentation of a dense shell generated spherically around the expanding region (Elmegreen and Lada, 1977). The latter has been extensively analysed e.g. (Deharveng et al., 2005; Zavagno et al., 2006; Dale et al., 2007), but may not explain all scenarios (Pomarès et al., 2009; Deharveng et al., 2010). RDI may complement C&C depending on the nature and character of the molecular cloud and HII regions. In particular, the balance of the two mechanisms may be determined by the anisotropy of the initial neutral medium into which the HII region expands (Pomarès et al., 2009; Walch et al., 2012).

The concept of triggered star formation by RDI has been supported on bases of observation (Morgan et al., 2008; Chauhan et al., 2009; Hayashi et al., 2012) as well as computational simulation (e.g. Miao et al. (2006, 2009); Bisbas et al. (2011b), see Section 1.5.3 for more).

## 1.3 HII REGIONS

---

Radiation with photon energies  $h\nu > 13.6$  eV is capable of photoionising atomic hydrogen. Into a predominantly hydrogen medium this changes the hydrodynamic properties of the gas directly, as ionised hydrogen has a mean molecular mass half that of atomic; as well as changing its temperature, as photons with greater than the ionisation threshold deliver additional energy into the resulting electron/proton.

Balancing the strong photoionisation heating effects are the cooling effects of optically thin line emission. Key among these is the collisionally excited OII emission; emission from this excited state resulting in production of photons which are not locally reabsorbed. Escaping the region, this represents a net ‘loss’ of energy from the system, and contributes to the balance between heating and cooling present in the region. Many transitions contributing to this cooling are in the category of ‘forbidden’ lines, excitation states which would usually be collisionally de-excited, but in the low densities of the HII region are given the time necessary to decay via emission of these optically thin lines.

This readily alters a gas which would be expected to be approximately 100 K with sound speeds of the order of  $1 \text{ km s}^{-1}$  to gas at  $\approx 10\,000$  K and  $\approx 13 \text{ km s}^{-1}$  (for isothermal sound speeds).

Such environments are created in the vicinity of massive stars, with surface temperatures sufficient to generate ionising fluxes capable of substantially affecting their environments. O stars can produce ionising photon luminosities in the range of  $5 \times 10^{47}$  to  $1 \times 10^{50} \text{ s}^{-1}$  (emission surface fluxes of approximately  $8 \times 10^{22}$  to  $7 \times 10^{24} \text{ cm}^{-2} \text{ s}^{-1}$ ) (Sternberg et al., 2003).

Initial behaviour of these massive stars involves a wave of radiation expanding spherically outwards from the star. Initially, this wave travels greatly supersonically relative to the sound speed of the undisturbed material. This ‘R’-type (for ‘rarefaction’) front continues to expand, with material overtaken by the front faster than that material is able to react hydrodynamically. This high temperature/pressure region is the early HII region.

As this spherical shell expands, the volume of material to be ionised increases cubically with radius, with the number of available ionising photons per unit area of the shell decreasing as the inverse square of radius. At some radial position, the front will reach a point at which all available photons are used re-ionising hydrogen atoms within the sphere which have undergone recombination, rather than be available for entirely new ionisation events. As this transition is approached, the speed of the front

reduces to sub-sonic, a D-type front (for ‘dense’). In this circumstance, material is forced into a shock front ahead of the ionisation front. This is the mechanism for the triggered star formation being investigated.

Pictured in Figure 1.1 is Messier 16, most commonly known as the *Eagle Nebula*. With visually stunning features, it is arguably the most well known of the HII regions. The central ‘cavity’ region, surrounded by the bright rimmed clouds and darker molecular gas, is the HII region itself. It is fascinating in and of itself, being the centre of multiple studies; an overview of its features in the context of star formation can be found by Oliveira (2008).

More details of the exact behaviour and physics of HII regions is present in Chapter 3, pertinent, as it is, to the description and implementation of the ionising radiation field needed for the code.

## 1.4 BRIGHT RIMMED CLOUDS

---

The edges of the HII regions, with their strong HII recombination emission lines contrast with the darker, obscuring molecular medium beyond ionisation front. This has made such features identifiable in observations and has long been catalogued and categorised, such as in Deharveng and Maucherat (1975); Lada and Black (1976); Hayashi et al. (1985), as a few examples. It is from their bright outline that their description as ‘Bright Rimmed Clouds’ (BRCs) is derived (earlier references sometimes to ‘Bright Rimmed Molecular Clouds’, BRMCs). In this section, the general structure morphologies, and existing nomenclature is examined.

Continuing the theme of the *Eagle Nebula* mentioned at the end of the previous section, pictured in Figure 1.2 are the ‘*Pillars of Creation*’, BRC features at the edge of the HII region.

### 1.4.1 REGULAR STRUCTURES

A catalogue of BRCs was compiled by Sugitani et al. (1991) and Sugitani and Ogura (1994) using a system of classification in which categories of BRCs are delineated by the overall curvature of the bright rim. This was a broadly qualitative distinction, based on the impression of their morphology. The groups were notated A, B and C BRCs, in order of increasing curvature. Type A BRCs are wide, low-curvature, ‘hill’-like features; type C BRCs are ‘cometary’ types, with a ‘head’ and a straight or tapered ‘tail’; and type B BRCs are those that fill the divide between clear type As and type Cs.

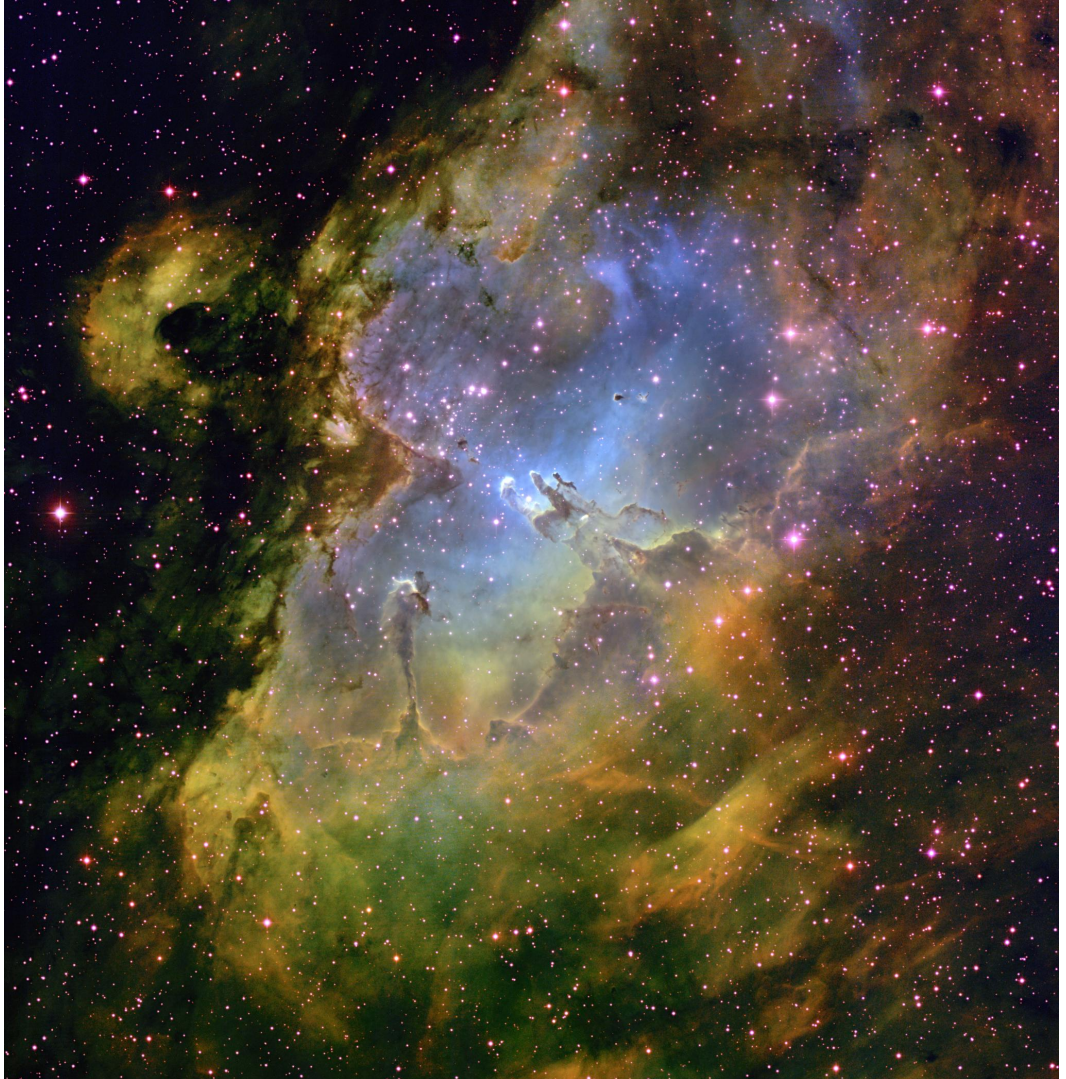


Figure 1.1: View of the entire M16 *Eagle Nebula* region. Taken by the National Science Foundation's telescope on Kitt Peak, it is a false colour image with red, green and blue corresponding to narrow-band observation in SII,  $H\alpha$  and OIII respectively. Image credit: T.A.Rector (NRAO/AUI/NSF and NOAO/AURA/NSF) and B.A.Wolpa (NOAO/AURA/NSF).



Figure 1.2: View of the ‘*Pillars of Creation*’ in the M16 *Eagle Nebula*. As with Figure 1.1, the colours red, green and blue map to observations in SII,  $H\alpha$  and OIII respectively. Image taken by the Hubble Space Telescope (HST), image credit: NASA, ESA, and the Hubble Heritage Team (STScI/AURA). This image in particular is a repeat observation (Jan, 2015) of a commonly used image taken by the HST in 1995.

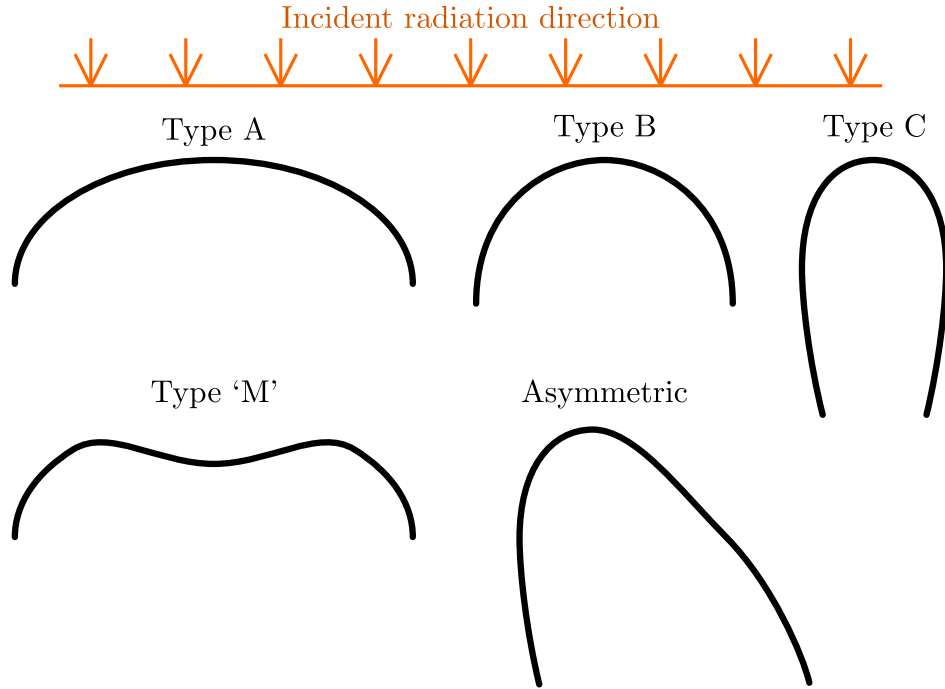


Figure 1.3: Diagrammatic representation of standard type A, B and C bright rimmed clouds, along with the type ‘M’ extension (Miao et al., 2010), and asymmetric morphologies. All are presented relative to the illuminating source as indicated.

The illustration in Figure 1.3 gives a general indication as to the degrees of curvature of each of the groups. In the four panels of Figure 1.4 are images of BRCs and their types from Digitized Sky Survey (DSS) data. The BRCs selected are from Sugitani et al. (1991) in which a catalogue was constructed for the northern hemisphere, but the images are taken from the specific sources listed in the figure caption.

A further category of BRC was posited, a type M morphology with observational and simulation support (Osterbrock, 1957; Karr et al., 2005; Urquhart et al., 2006; Miao et al., 2010), for high ionisation-state conditions; this is also illustrated within Figure 1.3.

#### 1.4.2 ASYMMETRIC STRUCTURES

Of the observed BRCs, when examined in detail, many do not fit in to a straightforward classification system. The major deviation from the basic curvature classifications are the presence of asymmetric structures, with different, or discontinuous, curvature either side of the axis between the ‘head’ or centre of the cloud and the illuminating star. Due to the expected ‘clumpy’ substructure of all molecular cloud regions, from both theory and observation (Williams et al., 2000), it can be expected that the region through which the ionisation front of an HII region expands will not be uniform, and will

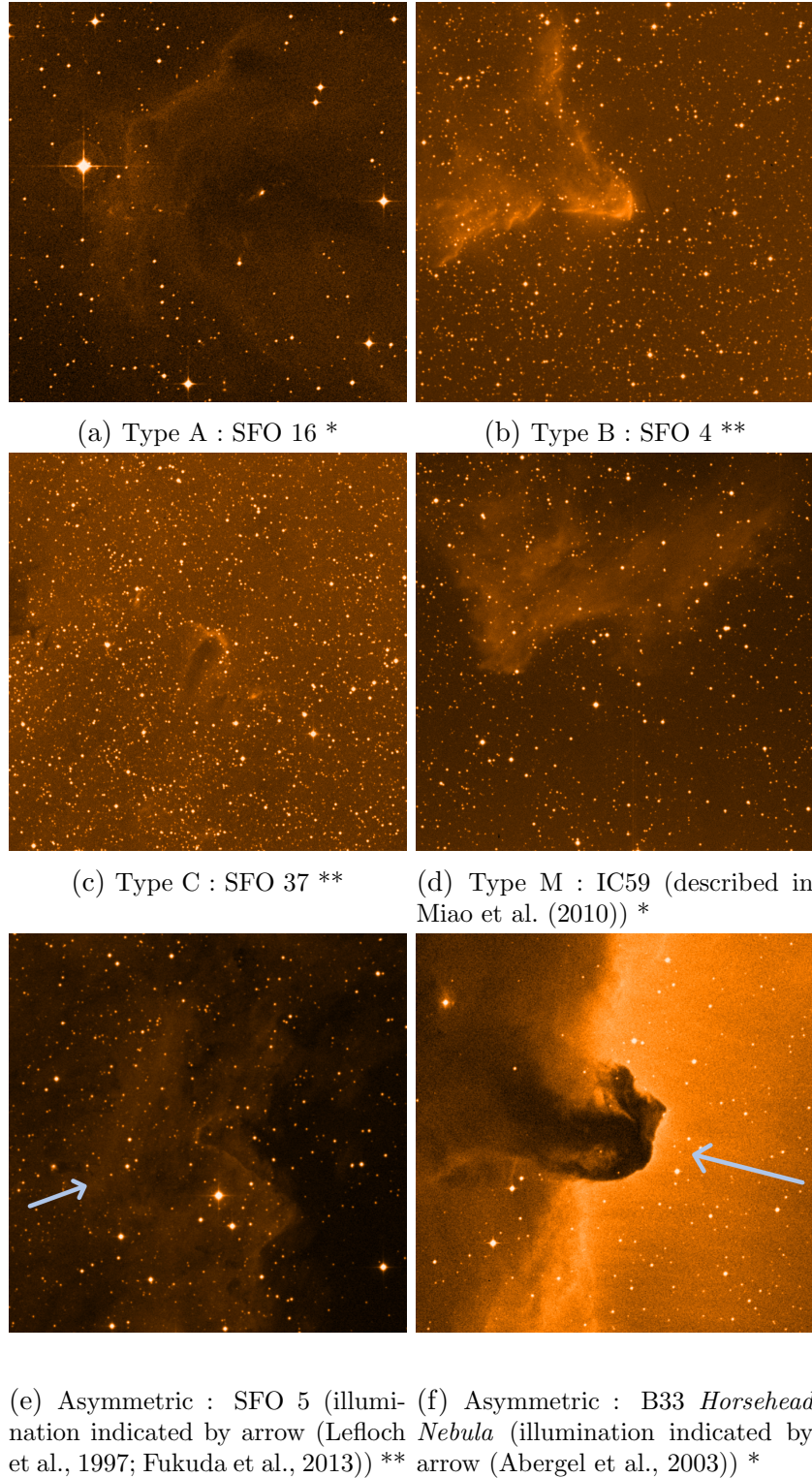


Figure 1.4: Images of BRCs and a MC illustrating the basic variation in morphology for the A/B/C/M type classifications of surface curvature, as well as two examples of irregular morphology (B33 being non-BRC). Images via Wenger et al. (2000) of DSS-2-Red data. All are presented as 15' by 15' in the ICRS frame.

\* Copyright © 1993-2000 by AAO and AURA

\*\* Copyright © 1992-2000, Caltech and AURA

feature density variations throughout. In such non-isotropic environments, assumptions of spherical initial conditions and symmetric structures of early models may not be sufficient. The generation of asymmetric structures may be explained by the presence of ‘oddly shaped’ initial structures during the formation. The gist of such morphologies is also illustrated in Figure 1.3.

An example of an asymmetric BRC is also presented in Section 1.4.1, SFO 5. In this instance the shape of the outer surface is not aligned with the axis of the incident illumination, illustrated with the arrow. Another, indirect, example which may owe aspects of its evolution to the same effects being described is shown in Section 1.4.1, the *Horsehead Nebula*. It is present in a photo-dissociation region (PDR), rather than directly on an HII boundary. However, it presents several of the features which are common to asymmetric BRCs, as well as being pertinent to results presented in Chapter 5, in which morphologically similar structures are generated.

## 1.5 THEORETICAL MODELS OF RDI

---

Multiple models exist, and have existed, to describe some of the aspects of BRCs and the HII regions at which they are formed. Here a brief summary of their scope and nature is given, though it is not exhaustive. Some key work includes the description of the scenario by Elmegreen and Lada (1977) and Whitworth (1979), which outlines many of the parameters and behaviours of the interaction of a growing HII region with its environment.

### 1.5.1 SEMI-ANALYTICAL

An important description of the dynamics of inwards directed shock fronts for a spherical molecular cloud (or spherical over-density within a diffuse medium), is given by Bertoldi (1989) and Bertoldi and McKee (1990). This also forms the basis for the subsequent numerical models of such regions, for it provides a basis of comparison between simulation and theory. Axi-symmetric spheres and the evolution of the shocks at their illuminated surface were examined, as well as the fate of the clouds which host them. Importantly, the work illustrates that within a substantial region of the parameter space, the ionisation front entering the cloud forms the necessary inwards-directed shock conducive for RDI.

### 1.5.2 NUMERICAL MODELS WITHOUT GRAVITY

As theoretical models were available for comparison for collapse of symmetric spheres, this provides an ideal starting point for many simulations. These circumstances have been studied extensively, and have shown formation of symmetric C type BRCs, along with potential embedded protostellar cores in investigations such as by Lefloch and Lazareff (1994). This work examined the evolution of lower mass (a maximum of  $20 M_{\odot}$ ) globules exposed to ionising radiation expanding upon similar 2D calculations by Sandford et al. (1982). These provide an insight into the underlying mechanics of the shock dynamics, but there exists a substantial parameter-space which has not yet been investigated for small scale (single molecular cloud) variations in initial shape, morphology and symmetry/asymmetry.

In addition, these early models tend to omit self-gravity. This can only be dismissed (as it was, in Lefloch and Lazareff (1994)) for low mass clouds, which can be expected to be magnetically supported against gravitational collapse. More massive clouds, or those for which support from magnetic effects cannot be assumed, require more detailed physics within the model.

### 1.5.3 IMPROVED NUMERICAL MODELS

As observational capabilities have provided more reference data on which to base models, and computational power has increased, the scope of numerical models has been able to expand and become more accurate. Small to medium scale models (individual clouds up to clusters of clumps) have been investigated from a variety of perspectives (Kessel-Deynet and Burkert, 2003; Miao et al., 2006, 2009; Gritschneider et al., 2009b; Miao et al., 2010; Bisbas et al., 2011b; Haworth and Harries, 2012; Tremblin et al., 2012). These models have increased the resolution and expanded the scope of the physics of the scenario, importantly including gravity in many cases, enabling the observation of core formation and the potential for protostars.

With expanded conditions, the entire range of regular BRC morphologies can subsequently be generated, as well as sequence them as a potential evolutionary chain  $A \rightarrow B \rightarrow C$ , as shown in Miao et al. (2009).

Tremblin et al. (2012) illustrates that the shape of the upper surface of a molecular cloud or density enhancement has substantial effects on the development of, for the parameter space investigated by them, pillar-like structures, but a wider general effect on surface morphology as a whole.

In addition to investigation of individual cloud features, investigation has been performed into large scale structures. This permits the evaluation of entire H II regions and

associated star formation statistics across the whole of a simulated region, combined with the interplay of numerous physical effects (Dale et al., 2005, 2007; Walch et al., 2012). Whilst this provides a useful (and in most cases spectacular) insight into this large scale behaviour, it leaves little leeway for exhaustive investigation of parameter space, as each simulation becomes sufficiently substantial as to require computational resources exceeding the capability to run a large number of instances of the model.

## 1.6 LIMITATIONS OF EXISTING NUMERICAL INVESTIGATIONS

---

Whilst large-scale simulations have an advantage in providing a wider scope, and more natural evolution of some features, there remains an advantage in investigating some effects on a smaller scale, in order to better characterise individual cloud features and behaviours, and finely observe a portion of the parameter space for initial conditions.

Investigations of initially spherically symmetric models have an automatic disadvantage in that, although it is a useful way to describe symmetric BRC structures, it is unlikely to reveal the formation mechanism for asymmetric BRC, such as the example in Figure 1.4. Symmetric initial conditions are bound to tend towards symmetric results. It can be seen from existing analysis of observed molecular clouds and cores, that the projections of cloud structures and substructures, at least, are ellipsoidal (Jones et al., 2001; Myers et al., 1991; Curry and Stahler, 2001; Rathborne et al., 2009). Whilst this does not definitively state their 3D shape due to the lack of depth information, a reasonable approach is to consider them as simple ellipsoidal structures; prolate or oblate ellipsoids.

The alternative, tri-axial ellipsoids, with all three axes different lengths, remains fairly likely; some theoretical investigations show an even distribution between broadly prolate and true tri-axial as well as some oblate structures (Jones et al., 2001; Gammie et al., 2003; Li et al., 2004). However, all tri-axial cloud populations modelled have suggested at least a sizeable fraction ( $\approx 41\%$  by one metric in Gammie et al. (2003)) which are broadly prolate. At worst, ellipsoidal clouds represent only a portion of clouds that exist, albeit a substantially more sizeable portion than spherical. In addition to the difficulties imposed by the vastly increased parameter space of true tri-axial clouds, it makes for a reasonable choice to investigate the more accessible option of ellipsoidal clouds first.

## 1.7 AN UPDATED MODEL

---

It is the intention of this thesis to attempt to characterise the kinematics and outcome morphologies of BRCs formed by the exposure of ellipsoidal uniform density molecular clouds to plane-parallel Extreme Ultraviolet (EUV, hydrogen ionising) radiation. Investigated herein will be a comprehensive combination of axial ratios, densities, ionising fluxes, and inclinations to the radiation to induce asymmetric formation. The physical processes of the model include a detailed ray-tracing implementation of the ionising radiation, along with a thermodynamic model and chemical evolution for multiple species of atoms.

## 1.8 THESIS STRUCTURE

---

**In Chapter 2, the computational methods underpinning this research are described.** This begins with the physical context into which the codes fit, especially what makes such codes suitable for describing the environments being modelled. Following this, the key equations of hydrodynamics which chain the numerical methods to the realities which they attempt to describe are presented. This is expanded upon with a look at the ‘non-standard’ physical processes which are (or are not) present in the scenario being modelled. Where relevant, this includes the reason for their inclusions or the justifications for being left out of the final model. The different approaches to hydrodynamics are then described, with emphasis on their suitability and limitations. Then, a description and brief history of the code used for this research is provided.

Subsequent sections of this chapter then deal with the exact implementations of the physical and computational processes in the code. This begins with the SPH method itself, then the addition to the code of chemistry processes and thermodynamics, the use of a Barnes-Hut ‘oct-tree’ for nearest neighbour and gravitational computation and the inclusion of isotropic far-ultraviolet (FUV) radiation. Finally, an examination is made of the manner in which initial conditions can be generated, which possess as many of the characteristics thought of as ‘ideal’ and as few of the inevitable drawbacks.

**In Chapter 3 the process key to the RDI mechanism is examined: the treatment of the ionising radiation.** For this research, an ionising radiation propagation routine was written from scratch, based on a model and algorithm produced by Kessel-Deynet and Burkert (2000). The chapter begins with an introduction to the

relevant physics, connecting with the specific scenario of the HII regions described in Chapter 1. This is then followed by a full description of the algorithm as implemented, with mention of expansions and modifications not deemed required for this thesis, but viable for future addition. Following this, a section covers the testing performed on the algorithm and code, comparisons with theory on various different metrics, and basic comparison with similar codes. This also incorporates the results of tests conducted on the code to determine that the theoretical suitability of the methods used are met in practice with this code in particular for convergence, and the uncertainties present in the results.

The final section of this chapter deals with the derived property ‘ $d_{\text{EUV}}$ ’, a value describing the ratio between the equilibrium penetration depth of the ionising radiation, and the longest scale length in the direction of radiation propagation. The value is used extensively for the description and categorisation of results, and is pertinent to a number of physical parameters of the clouds being investigated.

**The first major results are presented in Chapter 4, much of the content of which has been published as Kinnear et al. (2014).** This chapter deals with an HII boundary scenario in which prolate clouds of a variety of masses, densities and axial aspect ratios are subjected to incident ionising radiation perpendicular to their semi-major axes. The evolutions and properties of several series of cloud simulations are examined by various methods. The initial sections of the chapter deal with the definition and explanation of the problem, then the methods used to examine the results to find meaningful quantities and qualities. A program, `corefinder`, is described and used to investigate the properties of cores formed in the simulations.

**In Chapter 5, the parameter space of the simulated clouds is extended to cover those with semi-major axes at various inclinations to the incident radiation; with content which has been published as Kinnear et al. (2015).** The additional asymmetries introduced by this problem are examined, as well as further use and expansion of the methods of analysis used previously in Chapter 4.

**In Chapter 6, the conclusions are drawn and prospects of future work evaluated.** Summaries spanning both results chapters are presented, as well as several overviews of future topics which can be covered including sequential star formation, synthetic observations, comparisons with observations and further variations to the geometric initial conditions.

Throughout this thesis, rendered plots for SPH particle properties were produced using the `SPLASH` plotting code (Price, 2007). All other plots (unless otherwise stated) were produced in `Python` (Rossum, 1995) using the `matplotlib` plotting library (Hunter, 2007). The `Python` modules `NumPy` and `SciPy` were also used extensively for analysis

and plotting (van der Walt et al., 2011). Diagrams (unless otherwise stated), were produced using the **Inkscape** vector graphics utility (Inkscape Team, 2014).

## CHAPTER 2

---

# SMOOTHED PARTICLE HYDRODYNAMICS CODE

---

The dynamics of much of the universe on astrophysical scales can be described using fluid mechanics. This ranges from scales of planetary formation (e.g. Armitage (2011)), to stellar structure (e.g. Mihalas (1978)), individual and cluster star formation (McKee and Ostriker, 2007), giant molecular clouds (e.g. Dobbs and Pringle (2013)), galaxy evolution (Marinacci et al., 2014), and multiple galaxy interactions (Springel et al., 2005). Despite this multiple order of magnitude range, the majority of the underlying techniques and processes are common across many or all these scales, for instance the use of the almost ubiquitous viscous disk description of Shakura and Sunyaev (1973). This huge range of applicability makes an understanding of hydrodynamics a highly investigated and developed field.

Though the equations of hydrodynamics can describe the underlying mechanics of the scales and situations described, modelling these scenarios analytically rapidly encounters problems. The structures involved or distributions of properties are frequently inhomogeneous, with complex geometries, or geometries otherwise awkward to describe analytically. There can be highly non-linear thermodynamic effects: phase changes, radiative properties of materials at different densities and temperatures, as well as dissociation and ionisation from radiation sources. Magnetic fields and turbulence further complicate some of these scenarios. These issues are compounded by the

quantity of non-negligible physical processes taking part, each potentially providing dominant effects within different regimes of the evolution or properties of the subject. The result of these factors is that analytical solutions would either be too difficult to construct or, if constructed, would, by necessity, be limited to a subset of the overall problem. For these tasks, then, a numerical approach can be of great value.

With the ever increasing capability to implement and run larger scale computational models, hydrodynamics within astrophysics has received increasing attention and development. Its use can help illuminate areas of problems left dark through analytical work alone, as well as provide theoretical context for the ever increasing quantity and resolution of observations.

The particular code used in this work is referred to in subsequent sections as `RadCode II`, developed from `Cloud`, used for Nelson and Papaloizou (1993) and others. A description of the history of the code in particular is given in Section 2.8 following sections describing the suitability of the environment to simulation, and the physics and computational processes involved in such implementations.

## 2.1 PROPERTIES OF THE ISM

---

The interstellar medium (ISM) has been described in the context of its physical properties in Section 1.1. In this Section, we are concerned with which of those properties makes computational simulation, especially of the Lagrangian SPH method, a suitable basis to investigate the behaviour of the ISM.

ISM elemental abundances are summarised in Table 1.1. Hydrogen is the dominant component, at approximately 90% by number and 71% by mass. Despite this, the chemistry of the less abundant elements, especially carbon and oxygen, means that substantial non-linear thermodynamic effects govern some regimes of its evolution. In addition to this, phase changes in hydrogen, dissociated by Far Ultraviolet (FUV) radiation and ionised by Extreme Ultraviolet (EUV), also prevents simple treatment of the medium as an ideal gas.

The ISM is also subject to a large degree of inhomogeneity in density and structure, becoming more pronounced in molecular cloud regions where star formation is soon to, or is already, taking place. It is believed to be ‘clumpy’ at a vast range of length scales (Larson, 1981; Shu et al., 1987; Williams et al., 1994, 2000).

These factors can make simple analytical modelling of the medium somewhat abstracted from reality, providing a good base description of underlying physical effects, but preventing an accessible picture of its evolution in actuality. These varieties of

non-linear, highly dynamical effects and initial conditions, coupled with a basis in hydrodynamics, makes it an ideal candidate to be analysed by computational fluid dynamics.

When describing the process of star formation within the ISM, there are huge variations in scale of multiple parameters. Distances range from multiple parsecs down to stellar scales of the order of A.U., and densities vary from low density ISM material of  $\approx 10 \text{ cm}^{-3}$  up to protostar densities increasing above  $10^{13} \text{ cm}^{-3}$ .

## 2.2 HYDRODYNAMIC EQUATIONS

---

The hydrodynamic behaviour of a non-viscous, compressible fluid in the context of astrophysical material can be described by three key equations governing the dynamics, plus one for the coupling of material properties (internal energy specifically) and hydrodynamic properties. These equations are:

Mass continuity,

$$\frac{\partial \rho}{\partial t} + \nabla \cdot (\rho \mathbf{u}) = 0. \quad (2.1)$$

Momentum,

$$\rho \left( \frac{\partial \mathbf{u}}{\partial t} + (\mathbf{u} \cdot \nabla) \mathbf{u} + \nabla \Phi + \mathbf{S}_{\text{visc}} \right) + \nabla p = 0. \quad (2.2)$$

Energy,

$$\rho \frac{\partial e}{\partial t} + p \nabla \cdot \mathbf{u} + (\Lambda_{\text{cool}} - \Lambda_{\text{heat}}) = 0. \quad (2.3)$$

Equation of State,

$$p = \rho (\gamma - 1) e. \quad (2.4)$$

With the following definitions, along with dimensions of each parameter in descriptive form and fundamental units, ‘element’ in all cases used for brevity to refer to a ‘fluid element’:

$\rho$	element density	$p$	element pressure
$\text{kg m}^{-3}$	<i>mass length</i> <sup>-3</sup>	$\text{kg s}^{-2} \text{m}^{-1}$	<i>force length</i> <sup>-2</sup>
$\mathbf{u}$	element velocity	$\Phi$	gravitational potential
$\text{m s}^{-1}$	<i>length time</i> <sup>-1</sup>	$\text{m}^2 \text{s}^{-2}$	<i>energy mass</i> <sup>-1</sup>
$e$	element internal energy	$\mathbf{S}_{\text{visc}}$	element bulk viscosity
$\text{m}^2 \text{s}^{-2}$	<i>energy mass</i> <sup>-1</sup>	$\text{m s}^{-2}$	<i>force mass</i> <sup>-1</sup>
$\Lambda_{\text{cool}}$	non-adiabatic cooling rate	$t$	time
$\text{kg m}^{-3} \text{s}^{-1}$	<i>energy length</i> <sup>-3</sup> <i>time</i> <sup>-1</sup>	$\text{s}$	<i>time</i>
$\Lambda_{\text{heat}}$	non-adiabatic heating rate	$\gamma$	ratio of specific heats
$\text{kg m}^{-3} \text{s}^{-1}$	<i>energy length</i> <sup>-3</sup> <i>time</i> <sup>-1</sup>		<i>unitless</i>

$\nabla$  being the total spacial derivative,  $\nabla \mathbf{A} = \hat{\mathbf{i}} \frac{\partial \mathbf{A}}{\partial x} + \hat{\mathbf{j}} \frac{\partial \mathbf{A}}{\partial y} + \hat{\mathbf{k}} \frac{\partial \mathbf{A}}{\partial z}$  ( $\hat{\mathbf{i}}$ ,  $\hat{\mathbf{j}}$  and  $\hat{\mathbf{k}}$  the standard Cartesian unit vectors). These equations are ubiquitous throughout fluid dynamics and hydrodynamics, and form the underlying basis for almost all computational implementations.

The effective statement of the mass continuity equation proscribes that the amount of mass crossing any boundary must be conserved. Specifically: for a fluid element, the rate of change of density of that element ( $\frac{\partial \rho}{\partial t}$ ) combined with the divergence of the product of density and velocity ( $\nabla \cdot (\rho \mathbf{u})$ , being the density accumulation or loss within the element) must equal zero; for a constrained described volume, this corresponds to the equivalent statements for mass conservation rather than density.

For the momentum equation there are several separate behavioural components described. The terms in the brackets correspond to the rate of change of velocity with time ( $\frac{\partial \mathbf{u}}{\partial t}$ ), the rate of change of the velocity in its direction of travel ( $(\mathbf{u} \cdot \nabla) \mathbf{u}$ , being the rate travelling ‘with’ the motion), the spacial gradient of the gravitational potential ( $\nabla \Phi$ , being the gravitational force) and finally the viscous contributions ( $\mathbf{S}_{\text{visc}}$ ). These all represent the force per unit mass within the material. When taken as the product with density, outside of the brackets, the meaning of this sum of parameters is the force per unit volume for a fluid element. Added to the spacial gradient of the pressure at the element, these represent the net momentum per unit volume, which should be constant. As with the mass continuity, for a described volume, this represents conservation of momentum.

Energy conservation dictates the net gain or loss of energy from the material. For pure fluid dynamics, this is conserved for a closed system. Within the simulation, when incorporating radiative transfer and molecular line emission, it is not a closed system which is described. There can be net positive change in energy of the system (from incident radiation) and net loss of energy from the system through radiation (assumed to leave the system when optically thin). This is still technically conserved; the sum of

energy in the system and leaving the system to external sinks cannot exceed that being introduced to the system from external sources. Hydrodynamically on local scales, however, this happens ‘between’ steps, altering the internal energy  $e$ , and behaves as though energy is conserved hydrodynamically, as expected.

The first term ( $\rho \frac{\partial e}{\partial t}$ ) indicates the rate of change of the product of density internal energy of the element with time, i.e. rate of change of energy per unit volume with time, specifically for variations due to the equation of state/thermodynamical (the ‘random’ velocities corresponding to the temperature). The second term ( $p \nabla \cdot \mathbf{u}$ ) the product of the divergence of velocity with pressure, describes the work compressing or expanding material with or against pressure. The last term ( $\Lambda_{\text{cool}} - \Lambda_{\text{heat}}$ ) is the balance between any sources of non-adiabatic heating and cooling processes, such as those contributed by the chemical reactions and molecular line emission processes; described in Section 2.3.5.

Finally, the equation of state defines the internal behaviour of the material; its reaction to changes in energy, effectively. Importantly,  $e$  is taken to be a function of the mean molecular mass  $\mu$ , which changes drastically with ionisation. For rapidly ionised regions and pure hydrogen (as an example), this goes from 2 u whilst molecular down to 0.5 u when ionised (with u the atomic mass unit). This is accounted for in the code, and coupled to the chemical changes induced by the radiation.

## 2.3 FORCES AND PHYSICAL PROCESSES

---

Several terms in Equations (2.1) to (2.4) require calculation separately in order to evaluate the expressions in which they are part. This section elaborates upon how they are dealt with for the purposes of evaluation in general, and the implementation used for this work specifically. One addendum to this last point is that for some of the details on implementation, reference is made to ‘particles’. This is due to the selection of the Lagrangian Smooth Particle Hydrodynamics (SPH) method actually used for this research, the particulars of which are described later in Sections 2.4 and 2.5. The only concept required for the understanding of some of the implementations described in this section is that the continuous fluid is treated as discrete ‘particle’ fluid elements.

### 2.3.1 GRAVITY AND THE BARNES-HUT OCT TREE

Self gravity, that is, the gravitation of an element of a continuous fluid/object with the rest of the fluid/object, can be an important force in shaping astrophysical material.

This features in the equations described above as the  $\nabla\Phi$  term in Equation (2.2). The force acting on a mass element  $i$  by a mass element  $j$  can be given as,

$$\mathbf{F}_{ji} = -\nabla\Phi_{ji} = -\frac{G m_i m_j \mathbf{r}_{ji}}{d_{ij}^3}, \quad (2.5)$$

with  $m_i$  and  $m_j$  the masses of elements  $i$  and  $j$ ,  $\mathbf{r}_{ji}$  the vector connecting  $j$  to  $i$ ,  $G$  the universal gravitation constant, and  $d_{ij}$  trivially calculated as in Equation (2.6),

$$d_{ij}^2 = |\mathbf{r}_{ji}|^2 = (x_j - x_i)^2 + (y_j - y_i)^2 + (z_j - z_i)^2. \quad (2.6)$$

Within the SPH method, another requirement is a list of near-neighbours to any element (particle, in SPH), in order to calculate local derivatives of properties. This makes two purposes for which the calculation of mutual distances is required.

The inclusion of this calculation in particle-based simulations can either be conceptually simple, but enormously computationally expensive, or conceptually complex with a great saving in computational effort. The former description can be applied to the ‘ $\mathcal{O}(n^2)$ ’ methods. These can provide better accuracy, and are easy to understand, but their computational expense for large numbers of elements,  $n$ , means that for high mass resolution/spatial resolution simulations they are not a viable option. Calculation of the net force on a particle  $i$ ,  $\mathbf{F}_i$ , for every particle in a system of  $n$  particles, by finding every combination of  $d_{ji}$  can be performed as shown in Equation (2.7). This produces a summation of  $n$  particle contributions for every of  $n$  particles, hence the  $\mathcal{O}(n^2)$  computation order. In practice, only half as many are required, due to the symmetry of the gravitational forces ( $\mathbf{F}_{ij} = \mathbf{F}_{ji}$ ). However, this is of little impact to the overall computational intensity.

$$\mathbf{F}_i = \sum_{j=1}^n (j \neq i) \mathbf{F}_{ji} \quad (2.7)$$

The alternative is the, now commonly-used, Barnes-Hut ‘Oct Tree’ method, which scales with particle number as  $\mathcal{O}(n \log n)$ . It possesses a lower accuracy, though well within the bounds imposed by other uncertainties in calculations, and permits the high-resolution simulations of recent years to include gravity, with run-times orders of magnitude smaller than the  $\mathcal{O}(n^2)$  method above.

Posited in the mid 1980s (Appel, 1985; Barnes and Hut, 1986), the Barnes and Hut (1986) method being the progenitor for most modern implementations. Using a hierarchical nested tree system for describing the locations of groups of particles and collective properties of these groups (specifically their centre of mass), it permitted nearest neighbour searching and self gravity calculations to be reduced in computa-

tional complexity from  $\mathcal{O}(n^2)$  to  $\mathcal{O}(n \log n)$ . This permits multiple order-of-magnitude particle resolution increases without the computation time becoming infeasibly long.

The Oct Tree system removes the need for a great many of the comparisons, both building up a nearest neighbour list (needed for calculation of local gradients for SPH, see Section 2.5) and calculating gravitational forces using the same structure.

Initially, the computational space is divided into root octants. For each of these starting octants the list of particles contained within it is built up, along with the total mass and centre of mass of the octant. This is a fast operation, as simple rounded division operations on each axis can determine which octant each particle is located in without reference to any other particle, meaning linear complexity. This forms the first level of the tree.

For each octant, if the list of particles contained within is longer than one, it is subdivided an additional level. These 8 new sub-octants build up lists of contained particles of their own and a centre of mass in the same manner as the previous level. This recursive process is continued so long as there is an octant with more than one particle contained within. Once the Oct Tree is built, evaluation for the nearest neighbours and gravitational forces can begin.

For each focus particle, an evaluation of the octants at the top level of the tree is made. The exact form of this evaluation varies, but it usually takes the form of finding the angular size of the octant relative to the particle. If this angular size is above a certain value, the octant is ‘opened’ and the list of sub-octants evaluated in the same way. This leads to a distribution of octants which have been opened all the way down to a level revealing an individual particle, and octants which, at some level, fail to fulfil the criterion/criteria and are not opened. All particles within these unopened boxes need not be evaluated as a potential nearest neighbour, cutting out a substantial proportion of distances to be evaluated.

These nearest neighbour lists can then be applied to calculate the smoothing length, pressure forces or any other short-range interactions.

While the calculation could be done in a separate descent, most codes simultaneously perform the calculations for the gravitational forces. For each un-opened octant, the total mass of particles contained within and the centre of mass are used along with a quadrupole expansion to approximate the gravitational force from the entire collection of particles. Again, this cuts out a substantial proportion of possible direct particle-particle distances/interactions.

As mentioned previously, the computational cost of this algorithm is very substantially lower than a regular  $\mathcal{O}(n^2)$  search of every mutual distance. At  $\mathcal{O}(n \log n)$ , it permits a numbers of particles to be simulated which would be infeasibly time-

consuming for the alternative.

As virtually all things which provide such a substantial benefit, however, it comes at a cost. That cost is accuracy. Distant particles are no longer guaranteed to exert symmetric forces on one another, and so momentum is not strictly conserved. The errors produced, however, are minor on the scale of the systems involved, as examined originally by Barnes and Hut (1986).

### 2.3.2 ARTIFICIAL VISCOSITY

In the formal, hydrodynamic, sense, the astrophysical fluids investigated here are non-viscous. For the initial neutral material the value for the Reynolds number will be in the tens of thousands, for the ionised material it will be in the millions and the condensed ( $10^6 \text{ cm}^{-3}$ ) cold (10 K) gas in the hundreds of millions; any fluid with Reynolds numbers  $\gg 1$  can be considered non-viscous.

Artificial viscosity does not represent a ‘real’ fluid viscosity, but permits approximate treatment of shocks where the required scale lengths become far smaller than resolved by the particles/grid representing it. The thermodynamic behaviour of the shocks themselves are not resolved on any scale over which the calculations are taking place, and are missed as a result. Artificial viscosity ‘pretends’ to be the physical effects experienced at such a boundary, introducing the correct thermodynamic alterations produced; without directly representing the underlying physics. In addition, it stabilises a simulated fluid against numerical noise and error, usually at the cost of smoothing out some physically accurate higher frequency/smaller length scale effects. This expense can be justified as any such effects will be, by their nature of possessing properties likely to be smoothed out, near the resolvable limit of physical processes anyway.

Many implementations of the artificial viscosity are based on that developed by Monaghan and Gingold (1983). More recently developments in implementation include those laid out by Monaghan (1997) and Morris and Monaghan (1997), which especially provide benefit at higher resolutions. For the resolutions investigated here, further alteration to the, already extensively tested, hydrodynamics in this regards were not made. The product of the  $\alpha$  viscosity term and particle smoothing length is analogous to the mean free path of a traditional viscosity expression. The specific implementation for `Cloud` and unchanged for `RadCode II` is the form in Monaghan and Gingold (1983) with the addition of the  $\beta$  term for stability in high Mach numbers (e.g. Monaghan and Lattanzio (1991); Nelson and Papaloizou (1993)). The overall effect is given as a term  $\Pi_{ij}$  added to the pressure force for particle  $i$  for any near-neighbour  $j$  with mutual

velocity  $< 0$  (i.e. closing),

$$\Pi_{ij} = \frac{1}{\bar{\rho}_{ij}} \left( -\alpha \mu_{ij} \bar{c}_{ij} + \beta \mu_{ij}^2 \right), \quad (2.8)$$

in which  $\bar{A}_{ij} = \frac{1}{2}(A_i + A_j)$ ,  $\alpha$  and  $\beta$  the artificial viscosity scaling constants,  $c$  the sound speed and  $\rho$  the density.  $\mu_{ij}$  is an expression,

$$\mu_{ij} = h_{ij} \frac{\mathbf{v}_{ij} \cdot \mathbf{r}_{ij}}{|\mathbf{r}_{ij}|^2 + \eta^2}, \quad (2.9)$$

with  $h_{ij}$  the mutual SPH smoothing length,  $\mathbf{A}_{ij} = (\mathbf{A}_i - \mathbf{A}_j)$  with  $\mathbf{v}$  the velocity and  $\mathbf{r}$  the position.  $\eta^2$  is a term  $\eta^2 = 0.01 h_{ij}^2$ , preventing asymptotic behaviour as  $|\mathbf{r}_{ij}| \rightarrow 0$ .

For this work  $\alpha = 0.5$  and  $\beta = 1.0$ , based on those shown to converge for the code previously, see Nelson and Papaloizou (1994); Nelson and Langer (1997). These values fulfil the generally accepted range for convergence of  $\alpha = 0.5 - 1.0$  and  $\beta = 2\alpha$ , see for instance Springel (2010) as well as many other reviews of the SPH method.

### 2.3.3 THE FUV AND EUV RADIATION FIELDS

Far-Ultraviolet (FUV) radiation provides heating primarily through photo-ejection of electrons from dust grains. It is also responsible for the dissociation of various molecular species, including molecular hydrogen,  $\text{H}_2$ . However, unlike ionising Extreme-Ultraviolet (EUV) radiation, the absorption of FUV does not substantially affect the optical depth of the medium, the result of this is that the radiation strength attenuates predictably with column depth of the material. In the case of EUV, the absorption cross-section of the material drops drastically with increasing ionisation fraction.

The FUV scheme implemented in the code has two main interactions with the material. The first is direct absorption of FUV radiation onto dust grains, increasing the temperature of the medium; the second is via the chemical evolution. As described in Table 2.1, several of the chemical paths are created via FUV absorption to one of the components, making the rates proportional to the FUV radiation density, as well as any dependencies on reactant densities or temperatures.

Computationally, the FUV radiation is implemented by initially gridding the density data of particles. For each particle, a set of 26 rays are traced through the simplified gridded density to obtain column densities for each direction. These column densities are then converted first to visual extinction values,  $A_v$ , then applied to calculate flux rates for both heating of dust (whose flux is shown in Equation (2.10)) and the chemical

photo-dissociation rates used in Table 2.1.

$$f_{\text{dust}} = \sum_i \sum_j \sum_k \frac{4\pi}{26} I_{ijk} e^{-2.5 d_{\tau_{ijk}}}, \quad (2.10)$$

where  $I_{ijk}$  is the incident FUV radiation intensity from the  $ijk$ -direction, and  $d_{\tau_{ijk}}$  is the column density in the  $ijk$ -direction.

EUV radiation has additional complexities. Absorption of FUV radiation is by either dust grains, or molecules where their abundance is not drastically changed immediately upon absorption. This is what permits the use of the general ‘attenuation based on quantity of material traversed’ method. The same is not true of EUV. Upon absorption, EUV dramatically changes the optical properties of the material; ionised gas becomes transparent to the radiation which ionised it. As a result, the radiation profile through material with distance to the source must be calculated as a function of the radiation profile itself. A solver is necessary for a scenario which can be described as a set of differential equations. As this is a focus of this work, it warrants a description in more detail, and can be found in Chapter 3.

### 2.3.4 CHEMICAL PROCESSES

The chemical reaction pathways which are present in molecular gas are thought to be vital to the process of star formation (van Dishoeck and Blake, 1998). Multiple molecular species provide cooling through emission lines which cause gas temperatures to drop at higher densities, permitting further collapse. Although star formation itself is hypothesised to not be entirely reliant on existing molecular gas environments (Glover and Clark, 2012), the presence of high density molecular gas in observed active star forming regions is sufficient to suggest that chemical interactions in present-day star formation must at least play a part in pre-stellar dynamics in these regions.

The full range of chemical interactions within astrophysical gases is extensive and it is only plausible to deal with a subset in a dynamical simulation. There are 15 chemical species included in `RadCode II`, unchanged from the original `Cloud` code:  $\text{H}_2$ ,  $\text{He}$ ,  $\text{He}^+$ ,  $\text{He}_3$ ,  $\text{He}_3^+$ ,  $\text{C}$ ,  $\text{C}^+$ ,  $\text{O}$ ,  $\text{CO}$ ,  $\text{HCO}^+$ ,  $\text{CH}_x$ ,  $\text{OH}_x$ ,  $\text{M}$ ,  $\text{M}^+$  and free electrons,  $e$ .

Table 2.1 displays the entire list of chemical interactions and formation/destruction mechanisms implemented within the code. The chemical system within the code was designed to deal with lower temperature gas temperatures ( $< 200$  K), it provides chemical composition data below this threshold; above it, the rates are such that any chemical feedback effects to the hydrodynamics (through the coupled thermodynamics) diminish with increasing temperature. As such, chemical fractional densities are correct for gas temperatures  $< 200$  K and effectively default towards simple ‘high temperature’

fractional densities above that (maximum ionised states of atoms, few molecules).

All chemicals have the basic rate form, shown in Equation (2.11), creating a total series of ten such equations.

$$\frac{d B_{\text{species}}}{dt} = \sum_f \left( k([T], [A_v]) \left[ \prod (B_{\text{reactant and/or } B_{\text{catalyst}}}) \right] \right) - \sum_d \left( k([T], [A_v]) \left[ \prod (B_{\text{catalyst}}) \right] B_{\text{species}} \right), \quad (2.11)$$

in which,  $B_{\text{species/reactant/catalyst}}$  is the fractional abundance relative to hydrogen of the specified subscript,  $A_v$  is the visual extinction,  $T$  temperature in Kelvin, and  $k$  is the rate coefficient. The summations notated  $f$  and  $d$  are for any and all reactions/interactions involving formation and destruction of the species in question respectively. Segments of the equation in square brackets indicate ‘optional’ arguments, in that not all rates incorporate terms of that variety.

This set of differential equations is then solved for the timestep interval using the general purpose ‘Livermore Solver for Ordinary Differential Equations’, `lsode` package (Radhakrishnan and Hindmarsh, 1993), in `Cloud`, but could equally be processed by any solver for series of differential equations.

### 2.3.5 THERMODYNAMIC PROCESSES

In order to obtain the evolution of temperature throughout the system, the energy equation is solved numerically at each time step. This differs from most implementations where simplified relations are used. This is especially true for those where ionising radiation is present, in which temperature is frequently set as a linear superposition of ‘neutral’ and ‘ionised’ temperatures based on the ionisation fraction ( $T = X T_{\text{ionised}} + (1 - X) T_{\text{neutral}}$ ). Both heating and cooling in complex radiation field and chemical environments result in non-linear behaviour of the simulated gas in different circumstances. Accounting for the most dominant of these effects is the rationale for a full thermodynamic evolution being treated. The overall picture of the thermodynamic contributions is as follows:

**Heating:**

- Hydrodynamic
- Far-ultraviolet radiation incident on dust grains and ejected electrons
- Background cosmic ray rate
- Dust grain surface H<sub>2</sub> formation

Reactants	→ Products	Rate coefficient/expression
Cosmic Ray Interactions		[s <sup>-1</sup> molecule <sup>-1</sup> ]
cr + H <sub>2</sub>	→ H <sub>3</sub> <sup>+</sup> + e + H + cr	1.2 × 10 <sup>-17</sup>
cr + He	→ He <sup>+</sup> + e + cr	6.8 × 10 <sup>-18</sup>
Ion-molecule Interactions		[cm <sup>3</sup> s <sup>-1</sup> molecule <sup>-1</sup> ]
H <sub>3</sub> <sup>+</sup> + C	→ CH <sub>x</sub> + H <sub>2</sub>	2 × 10 <sup>-9</sup>
H <sub>3</sub> <sup>+</sup> + O	→ OH <sub>x</sub> + H <sub>2</sub>	8 × 10 <sup>-10</sup>
H <sub>3</sub> <sup>+</sup> + CO	→ HCO <sup>+</sup> + H <sub>2</sub>	1.7 × 10 <sup>-9</sup>
He <sup>+</sup> + H <sub>2</sub>	→ He + H + H <sup>+</sup>	7 × 10 <sup>-15</sup>
He <sup>+</sup> + CO	→ C <sup>+</sup> + O + He	1.6 × 10 <sup>-9</sup>
C <sup>+</sup> + H <sub>2</sub>	→ CH <sub>x</sub> + H	4 × 10 <sup>-16</sup>
C <sup>+</sup> + OH <sub>x</sub>	→ HCO <sup>+</sup>	1 × 10 <sup>-9</sup>
Neutral-neutral Interactions		[cm <sup>3</sup> s <sup>-1</sup> molecule <sup>-1</sup> ]
O + CH <sub>x</sub>	→ CO + H	2 × 10 <sup>-10</sup>
C + OH <sub>x</sub>	→ CO + H	5.8 × 10 <sup>-12</sup> T <sup>0.5</sup>
Electron recombinations		[cm <sup>3</sup> s <sup>-1</sup> molecule <sup>-1</sup> ]
He <sup>+</sup> + e	→ He + hν	9 × 10 <sup>-11</sup> T <sup>-0.64</sup>
H <sub>3</sub> <sup>+</sup> + e	→ H + H <sub>2</sub>	1.9 × 10 <sup>-6</sup> T <sup>-0.54</sup>
C <sup>+</sup> + e	→ C + hν	1.4 × 10 <sup>-10</sup> T <sup>-0.61</sup>
HCO <sup>+</sup> + e	→ CO + H	3.3 × 10 <sup>-5</sup> T <sup>-1.0</sup>
M <sup>+</sup> + e	→ M + hν	3.8 × 10 <sup>-10</sup> T <sup>-0.65</sup>
Charge transfer interactions		[cm <sup>3</sup> s <sup>-1</sup> molecule <sup>-1</sup> ]
H <sub>3</sub> <sup>+</sup> + M	→ M <sup>+</sup> + e + H <sub>2</sub>	2 × 10 <sup>-9</sup>
Photoreactions		[s <sup>-1</sup> molecule <sup>-1</sup> ]
hν + C	→ C <sup>+</sup> + e	3 × 10 <sup>-10</sup> G <sub>0</sub> e <sup>-3A<sub>v</sub></sup>
hν + CH <sub>x</sub>	→ C + H	1 × 10 <sup>-9</sup> G <sub>0</sub> e <sup>-1.5A<sub>v</sub></sup>
hν + CO	→ C + O	1 × 10 <sup>-10</sup> Θ G <sub>0</sub> e <sup>-3A<sub>v</sub></sup> †
hν + OH <sub>x</sub>	→ O + H	5 × 10 <sup>-10</sup> G <sub>0</sub> e <sup>-1.7A<sub>v</sub></sup>
hν + M	→ M <sup>+</sup> + e	2 × 10 <sup>-10</sup> G <sub>0</sub> e <sup>-1.9A<sub>v</sub></sup>
hν + HCO <sup>+</sup>	→ CO + H	1.5 × 10 <sup>-10</sup> G <sub>0</sub> e <sup>-2.5A<sub>v</sub></sup>

Table 2.1: Chemical Reaction Table. Elements and molecules presented in default notation, superscript ‘+’ indicates singly ionised. ‘M’ indicates the category for all metals, dealt with in abstract only. ‘cr’ indicates cosmic ray presence in the reaction. *hν* indicates a photon contributing to, or resulting from, the reaction. Data table is essentially the same as that shown in, for example, Nelson and Langer (1999), one of the original descriptions of the chemistry in the code. Values for rate coefficients, unless stated otherwise, are based on the UMIST catalogue data (Bergin et al., 1995).

† Rate and equation from Bergin et al. (1995), developed from the work of van Dishoeck and Black (1988). Θ indicates the CO self-shielding function.

- Extreme ultra-violet ionisation heating

**Cooling:**

- Hydrodynamic
- Atomic/molecular line emission (for lines where the mean-free-path of the photon would approach or exceed the length scale of the clouds; CO, C I, C II and O I included)
- O II collisional cooling
- Gas-dust cooling

The net change in internal energy of a particle,  $e$ , is modified as the summation of all contributions to energy change through these various sources and sinks. As this is also a feedback process, with many of the processes being temperature dependant, it must be solved numerically. This is done using a simple bisection method. For any step  $i$  of the bisection, the equation being minimised for this solution process is,

$$e_i = et_i - et_{i-1} - \Delta t (f_{\text{uv-grain}} + f_{\text{cr}} + f_{\text{H}_2\text{-grain}} + f_{\text{H I} \rightarrow \text{H II}} - f_{\text{emission}} - f_{\text{CO}} - f_{\text{gas-dust}} - f_{\text{H II} \rightarrow \text{H I}} - f_{\text{O II}}), \quad (2.12)$$

where  $et_j$  is the internal energy based on temperature for the guessed temperature at step  $j$ ; given by  $et_j = \frac{3}{2} r_\mu T_j$  with  $r_\mu$  the specific gas constant and  $T_j$  the guessed temperature for that step. The change in energy over the timestep  $\Delta t$  is the sum of all contributions to temperature change, each of these processes are as follows:

$f_{\text{uv-grain}}$	UV heating to dust grains	$f_{\text{cr}}$	cosmic ray heating
$f_{\text{H}_2\text{-grain}}$	H <sub>2</sub> grain formation heating	$f_{\text{emission}}$	optically thin line emission
$f_{\text{CO}}$	self-shielded CO line emission	$f_{\text{gas-dust}}$	gas-dust cooling
$f_{\text{H I} \rightarrow \text{H II}}$	ionisation heating	$f_{\text{H II} \rightarrow \text{H I}}$	hydrogen recombination cooling
$f_{\text{O II}}$	oxygen collisional cooling		

This bisection continues to estimate the temperature until the change is below a threshold. At this stage the internal energy / temperature is deemed ‘solved’ and the next particle is evaluated.

The calculation of the ionisation and recombination rates required to determine the solutions to  $f_{\text{H I} \rightarrow \text{H II}}$ ,  $f_{\text{H II} \rightarrow \text{H I}}$  and  $f_{\text{O II}}$  are described in full in Chapter 3.

### 2.3.6 TURBULENCE AND MAGNETIC FIELDS

Neither explicit turbulence, nor magnetic fields, are included within the simulations presented in this thesis. There is, however, an internal pressure term assuming the

implicit presence of them. This is in the form of a small additional contribution to the pressure terms in Equations (2.1) to (2.4), as examined analytically by, for example, Gorti and Hollenbach (2002).

The nature of turbulent motion within astrophysical clouds is only partially understood due to their numerous and complex origins and interactions, and the difficulties of determining which of these is active (or, to what extent) due to the limits of what can be observed (Elmegreen and Scalo, 2004; Scalo and Elmegreen, 2004). Initial turbulent velocity fields, based on power law distributions of wave-numbers are included in many simulations (see, for example, Klessen et al. (2000); Federrath et al. (2010)) to replicate observed inhomogeneity and motion of such clouds. Whilst included in some simulations, usually to specifically investigate the effects of the turbulence itself, in order to reduce the parameter-space being investigated it is frequently omitted.

Were it desired to include magnetic fields in the simulations performed, we begin with the issue that substantial difficulties exist in implementing magnetic fields and magnetic field effects into SPH codes. These generally manifest in the inability to fulfil the requirement of  $\nabla \cdot B = 0$ . This results in spurious sources and sinks of magnetic field-lines, and corresponding non-physical forces affecting particles. The intricacies and complexity of creating a suitable computational implementation of these effects are dealt with in detail in Price and Monaghan (2004a,b, 2005); Price (2010). The properties of the ISM described in Section 2.1 do not exclude the potential for the presence of, and effects resulting from, magnetic fields. However, the materials and time-scales of the sections of molecular clouds being examined permit the assumption that magnetic field effects present, if any, will not be a dominant factor in the dynamical evolution of the clouds compared to the effects of the shock fronts, ionisation region expansion and other radiative effects.

## 2.4 COMPUTATIONAL APPROACHES

---

In order to simulate the medium in which star formation occurs, some numerical system must be selected. The categories into which hydrodynamic simulation methods broadly fall are Eulerian and Lagrangian. The most simplistic manner in which the two methods can be described is that both use evaluation points within the fluid to determine its motion and properties. In the Eulerian system, these evaluation points stay fixed and the flux of material moving between them is described. In the Lagrangian system, the evaluation points move with some fixed fluid property (usually a mass-element), and their motion through space is calculated, describing the fluid. Both are ways to

describe a medium which, to all intents and purposes, is continuous; but which we must find a way to discretise for computation.

These methods each make use of either grids or ‘particles’. In a grid system, there are multiple volume elements with properties of the boundaries between itself and its neighbours. ‘Particles’ covers the use of single points, possessing certain properties; using some description of interaction with other nearby points. Complexities in implementation can be examined which utilise multiple combinations of the two basic systems (Eulerian and Lagrangian) and the two basic representations (grid and particle), however, the usual combinations are that Eulerian systems make use of some fixed grid, and Lagrangian systems make use of moving ‘particles’ (though Lagrangian grids are popular in other fields, especially those for which free-surfaces exist).

In a common Eulerian grid system, finite differences across grid cell boundaries permit calculation of spatial derivatives, and hence fluid flow rates and tracking of properties of fluid moving into and out of cells (see, for example, Trac and Pen (2003)). A common Lagrangian particle system is Smoothed Particle Hydrodynamics, SPH. In this, the continuous fluid is represented as a distribution of mass-element particles, the properties at each particle position is calculated with the use of properties of nearby surrounding particles, weighted by a smoothing kernel. This facilitates the calculation of the important spacial derivative terms vital to application of the hydrodynamic equations. Calculation of the spatial derivative for a true point particle otherwise being difficult or requiring convoluted methods of interpolating onto a grid or similar. This kernel-based SPH method was first developed and utilised in 1977 (Lucy, 1977; Gingold and Monaghan, 1977). Multiple developments have been made over time, greatly expanding the scope and utility of SPH applications. Perhaps the most important of these for astrophysical purposes was the Oct Tree system, which is described in more detail in Section 2.3.1.

Some of the desirable features of SPH over grid-based systems include its dynamic spacial resolution, accounting for wide density ranges and intrinsically resolving small scale, dense, features with high spacial resolution which is not intrinsic to grid methods (though it can be done, albeit via the inclusion of Adaptive Mesh Refinement (AMR) techniques); that it can calculate self-gravity with no issues and, in combination with the Oct Tree system, without great computational expense; it provides a simple support for a wide variety of arbitrarily shaped structures, some of which can easily cause problems on grid systems (any curved surfaces can be difficult to represent without axially aligned artefacts).

## 2.5 SMOOTHED PARTICLE HYDRODYNAMICS

---

### 2.5.1 BASIC SPH THEORY

Smoothed Particle Hydrodynamics (SPH) is predicated on the concept of finding the value and derivative of a property at a point location through the use of arbitrarily positioned evaluation points, weighted by a smoothing Kernel extending from the point location. With the evaluation spanned across the volume surrounding the target, and a well-defined gradient of any property, a collection of such point locations, as ‘particles’, can fulfil the description of a continuous fluid, the behaviour of which can be governed by the equations of Section 2.2. This section will attempt to provide an overview of the theory and basic implementation of an SPH-based computational simulation. The term was coined with Gingold and Monaghan (1977) with similar work by Lucy (1977) and has since undergone numerous developments and refinements.

Arguably the most important concept within SPH is the smoothing kernel. Any problem which is effectively continuous, in order to be examined numerically, must be discretised. The method of creating this discrete form of a continuous problem determines the capabilities and characteristic behaviours of that method. Some aspects of which are likely to be undesirable, but need to be understood in order to account for their effects on resultant data.

For gas dynamics, it is imperative to consider the forces produced by pressure gradients. The momentum conserving expression, Equation (2.2), exemplifies this. It is this process which underpins the dynamics of gases. For a grid system one can, without too much difficulty, consider these gradients as examined spatially across grid cell boundaries, across grid cells as a whole, or a combination of both, all through evaluations of finite differences across those intervals. For a particle based system, with arbitrarily distributed particles, gradients are far more difficult to evaluate. It is the ‘smoothing kernel’, describing the location of a particle as an evaluation point of a distributed weighting function, which permits the properties at the location of a single particle (and therefore, by extension, the properties for that particle) to be determined.

Properties for a particle  $i$  are calculated as a function of the sum of the product of the properties of each neighbour particle  $j$  with the value of the smoothing kernel at the distance  $d_{ij}$ . The gradient of the smoothing kernel at each location is also evaluated, to be used for proper calculation of the pressure forces on each particle.

A smoothing kernel can be described as a function of the radial distance away from its centre  $\mathbf{x}_{\text{kernel}}$  to some position  $\mathbf{x}_j$   $|\mathbf{x}_{\text{kernel}} - \mathbf{x}_j|$  and the smoothing length (char-

acteristic width) of the kernel,  $h$ . Referring to the kernel function as  $W$ , a kernel evaluation is expressed as,  $W(r, h)$ . The exact properties of this function are examined in Section 2.5.2.

Defining the evaluation in this way means that a property  $A$  at the location of particle  $i$ ,  $\mathbf{x}_i$ , with contributions from  $N$  neighbouring particles is expressed as Equation (2.13).

$$A_i = \sum_{j=1}^N m_j \frac{A_j}{\rho_j} W(|\mathbf{x}_i - \mathbf{x}_j|, h_i). \quad (2.13)$$

For convenience of notation the value of the property  $A$  at the position of particle  $i$ ,  $A_{\mathbf{x}_i}$  is notated as, simply,  $A_i$ . This is also appropriate to the purpose of the evaluation, for which the particle itself takes on the properties of the evaluation of the smoothing kernel at its location.  $\rho$  is the density, and  $m$  the SPH particle mass. Note, also, the smoothing length argument of the kernel is  $h_i$ , the smoothing length of the particle currently the focus of the evaluation, this is a necessary distinction when considering formulations utilising variable smoothing length. When determining the density for a given particle, the reliance on appearing to require the density of the near particles already would be a problem, though the expression cancels when the property  $A_i = \rho_i$ , giving,

$$\rho_i = \sum_{j=1}^N m_j W(|\mathbf{x}_i - \mathbf{x}_j|, h_i). \quad (2.14)$$

These are the basic form of the equations for a property which is not a derivative (these cannot provide a pressure gradient term for Equation (2.2)). Before examining the required extension to evaluate derivative properties, the application of the smoothing kernel itself can be altered. Using only the smoothing length of one position, projected onto the other, will fail to adequately conserve both linear and angular momentum. This is as a result of the interactions being asymmetric. These can be symmetrised by incorporating mutual smoothing lengths (Hernquist and Katz, 1989). This results in the following, altered, expression for a property  $A_i$ ,

$$A_i = \sum_{j=1}^N m_j \frac{A_j}{\rho_j} \frac{W(|\mathbf{x}_i - \mathbf{x}_j|, h_i) + W(|\mathbf{x}_j - \mathbf{x}_i|, h_j)}{2}. \quad (2.15)$$

In each evaluation, both the position of particle  $j$  on  $i$ 's smoothing kernel *and* the position of  $i$  on  $j$ 's is used. This ensure that, when particle  $j$  is the focus, and  $A_j$  is being calculated; the effect of  $i$  on it, will be the mirror of it on  $i$ .

To find the derivative of a property,  $\nabla A$ , at the position of particle  $i$ , the full form,

using mutual smoothing lengths, becomes,

$$\nabla A_i = \sum_{j=1}^N m_j \frac{A_j}{\rho_j} \frac{\nabla W(|\mathbf{x}_i - \mathbf{x}_j|, h_i) + \nabla W(|\mathbf{x}_j - \mathbf{x}_i|, h_j)}{2}. \quad (2.16)$$

Having determined the manner in which SPH particle properties can be calculated, the next priority is to define a suitable kernel over which the evaluation is to be applied.

## 2.5.2 THE SMOOTHING KERNEL FUNCTION $W$

The important aspects of an implementation are the restricting criteria on producing a valid kernel form. Their integral over all space should be unity, they should tend to the Dirac Delta Function as  $h$  tends to zero, and must be continuous and differentiable. A basic kernel shape can be taken as a Gaussian, with  $h = \sigma$ ,

$$W(r, h) = \frac{1}{h^3 \pi^{3/2}} \exp\left(-\left(\frac{r}{h}\right)^2\right). \quad (2.17)$$

This kernel form is actually not especially effective, suffering from a number of issues in a practical implementation.

One key issue with the Gaussian kernel function is that it is not ‘compact’, there is no cut-off distance, beyond which evaluations are not performed. To properly evaluate the kernel, one must examine every particle in the simulation. This is a problem computationally, where as few comparisons and operations as possible are desired. A commonly used (for example, **SEREN** (Hubber et al., 2011), **Gadget** and **Gadget-2** (Springel et al., 2001; Springel, 2005), **VINE** (Wetzstein et al., 2009) and others) alternative kernel is an  $M_4$  spine of a form described by Monaghan and Lattanzio (1985). This is expressed as a sequence of three connected polynomials,

$$W_{M_4}(r, h) = \begin{cases} \frac{1}{4\pi} \left( (2 - \frac{r}{h})^3 - 4 (1 - \frac{r}{h})^3 \right), & \text{for } 0 \leq \frac{r}{h} \leq 1, \\ \frac{1}{4\pi} (2 - \frac{r}{h})^3, & \text{for } 1 < \frac{r}{h} \leq 2, \\ 0, & \text{for } \frac{r}{h} > 2. \end{cases} \quad (2.18)$$

In this kernel, the weighting value for all points further than  $2h$  from the focus are explicitly zero. The implication of this is that only  $N_{\text{near}}$  other particles need be evaluated. This kernel has been extensively evaluated, with no preferable alternative found for a wide variety of alterations (e.g. Fulk and Quinn (1996)), evident in its continued and extensive use.

After having selected a suitable kernel function, selection of the size of the smoothing length,  $h$  for a particle becomes the next priority. Selecting a simple fixed smooth-

ing length is not optimal for situations in which particles become either widely spaced relative to  $h$  or excessively close together. In practice, a variable smoothing length is desired, the volume of the function possesses the same, or a similar, number of evaluation points (other particles) at all times. Various computational approaches are available for determining a suitable smoothing length. Consequentially, there are adaptations based on: current particle density (Miyama et al., 1984), the rate of change of density (Evrard, 1988) or to fit a target number of other particles within  $2h$  (Hernquist and Katz, 1989) (citations are as early examples of each practice).

In the case of `Cloud`, an estimate is made for the smoothing length based on the previous step's value, a tree descent is performed and the number of particles within  $2h$  of the particle is found. If this is within a tolerance of a target number,  $N_{\text{near}}$ , of 'nearest neighbours' it is kept, otherwise it is shrunk or grown and a new descent performed to optimise the length. Results are shown to be most consistent when this tolerance is zero, i.e. that the number of nearest neighbours found must be exactly equal to the target number (Nelson and Papaloizou, 1994) (though there are concerns with such methods which suggest it would be desirable to migrate away from them as precision elsewhere is obtained (Price, 2012)). However, the tolerance can be used in order to greatly increase the speed of the algorithm adjusting the smoothing length, usually at the expense of only minimal sacrifices in accuracy. In particular, re-searching the tree when a new estimate of  $h$  is made is computationally expensive and repeated attempts should be avoided where possible.

With this kernel scheme, and the methods to evaluate any arbitrary property and differential of a property possessed by the SPH particles, we now have a coherent system to implement the Lagrangian formulation of hydrodynamics on a particle based system. Properties for all particles (in fact, any arbitrary location) can be calculated using this scheme.

## 2.6 INTEGRATION SCHEMES

---

All dynamical codes must make use of some scheme with which to advance through time. This is a non-trivial issue due to the nature of discretising a continuous problem, much as the issues for other areas of computational calculation including those already discussed. The basis of the problem can be considered as that, for a single moving point, subject to some acceleration  $\mathbf{a}_i$  dependant on position  $\mathbf{x}_i$ , at any moment it will have a spontaneous velocity  $\mathbf{v}_i$ , appropriate to that particular instant  $i$ . If time is stepped discretely by  $\Delta t$ , then a new position at the end of that step in time  $\mathbf{x}_{i+1}$  can be treated

simply as the current position plus the product of the velocity and length of the time step,  $\mathbf{x}_{i+1} = \mathbf{x}_i + \mathbf{v}_i \Delta t$ . However, as the acceleration, and hence velocity, is a function of the position, all of the changes in the acceleration and velocity during that timestep are ignored. In regions or scenarios where the change of acceleration with position is small for a given time step, this is not a problem. For all circumstances, however, where it changes strongly with position, key dynamics could be lost in the intervening time or accumulation of small differences could result in a different outcome.

There are then two key problems, one is to make a scheme for advancing the time step which will minimize issues with varying acceleration during the step; and the second is to determine, for that scheme, what a suitable size of time step should be utilised to keep the scheme within reasonable margins of error.

### 2.6.1 LEAP FROG ALGORITHM

Cloud makes use of a ‘leap frog’ integration scheme for the time stepping. The concept of the leap frog method is that velocities and position updates are calculated one half-timestep out of sync. This is a somewhat approximate method, explicit solvers being preferred for accuracy. However, it has been shown that it produces acceptably small errors (Monaghan, 1992) and, importantly, is fast to compute. It is a scheme which is second-order accurate in  $\Delta t$ .

In this formulation, rather than the basic equations for stepping time described in Section 2.6, updates are performed with Equations (2.19) and (2.20).

$$\mathbf{v}_{i+\frac{1}{2}} = \mathbf{v}_{i-\frac{1}{2}} + \mathbf{a}_i \Delta t, \quad (2.19)$$

$$\mathbf{x}_{i+1} = \mathbf{x}_i + \mathbf{v}_{i+\frac{1}{2}} \Delta t. \quad (2.20)$$

On its own, this would be sufficient for all cases where the acceleration  $\mathbf{a}$  is dependant only on the position  $\mathbf{x}$  (which are available at the same time-offsets). For SPH formulations incorporating artificial viscosity,  $\mathbf{a}$  is also dependant on  $\mathbf{v}$ , which is currently only available one half-timestep out of sync. This is not sufficient to maintain second-order  $\Delta t$  accuracy. In order to calculate  $\mathbf{a}$ , an estimate of the timestep-centred velocity  $\mathbf{v}_i$  is required, this is calculated as,

$$\mathbf{v}_i = \mathbf{v}_{i-\frac{1}{2}} + 0.5 \mathbf{a}_i \Delta t. \quad (2.21)$$

An attempt at graphically illustrating this sequence of equations is displayed in Figure 2.1. In this, each circle node represents a calculated version of the quantity

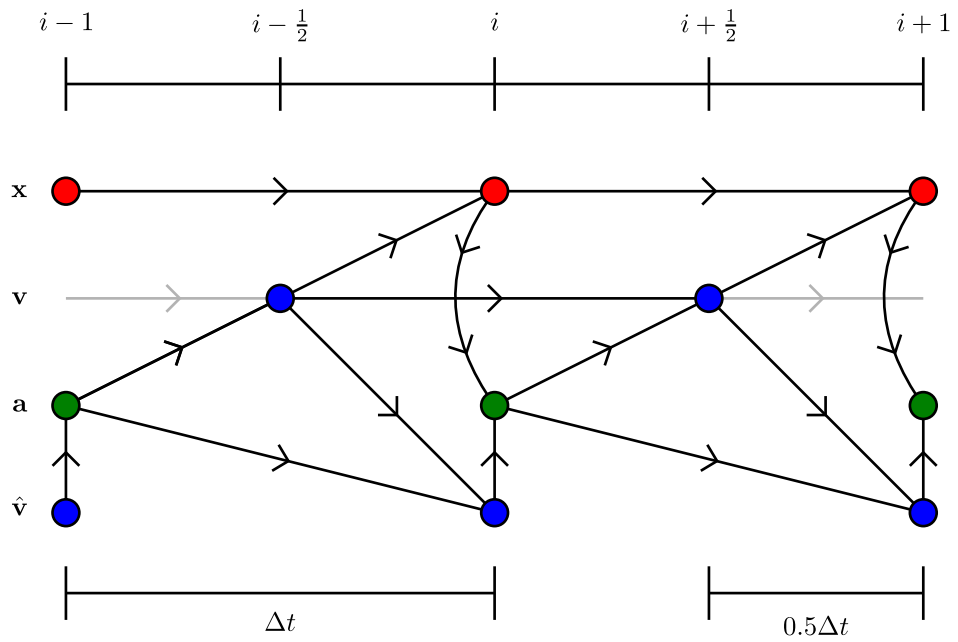


Figure 2.1: Diagrammatic illustration of the leap frog integration scheme with the inclusion of  $\mathbf{a}$  dependence on  $\mathbf{v}$  due to artificial viscosity.  $\hat{\mathbf{v}}$  is the additional ‘timestep centred’ velocity. Each circular node represents a calculated value for the property notated on the left. Lines from one node to a second node represent the use of the first value in calculating the second. Of interest is that the value for a parameter based on the same one full timestep ago, is calculated using another quantity mid-way between, representing the best available value for the continuous time between the steps. The spontaneously calculated property, acceleration  $\mathbf{a}$  is calculated using other properties which are only timestep-synchronised.

notated on the left of the diagram. Any lines leading from one node to another, represent use of that value in calculating the other. It can be seen that the two values contributing to the  $\mathbf{a}$  values are both ‘time-synchronised’, aligned vertically.

Whilst this method, at second order  $\Delta t$  accuracy would not, on its own, be sufficient for gravitational  $n$ -body simulations (for which more elaborate solvers are used), due to the nature of the fluid dynamic interactions across nearest neighbours, the accuracy is well within the bounds of that required for the purpose.

## 2.6.2 COURANT-FRIEDRICHS-LEWY CONDITION

In order to retain a good accuracy, whilst not wasting time calculating unnecessary steps, it is desirable to have an adaptive timestep, rather than a fixed one. The size of a timestep for the majority of dynamical simulations is set using an extension of the Courant-Friedrichs-Lewy (CFL) Condition (Courant et al., 1928). The gist of this method for a basic setup can be thought of as though, for some characteristic change in velocity in one timestep  $\Delta t$   $|\mathbf{a}_{\text{char}}|$  and length scale  $l_{\text{char}}$  a limit is imposed on the size of the timestep  $\Delta t$  such that the velocity difference  $\Delta t |\mathbf{a}_{\text{char}}|$  is some fraction  $k$  of the characteristic velocity, travelling  $l_{\text{char}}$  in the same  $\Delta t$ . In other words,

$$|\mathbf{a}_{\text{char}}| \Delta t < k \frac{l_{\text{char}}}{\Delta t}, \quad (2.22)$$

or,

$$\Delta t^2 < k \frac{l_{\text{char}}}{|\mathbf{a}_{\text{char}}|}, \quad (2.23)$$

$$\Delta t = C \sqrt{\frac{l_{\text{char}}}{|\mathbf{a}_{\text{char}}|}}, \quad (2.24)$$

where  $C$  is a selected  $k^2$  for a specific value rather than a boundary condition, selected as  $0 \leq C \leq 1$ . How the length scale  $l_{\text{char}}$  and accelerations  $|\mathbf{a}_{\text{char}}|$  are evaluated can vary substantially.

In practice, variations from this are utilised. The formulation introduced by Monaghan (1992) is summarised as  $\Delta t = C \min(\Delta t_f, \Delta t_{cv})$ , where,

$$\Delta t_f = \min_i \left( \frac{h_i}{|\mathbf{a}_i|} \right)^{1/2} \quad (2.25)$$

$$\Delta t_{cv} = \min_i \left( \frac{h_i}{c_i + 0.6 (\alpha c_i + \beta \max_j (|\mu_{ij}|))} \right). \quad (2.26)$$

In these equations, the minimum is taken across all particles.  $c_i$  is the sound speed

of particle  $i$ , and  $\mu_{ij}$  the artificial viscosity parameter of nearest-neighbour particle  $j$  on particle  $i$  (see Section 2.3.2).  $\alpha$  and  $\beta$  are the viscosity coefficients as described in Equation (2.8).

Cloud uses a combination of this method and that of Hernquist and Katz (1989), where the  $\Delta t_{cv}$  equation (Equation (2.26)) is replaced with,

$$\Delta t_{hk} = \min_i \left( \frac{h_i}{h_i |\nabla \cdot \mathbf{v}_i| + c_i + 1.2 (\alpha c_i + \beta \max_j (|\mu_{ij}|))} \right). \quad (2.27)$$

As with the previous method, the final timestep size is then taken as,

$$\Delta t = C \min (\Delta t_f, \Delta t_{hk}). \quad (2.28)$$

This is not the implementation envisioned by Hernquist and Katz (1989); where the calculation is performed for each individual particle and retained. The method then uses independent particle timesteps. This process, sometimes referred to as a sub-timestep format, effectively scales the time resolution in much the same way that the spacial resolution is automatically varied. This is accompanied by its own advantages and disadvantages. Ensuring that the timestep resolution is enforced in a way which is self-consistent, and an increase in code complexity; being weighed against larger scale computational efficiency.

At the very beginning of the simulation, various sharp changes occur and it can be desirable to artificially alter the Courant number to a smaller value to prevent steep changes of parameters effectively bypassing the normal scaling by the timestep size. For this purpose, in the code used for this thesis, a total of three effective Courant number values are used. A base value of  $C_{\text{base}} = 0.3$  is used for the majority of the simulation. For the very first step, a modified value of  $C_{\text{first}} = 0.001 C_{\text{base}}$  is used; this is primarily to account for the changes in internal energy and associated dynamics caused by the lack of a term related to the chemistry in the timestep calculation. A second reduced-timestep regime was implemented with the ionising radiation code; for  $N_{\text{slow}}$  steps after the initial step of the simulation, the Courant number is set to  $C_{\text{slow}} = 0.01 C_{\text{base}}$ . This is to account for and resolve the advance of the ionisation front for its initial, sudden expansion through the material at radiation-facing surfaces of the cloud during the R-type front phrase. Ideally, an additional factor would have been added to either of Equations (2.26) and (2.27), however early extremely high time resolution steps were found to reliably resolve any motion of the front without further alteration to the basic equations.  $N_{\text{slow}} = 50$  was used, having been found to provide a large margin of error on tracking the initial progress of the ionisation front (Section 3.1.4).

## 2.7 INITIAL DISTRIBUTION OF SPH PARTICLES

---

Results from computational simulations are always affected by the initial conditions and for certain circumstances even minor variations in initial conditions can have significant effects in the evolution of a simulation. SPH in particular suffers from this, in that an initial distribution of particles invariably introduces inhomogeneities in the inter-particle distance interactions. Various methods are available with which to generate distributions of particles with as little noise as possible. However, an alternative lies in intentionally introducing variation which will dominate over the inter-particle scale variations. This may seem to simply transfer the uncertainty to a different source, the difference lies in the knowledge of how the variation was generated. Particle position variation is unpredictable and difficult to evaluate or account for, whereas an intentionally introduced effect can be controlled and defined more completely.

### 2.7.1 PARTICLE DISTRIBUTION METHODS

To limit the range of effects being accounted for in this investigation, the decision was made to attempt to use homogeneous, uniform density clouds. Multiple methods exist for ensuring that the density is the same throughout the particle distribution, though each has its flaws.

An obvious choice for ensuring that the distribution of nearest neighbour distances for every particle is identical would be to arrange the particles as a grid of some variety, a ‘crystalline’ structure. Either Primitive Cubic (PC) or Body-Centred Cubic (BCC) being simple to produce choices for such a distribution. The disadvantage of this solution is that the particles themselves being distributed in too regular a global pattern is, itself, undesirable. Such global patterns result in grid-aligned anomalies in the simulation results (Diehl et al., 2012). Similar effects are observed when using Eulerian grid codes, grid aligned effects can become noticeable or problematic.

Another method involves using uniform randomly distributed position components created by a random number generator. For a suitably reliable random number generator, this will create a set of particles whose properties are, *on average across the entire placement region*, uniform. On small scales, however, substantial variation in local particle number density is exhibited. This will result in a broad range of actual particle densities, as can be seen in Figures 2.2 and 2.3. The densities displayed in these plots was calculated through the SPH smoothing kernel method as in Equation (2.14), meaning that the distributions shown are those that would be present when run as

actual simulations.

This method can be substantially improved upon by taking the initial distribution and applying some method to permit movement of the particles with the objective of normalising the distance distribution of nearest neighbours. The result of making the inter-particle distance distributions even is to substantially decrease the range of densities, as calculated through the SPH kernel method. An effective way to do this is to process the initial distribution with a pure hydrodynamic code with periodic boundaries. For an effective ideal gas with no solid boundaries, natural pressure equilibrating motion will transition the particles to a configuration with uniform density. For the simulations presented here, this was done with the `Gadget2` code (Springel et al., 2001; Springel, 2005); these generated distributions will be referred to as ‘glass-like’ due to their amorphous structure. Extracting a shape from this cube is then performed using a ‘cookie-cutting’ method. A function returning a boolean indicating whether a particle is inside or outside of the desired shape is generated. This is applied to the initial cube of particles and those particles fulfilling the criteria are output, those that do not are discarded.

To produce a target particle count  $N_{\text{target}}$ , a solution by bisection method was employed. There will be some unknown desired size of the shape to contain  $N_{\text{target}}$ . This size will be  $R_{\text{target}}$ . An initial estimate is made of the size of the shape needed to contain the desired number of particles,  $R_{i=0}$ . If the contained number of particles  $N_i$  is less than  $N_{\text{target}}$ , a new estimate is made of  $R_{i+1} = R_i + R_i 2^{-i}$ . If  $N_i > N_{\text{target}}$ , then  $R_{i+1} = R_i - R_i 2^{-i}$ . In addition, for the version of the algorithm implemented, the dataset in memory for the particles then discards all particles shown to be  $> R_{\text{target}}$ , resulting in a smaller dataset to be searched for the next iteration. This is continued until  $N_i = N_{\text{target}}$ , or until  $i$  exceeds a limiting threshold, in which case an error is returned.

## 2.7.2 PARTICLE DISTRIBUTION EFFECTIVENESS

To present a sample case, a spherical cloud was defined with a mass of  $30 M_{\odot}$  and radius of 1 pc for a target mean density of  $144.80 \text{ cm}^{-3}$  for hydrogen number density. Distributions of 500 000 particles were generated using the uniform random number generation method and a BCC crystalline arrangement as a simple sphere. A box of particles was generated with the `gfortran` random number generator of 7 077 888 particles; 256 timesteps were used in `Gadget2` to reach a refined pressure equilibrium. A 500 000 particle sphere was then extracted from this using the bisection method described above.

For the analysis, we will look at subsets of the entire generated cloud. One is the

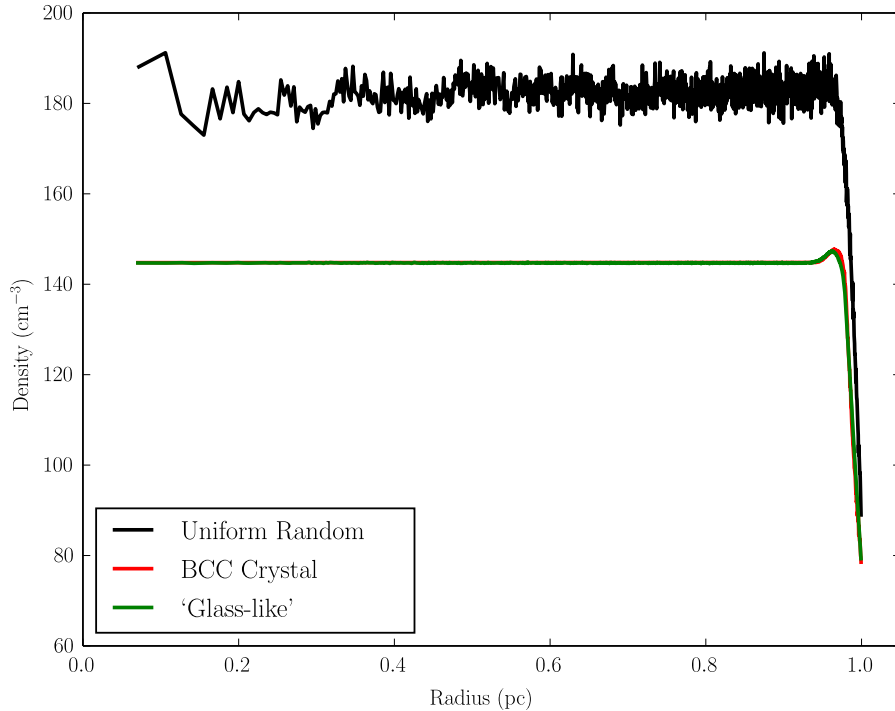


Figure 2.2: Radially binned density for uniform random, glass-like and BCC crystalline particle distributions, intended to represent a homogeneous density of  $144.80 \text{ cm}^{-3}$ . The crystalline distribution is partially obscured by the glass-like distribution for much of the inner portion of the cloud, as the mean values are more similar than can be easily distinguished.

internal region of the cloud (all particles at greater than 2 smoothing lengths from the edge of the cloud), and one set which includes the ‘surface’ particles, those whose distances to the edge of the cloud are smaller than 2 smoothing lengths.

Looking first at the interior region of the cloud, an enormous benefit can be observed in switching method from the uniform random number distribution. The densities and standard deviations are shown in Table 2.2. The key difference is between the mean and standard deviations for the uniform random number distribution and the glass-like distribution. The standard deviation of the densities drops from  $50.2 \text{ cm}^{-3}$  for uniform random to  $1.15 \text{ cm}^{-3}$  for the glass-like distribution. The production of severe under- and over- dense spots within the distributions also results in a poor value for the mean density, giving a percentage difference of approximately 26% from  $n_{\text{target}}$ . This compares with 0.03% for the glass-like, and less than 0.001% for the crystal.

It is of note that the density standard deviation for the BCC crystalline particle distribution in the ‘true’ interior of the cloud is effectively zero (within the machine precision used), where particles are far enough inside that no other particle within their

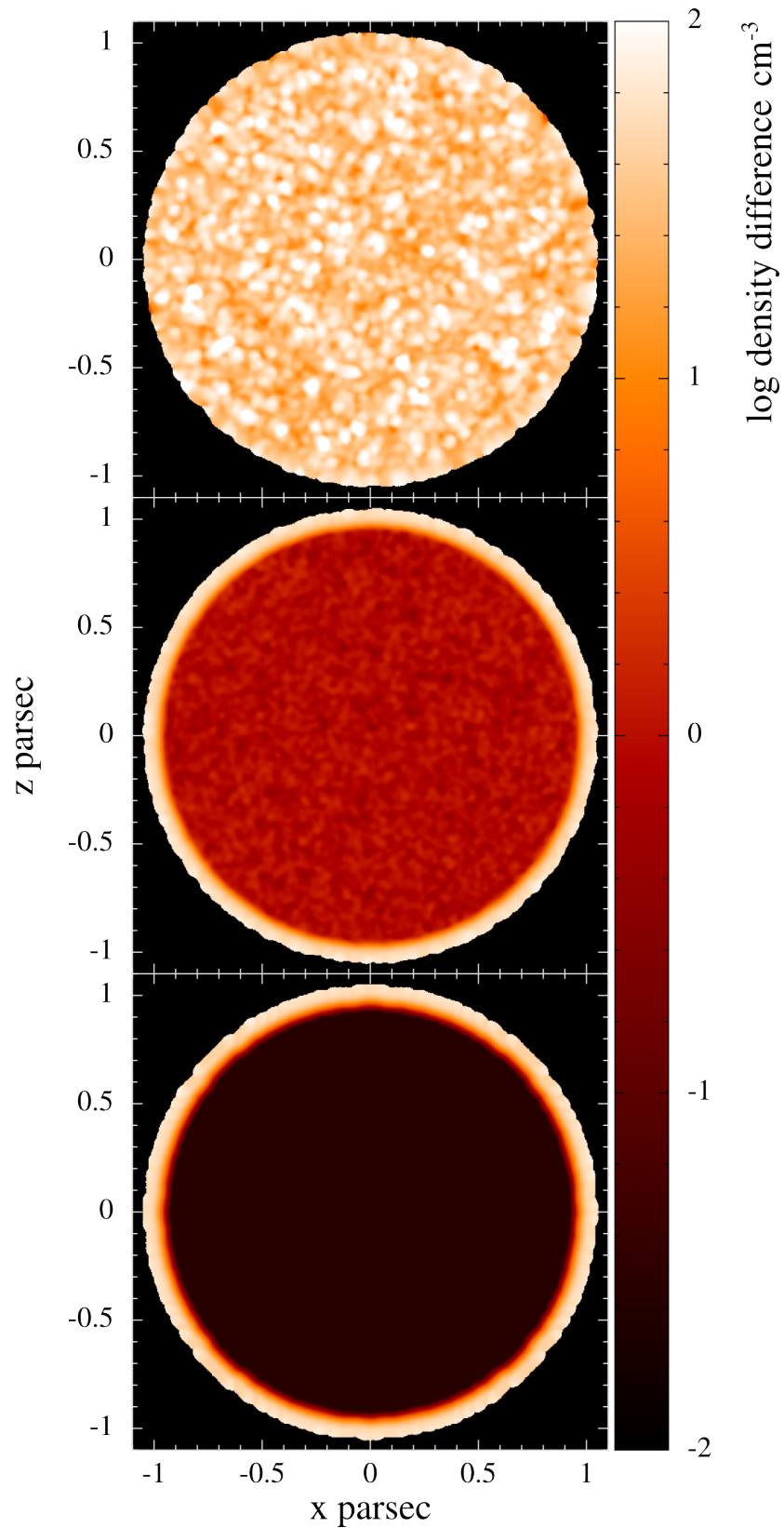


Figure 2.3: Log of the cross-sectional number density difference rendered images of: (top) uniform random number generated distribution (middle) glass-like distribution (bottom) BCC crystalline distribution. Note the improvement in homogeneity from top to bottom, as well as the edge feature in the glass-like and crystalline distribution.

	Interior			Full		
	Median	Mean	$\sigma$	Median	Mean	$\sigma$
Uniform Random	177.146	182.768	50.1941	174.034	179.128	51.2428
Glass-like	144.746	144.756	1.15076	144.692	142.442	10.3048
BCC Crystalline	144.773	144.799	0.15705	144.773	142.467	10.6322

Table 2.2: Statistical properties for the densities of particles produced through different distributions intended to represent the same simulated object. All values are in  $\text{cm}^{-3}$ . The target density was  $144.80 \text{ cm}^{-3}$ .

smoothing length itself has a smoothing length that exceeds the radius of the cloud. This is due to the calculation for density being for effectively the same layout of particles within the smoothing range, with those particles also having identical properties.

These statistics illustrate the misleading accuracy of the crystalline distribution. The exceptional values for the density distribution are more than offset by the undesirable, and un-physical, prominence of crystal plane-aligned features in the evolution and results of simulations with this basis (Diehl et al., 2012).

### 2.7.3 EDGE EFFECT

A noticeable effect which has not been discussed so far, but hinted at, is the difference between the ‘body’ / ‘bulk’ density, and the ‘edge’ densities. The SPH formulation used includes an adaptive smoothing length. This is described in greater detail in Section 2.5.2, but is summarised here in direct relation to the effect being examined for convenience. SPH particle density can be thought of as the mean density obtained by extending an effective volume with radius  $2h$  until it contains  $N_{\text{TOL}}$  nearby particles. It can be thought that it is then the combination of the SPH particle’s fixed mass and the volume defined by the  $2h$  radius sphere encompassing  $N_{\text{TOL}}$  particles which gives the density.

This means that particles close to the edge of cloud will extend this  $2h$  radius further to contain  $N_{\text{TOL}}$  particles than those deep within the cloud. This effect makes perfect sense when considering the intended nature of the SPH particle. Each particle is intended to represent an mass element of a continuous fluid. The particles near the edge of the cloud are attempting to bridge the gap between the constant density material within the cloud, and the apparent vacuum outside of the cloud. SPH particles with variable smoothing lengths are especially poorly adjusted to representing bodies with ‘hard’ boundaries. This is a specific case of their properties of generally not being effective at representing any discontinuity.

As the evaluation of the smoothing kernel for a single particle  $i$  at the position of another particle  $j$  is actually performed with *mutual* smoothing lengths,  $h_{ij} =$

$0.5(h_i + h_j)$ . This means that the effect is not limited to only those particles which possess a smoothing volume which exceeds the bounds of the intended cloud shape, but also those which merely evaluate a neighbour particle which has such a smoothing volume. This is the reason that the standard deviation value for the crystalline structures only falls to effectively zero for particles with approaching a  $4h$  separation from the edge of the cloud.

This is also the cause of the slight *increase* in density just prior to the drop off for the crystalline and glass-like distributions. This is likely due to the interaction lists for each particle being symmetrised. Consider a particle  $i$ , greater than  $2h_i$  from the actual edge, but within the smoothing radius of a particle  $j$  which is on the edge. Its own  $2h_i$  limit does not include a low density boundary particle, but particle  $j$  *does* contribute effective density via its own, larger, value of  $h_j$  in the mutual smoothing length. This results in a very slightly greater density contribution for borderline boundary particles. The size of this lip is of the order of a few percent more dense than the bulk material, of the same magnitude as the standard deviation for the density across the entire distribution and substantially smaller than the variation in the uniform random distribution. Combined with the behaviour of the ionisation equilibrium depth described later, it can be safely neglected.

These effects can be mitigated by altering the SPH particle distribution near the boundary, placing particles in a more densely packed configuration. This would create an artificial SPH particle density increase, balancing the material density decrease resultant at the same locations. Or alternatively placing virtual particles as an outer-surface bound (Liu and Liu, 2003).

These are difficult effects to achieve correctly, however. In addition, secondary effects as a result of forcing the particle distribution in this manner are difficult to predict, and may require other alterations to reduce; or are simply not suitable (in this case the boundary cannot be treated as a specific free surface, for instance).

Given the nature of the simulations to be performed, clouds subjected to ionising EUV radiation, some justifications can be examined which permit leaving the edge effects as they are.

The equilibrium penetration depth of the EUV radiation is given in Equation (3.12) in the next Section. The summary of the reasoning for the establishment of this depth is the position within the cloud at which the number of recombinations along a ‘beam’ reaching that depth, equals the supplied flux. This depth is reached in several recombination timescales,  $t_{\text{rec}} = (n\alpha_B)^{-1}$ , which is of the order of a few  $10^2$  years. The hydrodynamical timescales are taken to be sufficiently large in comparison that this depth is reached before the material being ionised has an opportunity to undergo

motion and expansion in response. This means that the key boundary for the shock generation is at this equilibrium depth. As long as this position exceeds a depth at which the edge effects have reduced (as seen previously), the edge effect itself can be neglected.

For the example clouds described in this section, for instance, the actual penetration depth calculated from the outer radius inwards is 0.067(1) pc for both of the glass-like and crystalline; and 0.047 pc for the uniform random. These were calculated using a simple numerical binning for the density structure and can only be treated as approximate, the actual radiation transfer algorithm evaluates the system in more detail. These are both positioned past the depth at which the edge effects no longer affect the number density. The crystalline distribution becomes perfectly uniform at a depth of 0.03 pc and the glass-like reaches a minimum standard deviation at approximately 0.04 pc.

## 2.8 CODE BACKGROUND

---

This section contains a short overview of the lineage and development of the code used for this research and its features, as well a broad categorisation of the relative advantages and disadvantages of the use of this code compared to others. In other published literature, the code used is referred to as `RadCode II` to distinguish it from the older version of the same code with a different EUV radiation implementation (`RadCode I`) and the original code without any ionising radiation (`Cloud`).

The majority of `Cloud` was developed by Richard Nelson (Nelson and Papaloizou, 1993). It was combined with chemistry routines written by William Langer in 1993 with heating and cooling terms based on Goldsmith and Langer (1978). At this stage it contained: a Smoothed Particle Hydrodynamics (SPH) basis with ; a hierarchical Barnes and Hut Oct Tree system for nearest neighbour searching and gravitational interactions; simple artificial viscosity; a grid-based radiative transfer algorithm for Far Ultraviolet (FUV) radiation; a chemical evolution solver for 12 chemical species; thermal evolution solver with heating and cooling terms derived from the FUV and chemical state solutions, along with constants for cosmic rays and dust temperature; all evolved through time with a leapfrog integration scheme. A number of publications were made using this basic system (Nelson and Papaloizou, 1993, 1994; Nelson and Langer, 1997; Nelson, 1998; Nelson and Langer, 1999).

The code was subsequently expanded to include a host of processes permitting uni-directional ionising Extreme Ultraviolet (EUV) radiation to be modelled, forming

**RadCode I** (Miao et al., 2006, 2009, 2010). This system utilised the existing radiative transfer grid system used by the FUV system, where ionisation state of a single particle was calculated by the attenuation of the initial ionising flux through grid cells of averaged properties for the particles within each grid cell between the source and the particle, up to a distance of  $2h$  from the particle. Within this distance the ionisation state was solved explicitly using the particle's density and the smoothing kernel. Several iterations of this were performed per time-step to converge on the solution for the ionisation state of all particles. This method presented convenience of implementation, and comparatively rapid computation, whilst suffering from low resolution.

As part of the development of this thesis, a new ionising radiation scheme was written and implemented with improved resolution and minimal increase in computational expense. The new method is a ray tracing routine based directly on Kessel-Deynet and Burkert (2003), in which the ionisation state for each particle is computed in order of increasing distance from the source, utilising the ionisation state of already computed particles to obtain the attenuation of the initial flux prior to reaching each subsequent particle. This builds up a complete picture of the ionisation profile from the source outwards. The version with this implemented is the aforementioned **RadCode II**. The concepts and development of the **RadCode II** ionising radiation field code are elaborated upon in the next Chapter.

## CHAPTER 3

---

# IONISING RADIATION AND CODE IMPLEMENTATION

---

In active regions of star formation, feedback of radiation into the progenitor cloud environment is considered to be one of the key factors for the prospect for further star formation in the region. Massive stars, with strong, ionising radiation fields are capable of clearing out their local environment. The radiation has the contradictory effects of both inhibiting and, potentially, driving star formation.

Atomic hydrogen is highly opaque to the ionising radiation, and fully ionised hydrogen is transparent. In any ionised gas, however, protons and electrons will undergo recombination. Each of these recombined hydrogen atoms in the ionised region will then provide a source of opacity, which will expend further photons to reionise. The result of the incident radiation is the advance of an ionisation front determined by the quantity of photons reaching the front boundary itself after the reionisation ‘expenditure’. With a large reservoir of photons, early expansion of an HII region is rapid relative to the sound speeds of the gases. The front will advance faster than the material can react hydrodynamically, being supersonic. For this period the front is termed ‘R-type’ for ‘rarefaction’. Each ionisation event adds energy to the gas, any photon with more than the 13.6 eV required to ionise the hydrogen atoms deposits the remainder as kinetic energy into the liberated pair of proton and electron, gradually increasing the temperature. A high pressure internal environment is left behind as the front advances.

As the HII region volume increases, the number of recombinations/reionisations increases as the cube of the radial size (hence a decrease in available photons at the same rate), and the available photons per unit area of the surface decreases as the inverse square of the radial size. This leads to a comparatively rapid cut-off of available photons as a critical distance, the Strömgren radius (Equation (3.1), Strömgren (1939)), is reached. This represents the distance at which the total available ionising luminosity is spent reionising recombined hydrogen within the HII region volume, with the flux of photons at the outer surface being zero.

$$r_{\text{Strömgren}} = \left( \frac{3}{4} \frac{N_{\text{Lyman}}}{\pi \alpha_B n^2} \right)^{\frac{1}{3}} \quad (3.1)$$

Where  $N_{\text{Lyman}}$  is the total quantity of ionising photons emitted by the central star per unit time,  $n$  is the (atomic) hydrogen number density behind the front and  $\alpha_B$  is the recombination coefficient of proton-electron in units of volume of material per second (the subscript  $B$  indicates the recombination coefficient under a certain approximation which avoids the contribution to ground-state recombinations, described in Section 3.1.1).

In practice the speed of the advance of the front decreases prior to reaching this distance, due to the fall-off in the number of available photons for new ionisation events. As this speed decreases it becomes trans-sonic and sub-sonic relative to the undisturbed material, becoming a so-called ‘D’-type front (for ‘dense’). This means that the ionisation front is moving slowly enough for the material to react and move before it passes. Now, the circumstance is such that there will be a boundary with the same density either side, but behind the front, a pressure of the order of 200 times greater than that ahead (assuming ideal gas behaviour with the parameters for temperatures and mean molecular masses given at the beginning of the section). This pressure discontinuity drives a shock wave normal to the surface of the boundary.

Specifically, there are two threshold velocities, determined by the jump conditions across the ionisation front.  $v_R$  and  $v_D$ , for the R-type and D-type velocities, respectively; and where  $v_R < v_D$ . These are with respect to the ionisation front itself, not the frame of rest of the source star. When the front velocity  $v$  fulfils  $v > v_R$ , it exhibits the R-type front properties, expanding supersonically through the material. As this decelerates due to fewer available ionising photons relative to the density of the material through which the ionisation front is incident, the velocity of the front approaches R-critical,  $v = v_R$ . Below this there is a jump, where an effective isothermal shock is instigated; the velocity of the front falls to D-critical  $v = v_D$  and decreases from this point. This is not derived fully here as it is dealt with in depth in many other sources,

in particular Shu (1991b).

The shock which has been generated, the result of the steep pressure discontinuity between the undisturbed medium and the ionised medium, will continue to propagate ahead of the ionisation front at a velocity  $v_s \approx \sqrt{\frac{F_{\text{Lyman}}}{n}}$  (Bertoldi, 1989). Initially driven and maintained by the steep pressure gradient provided by the ionisation front, it will also dissipate as the ionisation front slows behind it, it loses inertia, and spreads over increasingly large areas.

It is this environment which is of interest for this thesis. In order to investigate this computationally, a good understanding of the radiation field is required.

### 3.1 ALGORITHM IMPLEMENTATION AND INTEGRATION INTO SPH CODE

---

The code used for this research was furnished with an improved ionising radiation transfer routine as part of the project. This implementation was based on that described by Kessel-Deynet and Burkert (2000). This section elaborates the details of the computational process and implementation.

The core concept of a radiation transfer algorithm is the determination of the attenuation and energy deposited at all positions within the material being subjected to the radiation. For some radiation/medium combinations, this is straightforward and attenuation is some fixed function with depth into the medium from the source of the radiation. This is the case for the FUV radiation incident on the molecular clouds dealt with here.

For ionising radiation, feedback exists which complicates the scenario. With the FUV example, the absorption of the FUV radiation changes the temperature and chemistry of the medium, but none of the factors (more or less) relating to the medium's opacity. For ionising radiation, medium which absorbs some amount of the radiation is partially ionised. The (predominantly) proton-electron ionised material becomes virtually transparent to the radiation. This results in the need to solve a set of partial differential equations, either implicitly or explicitly, for the regions through which the radiation is travelling.

In practice for such a code, this is done numerically and iteratively. Such a routine can be computationally expensive, and there is a necessity to balance computational expense against accuracy.

### 3.1.1 MATHEMATICAL FORMULATION

As the dimensions and units for these derivations can be awkward to keep track of, each new parameter is introduced with a statement of its dimensions and the units in which any value for that parameter will be stated in. For any gas element, the ionisation rate can be given as stated in Equation (3.2), where the rate is the product of the un-ionised atomic hydrogen number density ( $n_{\text{HI}}$  in units of  $\text{cm}^{-3}$  wherever values are stated), the hydrogen ionisation cross section ( $\bar{\sigma}$ , in  $\text{cm}^2$ ) and the ionising flux incident on the gas element ( $F$ , in  $\text{cm}^{-2}\text{s}^{-1}$ ). This can be rephrased using the ionisation fraction  $X$  as a parameter, along with the total hydrogen number density  $n$  (neutral + ions). Note that this is specifically only formally correct for plane-parallel radiation, and no more than an approximation where the divergence of the radiation field across the depth of the SPH particle smoothing length can be ignored. For a correct implementation for point sources, the term  $F$  would have to be adjusted for this divergence.

$$R_I = n_{\text{HI}} \bar{\sigma} F = (1 - X) n \bar{\sigma} F. \quad (3.2)$$

The remaining flux after attenuation between the source and the location being examined is given as shown in Equation (3.3).

$$F = F_0 e^{-\tau}, \quad (3.3)$$

with the optical depth  $\tau$  for a given depth of material  $\Delta x$ ,

$$\tau = \bar{\sigma} n (1 - X) \Delta x. \quad (3.4)$$

The recombination rate for any gas element is given in Equation (3.5). For this relation, the electron number density ( $n_e$ ) can be replaced with the product of the ionisation fraction and the total hydrogen number density. This only technically applies when the gas is 100% hydrogen, and the only source of free electrons is already ionised hydrogen (i.e. one per hydrogen ion). The true formulation in the code retains the  $n_e$  expression, as electrons contributing from other ionised sources are counted. Nonetheless, the approximation is an extremely good one and the use of  $n_e$  in the code could be dispensed with, as for the gases considered the free electrons from hydrogen ions vastly outnumber any other sources (by a factor in the region of millions). The  $\alpha_B$  term is the hydrogen recombination coefficient, expressed in units of  $\text{cm}^3\text{s}^{-1}$  where values are given. It is the variant of the term accounting for the ‘on-the-spot’ approximation, in which photons produced by recombination to the ground state (i.e. also capable of ionisation) are not added to a diffuse field, but assumed to be re-absorbed in the immediate region

of the emission (Spitzer, 1978; Shu, 1991a). Specifically, that the total recombination coefficient, which is usually the sum of recombinations into any energy level  $i$ ,  $\alpha_{\text{tot}} = \sum_{i=0}^n \alpha_i$  (in a greatly simplified notation), can be assumed to be the sum instead from recombinations into the first excited state at lowest  $\alpha_B = \sum_{i=1}^n \alpha_i$ . This simplifies the scenario and is massively beneficial computationally, as it avoids treatment of a secondary, non-directional radiation field.

$$R_R = n_e^2 \alpha_B = X^2 n^2 \alpha_B \quad (3.5)$$

Each of the rates in Equations (3.2) and (3.5) are based on number density rates and act in units of  $\text{cm}^{-3} \text{s}^{-1}$ . The net rate resulting in change to the electron number density and ionisation fraction, therefore, are Equations (3.6) and (3.7) respectively.

$$\frac{d n_e}{dt} = R_I - R_R \quad (3.6)$$

$$\frac{d X}{dt} = \frac{R_I - R_R}{n} \quad (3.7)$$

It is shown in Kessel-Deynet and Burkert (2000) that, for a single fluid element such as an SPH particle, the actual depth of the ionisation front itself for realistic purposes is many times smaller than the SPH particle length scales. This means that the front is a discontinuity relative to the SPH particle. As such, the ionisation fraction  $X$  of an SPH particle describes the proportion of the mass of the SPH particle through which the sharp front has travelled. In effect, the position on sub-SPH resolutions at which the front has reached.

With these rates obtained, heating and cooling rates can be calculated to integrate with the thermodynamic evolution described in Section 2.3.5. Heating and cooling through the terms  $f_{\text{HI} \rightarrow \text{HII}}$ ,  $f_{\text{HII} \rightarrow \text{HI}}$  and  $f_{\text{OII}}$ ; the ionisation heating and recombination cooling, as well as the oxygen line cooling, constituting the dominant contributions to temperature equilibrium in the ionised regions.

The ionisation heating contribution is determined by the product of the ionisation rate with the average photon energy above 13.6 eV for a blackbody of temperature  $T_*$ , the temperature of the illuminating star (Cantó et al., 1998). The recombination cooling given by the recombination rate to non-ground states (for which recombination is assumed to be immediately reabsorbed by the ‘on-the-spot’ approximation) and the average electron kinetic energy,  $k_B T_e$  (Hummer and Seaton, 1963). For  $f_{\text{OII}}$ , the formulation for emission of excited OII population photons is taken from Raga et al. (2002).

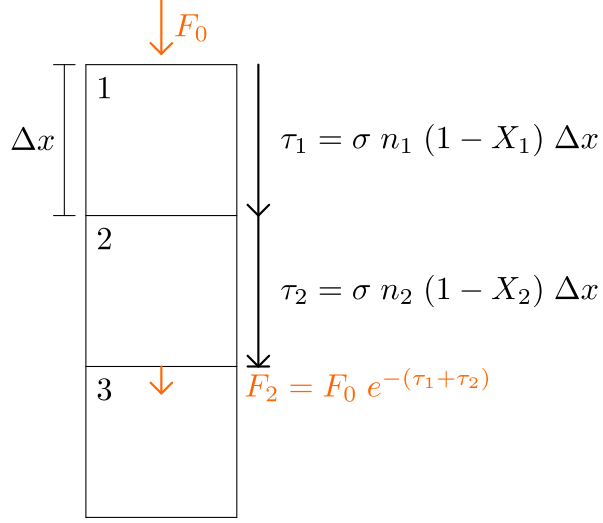


Figure 3.1: One-dimensional grid-based implementation of the algorithm for radiation propagation.

### 3.1.1(a) ONE-DIMENSIONAL EXAMPLE

To illustrate the method of the calculation, one can first consider a simple, one-dimensional grid implementation, without ray tracing for evaluation points. There is a grid as shown in Figure 3.1. Each cell  $i$  of the three cells has density, ionisation fraction and optical depth of  $n_i$ ,  $X_i$  and  $\tau_i$  respectively. Each cell has a flux entering it of  $F_{i-1}$  and exiting it of  $F_i$ . All have physical depth  $\Delta x$ , and are being calculated for a step in time of  $\Delta t$  from  $t = t_0$  to  $t = t_1$ . The ionising radiation is incident on the top of cell 1 with a flux  $F_0$ . The the purpose of the initial illustration, assume that cells 1 and 2 each have already been calculated, and cell 3 is being examined in order to find  $X_3$  and, by necessity,  $\tau_3$ .

The equation for the new value of  $X_3$  is,

$$X_3^{t_1} = X_3^{t_0} + \frac{d X_3}{dt} \Delta t, \quad (3.8)$$

where,

$$\frac{d X_3}{dt} = \frac{R_I(X_3, n_3, F_2) - R_R(X_3, n_3)}{n}. \quad (3.9)$$

$F_2$ , the flux exiting cell 2 to enter cell 3, is given as  $F_2 = F_0 e^{-(\tau_1 + \tau_2)}$ ; attenuated by the total optical depth through cells 1 and 2, as also shown in Figure 3.1.

It is important to notice that the ionisation fraction of any cell  $i$  is dependant only on the solutions for the timestep of the cells that are between it any the radiation source. This means that, provided there is only a single radiation source, the cells can be calculated for each timestep outwards from the radiation source, without needing

to go back to a previous cell and recalculate.

From a numerical standpoint it is important to determine how to solve Equation (3.9). The problem has a number of aspects which make it easier to solve. It has well defined boundaries,  $0 \leq X \leq 1$ , this means that a solution-by-bisection method can be implemented with ease. However, it provides a mediocre computational efficiency with only linear convergence on a solution. Utilising the, only slightly more complex, Newton-Raphson solver provides a quadratic convergence and is preferred for this task, though a bisection solver was implemented initially in order test the method, and validate that the results from the solvers were matching.

### 3.1.2 RAY TRACING

For any single SPH particle within the cloud, calculating its ionisation rate and fraction depend on the knowledge of the obscuring medium between it and the radiation source. This is accomplished here using a ‘ray tracing’ method. Ray tracing is a somewhat general term for a variety of techniques used to trace, or approximate, the path of illumination from some source or sources, towards or through opaque or translucent media. For the algorithm from Kessel-Deynet and Burkert (2000) this process is performed on a per-SPH-particle basis; where the path for a projected ‘ray’ is effectively evaluated from the SPH particle back towards the radiation source. The nearest other SPH particles along the length of this path are selected as representative evaluation points to describe the optical depth from the source to the particle.

As shown in Section 3.1.1, the entire field of SPH-particles only requires a single pass to determine a solution, as long as the SPH particles can be perfectly ordered in distance from the radiation source. More generally, they must be able to be ordered such that for any single SPH particle, the path from it to any radiation source, or sources, does not require another SPH particle to act as an evaluation point if that SPH particle has not itself already been evaluated. With a single radiation source, this is trivial, and distance from the source is the only criteria that needs be evaluated.

For the investigation here, it was simplified further by the radiation source having been selected to be plane-parallel rather than a point source. This assumption means that the particles need only be ordered by their  $z$ -coordinate (the axis of the radiation) a parameter already stored, rather than requiring the calculation of  $d^2 = (x - x_{\text{source}})^2 + (y - y_{\text{source}})^2 + (z - z_{\text{source}})^2$  for every particle prior to the use of a sorting algorithm. The sorting algorithm used in this implementation was a simple heap sort, with order  $\mathcal{O}(n \log n)$ , which was tested extensively and runs effectively. It was adapted from Rosetta Code (Rosetta Code, 2015) under the GNU Free Documentation License.

Once this ordering is performed, the system is almost identical to the 1D grid

described in Section 3.1.1 except that the grid cells are determined by selecting representative particles along the line of sight from the particle being evaluated back to the source. Each ‘cell’ (evaluation interval, herein) is then the evaluation point centred interval to the same for the nearer and farther evaluation points. This is illustrated in Figure 3.2, as the concept described in words is unwieldy.

First, the neighbours of the particle  $i$  being evaluated are known to at least within  $2h_i$  of its position. The particle from this list which is closest to the line of sight (defined by the minimum opening angle) is selected as an evaluation point, provided that it is also within  $2a_i$  physical offset from the line of sight. This additional criteria effectively defines the ‘upper surface’ of the cloud, by setting the condition under which a path is determined to have no further evaluation points between the last position and the ionising source.

Key steps, illustrated in Figure 3.2, are as described below. In the explanation, the particle for which the ionisation properties are being determined is the ‘focus particle’. The straight line directly connecting the focus particle to the source is the ‘line of sight’ (LOS). each particle selected en-route to the source is an ‘evaluation particle’  $i$  which provides ‘evaluation points’ on the LOS at positions perpendicular to the true location of the evaluation particle. Each particle  $i$  has its own neighbours  $j$ . When the LOS is split into segments for the evaluation of the behaviour of the radiation travelling to the focus particle, each 1D segment associated with an evaluation point is an ‘evaluation interval’.

- (a) First, the neighbours of the focus particle are known to at least within  $2h_{\text{focus}}$  of its position. Any particle  $i$  from this list which is closest to the line of sight (minimum opening angle) is selected as an evaluation point, provided that it is also within  $2a_i$  perpendicular offset from the line of sight. Evaluation points are indicated as crosses in Figure 3.2.
- (b)-(d) This process continues from the previously selected evaluation particle. Within  $2h_i$  of evaluation particle  $i$ , the next neighbour particle  $j$  that is: (1) nearer to the radiation source than  $i$ , (2) within  $2a_j$  of the LOS, (3) smallest opening angle  $\theta_{\text{source-focus-}j}$  by the angle formed by the source, to the focus particle, to particle  $j$  (i.e. not the smallest angle source- $i$ - $j$ ). This selects the next evaluation point, and continues until a circumstance shown in the next panel, (e).
- (e) once an evaluation particle  $i$  is reached for which none of its own neighbours  $j$  satisfy all of the requirements in the previous point (nearer,  $2a_j$  from LOS, smallest opening angle), the evaluation deems itself to have reached the end of the representative medium between the focus particle and the source.

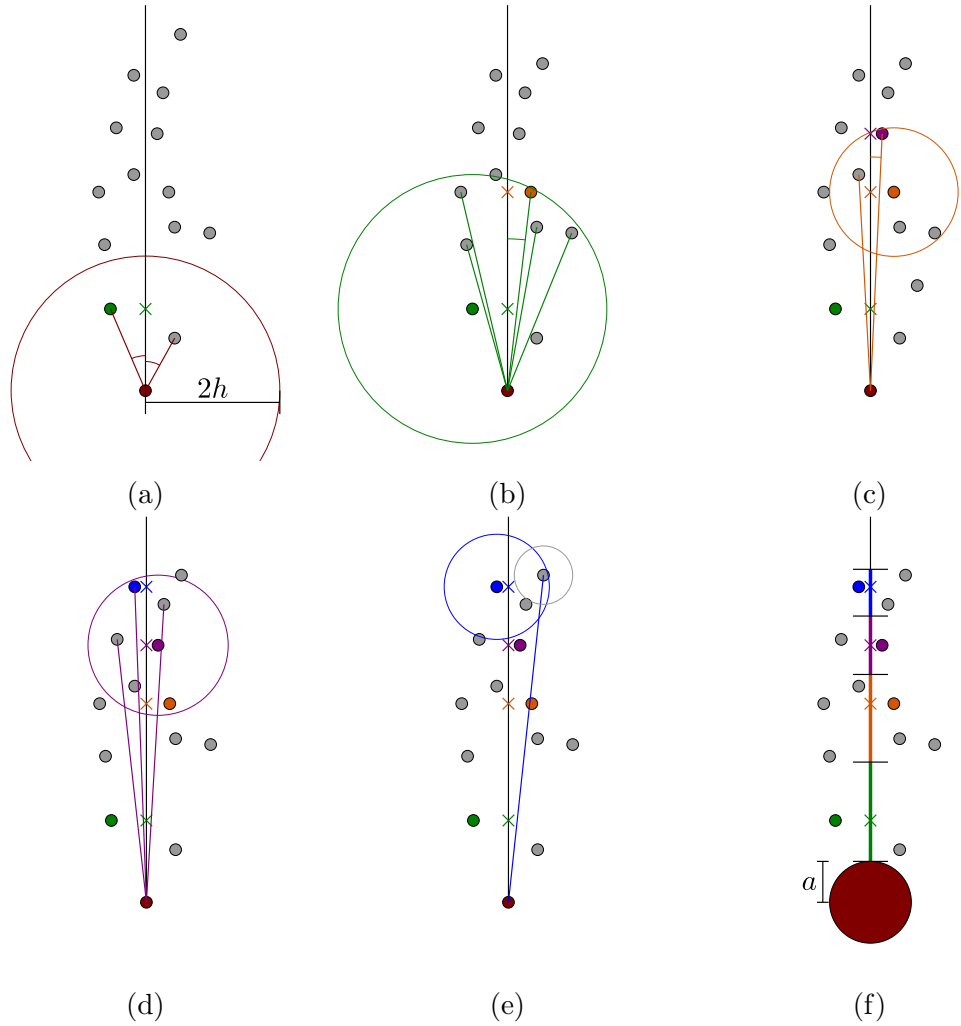


Figure 3.2: Illustration of the building and creation of the evaluation point and evaluation intervals, in the ray tracing algorithm for radiation transfer. In sequence, (a) to (e), the construction of the evaluation points used to determine the flux reaching the focus particle (red, at the foot of each panel) and therefore its own optical depth and change in ionisation fraction. Also (f), the conversion of the evaluation point positions into 1D evaluation intervals. See text for a full description of the process.

- (f) the evaluation points for each evaluation particle are converted into evaluation intervals. Each interval extends half-way between its own evaluation point and the adjacent evaluation points. This is bar two exceptions, the initial evaluation point has an interval for which the ‘near’ side extends all the way to within  $2a_{\text{focus}}$  of the focus particle. The final evaluation point has an interval for which the ‘far’ side extends to  $2a_{\text{final}}$  of the evaluation point.

This is the algorithm as laid out by Kessel-Deynet and Burkert (2000); however, alterations were made to adjust for circumstances found to be of issue in the code. There is an initial stage of binning the particle IDs into  $N_{\text{col}} \times N_{\text{col}}$  columns, where the bounds of the columns are the outermost positions of the particles.  $N_{\text{col}}$  was set as the required value to fill the area of particles with columns of area  $\langle h \rangle^2$ , the mean smoothing length squared. These column lists are used as an additional search regime for when an alleged ‘final’ evaluation particle is found.

This additional search determines whether there is a possibility of more particles between the ‘final’ particle and the radiation source, which are outside the range of the nearest neighbour list. This additional search was added as, for lower resolutions, it was found in testing that configurations of particles could arise where the evaluation path appeared to reach the radiation source, despite still having further material ‘in the way’. This can occur if the cloud has any stratification of dense-diffuse-dense in the direction of the radiation; or regions near the outer edge of the material. The distribution of particles in the ‘diffuse’ portion could be such that an evaluation path from the dense region farthest from the radiation could create evaluation paths appearing to end once they reached the diffuse region.

As the columns are constructed after the sorting of particles by their distance to the radiation source, they are also so sorted within the column lists. This makes the searches in the columns for possible particles ahead of the ‘final’ evaluation particle quicker than might otherwise be the case. Whilst it is not intrinsically computationally efficient, as it only needs to be performed once per evaluation path (and so once per particle) and the search is linear for the quantity of particles in the list, it is only marginally slower than  $\mathcal{O}(n)$  and was believed to be a justifiable computational expense.

### 3.1.3 OPTICAL PATH EVALUATION

As previously described, once the evaluation path is built up as described, it is then operated on in the same manner as the simple gridded example as shown in Section 3.1.1. In this case, however, rather than a uniform  $\Delta x$  depth to each evaluation segment,

the evaluation interval length is used, with the properties of the evaluation particle assumed to apply along that interval’s length. The definition of the optical depths per-evaluation interval remain in the form described by Equation (3.4).

### 3.1.4 TIMESTEP MODIFICATION

The characteristic timescale of the ionising radiation is the recombination time,

$$t_{\text{rec}} = (n \alpha_B)^{-1}. \quad (3.10)$$

It is in several instances of this time that all of the dynamic radiation processes occur. For the vast majority of the simulation, this will be far smaller than the characteristic timestep based on the hydrodynamic properties of the simulation, the HK timestep Equation (2.27), an expansion of the Courant-Friedrichs-Lewy condition described in Section 2.6.2. However, this does not necessitate that the simulation timestep be reduced to  $t_{\text{rec}}$ . As shown in Kessel-Deynet and Burkert (2000), the equilibrium position of the ionisation front can be represented ‘macroscopically’. The larger timestep can be used, with the assumption that the ionising radiation is simply ‘keeping up’ with the equilibrium position of the gas which, after an initial expansion phase whilst still an R-type front, is set by the hydrodynamic constraints of the gas changing.

As such, it is only important to resolve the front in time whilst it is undergoing R-type expansion. Failure to do so during this phase would result in the ionisation front advancing to a particular position, at which location the shock front would be initiated. On the next timestep, this failure can result in the ionisation front jumping past the new infant shock front, establishing *another* such front further on. This is obviously hugely non-physical and means that the establishment of the initial equilibrium position of the ionisation front prior to shock propagation must be determined correctly.

For this purpose a crude alteration to the timestepping routine was implemented. This was based on an empirical assessment using the testing results in Section 3.2. The first  $N_{\text{slow}}$  timesteps are advanced at a Courant parameter value of  $C_{\text{slow}} = 0.01 C_{\text{base}}$ . This provides adequate time for the front to have advanced to its equilibrium position in resolved steps for the densities examined in this thesis.

As described, this is an implementation based on empirical results, done so for efficiency in time and computation. A more robust implementation, for more generalised initial conditions, would require an evaluation of the specific  $t_{\text{rec}}$  value and additional modifications to the timestepping algorithm. Nonetheless, through the testing no indication of a failure to converge the solution for the initial shock front was determined with this criteria, for the range of parameters investigated for this thesis.

## 3.2 IONISING RADIATION TESTING

---

In order to test the validity of the code for propagation of ionising radiation, a series of tests were conducted for several standard models (Gritschneider et al., 2009a; Kessel-Deynet and Burkert, 2003; Lefloch and Lazareff, 1994). This provides a grounding of comparison with well established analytical solutions or popularly used testing models.

There are two test scenarios being investigated.

1. A uniform density box of material with constant pressure (not periodic or reflective) boundary conditions, excluding hydrodynamics. This investigates the simple propagation of the ionisation front through uniform material, observing both rate of propagation and the profile of the ionisation front with depth. This is conceptually similar to the manner of process in an R-type ionisation front, where the ionisation front velocity is far greater than the sound speed of the medium. The effective process being investigated is the code's ability to conform to a 1D plane-parallel formulation of the expansion and equilibrium of a Strömngren sphere (Strömngren, 1939).
2. Hydrodynamic implosion. In this scenario, replicating that of Lefloch and Lazareff (1994), a cold, neutral sphere of material is placed inside a hot, diffuse medium. This directly mimics the boundary across the ionisation front generated by the first test, but reducing the number of variables being examined. The direct effect of the ionising code on the hydrodynamics is exclusively via the change to each particle's internal energy/temperature. With the ionisation propagation and structure determined to be physical, the remaining test is on the shock conditions themselves.

### 3.2.1 IONISATION WITHOUT HYDRODYNAMICS

Of initial importance is testing the ionising radiation process itself, without considering the complications of dynamic media reacting to the radiation. These tests consist of the propagation of plane-parallel ionising radiation into a static, isothermal column of fixed density material.

### 3.2.1(a) ANALYTICAL SOLUTIONS FOR THE PROPAGATION OF THE IONISATION FRONT

The equilibrium condition for the simplest static geometry which can be constructed assumes the ionisation front to be a step function with the discontinuity at the front, between neutral material with zero ionisation fraction, and ionised material with  $X_i$  ionisation fraction. The gas in a cuboid box, of constant Hydrogen number density,  $n$ , is illuminated by a constant flux directed along one axis at the surface of the material (depth = 0),  $F_0$ .  $x = 0$  will always be the edge of the material with the incident radiation, directed in the positive  $x$  direction.

The equilibrium depth,  $x_s$ , is the depth at which the sum of the recombinations per unit area and unit time equals the supplied flux,  $F_0$ ,

$$x_s n^2 \alpha_B X_i^2 = F_0, \quad (3.11)$$

where  $X_i$  is the ionisation fraction within the ionised region,

$$x_s = \frac{F_0}{n^2 \alpha_B X_i^2}. \quad (3.12)$$

This notional equilibrium depth is not realised in practice, as the assumption of a discontinuous jump at the front, while thin, is still technically smoothly varying. In the case of the code implementation, this will be exaggerated by the discretised nature of computational simulation. The ideal solution assumes that the material is capable of becoming perfectly ionised, providing a value for  $X_i$  of 1. This corresponding value of  $x_s$  is defined as  $x_{s0}$ .

The profile for the advance of the front can be derived to obtain a theoretical comparison to the simulation results. The basic expression for this can be given as,

$$\frac{dx}{dt} = \frac{F_0 - x \alpha_B n^2 X_i^2}{n}, \quad (3.13)$$

consisting of the distance by which the ionising flux would advance the front in a given time  $\Delta t$  ( $F_0 \Delta t/n$ ) and the recombination would recede it in the same time ( $x \alpha_B n^2 X_i^2 \Delta t/n$ ), expressed in a continuous form. In a form with previously established parameters for recombination timescale and equilibrium depth,  $t_{\text{rec}}$  and  $x_s$ , this becomes,

$$\frac{dx}{dt} = \frac{x_{s0} - x X_i^2}{t_{\text{rec}}}, \quad (3.14)$$

for which the solution is,

$$x = \frac{x_{s0}}{X_i^2} \left(1 - e^{-\frac{t X_i^2}{t_{\text{rec}}}}\right). \quad (3.15)$$

The equilibrium condition is approximately reached within a few recombination timescales,  $t_{\text{rec}} = (n \alpha_B)^{-1}$ , as can be seen from the form of Equation (3.15). This time is generally short in comparison with the evolution timescales of the astrophysical conditions being examined, but can be looked at in more detail to ensure the veracity of this short-timescale process, and evaluate the computational implementation.

### 3.2.1(b) IONISATION STRUCTURE AT EQUILIBRIUM

Another useful diagnostic for the accuracy of the radiation absorption with depth is the exact profile of the ionisation fraction over the depth that it is absorbed. This is especially useful as it is independent of any definitions of an artificial, binary condition discontinuity between fully ionised, and fully neutral gas. The profile of the ionisation fraction with depth can be derived to obtain a differential equation in a form comparable with computational results as follows.

Beginning with the equation for the ionisation equilibrium,

$$n (1 - X_x) F_x \bar{\sigma} = n^2 X_x^2 \alpha_B, \quad (3.16)$$

the radiation flux at depth  $x$ ,  $F_x$ , is described in terms of the incident radiation,  $F_0$  and the optical depth to  $x$ ,  $\tau_x$ ,

$$n (1 - X_x) F_0 e^{-\tau_x} \bar{\sigma} = n^2 X_x^2 \alpha_B, \quad (3.17)$$

where  $\tau_x$  is given by,

$$\tau_x = \int_0^x \bar{\sigma} n (1 - X_s) ds. \quad (3.18)$$

The radiation equilibrium depth  $x_{s0}$ , is given by  $x_{s0} = F_0/n^2 \alpha_B$ , permitting us to factor out  $F_0$  and then divide through by  $n^2 \alpha_B$  to simplify the equation,

$$n (1 - X_x) x_{s0} e^{-\tau_x} \bar{\sigma} = X_x^2. \quad (3.19)$$

This can then be differentiated with respect to  $x$ ,

$$n x_{s0} \bar{\sigma} \left( (1 - X_x) \frac{d}{dx} e^{-\tau_x} + e^{-\tau_x} \frac{d}{dx} (1 - X_x) \right) = \frac{d}{dx} X_x^2, \quad (3.20)$$

$$n x_{s0} \bar{\sigma} \left( -(1 - X_x) e^{-\tau_x} \frac{d\tau_x}{dx} + e^{-\tau_x} \frac{d}{dx}(1 - X_x) \right) = \frac{d}{dx} X_x^2, \quad (3.21)$$

$$n x_{s0} \bar{\sigma} e^{-\tau_x} \left( -\frac{d\tau_x}{dx} (1 - X_x) - \frac{dX_x}{dx} \right) = 2 X_x \frac{dX_x}{dx}. \quad (3.22)$$

This can be greatly simplified by observing that, as shown by Equation (3.19),

$$\frac{X_x^2}{e^{-\tau_x} (1 - X_x) \bar{\sigma} n x_{s0}} = 1, \quad (3.23)$$

multiplying through by this results in,

$$-X_x^2 \frac{d\tau_x}{dx} - \frac{X_x^2}{1 - X_x} \frac{dX_x}{dx} = 2 X_x \frac{dX_x}{dx}. \quad (3.24)$$

Simplifying further, and expanding the differential  $\frac{d\tau_x}{dx}$  using Equation (3.18), we obtain,

$$-X_x (\bar{\sigma} n (1 - X_x)) - \frac{X_x}{1 - X_x} \frac{dX_x}{dx} = 2 \frac{dX_x}{dx}. \quad (3.25)$$

Consolidating the remaining differential, we can get,

$$\left( 2 + \frac{X_x}{1 - X_x} \right) \frac{dX_x}{dx} = -X_x \bar{\sigma} n (1 - X_x), \quad (3.26)$$

alternatively able to be expressed as,

$$\frac{2 - X_x}{1 - X_x} \frac{dX_x}{dx} = -X_x \bar{\sigma} n (1 - X_x), \quad (3.27)$$

resulting in the final differential equation,

$$\frac{dX_x}{dx} = -\frac{X_x (1 - X_x)^2}{2 - X_x} \bar{\sigma} n. \quad (3.28)$$

This is coupled with a boundary condition, being the ionisation fraction at  $x = 0$  for a complete solution. This result, however, is extremely sensitive to minor variations in that boundary condition. As the boundary ionisation fraction approaches 1.0, the effective location of the front tends to infinity. The solution to this is examined in Section 3.2.1(e).

### 3.2.1(c) IONISATION FRONT DETERMINATION FOR NUMERICAL SIMULATIONS

In order to compare the subsequent numerical test results with the analytical solutions, parameters were chosen to keep the tests in line with those performed by Gritschneider et al. (2009a).

The recombination coefficient,  $\alpha_B$ , was set as  $2.7 \times 10^{-13} \text{ cm}^3 \text{ s}^{-1}$ , and the absorption cross section,  $\bar{\sigma}$ , to  $3.52 \times 10^{-18} \text{ cm}^2$ . The flux was set as  $8.33 \times 10^7 \text{ s}^{-1} \text{ cm}^{-2}$  and the density of the material was fixed at  $10 \text{ cm}^{-3}$ . These values give the equilibrium depth and recombination timescale as  $x_{s0} = 1.00 \text{ pc}$  and  $t_{\text{rec}} = 11.7 \text{ kyr}$ .

To determine the ionisation front evolution with time from the numerical simulation results, it is necessary to find a way to suitably define the position  $x$  of the front for the effectively continuous and smoothly varying interface layer which exists between the highly ionised and neutral gases. There are several ways of defining this, utilising varying assumptions and processes. Any ‘geometric’ method, defining a position on the shape of the front, must define a ionisation fraction threshold,  $X_{\text{thresh}}$ ; for which, wherever the ionisation fraction profile crosses this threshold is the location at which the ‘position’ of the front is defined.

1. A naïve, but straightforward and generally representative, assumption is to set  $X_{\text{thresh}} = 0.5$ , that at whatever depth the gas becomes more neutral than it is ionised is the front. If the front profile were symmetric about this threshold this would fulfil other criteria, however this is not the case.
2. Perhaps a better basis relates to the quantity of material which is actually ionised, the integral of the ionisation fraction profile with depth. It is then possible to compare the integral of a step function which switches from 1 to 0 at the depth  $x_s$ , and the integral for a smooth front profile described in Section 3.2.1(b). A numerical solver by bisection was used to evaluate this problem, minimising the function

$$f = \left| \int X_{\text{step}} dx - \int X_{\text{smooth}} dx \right|, \quad (3.29)$$

using the smooth profile boundary condition  $X_0$  as the free parameter. The step function with depth being  $X_{\text{step}}$  and the numerically calculated solution to the differential equation given in Equation (3.28) being  $X_{\text{smooth}}$ . Once a minimum has been found, the ionisation fraction at which the two profiles cross can be found. This provides a threshold value  $X_{\text{thresh}}$  to be used in the same manner as the previous method. Using this process, a value was found for  $X_{\text{thresh}}$  of 0.734 299 for  $X_i = 1$ ,  $x_s = x_{s0}$  (for which the boundary condition was found to be

$X_0 = 0.990586$ ). This means that a smooth ionisation profile crossing the step function at  $X = 0.734299$  provides the same quantity of ionised material as the step function itself.

Using this threshold throughout assumes that the shape of the front takes the same form throughout the evolution. This is not the case; meaning that the position of the front for the simulation will be inaccurate at early times, but tend towards this correct solution as time progresses.

3. Rather than describe the position of the front in terms of the shape of the front at each step, this can be bypassed, and the underlying mechanism for the previous method can be used directly. For this a quantity  $x'$  can be introduced, which is the integral of the ionisation fraction the material with depth over all space,

$$x' = \int_0^{\infty} X_x dx. \quad (3.30)$$

This quantity is the column depth of material ionised.

As the SPH particles comprising the material are known to be spread evenly along the length of the material, it is a simple process to obtain the equivalent discretised quantity for the simulations. This can be defined as the summation,

$$x' = \sum_{i=1}^{n_{\text{partic}}} X_i \Delta x, \quad (3.31)$$

where  $\Delta x = x_{\text{max}}/n_{\text{partic}}$ , the approximate depth represented by any single particle in the collection; the total depth divided by the number of particles,  $n_{\text{partic}}$ . This also gives the property  $x_s'$ , the same calculation for the point at which the front has reached equilibrium.

It is method 3 which shall be used, as it means that the solution given by Equation (3.15) can be used with  $X_i = 1$ ; due to the correspondence of the quantity of material being ionised. The description for method 2 is presented here regardless as it is used to calculate the correct boundary conditions for the analytical solution of Section 3.2.1(b).

Figure 3.3 is an illustration of the raw data for a 50 000 particle simulation after a short while running, but before equilibrium is reached. The lowest particle count was selected as the variations in both methods 2 and 3 are expected to be sensitive to particle count, the differences will therefore be exaggerated here and represent an upper bound on the uncertainties. Plotted along with the raw particle distribution is a horizontal line at  $X_{\text{thresh}}$  and vertical lines indicating the front position using methods 2

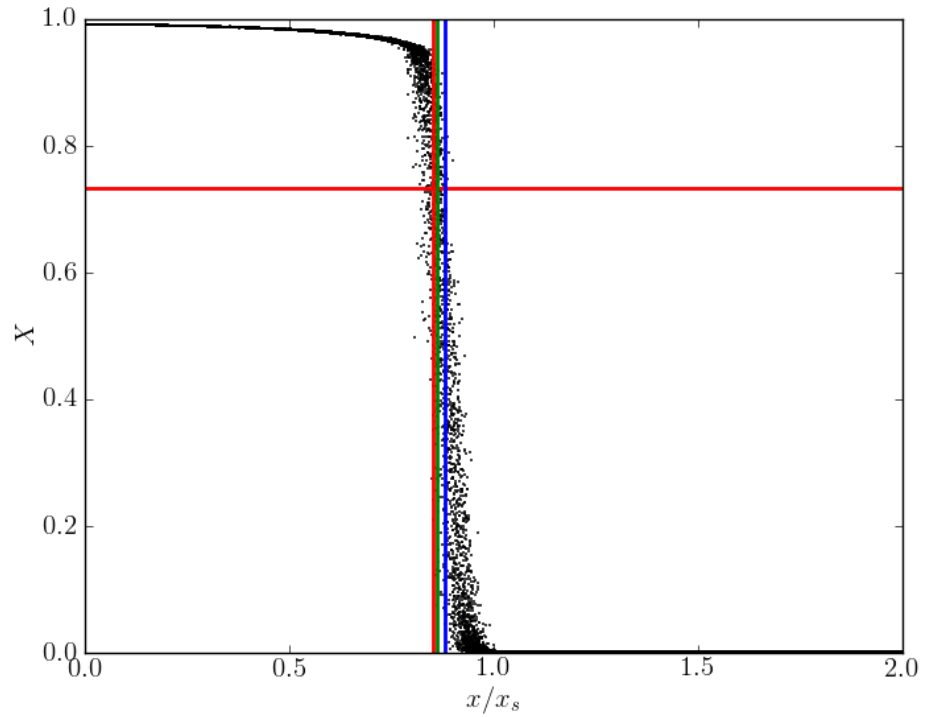


Figure 3.3: 50 000 particle simulation for 1D, non-hydrodynamic ionisation front propagation test at 24.82 kyr ( $\approx 2.1 t_{\text{rec}}$ ). Shown are the particle ionisation fractions with depth; the red horizontal line is at  $X_{\text{thresh}} = 0.734\,299$ , the red vertical blue line is the Gaussian-based fit to the weighted-mean position of the particles at the same  $X_{\text{thresh}}$ , the blue vertical line is the analytical solution position based on Equation (3.15); and the green vertical line is given by the particle ionisation fraction integral described in Equation (3.31).

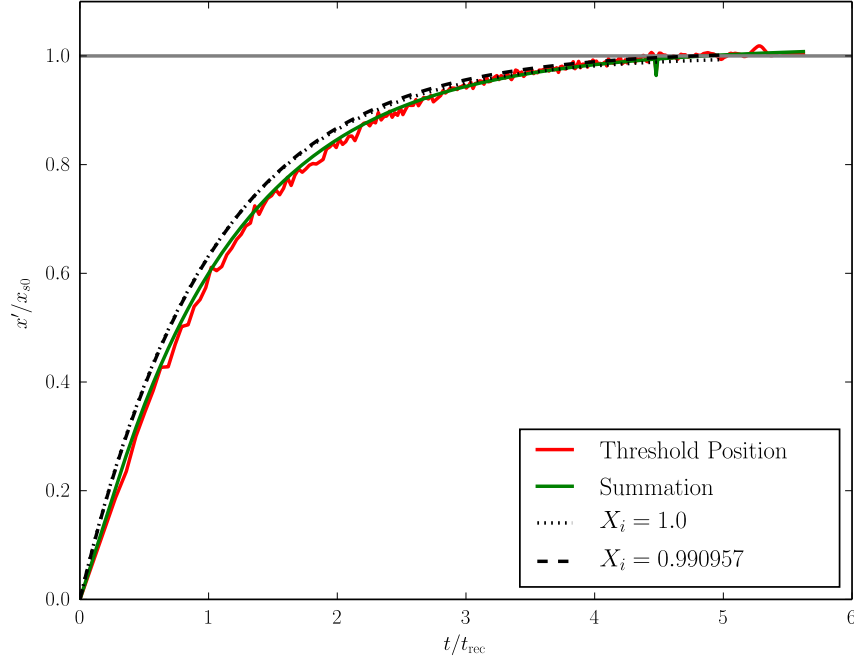


Figure 3.4: Results for 50 000 particles for static medium ionisation front propagation tests. Illustrated by a solid red line is the position with time of the ionisation front using the  $X_{\text{thresh}} = 0.734299$  criteria, and the solid green line the direct summation/integral method given by Equation (3.31); as well as the analytical solutions of Equation (3.15) for  $X_0 = 1$  and  $X_0 = 0.990586$ .

and 3. The method 2 position was calculated using the particle positions for a Gaussian weighted average centred on  $X_{\text{thresh}}$ . The Gaussian width,  $\sigma_{\text{gauss}}$  was selected as 0.001, an arbitrary value small enough to be a narrow selection, but large enough to include sufficient particles for a valuable estimation; only particles within  $7\sigma_{\text{gauss}}$  were used. The number of particles within that range varies for each test and total particle count, but for the 50 000 particle test displayed, this value varied between 100 and 200. This plot represents relative positions of the lines around the maximum that they diverged; as time increases the line positions become closer to the extent that they invariably overlap.

Figure 3.4 is a comparison of these two methods, the position corresponding to method 2, the particle ionisation fraction of  $X = X_{\text{thresh}} = 0.734299$ , and the integral equivalent through method 3. The results converge towards the same solution as equilibrium is reached towards  $t/t_{\text{rec}} = 5$ , but present a slightly different profile at earlier  $t/t_{\text{rec}}$ . The values differ by no more than  $0.03/x_{s0}$  even within the steepest section of the profile, indicating that the variation of the shape of the ionisation front with time is only minor; the  $X_{\text{thresh}}$  based value for position along the front is also less smooth

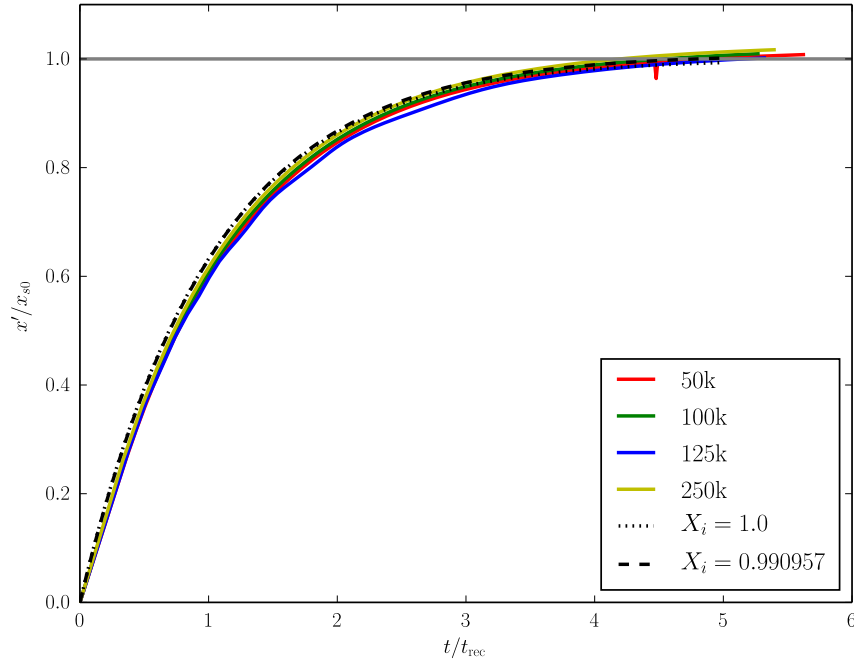


Figure 3.5: Profiles of ionisation front position with time for varied particle number of the static medium ionisation front propagation tests. Illustrated are the positions with time of the ionisation front using the integral method described in the text, for 50 000, 100 000 and 250 000 particles in a glass-like structure, and 125 000 particles in a cubic grid structure. The dashed line indicates the analytical solution for the propagation of a discontinuous front through the same medium.

than the summation process.

### 3.2.1(d) NUMERICAL RESULTS FOR IONISATION FRONT PROPAGATION

Figure 3.5 contains the results for tests of 50 000, 100 000 and 250 000 particles in the glass-like structure described in Section 2.7.1, as well as a 125 000 particle  $50 \times 50 \times 50$  cubic grid; again mirroring the test setup used by Gritschneider et al. (2009a). The 50 000 particle test was included as the baseline for previous tests run to produce quick results for feedback into checking the code.

The numerical results appear to overestimate  $x_s'$ , ending at 1.007 9, 1.009 6, 1.001 8 and 1.016 9 for 50 000, 100 000, 125 000 and 250 000 particles respectively. However, in the case of each numerical simulation, the maximum ionisation fraction observed for any particle is approximately 0.990 6. If one uses the full form of the equilibrium depth equation,  $x_s = F_0/(n^2 \alpha_B X_i^2)$ , using  $X_i = 0.990 6$ ,  $x_s'$  is given as 1.009. The use of this

value for  $X_i$  can be justified by the boundary condition calculation in Section 3.2.1(b).

### 3.2.1(e) INVESTIGATION OF EQUILIBRIUM IONISATION PROFILE

The exact profile with depth of the ionisation front from the tests already described with the analytical solution for the front given in Section 3.2.1(b) can be compared. As described there, however, determining the correct boundary condition is of importance, as the apparent penetration depth of the front in the analytical solution is highly sensitive to this parameter.

Calculating the boundary condition can be done analytically by determining a non-empirical value for  $X_0$  first. Using Equation (3.16) and the knowledge that, at the surface ( $x = 0$ ),  $\tau_x = 0$ , we have,

$$n (1 - X_0) F_0 \bar{\sigma} = n^2 X_0^2 \alpha_B, \quad (3.32)$$

this provides us with an equation which can be solved for  $X_0$ . The solution has the form (using  $a = F_0 n \bar{\sigma}$  and  $b = n^2 \alpha_B$ ),

$$X_0^{\text{calc}} = \frac{\sqrt{a^2 + 4 a b} - a}{2 b}. \quad (3.33)$$

For the physical situation being investigated, this gives a value for  $X_0$  of  $X_0^{\text{calc}} = 0.990\,957$ . This boundary condition can be examined with the property used to define the step function position of the front, the integral of the ionisation fraction over depth, giving a value of  $x' = 1.046x_{s0}$ . This is in excess of the solutions for  $x'_s$  using Equation (3.12) for either the ideal case  $X_i = 1$ ,  $x_s = x'_s = x_{s0}$ , or the modified case  $X_i = X_0^{\text{calc}} = 0.990\,957$  ( $x'_s = 1.010$ ). As a result, the profile appears correspondingly deeper than the simulation results, for which the integral was never more than 1.017.

Selection of the suitable boundary can also be investigated empirically using the method for finding  $X_{\text{thresh}}$  (Method 2) in Section 3.2.1(c), such that the integrated quantity  $x'_s$  for the profile matches up with the calculated value of that quantity. This gives a boundary value of  $X_0 = 0.990\,586$  for  $X_i = 1.0$ ; and  $X_0 = 0.990\,591$  for  $X_i = X_0^{\text{calc}}$ . Both fall close to the maximum ionisation fraction of any SPH particle in the simulations, all being in the vicinity of 0.990 6.

Figure 3.6 shows the results for these tests, displaying profiles for each of the particle numbers used previously (50 000, 100 000 and 250 000 in a glass distribution; 125 000 on a simple cubic lattice). In addition, two of the analytical solutions discussed are shown; firstly the case where the boundary condition  $X_0 = X_0^{\text{calc}}$ , and secondly the ‘best fit’ condition of  $X_0 = 0.990\,591$ . In the case of the former, it can be seen how much further

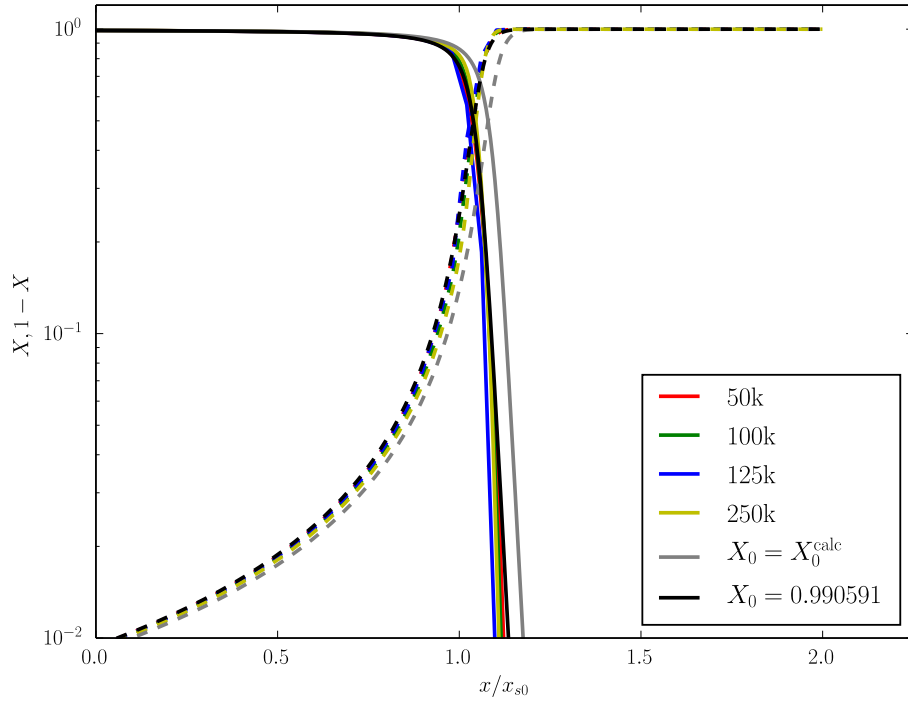


Figure 3.6: Results for varied particle number for the ionisation fraction profile at equilibrium. Illustrated are the Gaussian-smoothed fits to the particle distributions of ionisation fraction with depth at  $t \approx 5t_{\text{rec}}$ . Shown are lines for 50 000, 100 000 and 250 000 particles in a glass-like structure, and 125 000 particles in a cubic grid structure. Solid lines are the ionised fraction, dashed lines are the neutral fraction. The grey line represents the analytical solution based on Equation (3.28) for the boundary condition  $X_0 = X_0^{\text{calc}}$ , and the black line that but with the boundary condition  $X_0 = 0.990591$ .

into the cloud the profile appears to have progressed. The latter provides a modified profile matching up with the analytical solution for the integrated penetration depth,  $x_s'$ . This form provides a close fit with the displayed numerical results.

### 3.2.2 IONISATION INCLUDING HYDRODYNAMICS - HYDRODYNAMIC IMPLOSION

The key interaction between the ionising radiation and the hydrodynamics components of the code is not directly, but via the intermediate step of altering the internal energy of the particles affected. Once the ionising radiation has done this, the behaviour of the particles reaction to this change in internal energy is purely hydrodynamic. This can be exploited to create a pure hydrodynamic test case which investigates whether the alterations to the material which would be caused by the ionising radiation would be followed through correctly by the hydrodynamics.

The concept of this test is a hydrodynamic implosion scenario, described and used by Lefloch and Lazareff (1994). For the same purpose, a central, high density ( $n_c = 100 \text{ cm}^{-3}$ ), low pressure ‘cold’ sphere is embedded in a low density ( $n_h = 10 \text{ cm}^{-3}$ ), high pressure ‘hot’ medium. The respective temperatures are selected such that a specific pressure ratio between the cold sphere and the warm medium of  $P_h/P_c = 20$  is set. This requires  $T_c = 100 \text{ K}$  and  $T_h = 20\,000 \text{ K}$ . This is designed to reflect the pressure gradient across a newly ionised boundary region, created within the scale times described previously. The ‘hot’ temperature is  $T_h = 20\,000 \text{ K}$  rather than the expected ionised equilibrium temperature of  $T_h \approx 10\,000 \text{ K}$  because a single equation of state is used with a non-varying mean molecular weight. In the full version of the ionisation code, the mean molecular weight decreases with increasing ionisation fraction, in this artificial configuration this is not set to occur, and so a higher temperature is used to account for this. Specifically, pure atomic hydrogen has a mean molecular weight of  $\mu_{\text{HI}} \approx 1 \text{ u}$ ; when fully ionised, the effectively massless electrons (relative to the protons) in a ratio of one per hydrogen ion, reduce this to  $\mu_{\text{HII}} \approx 0.5 \text{ u}$ . A factor of two increase in temperature is therefore needed to represent this with a fixed  $\mu = \mu_{\text{HI}}$ .

In practice, boundary issues described in Section 2.7.3 result in a slightly higher initial mean pressure ratio of  $P_h/P_c \approx 25.8$  due to the manner in which density is calculated from the initial conditions. Figure 3.7 illustrates this issue, showing the initial density distribution for the simulation. An unavoidable (for the manner in which the code behaves) density mixing region exists for each particle  $i$  within  $2h_i$  of the boundary between hot material and cold material. For the resultant actual densities, the net pressure ratio is that which provides the value of  $P_h/P_c \approx 25.8$ .

For initial pressures of  $P_h$  and  $P_c$  for the hot and cold material respectively, and an

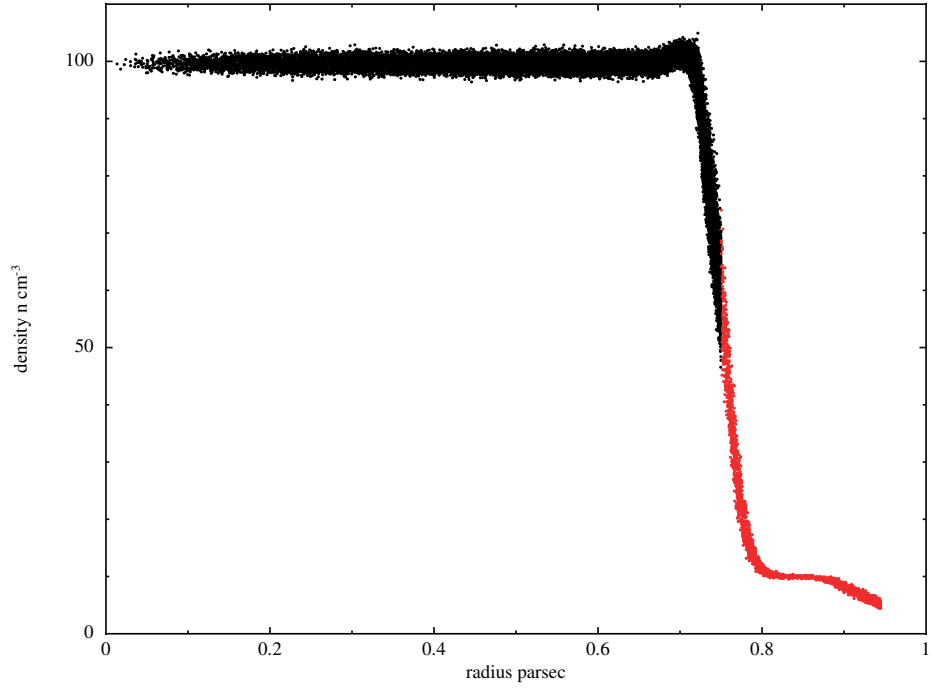


Figure 3.7: Profile of initial density with radius for hydrodynamic implosion test. All SPH particles at  $r \leq 0.75$  pc (black dots) are the ‘cold’ sphere at  $T_c = 100$  K, and all SPH particles  $r > 0.75$  pc (red dots) are the ‘hot’ medium at  $T_h = 20\,000$  K.

equation of state where  $P \propto n T$ , will result in an equilibration of pressures at some compressed radius  $R_{\text{eq}}$ . This is calculated assuming that the material compresses with uniform density throughout the cold material, and that the ‘hot’ material is of fixed pressure. Neither statement is true, but provides a useful reference point.

Given the equation of state  $P \propto n T$ , where the constant of proportionality is the same for both materials, solving for an equilibrium state is a ratio of the volumes of the initial sphere and the compressed sphere, giving,

$$R_{\text{eq}} = R_0 \left( \frac{P_c}{P_h} \right)^{\frac{1}{3}}. \quad (3.34)$$

For Lefloch and Lazareff (1994), the parameter  $R_{\text{eq}} \approx 0.28$  pc for the exact values of the two densities. For the simulation here, the mean pressure ratio of  $P_h/P_c \approx 25.8$  results in  $R_{\text{eq}} \approx 0.25$  pc. Simply that the higher pressure difference should result in a more compact sphere.

Figure 3.8 displays the profile of the average radius at which the boundary between the cold and hot material resides (averaged over all directions, as the collapse cannot be perfectly spherically symmetric) over time. The horizontal red and blue dashed

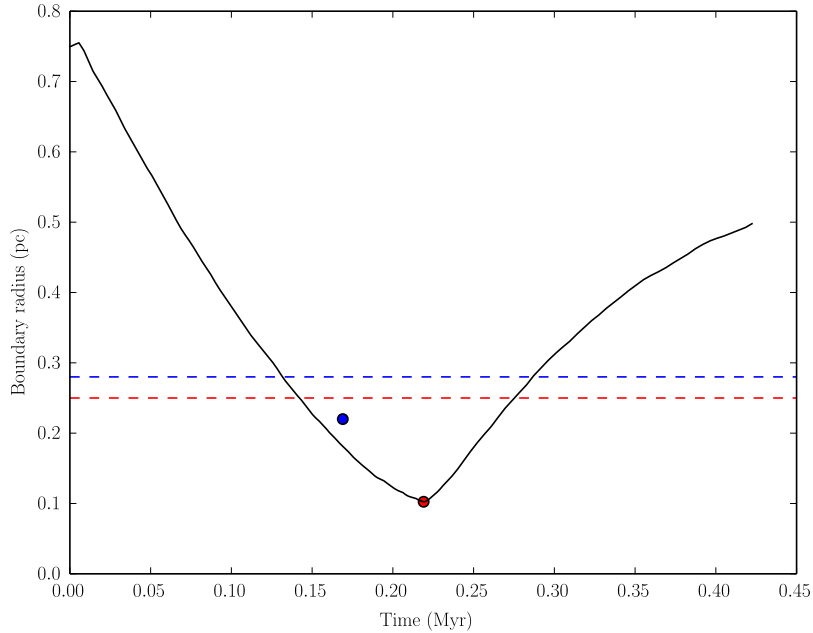


Figure 3.8: Profile of boundary radius between the cold and hot material of the hydrodynamical implosion with time. The red and blue dots indicate the radius and time of maximum compression for this simulation and Lefloch and Lazareff (1994) respectively. The horizontal red and blue dashed lines indicate the values of  $R_{\text{eq}}$  for this simulation and Lefloch and Lazareff (1994), respectively.

lines indicate  $R_{\text{eq}}$  for this simulation and Lefloch and Lazareff (1994) respectively. This radius is (expectedly) overshoot in both cases due to the inertia of the collapse. Indicating the result of this overshoot, a red dot at the radius and time of maximum compression for this simulation, and a blue dot at the approximate location for the same from Lefloch and Lazareff (1994). In addition, Figure 3.9 shows two density cross-sections; one early in the collapse and one at maximum compression.

The behaviour observed is as expected, with the cold sphere undergoing compression with a hydraulic shock driven inwards by the initial pressure discontinuity. The path of the collapse through radius/time space very closely passes the reference point for Lefloch and Lazareff (1994) at approximately  $r = 0.22$  pc at  $t = 0.169$  Myr. Maximum compression in this test occurred at 0.219 Myr with a radius of 0.102 pc; the average velocity of the boundary during its compression was  $\approx 2.9 \text{ km s}^{-1}$ ; the specific number isn't available for Lefloch and Lazareff (1994), but would be  $\approx 3.1 \text{ km s}^{-1}$  to reach the stated minimum radius for the available value for time. The slight difference is likely caused by the density mixing layer resulting in a slower shock due to the gentler initial pressure gradient (despite the slightly higher net pressure gradient).

This outcome is consistent with with the expected pattern and profile for such a

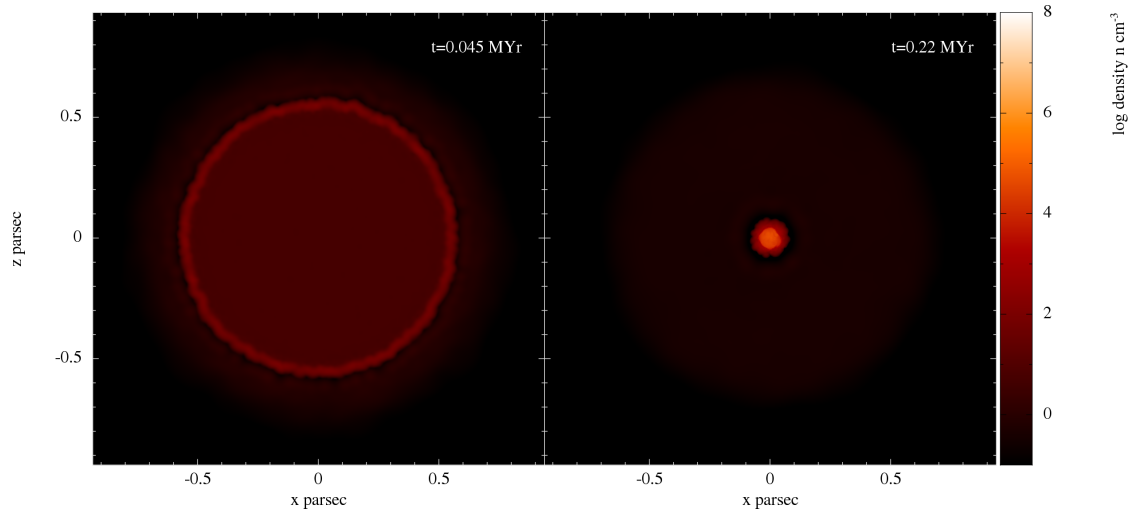


Figure 3.9: Snapshots of the cross-sectional density through the  $x$ - $z$  plane of the collapsing sphere during the early shock (left hand frame,  $t = 0.045$  Myr) and at approximately maximum compression (right hand frame,  $t = 0.219$  Myr).

compression. Despite limitations in replicating the exact initial conditions due to the nature of the SPH particles, the evolution matched that expected from Lefloch and Lazareff (1994).

### 3.3 CONVERGENCE TESTING

Given that the particle distribution for SPH initial conditions selected is still ultimately random, it is important to determine how much of an effect variations in the particle distribution has on the final result of the evolution of a simulated cloud, especially with the addition of the strong dynamical changes induced by the addition of the EUV radiation field. A series of tests were conducted with clouds whose parameters were identical, but whose particle distributions were independently generated. Conceptually, one would hope that the evolutions of these clouds would be identical, in practice, they will vary to at least some degree. The key is determining the extent of these variation, and hence get an impression as to whether any single result from a particular particle distribution is suitably representative of a ‘perfect’ result.

#### 3.3.1 MASS RESOLUTION

Determining the correct resolution to use for the purposes of any simulation is a vital aspect of being able to make sense of, and justify, the results that they produce. For this purpose, a spherical,  $M = 30 M_{\odot}$ ,  $n = 1\,200 \text{ cm}^{-3}$  simulation set was generated, at

Particle count	$M_{\odot}/\text{particle}$	particles/ $M_{\odot}$
5 000	$1.5 \times 10^{-3}$	167
10 000	$3.0 \times 10^{-3}$	333
20 000	$1.5 \times 10^{-3}$	667
50 000	$6.0 \times 10^{-4}$	1 667
100 000	$3.0 \times 10^{-4}$	3 333
125 000	$2.4 \times 10^{-4}$	4 167
150 000	$2.0 \times 10^{-4}$	5 000
200 000	$1.5 \times 10^{-4}$	6 667
300 000	$1.0 \times 10^{-4}$	10 000

Table 3.1: Table of the particle counts and mass resolutions for the mass resolution convergence testing simulations. Each of the ‘particles/ $M_{\odot}$ ’ mass resolutions are rounded to the nearest particle.

a variety of mass resolutions. Eight instances of each test were run, with the particle count and mass resolutions described in Table 3.1.

Figure 3.10 shows the profile of the time at which each of the simulations reached a mean density (across all SPH particles) of  $10^8 \text{ cm}^{-3}$ . In addition, the red pluses with error bars indicate the mean time for that resolution, and  $\pm 2\sigma$  for the values.

Rendered images of the final step for one of each of the resolution results are shown in Figures 3.11 and 3.12. Variations due to increasing resolution are clear, with the profile of the cloud becoming more distinct and finer details beginning to show. Figure 3.13 shows a direct comparison between the particle resolutions of 50 000, 100 000 and 300 000 at 0.120 Myr. Variations have reduced to a minimal amount by 100 000, though lacking in some of the features present in the higher resolution simulations. In general, the formation of density-related features appears to be delayed at lower resolutions, as is apparent from Figure 3.10.

For the 100 000 particle case, in the  $30 M_{\odot}$  cloud, assuming a worst case scenario of the material falling below 10 K (towards the minimum equilibrium temperature in the code of 5 K); the estimate of the critical density for artificial fragmentation found by Bate and Burkert (1997) can be used, being,

$$\rho_{\text{crit}} = \left( \frac{3}{4\pi} \right) \left( \frac{5 R_g T}{2 G \mu} \right)^3 \left( \frac{N_{\text{tot}}}{2 N_{\text{near}} M_{\text{tot}}} \right)^2. \quad (3.35)$$

Converting the units to particle number density for convenience, this gives a value  $n_{\text{crit}} \approx 10^8 \text{ cm}^{-3}$ . This may seem a severe limit, but requires accounting for that the temperature used is assumed to apply to every particle in the simulation. In practice, temperatures as low as  $T < 10 \text{ K}$  are only attainable once high densities have already been reached.

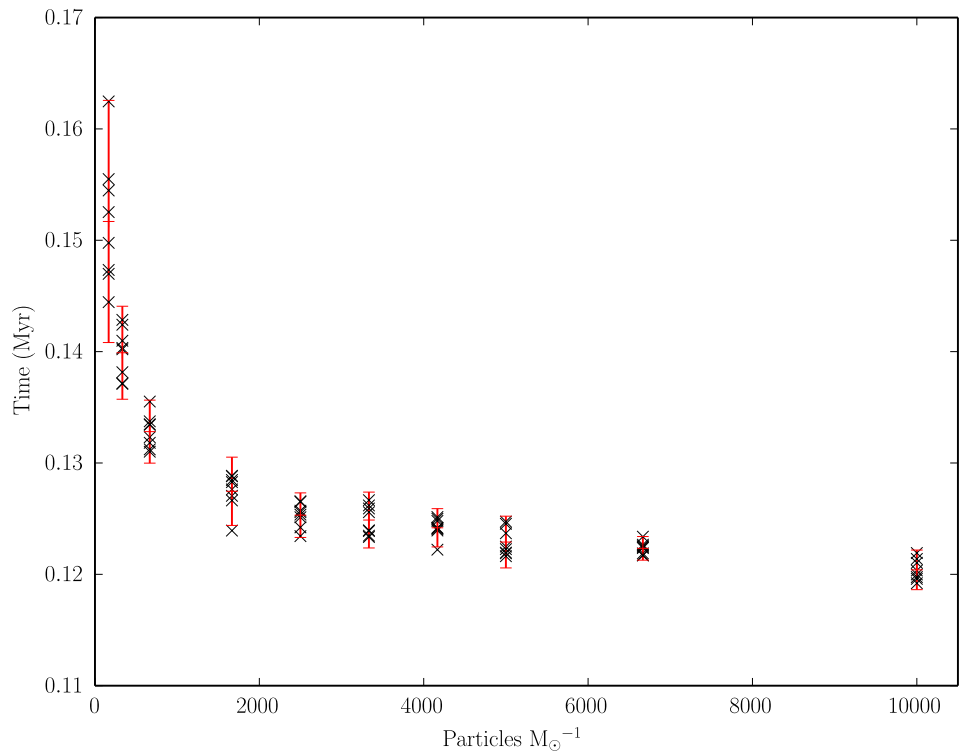


Figure 3.10: Times in the resolution convergence testing simulations at which an all-simulation mean density of  $\langle n \rangle = 10^8 \text{ cm}^{-3}$  is reached (interpolated between output snapshots), across several of the resolutions examined. Black crosses are simulation results, red pluses with error bars are the means and  $\pm 2\sigma$ .

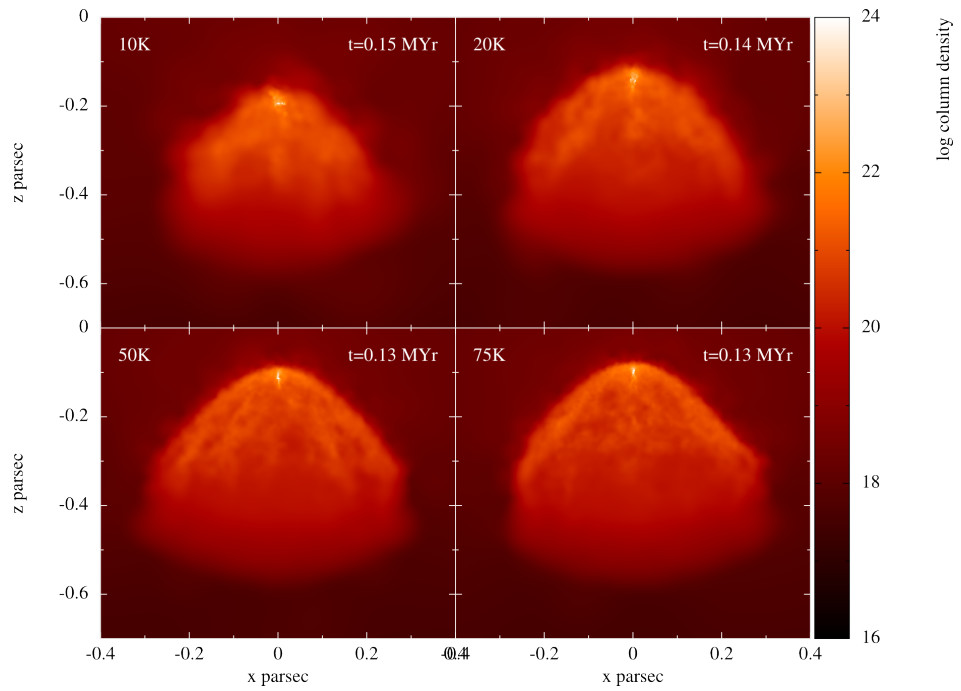


Figure 3.11: Column density renders of one of each of the particle resolution simulations for particle numbers of 10 000, 20 000, 50 000 and 75 000 (indicated in upper left corner of each panel; column density is in  $\text{cm}^{-2}$ ).

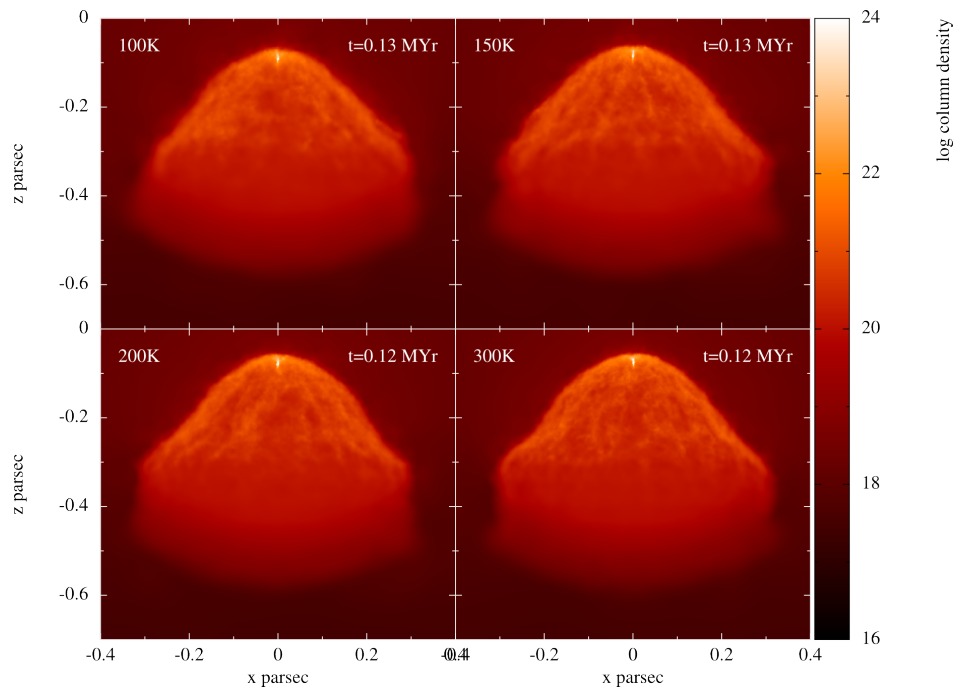


Figure 3.12: Column density renders of one of each of the particle resolution simulations for particle numbers of 100 000, 150 000, 200 000 and 300 000 (indicated in upper left corner of each panel; column density is in  $\text{cm}^{-2}$ ).

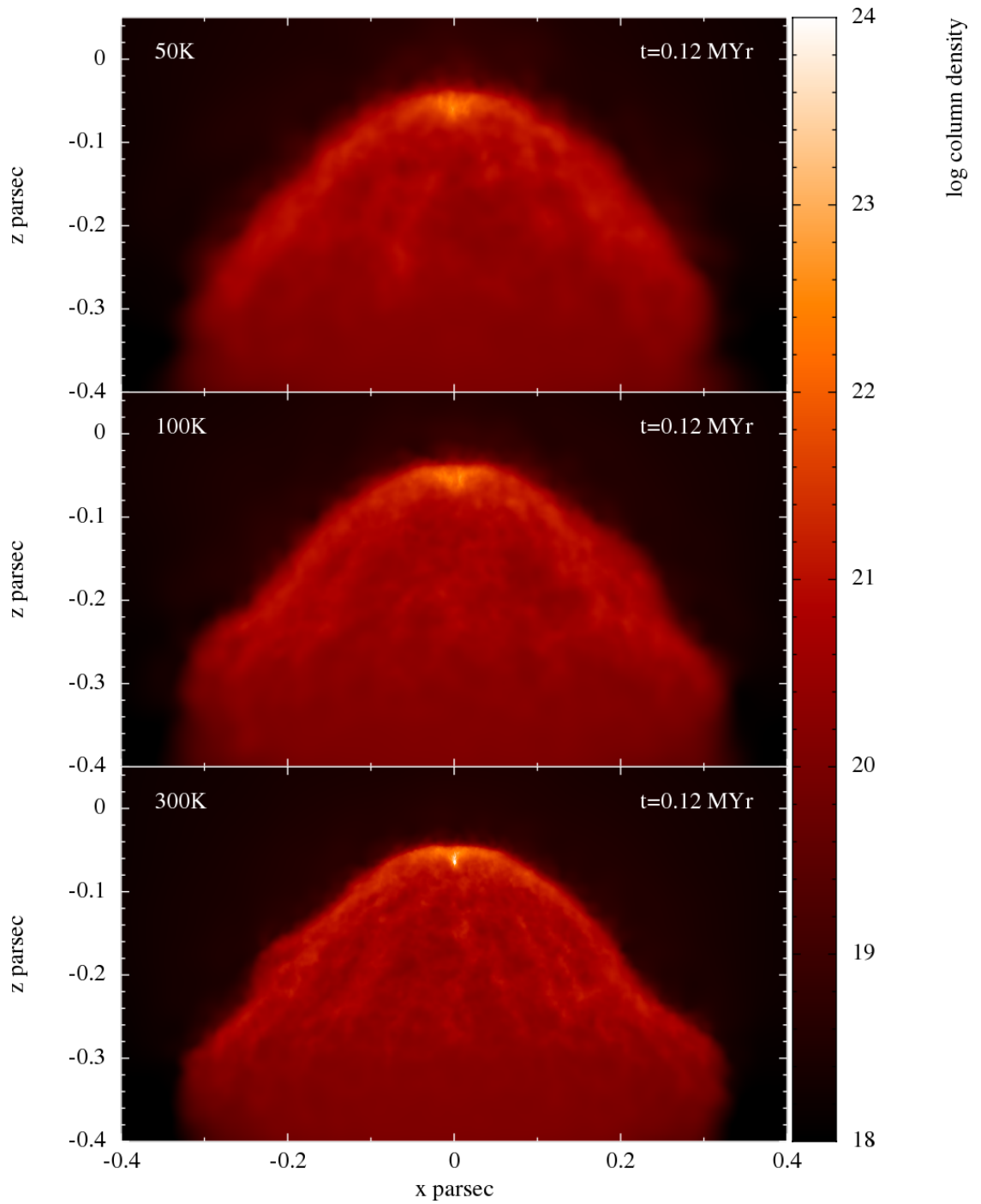


Figure 3.13: Column density renders at  $t = 0.120$  Myr of one of each of the particle resolution simulations for particle numbers of 50 000, 100 000 and 300 000 (indicated in upper left corner of each panel; column density is in  $\text{cm}^{-2}$ ).

This threshold is convenient, but not strictly calibrated for simulations with extensive additional physics. For instance, it does not account for the radiative cooling functions produced by the formation of molecules at high densities. It can be deemed to give an impression of the validity of the simulations, rather than a definitive arbiter of whether or not it is correct.

This critical density threshold calculation is used in Section 4.2 as one of the criteria for evaluating legitimate cores. It is calculated locally, per-particle, in order to determine whether regions of high density particles are genuinely separate, or could be the result of artificial fragmentation.

Shown in Figure 3.14 is the plot of the percentages of particles exceeding this criteria locally at  $t = 0.120$  Myr in the simulation. A few anomalously low values for some of the lower particle counts, including values of zero, are from simulations in which noise has prevented collapse to a high density point by 0.120 Myr, being low due to the absence of any especially high densities. Very low / zero values in some of the higher resolution tests are due to the simultaneous formation of multiple separate peaks/cores prior to the artificial fragmentation limit, with especially high densities still not reached. The profile retains a degree of variation, but exhibits no obvious net change after the 3 333 particles/ $M_{\odot}$  - 100 000 particles mark. After this point the means for each resolution are all well within  $2\sigma$  of each other. This can be interpreted as indicating that, whatever other reasons for variation the simulation may have, they have ceased to depend strongly upon the resolution in the region of 2 500 to 3 333 particles/ $M_{\odot}$ . This can provide a reasonable lower resolution limit of approximately 3 333 particles/ $M_{\odot}$ .

Ultimately, the selection of a resolution at which to run a series of simulations is weighted on the factors of accuracy and CPU-time. Once results are deemed to have converged for increasing resolution, resolving details at smaller length scales may be desirable, but encounters increasing CPU-time costs which, at some point, makes increasing resolution infeasible.

### 3.3.2 SPHERICAL CLOUD UNIFORMITY

Having selected 100 000 particles / 3 333 particles/ $M_{\odot}$  as a suitable resolution; a larger series of tests were conducted in order to assess the degree of variability due to the randomised nature of the particle distribution. The first of these sets was for a simple spherical cloud, and in the next section, an ellipsoidal cloud is examined in the same manner.

Starting with a cloud with general properties matching those used in Chapters 4 and 5: a cloud of prolate aspect ratio,  $\gamma = 1$ , total initial mass  $M = 30 M_{\odot}$  and initial density of  $n = 1\,200\text{ cm}^{-3}$ , subject to an ionising flux of  $10^9\text{ cm}^{-2}\text{ s}^{-1}$ . 32 instances of

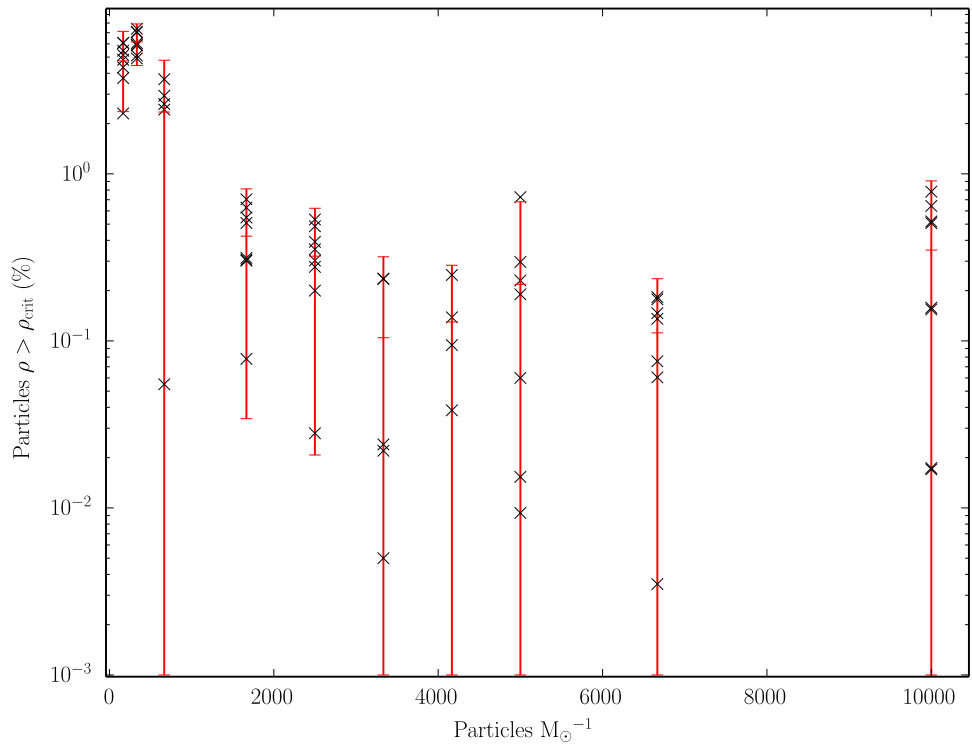


Figure 3.14: Percentage of particles exceeding the strict Jeans critical density threshold for artificial fragmentation at  $t = 0.120$  Myr, versus particle resolution. Black crosses are from individual simulations, red pluses with error bars are the means and  $\pm 2\sigma$ .

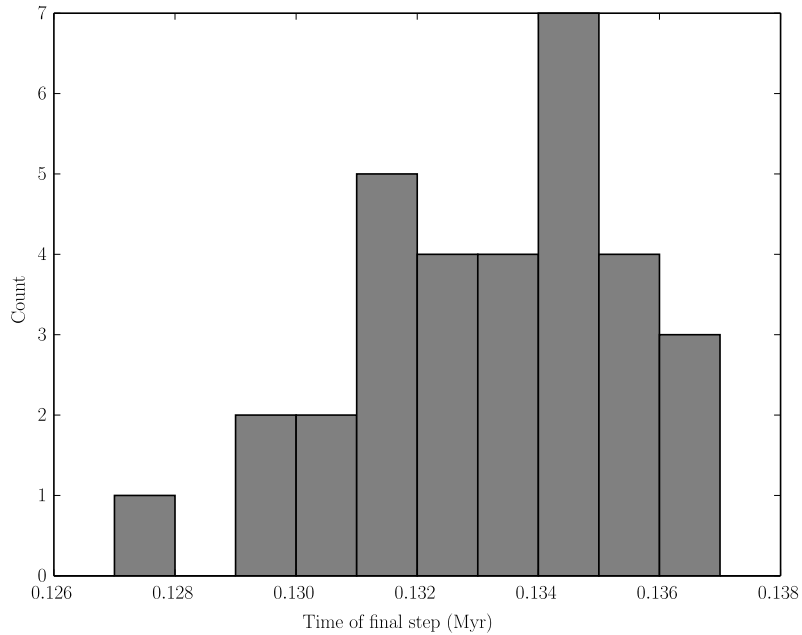


Figure 3.15: Distribution of the time of the final timestep for 32 simulations with identical initial conditions but varied particle distributions. The mean is 0.133 Myr, the standard deviation 0.002 Myr.

this cloud were generated with the glass-like technique described in Section 2.7.1, each using random positions and orientations within an initial box of 7 077 888 particles; with 100 000 particles for the simulations themselves, determined from the mass resolution requirements in the previous section. Several interesting comparisons can be made between these tests, shown in Figures 3.15 to 3.17 are the distributions of the times, masses above  $10^8 \text{ cm}^{-3}$ , and maximum densities at the end of the simulations respectively.

As can be seen in Figure 3.15, the simulations ran to varied times. The minimum, mean and maximum of these times were 0.127, 0.133 and 0.136 Myr respectively; the standard deviation of the distribution being 0.002 Myr. In order to best compare the simulations to one another, the final common time of all will be taken, i.e. the minimum final time, 0.1275 Myr. As the simulations do not output timesteps by simulated time intervals, but by computational timestep intervals, this means that it is impossible to select an exact common time between the simulations, and the closest output to the target time for each simulation is taken instead. This means that for each of the subsequent ‘final common time’ data, the effective time is technically 0.1275(1) Myr with two standard deviations taken as the ‘uncertainty’.

With this in mind, similar plots to Figures 3.16 and 3.17 can be produced at a time where the simulations should still be ‘in sync’. Figures 3.18 and 3.19 are just such

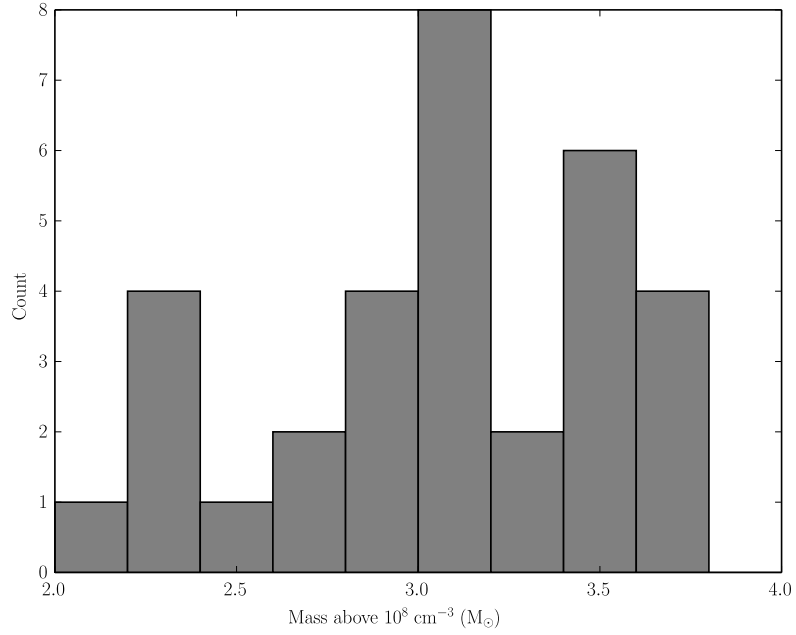


Figure 3.16: Distribution of the masses above a density threshold of  $10^8 \text{ cm}^{-3}$  at the final timestep for 32 simulations with identical initial conditions but varied particle distributions. The mean is  $3.07 M_\odot$ , the standard deviation  $0.46 M_\odot$ .

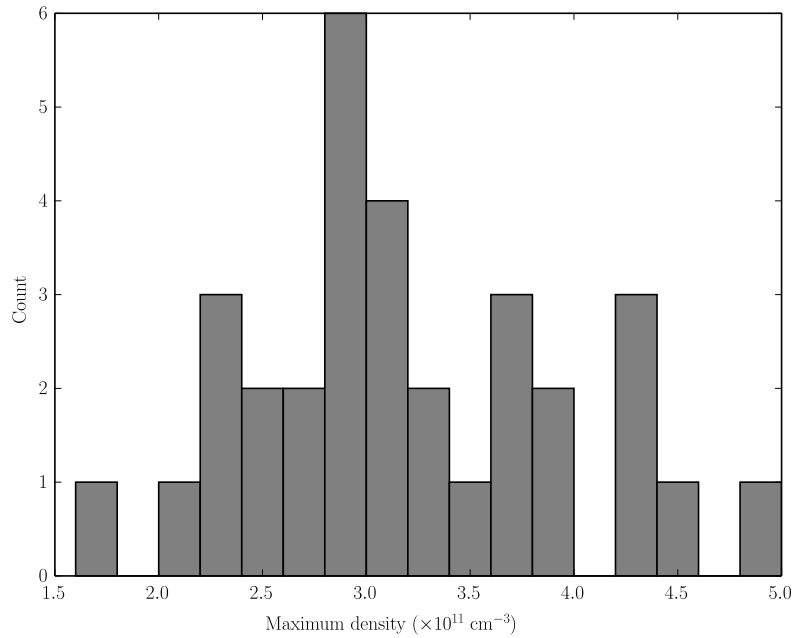


Figure 3.17: Distribution of the maximum density at the final timestep for 32 simulations with identical initial conditions but varied particle distributions. The mean is  $3.18 \times 10^{11} \text{ cm}^{-3}$ , the standard deviation  $0.73 \times 10^{11} \text{ cm}^{-3}$ .

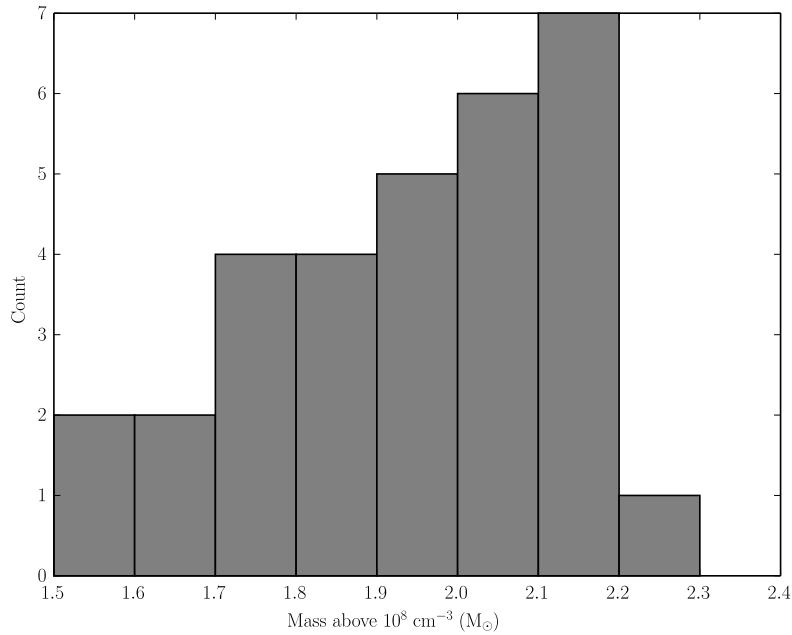


Figure 3.18: Distribution of the masses above a density threshold of  $10^8 \text{ cm}^{-3}$  at the common time of  $t = 0.1275(1) \text{ Myr}$  for 32 simulations with identical initial conditions but varied particle distributions. The mean is  $1.96 M_{\odot}$ , the standard deviation  $0.20 M_{\odot}$ .

illustrations of the data. The distribution is narrower for the distribution of masses above the density threshold of  $10^8 \text{ cm}^{-3}$  (Figure 3.18); though has increased for the distribution of maximum densities (Figure 3.19).

The wide variation in the maximum density is not necessarily of any concern, as any sampling technique based on taking the value of any single particle becomes exceptionally susceptible to very localised variations skewing the impression of the whole picture.

The distribution sampling at any single time after (it can be presumed) variations in the outcome of the evolution have already set in, provides an un-converged data set. However, the overall profile of the evolution (on the size scales of the cloud itself, rather than the core regions) can be seen to be essentially the same. A sample of nine clouds at  $t = 0.1275(1) \text{ Myr}$  are presented as column density rendered maps in Figure 3.20 (at the length scale presented, the equivalent plots for  $t = t_{\text{final}}$  are indistinguishable). The structure on the length scale of the original cloud is very similar in each case, a dome of increased density relative the the surroundings, with a central intrusion into the apex of the dome of a high density spike. In this spike, created by the converged high-density shocks, are located one or more ‘core’ structures. These are undergoing gravitational collapse, and are the cause of the rapidly increasing densities

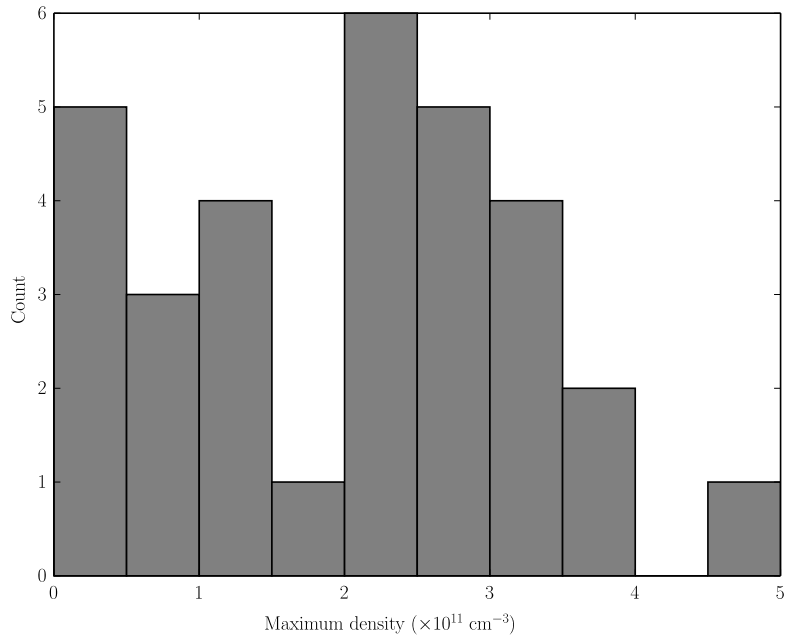


Figure 3.19: Distribution of the maximum density at the common time of  $t = 0.1275(1)$  Myr for 32 simulations with identical initial conditions but varied particle distributions. The mean is  $2.12 \times 10^{11} \text{ cm}^{-3}$ , the standard deviation  $1.30 \times 10^{11} \text{ cm}^{-3}$ .

and corresponding vanishingly small timesteps, preventing the continued simulated evolution of the cloud.

Figure 3.21 presents the same clouds as displayed in Figure 3.20, but zoomed in on the high density spike at the apex of the cloud. This region does experience changes between the final common time and the actual final timestep for each simulation. In particular, for many of the simulations, core collapse is able to continue slightly further, illustrating more distinct cores and general further motion downwards as the entire cloud recoils from the rocket effect. Figure 3.22 presents the same, zoomed in, view of the nine clouds, but for each cloud’s own final timestep.

More variation, and more definition in the core shapes and positions, is clear in Figure 3.22. The variation in the vertical position in the cores is a function of the time at which the snapshot occurs, as the net vertical velocities of the high density material,  $v_z[n > 10^8]$ , at  $t = 0.1275(1)$  Myr is very similar across the 32 simulations ( $\langle v_z[n > 10^8] \rangle = -2.27(1) \text{ km s}^{-1}$ ). Interesting substructure, beyond simple high density spherical cores can be observed, in particular a number of compact linear structures. The exact nature of these structures and their formation mechanisms, however, is beyond the scope of the current investigation in to the uniformity exhibited between variations in particle distribution. Further investigation into the configuration of cores

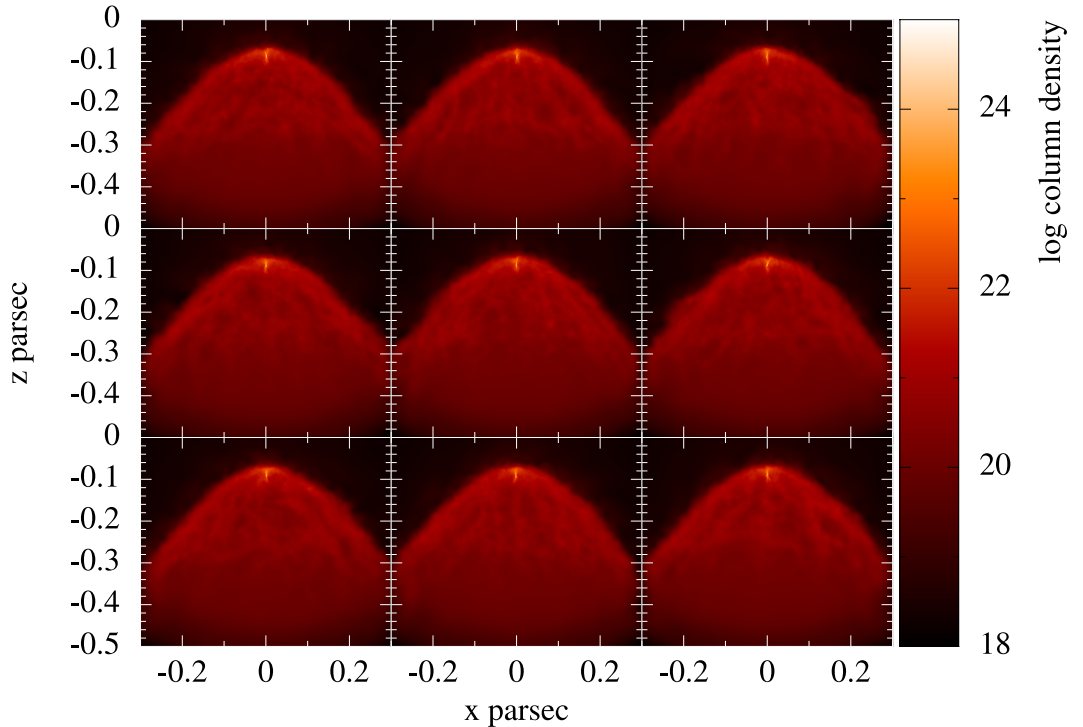


Figure 3.20: Snapshots of rendered column density at  $t = 0.1275(1)$  Myr for 9 simulations with identical initial conditions but varied particle distributions. Column density is in  $\text{cm}^{-2}$ .

and their surrounding structures is undertaken in Chapters 4 and 5.

An alternative illustration of the agreement between the separate simulations is to observe the time evolution of some properties of the simulations. Presented in Figure 3.23 are the time evolutions of the mean and maximum densities for each of the 32 simulations; along with the running averages for each statistic with time. Taking this picture further, the ratio between the individual mean density profiles with time to the spline-fitted profile can be examined; this is presented in Figure 3.24. It can be seen that the variation between the simulations hovers at around 1% for much of the evolution, diverging upon the formation of cores in any of the simulations.

### 3.3.3 INCLINED ELLIPSOIDAL CLOUD

It is important to guarantee that more ‘extreme’ asymmetric cases exhibit similar basic uniformity as the spherical clouds shown so far. For this an ellipsoidal cloud with an axial ratio of 2 and inclination of  $45^\circ$  is examined. As with the spherical cloud tests, 32 instances of this cloud were generated with the glass-like technique described in Section 2.7.1, again using random positions and orientations. Shown in Figure 3.25 are the distribution of the times at the end of the simulations, plotted with both these results and the sphere results shown in Figure 3.15. Other parameters are summarised

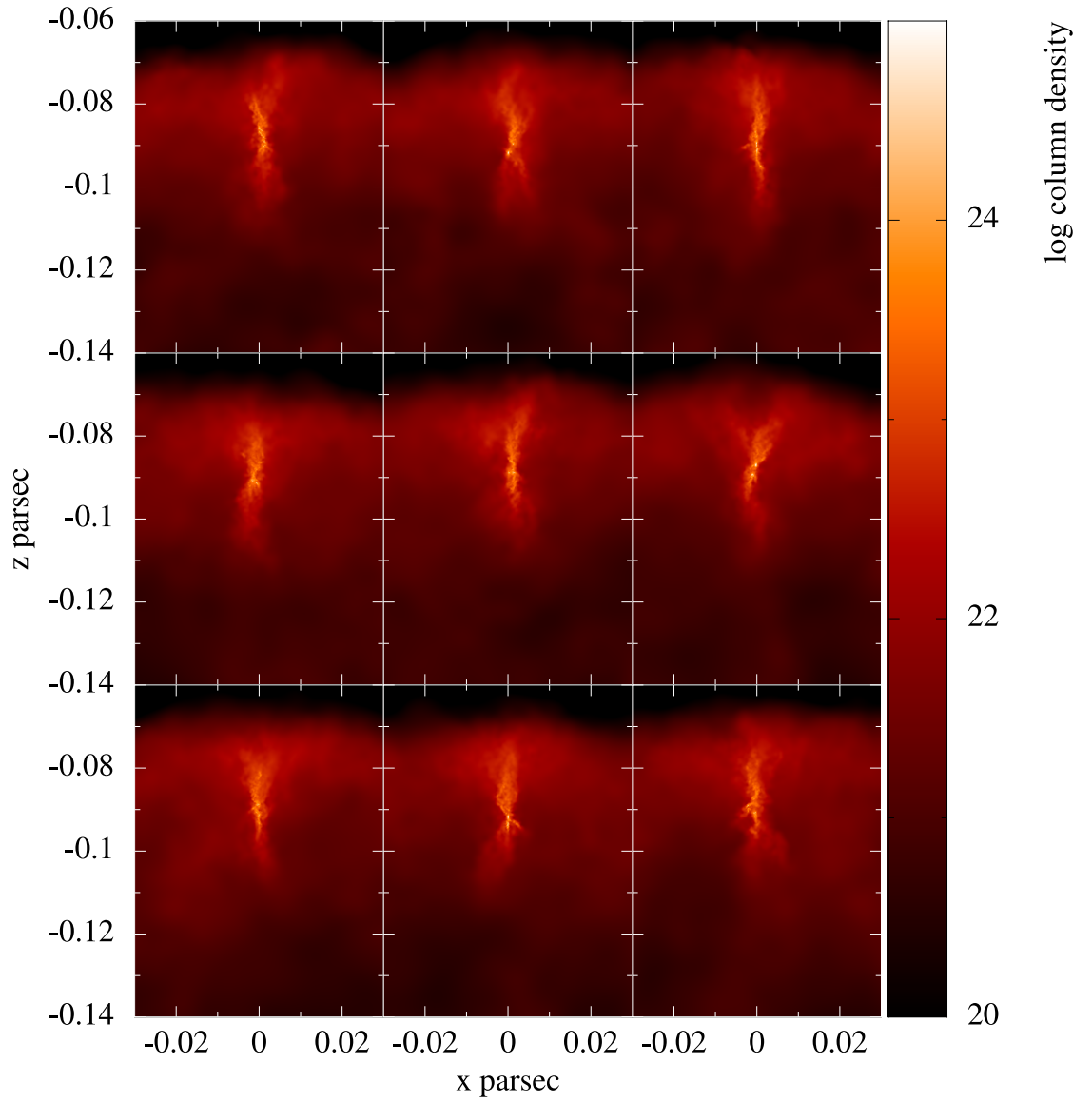


Figure 3.21: Snapshots of rendered column density at  $t = 0.1275(1)$  Myr for 9 simulations with identical initial conditions but varied particle distributions. Detail of the high density spike structure at the apex of the cloud. Column density is in  $\text{cm}^{-2}$ .

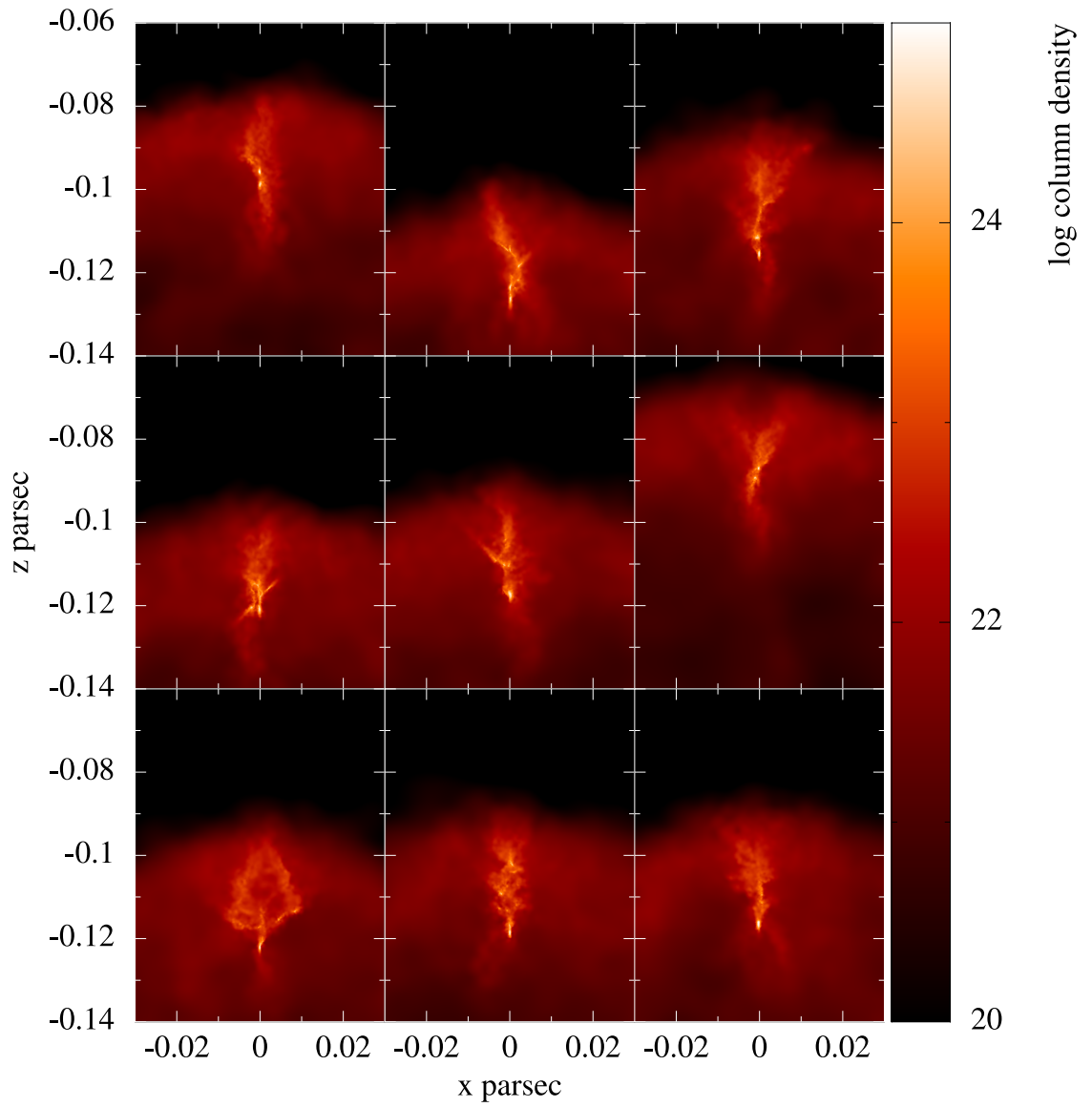


Figure 3.22: Snapshots of rendered column density at the final timestep for each of 9 simulations with identical initial conditions but varied particle distributions. Detail of the high density spike structure at the apex of the cloud. Column density is in  $\text{cm}^{-2}$ .

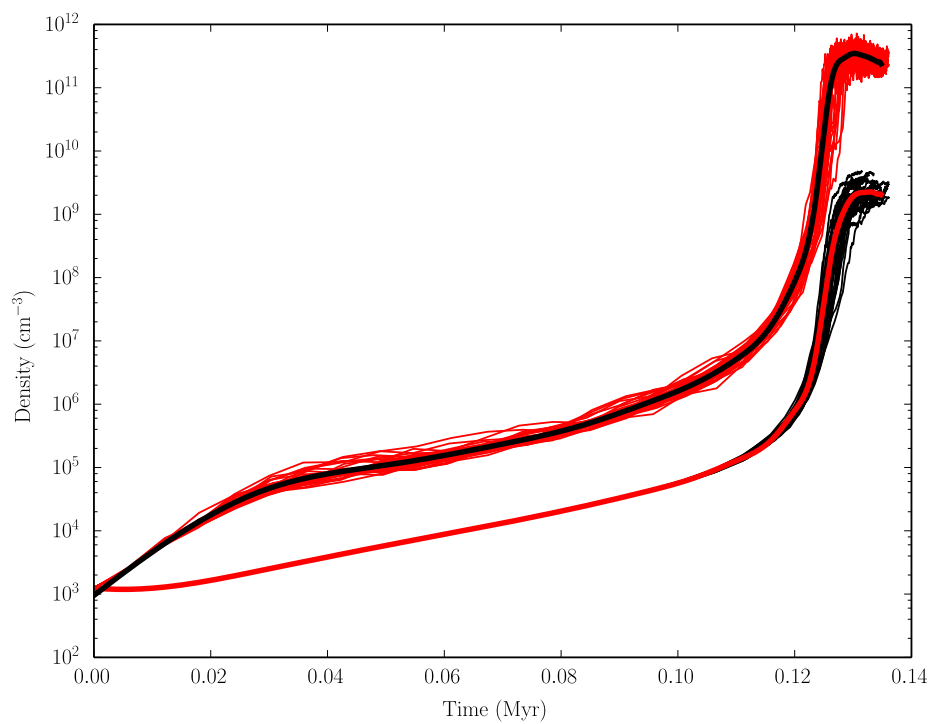


Figure 3.23: Time evolution of the mean (lower, black lines) and maximum (upper, red lines) densities. Presented as solid, smooth lines in contrasting colours and in front of each of the data sets is a spline-based best fit for each parameter.

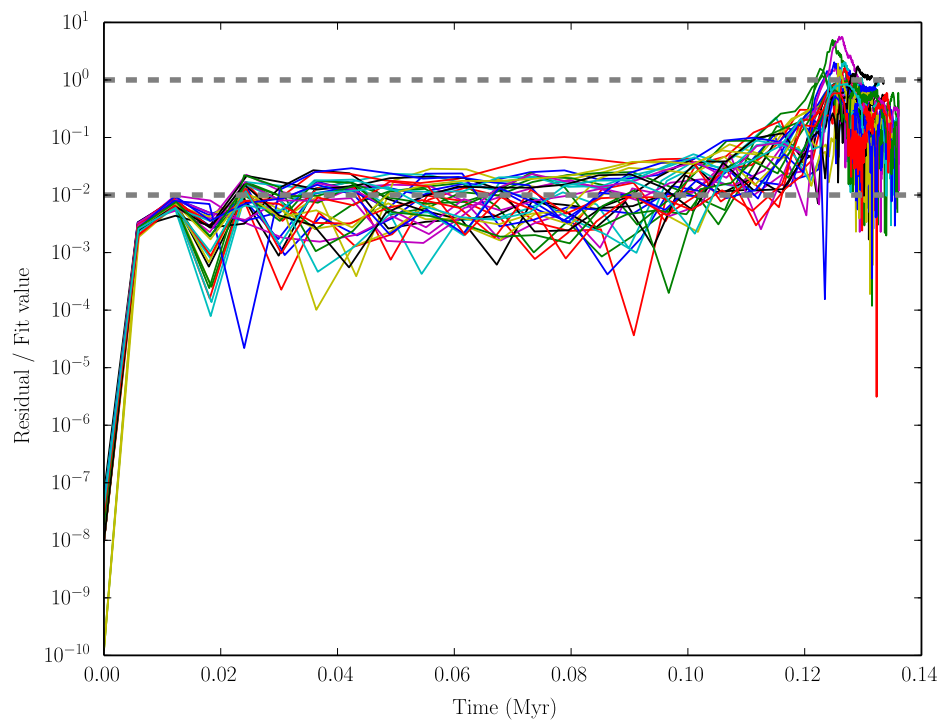


Figure 3.24: Time evolution of the fractional differences between the density of each of the 32 simulations to the spline-based best fit line. Two horizontal dashed lines indicate 100 % and 1 % difference.

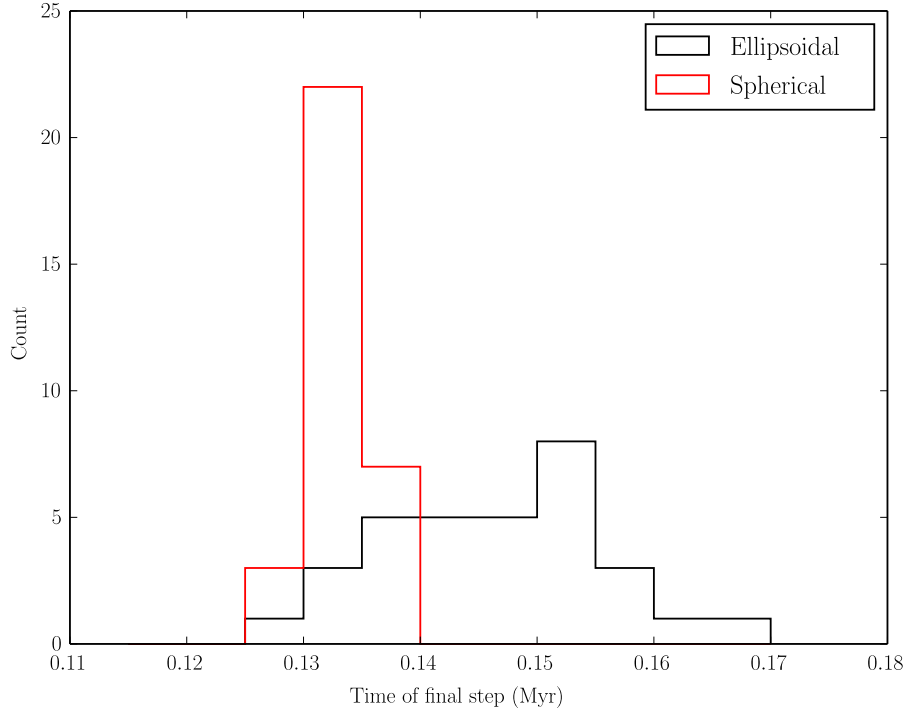


Figure 3.25: Distribution of the time of the final timestep for 32 simulations with identical initial conditions but varied particle distributions. The black line is the histogram for the angled ellipsoid initial conditions, with a mean of 0.147 Myr, and standard deviation 0.009 Myr. The red line is a re-plot of the data presented in Figure 3.15, presented for comparison.

in the Table 3.2.

The distribution seen in Figure 3.25 is clearly unfavourable for the angled ellipse initial conditions compared to the sphere initial conditions. This effect is to be expected, however, with a greater degree of asymmetry and dynamic variation causing more varied outcomes. The picture is better, however, when looking at the other parameters, listed in Table 3.2. In this, it is shown that the absolute variation in the values ( $\sigma$  in each pair of columns), is the same or smaller than for the sphere. This suggests that although the formation times present a greater uncertainty in their values, the properties of the cloud and its cores once formation occurs is fairly consistent.

A major caveat to the data presented thus far, however, is that it is taken from specific frames of output. These are performed at regular timestep intervals, and due to the variable timestep used by the simulation, do not all sync up in time. This means that when a specific time for a simulation is evaluated, it is done so for the *nearest available output* with respect to time. This means that certain quantities will appear to have a variance greater than the simulation may actually be exhibiting, but has been

Parameter	Spherical		Ellipsoidal	
	Mean	$\sigma$	Mean	$\sigma$
$t_{\text{final}}$ (Myr)	0.133	0.002	0.147	0.009
Mass at $t = t_{\text{final}}$ ( $M_{\odot}$ )	3.07	0.46	0.90	0.34
Max Density at $t = t_{\text{final}}$ ( $\times 10^{11} \text{ cm}^{-3}$ )	3.18	0.73	1.54	0.45
Mass at $t = t_{\text{common}}$ ( $M_{\odot}$ )	1.96	0.20	0.25	0.20
Max Density at $t = t_{\text{common}}$ ( $\times 10^{11} \text{ cm}^{-3}$ )	2.12	1.30	1.01	0.89

Table 3.2: Statistical properties for two sets of 32 simulations, one a spherical cloud and one an ellipsoidal cloud with axial ratio  $\gamma = 2$  and inclination  $\varphi = 45^\circ$ . The other initial conditions of both cloud types were identical, with  $n = 1200 \text{ cm}^{-3}$ ,  $M = 30 M_{\odot}$  and  $F = 10^9 \text{ cm}^{-2} \text{ s}^{-1}$ . Each of the 64 clouds had different particles distributions, obtained randomly using the glass-like method described in Section 2.7.1.  $t_{\text{final}}$  are the times at which the simulations ended due to timestep contraction as a result of high-density core formation.  $t_{\text{common}}$  indicates the final time of the earliest simulation to finish, in other words the final time at which all simulations have data. The masses indicated are the mass for all material  $n > 10^8 \text{ cm}^{-3}$ .

added by the limited time frequency sampling. If, instead, the profile of the maximum particle density with time is taken, and linearly interpolate those data; a time at which a selected density is first reached can be obtained. For the tests above, for a density of  $10^8 \text{ cm}^{-3}$ , the mean interpolated time for that density's first occurrence is 0.117 Myr with a standard deviation of only 0.003 Myr, just over 2% compared to the just in excess of 6% for the value shown in Table 3.2.

Figure 3.27 presents the equivalent to the Figure 3.21 plot, displaying rendered images of column density for nine of the angled ellipsoid clouds at  $t = t_{\text{common}}$ , the largest time at which all simulations are still running. Several of the clouds have already formed high density core structures, whereas some are still densities associated with the bulk cloud material at that stage. Figure 3.26 illustrates a representative view of the final morphology of the entire series of clouds. It shows a ‘spine’ like structure along the upper centre of the remainder of the cloud, with a condensed ‘head’ at the top right of the structure, this region being where the core formation appears to occur. At the scale of the entire cloud, the end results are all as morphologically similar as those instances for the spherical cloud shown in Figure 3.20.

Figure 3.28 is the equivalent of Figure 3.27 but at  $t = t_{\text{final}}$ , each cloud is shown at that cloud's own final timestep, those times are shown in the upper left corner of each panel. The scope of the axes has had to be enlarged substantially relative to the same frames in Figure 3.27, to account for the variation in formation time having progress the motion of cloud material due to the rocket effect by varying amounts. Similar manners of shape and core qualities are observable in each frame, however, despite

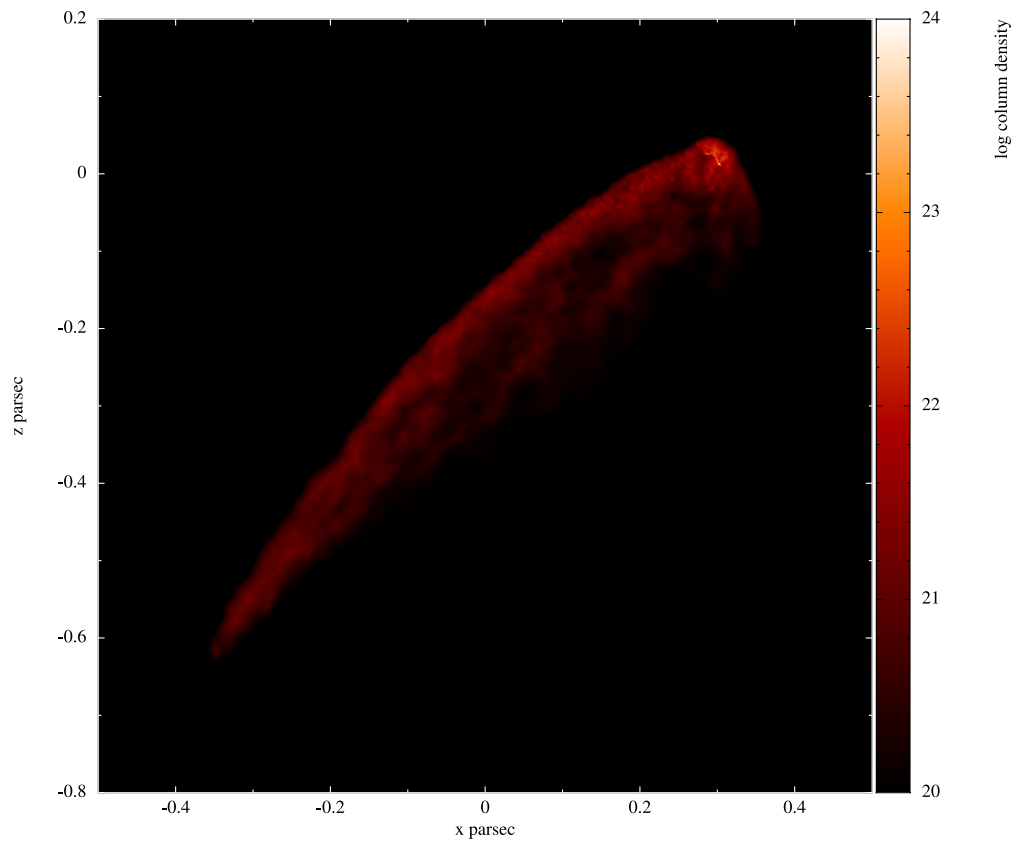


Figure 3.26: Rendered column density at  $t = 0.3$  Myr for one of the ellipsoidal test clouds, taken as a representative sample case. Column density is in  $\text{cm}^{-2}$ .

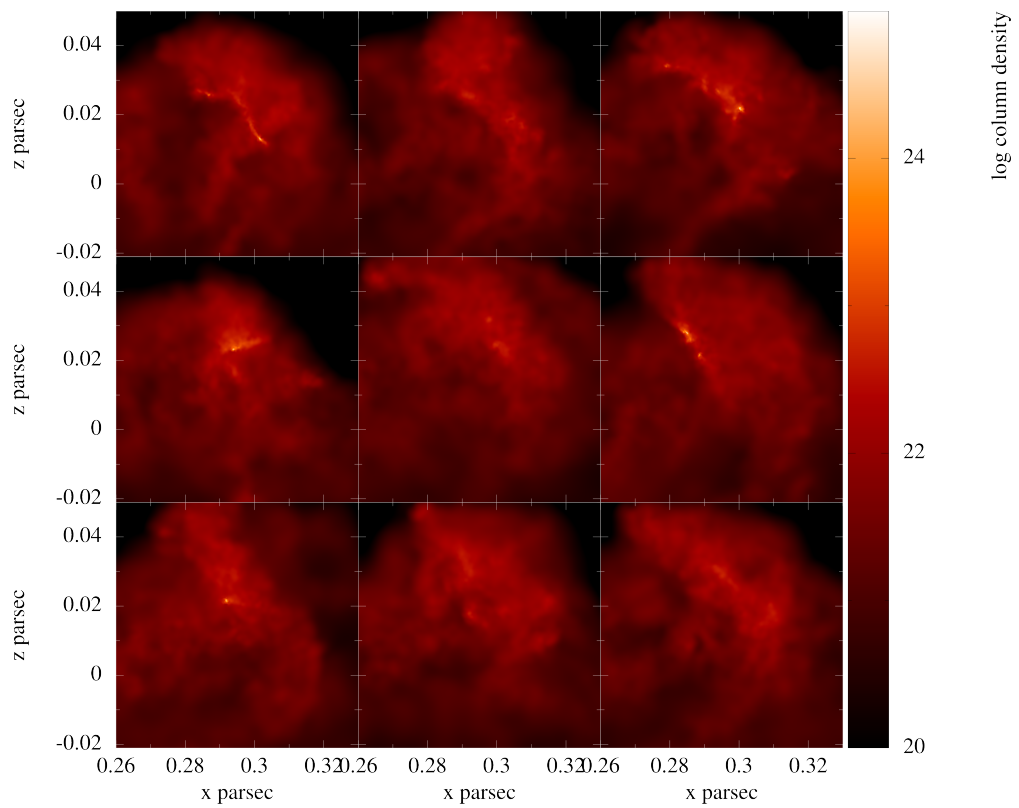


Figure 3.27: Snapshots of rendered column density at  $t = 0.1300(1)$  Myr for nine inclined ellipsoidal simulations with identical initial conditions but varied particle distributions. Detail of the high density spike structure at the apex of the cloud. Column density is in  $\text{cm}^{-2}$ .

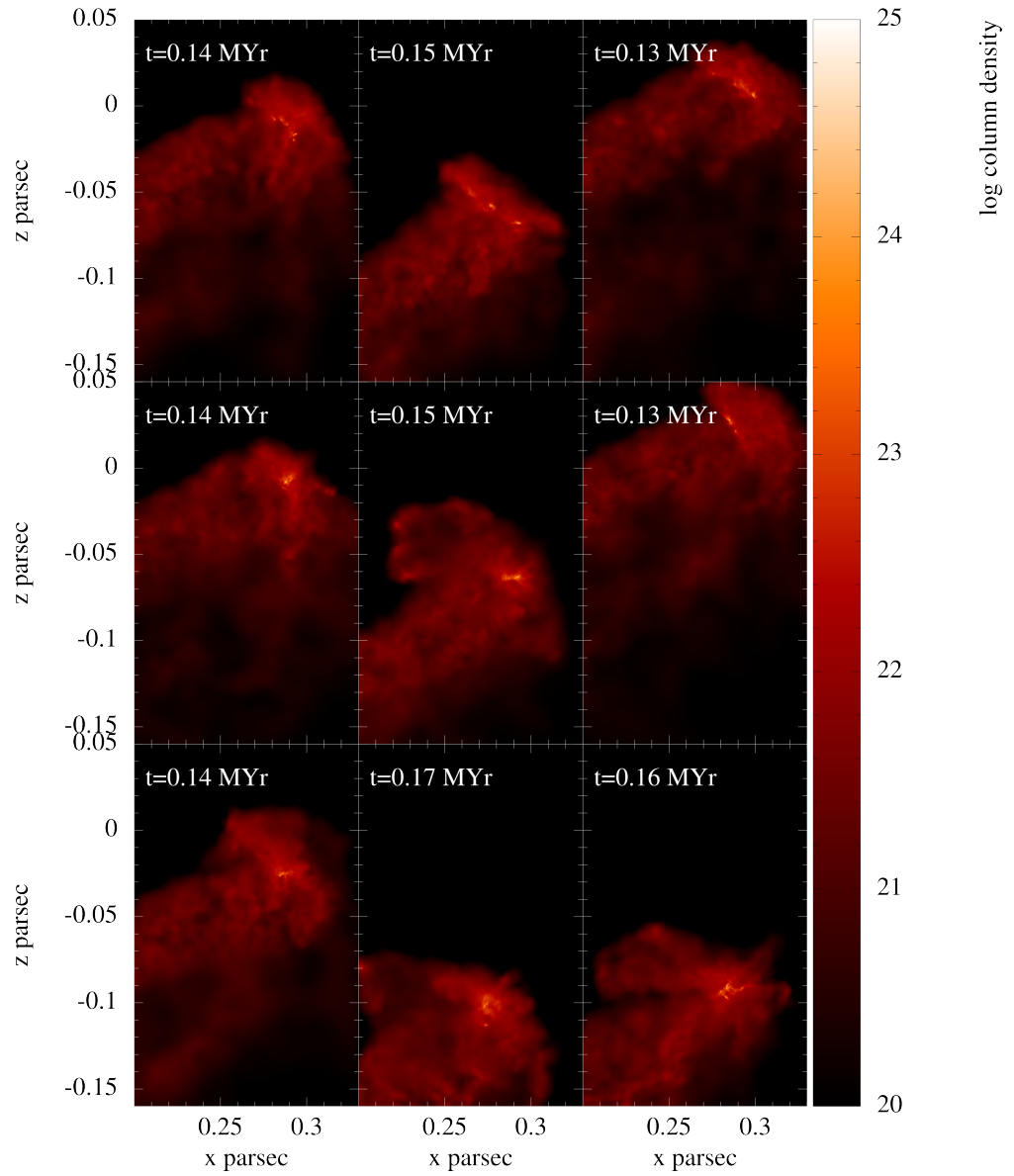


Figure 3.28: Snapshots of rendered column density at the final timestep for each of nine inclined ellipsoidal simulations with identical initial conditions but varied particle distributions. Detail of the high density spike structure at the apex of the cloud. Column density is in  $\text{cm}^{-2}$ .

the larger variation in position and time when compared to the same results for the spherical cloud (Figure 3.22).

### 3.3.4 SUMMARY

For the reasons presented previously, and the requirements necessitated by desire to reduce computational time, 3333 particles/ $M_{\odot}$  was deemed suitable as the approximate resolution requirement for converged simulations. It will be used throughout as standard.

In conclusion, whilst random variation due to the initial particle distribution causes variation in the measured parameters, the general pattern of results remains consistent. It can be said that, while any single test at the resolutions used doesn't provide a perfect representation of the results for the specified physical initial conditions only, it produces 'variations on a theme', where the key properties and dynamic behaviours are representative of the initial set up, if not unique to it.

## 3.4 THE EUV RADIATION PENETRATION DEPTH PARAMETER

---

The peculiar dichotomy of the RDI mechanism is that the expectation of a compressive shock front, driving material to high densities, is held in a balance against the 'destructive' effect of the radiation, strong photo-evaporation removing material from the cloud and reducing potential for star formation. It is the exact balance of these two effects which can be expected to determine whether, and to what efficiency, a given cloud can be induced to form stars, or to vanish as a 'cloud', merging with the material of the HII region itself.

In order to better describe the dynamics of the clouds investigated, it can be useful to search for some parameter which correlates with the key observed features of the evolution of the system. For the system here, whose evolution is driven by the EUV radiation flux and the geometry of the cloud, it is important to define a parameter which pertains to both.

Equation (3.12) in Section 3.2.1(a) shows the equilibrium depth for the EUV radiation. For an assumption of perfect ionisation, an approximation is given by  $d = \frac{F_0}{n^2 \alpha_B}$ , where  $F_0$  is the ionising radiation flux,  $n$  the initial density of the material upon which the radiation is incident and  $\alpha_B$  the recombination coefficient, taken as

$2 \times 10^{-13} \text{ cm}^3 \text{ s}^{-1}$  for these purposes (Dyson and Williams, 1997). This parameter describes the depth into the cloud at which the ionising radiation reaches a point at which the total supplied flux is expended reionising material up to that depth, rather than ionising new material. This takes place on timescales shorter than those of the dynamical effect (explained in Section 3.2.1(a)), effectively ‘instantly’ from the perspective of the global evolution of the clouds being investigated.

As has been mentioned, hydrodynamical effects will only begin to take effect to any degree after the radiation has achieved this penetration into the cloud. As such, the initial equilibrium depth of the cloud can be described as part of the effective initial conditions, and incorporated into the desired parameter to describe the evolutionary prospects of the cloud.

This will be examined in two sections. First, for the condition where the major axis of the cloud is perpendicular to the axis of the radiation ( $\varphi = 0^\circ$  inclination), in which the maximum depth through the cloud along the radiation axis is simply two times the semi-minor axis. Second for the asymmetric condition where  $\varphi \neq 0^\circ$ , which introduces an additional complexity.

### 3.4.1 CLOUDS WITH $\varphi = 0^\circ$ INCLINATION

To account for the geometry of the clouds investigated, the following parameter can be defined, being the ratio between the ionisation equilibrium depth, and the semi-minor axis of the cloud (half of its total depth in the direction of the radiation, for clouds of  $\varphi = 0^\circ$ ),

$$d_{\text{EUV}} = \frac{\left(\frac{F_0}{\alpha_B n^2}\right)}{\left(\frac{a}{\gamma}\right)} = \frac{F_0 \gamma}{n^2 \alpha_B a}, \quad (3.36)$$

this is expressed as a percentage, representing the proportion of the half-depth of the initial cloud through which the radiation will advance prior to substantial dynamical effects.

This parameter is comparable to those used by Lefloch and Lazareff (1994, 1995),  $\Delta$  and  $\Gamma$ . These acted as measures of the overpressure of the ionised gas and the ratio of photon re-ionisation/new ionisation events, respectively; and characterised ionisation shock propagation scenarios in a similar manner.

It will be seen that for  $d_{\text{EUV}} \leq 1\%$  the clouds are ‘shock dominated’ with the convergence of the shock front from their origins on the curved upper surface of the cloud resulting in preferential core formation wherever the locations of peak convergence are. As  $d_{\text{EUV}}$  increases further, of the order of  $1\% < d_{\text{EUV}} < 10\%$ , the locations of peak convergence do not gather sufficient material to create densities high enough for core

formation. This results in a more prolonged collapse, where collection of disturbed material along a line coincident with the semi-major axis results in sporadic core formation along the whole length of the final structure; this is termed ‘linear convergence dominated’. At extreme  $d_{\text{EUV}} (> 10\%)$ , the cloud tends not to survive, with too much material being evaporated and insufficient convergence of shock fronts to trigger collapse. Cores may form, but due to the linear convergence mechanism, and sporadically. This mode is termed ‘photoevaporation dominated’.

### 3.4.2 CLOUDS WITH $\varphi \neq 0^\circ$ INCLINATIONS

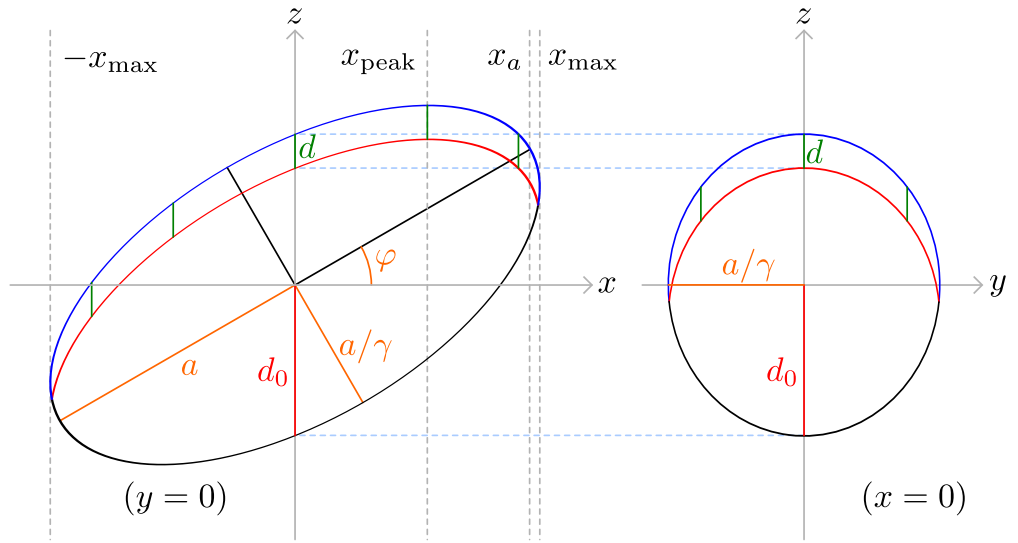


Figure 3.29: An overall illustration of the geometry and parameters relevant for inclined clouds. On the left is a cross-section through the  $x-z$  plane at  $y=0$ , and on the right is a cross-section through the  $y-z$  plane at  $x=0$ . The parameters and lines in orange are the geometric definitions of the cloud, semi-major axis  $a$ , semi-minor axis  $a/\gamma$  (expressed as a function of the axial ratio  $\gamma$ ) and the cloud inclination  $\varphi$ . The curved black line ellipse arc is the initially unaffected surface of the cloud; the upper blue ellipse arc is the original upper surface; and the upper red ellipse arc is the modified upper surface, after penetration of the ionising radiation to the equilibrium depth  $d$ . That equilibrium depth is shown throughout as the short, green, vertical lines. The half-depth of the longest vertical path through the ellipsoid at  $(y=0, x=0)$  is  $d_0$ , where  $d_{\text{EUV}} = d/d_0$ . In addition, the vertical, grey, dashed lines are labelled for parameters used for identification of features in other sections.  $x_{\text{max}}$  is the farthest distance along the  $x$ -axis that any part of the cloud extends to,  $x_{\text{peak}}$  is the location of the  $x$ -axis of the peak or apex of the cloud (the  $x$  position for maximum  $y$ ), and  $x_a$  is the projected distance  $x_a = a \cos \varphi$  of the semi-major axis.

When dealing with clouds whose major axis is not perpendicular to the direction of the radiation, a more general scheme must be devised. It is necessary to calculate the

longest straight-line path through an ellipse aligned for a particular direction. This will be a line through the centre of the ellipse. All of the relevant geometry and parameters are displayed in Figure 3.29.

The polar form of the equations for an ellipse can be stated as,

$$r(\theta) = \frac{a b}{\sqrt{(b \sin \theta)^2 + (a \cos \theta)^2}}. \quad (3.37)$$

This gives the half-distance for the longest path for  $\theta = \varphi$  for any inclination  $\varphi$ . The half-distance is taken as it conveniently means that  $\theta = \varphi = 0$  and  $90^\circ$  results in the semi-minor and semi-major axes respectively; rather than two times each. Presented as a function of  $a$  and  $\gamma$  as in Equation (3.36), the general expression for  $d_{\text{EUV}}$  can be given as,

$$d_{\text{EUV}} = \frac{F_0 \gamma}{n^2 a \alpha_B} \sqrt{\cos^2 \varphi + \frac{\sin^2 \varphi}{\gamma^2}}. \quad (3.38)$$

This equation presents the entire picture of the  $d_{\text{EUV}}$  parameter for combinations of all of the parameters to be investigated. The intent is that it acts as an effective mechanism through which to describe the relation between initial conditions of all varieties and aspects of the evolution for those conditions.

It is of not insignificant note that the projected area of this ellipsoid on the  $x - y$  plane can be expressed as,

$$A(a, \gamma, \varphi) = \frac{\pi a^2}{\gamma} \sqrt{\cos^2 \varphi + \frac{\sin^2 \varphi}{\gamma^2}}. \quad (3.39)$$

Expressing the relationship between  $d_{\text{EUV}}$  and the area of the cloud intercepting the EUV radiation with a proportionality constant of  $\chi$ ,

$$d_{\text{EUV}} = \chi A, \quad (3.40)$$

which gives  $\chi$  as,

$$\chi = \frac{F_0 \gamma^2}{\pi n^2 \alpha_B a^3}. \quad (3.41)$$

The mass of an ellipsoidal cloud with particular density and geometric parameters is  $M = (4 m_{\text{H}_2} n \pi a^3)/(3 \gamma^2)$  (where  $m_{\text{H}_2}$  is the mass of a hydrogen molecule, and  $n m_{\text{H}_2} = \rho$  gives the actual mass density), substituting this in to Equation (3.41) gives,

$$\chi = \frac{4 m_{\text{H}_2} F_0}{3 n \alpha_B M}. \quad (3.42)$$

Returning to Equation (3.40), this gives an alternative description of  $d_{\text{EUV}}$  as,

$$d_{\text{EUV}} = \frac{4 m_{\text{H}_2} F_0 A}{3 n \alpha_B M}. \quad (3.43)$$

This shows the nature of the degeneracy within  $d_{\text{EUV}}$ . For constant  $M$ ,  $n$  and exposed to the same  $F_0$ , clouds of a variety of geometry and inclination combinations can result in the same projected area, and will give the same  $d_{\text{EUV}}$ . If the dynamics of the exact geometry of the upper surface of the clouds are the dominant factor in determining the path of the evolution of that cloud, this may limit the ability of the  $d_{\text{EUV}}$  parameter to describe all of these scenarios. If the dynamics are determined by the initial radiation state, described by  $d_{\text{EUV}}$ , then the whole picture may be given by the single parameter.

### 3.4.3 EFFECTIVE INITIAL GEOMETRY

With ionising radiation incident on the upper surface of the clouds, a surface layer, to the aforementioned equilibrium depth, will be ‘instantly’ (on hydrodynamic timescales) ionised. This mass is lost before hydrodynamical effects take over. It is possible, then to calculate an ‘effective’ initial mass, modified by the amount lost from the surface of the cloud. The manner in which the plane-parallel ionising radiation acts such that the initial surface is the same shape as the original cloud, shifted down by the equilibrium depth. The effective initial cloud will be the intersection of the original ellipsoid, and this shifted ellipsoid.

Shown in Figure 3.30 is a plot of the ‘effective initial mass’ (mass remaining neutral after several recombination timescales) for clouds of initial mass  $M = 30 M_\odot$  and  $\varphi = 0^\circ$  at three densities used in subsequent sections, 100, 600 and  $1\,200 \text{ cm}^{-3}$ , with an incident flux of  $2 \times 10^9 \text{ cm}^{-2} \text{ s}^{-1}$ . The results are strongly density dependent, as would be expected, and show that the fraction of initially ionised material increases non-linearly with increasing axial ratio. In all cases the least initial material is found at the highest ratio, 8.0 in Figure 3.30, where it has fallen to ratios/masses of 59%/17.60  $M_\odot$ , 98%/29.37  $M_\odot$  and 99%/29.79  $M_\odot$  for 100, 600 and  $1\,200 \text{ cm}^{-3}$  respectively.

Shown in Figure 3.31 are the effective initial mass profiles for  $30 M_\odot$ ,  $100 \text{ cm}^{-3}$  clouds at inclinations of  $0$  to  $90^\circ$  in steps of  $15^\circ$ .

The point described at the end of Section 3.4.2, in which the degeneracy of certain properties with regards to  $d_{\text{EUV}}$  can be observed if the data from Figure 3.31 is taken and replotted as the effective initial mass as a function of the value for  $d_{\text{EUV}}$  calculated for each cloud. This extends to adding clouds of varied initial density (50 and  $600 \text{ cm}^{-3}$  in addition to  $100 \text{ cm}^{-3}$ ). The values for  $d_{\text{EUV}}$ , and correspondingly the effective initial mass overlap broadly between the inclinations and densities.

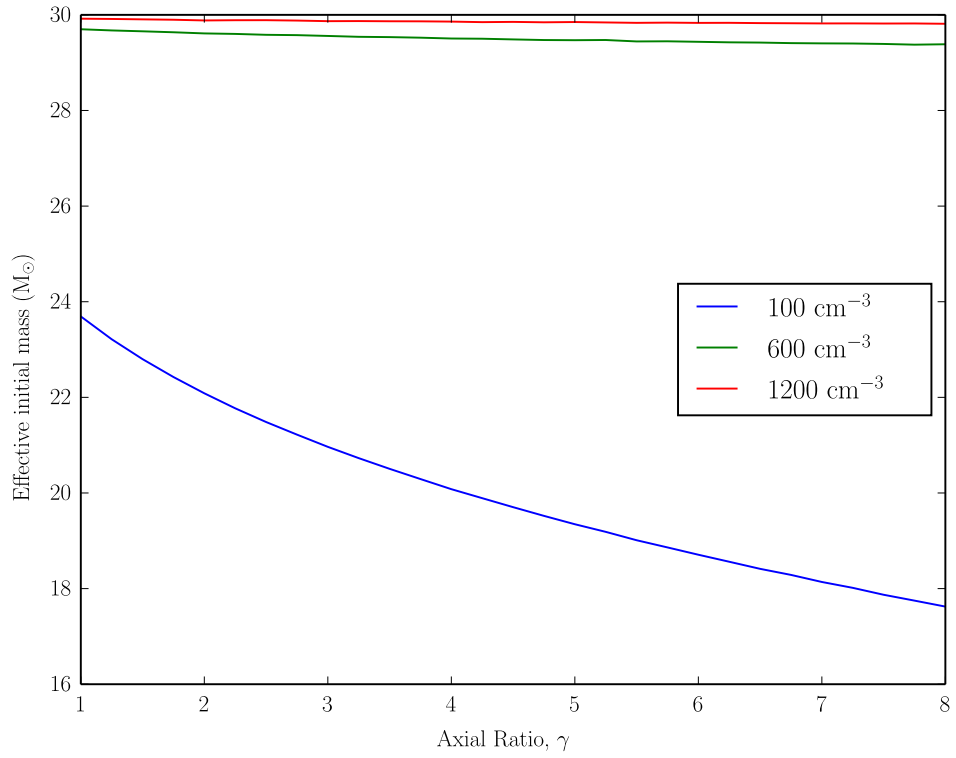


Figure 3.30: Profiles of initially neutral material after one equilibrium depth of ionising radiation (at a flux of  $2 \times 10^9 \text{ cm}^{-2} \text{ s}^{-1}$ ) is applied to initial clouds of  $M = 30 M_{\odot}$  and  $\varphi = 0^{\circ}$  at the indicated densities.

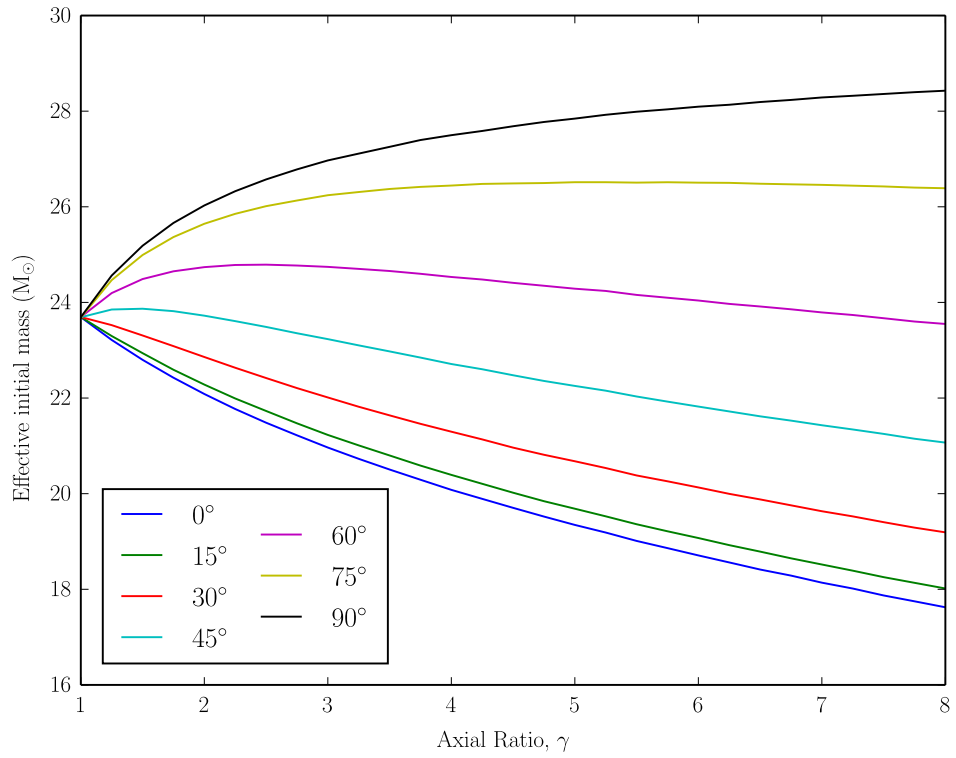


Figure 3.31: Effective initial mass profiles as a function of the cloud ratio, for  $30 M_{\odot}$ ,  $100 \text{ cm}^{-3}$  clouds at the indicated inclinations.

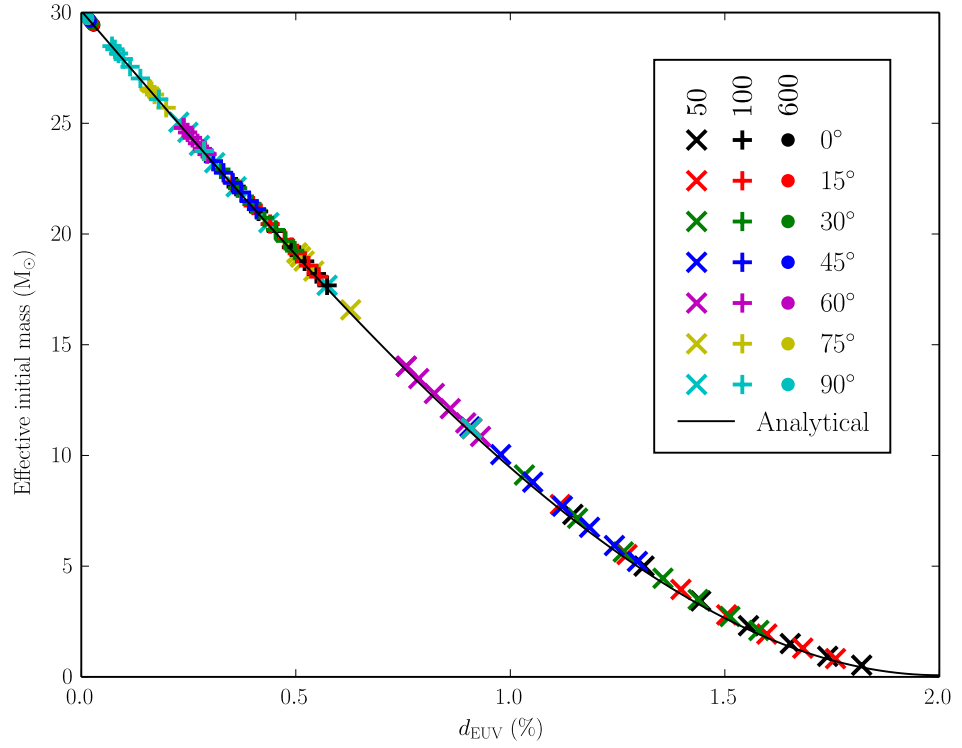


Figure 3.32: Effective initial mass profiles for  $30 M_{\odot}$  clouds. Numerical results as data points for  $50$ ,  $100$  and  $600 \text{ cm}^{-3}$  clouds at inclinations ranges of  $0$  to  $90^{\circ}$  in steps of  $15^{\circ}$  and axial ratios of  $1$  to  $8$  in steps of  $1$ . Each are plotted as a function of the cloud's value of  $d_{\text{EUV}}$ . The solid line indicates the analytical profile.

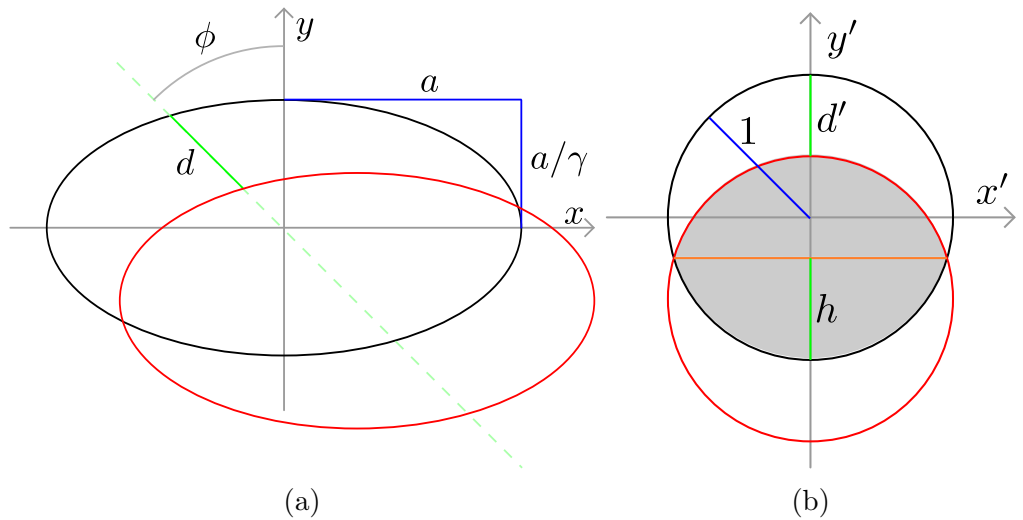


Figure 3.33: Geometric illustration of the displaced cloud surface by the ionisation depth as cross-sections of the original ellipsoids (a), and the corresponding geometry with the transforms applied to simplify to unit spheres (b).

To calculate the analytical solution for the remaining neutral mass for the initial conditions, it is necessary to consider the described pair of ellipsoids and find the ratio between the volume of the intersection region, to the volume of a single ellipsoid. Working with ellipsoids is awkward and given that only a single translation is made (offset at an inclination can be considered as simply a translation along that same inclination angle by the same amount) the entire scenario can be reduced by scaling transformations to conformally map to two unit circles, greatly simplifying the calculations. The scenario is illustrated the two panels of Figure 3.33. Figure 3.33a describes the familiar scenario in coordinates fixed to the axes of the ellipse.  $d$  in this panel is the equilibrium depth,  $d = \frac{F_0}{n^2 a}$  without dividing by a scale-length (as with  $d_{\text{EUV}}$  itself). Figure 3.33b shows the situation after translations have been applied to produce two unit spheres. Specifically, relative to the original coordinate system  $(x, y, z)$ , we have a new coordinate system  $(x', y', z)$  where,

$$x' = \frac{x}{a}, \quad (3.44)$$

$$y' = \frac{y \gamma}{a}. \quad (3.45)$$

The scenario displayed in Figure 3.33b has then also been rotated (due to the introduced circular symmetry) for ease of illustration.

The equilibrium depth in this new coordinate system is  $d'$ , this is calculated using the simple statement that the two axial components of  $d$  are  $d_x = d \sin \phi$  and  $d_y = d \cos \phi$ . This gives transformed coordinates of,

$$d_{x'} = \frac{d \sin \phi}{a}, \quad (3.46)$$

$$d_{y'} = \frac{d \gamma \cos \phi}{a}, \quad (3.47)$$

with their magnitude,

$$d' = \frac{d}{a} \sqrt{\sin^2 \phi + \gamma^2 \cos^2 \phi}. \quad (3.48)$$

Conveniently, though to be expected, as it is just the proportion of the equilibrium depth to a scale length,  $d' = d_{\text{EUV}}$  (as can be shown through the use of trigonometric identities). In Figure 3.33b this offset is represented as an axially aligned line simply because the orientation becomes irrelevant in the circularly symmetric scenario, and it makes the presentation of other aspects of the scenario less complicated to view.

Having created a system of two unit spheres with a known offset, the important

parameter to determine is the ratio of the intersecting volume to the volume of the original. This ratio is the same in both coordinate systems, and will provide the true ratio of both volume and mass (due to constant density) and hence the effective initial neutral mass. Importantly, the system now also has mirrored symmetry about the orange line in Figure 3.33b representing the plane at which the two spheres intersect.

The volume of a spherical ‘cap’ is given by,

$$V_{\text{cap}} = \frac{\pi h^2}{3} (3r - h), \quad (3.49)$$

where  $h$  is the height of the cap, and  $r$  the radius of the sphere. As we have a unit sphere, and two of these caps, one either side of the plane of symmetry, this gives,

$$V_{\text{cap}} = \frac{2\pi h^2}{3} (3 - h). \quad (3.50)$$

$2h$  can be seen to be the diameter of the sphere minus the offset, giving  $h = 1 - \frac{1}{2}d'$ , and an expression for the total intersection volume (the overlapping region between the red and black circles of Figure 3.33b) of,

$$V = \frac{2\pi}{3} \left(1 - \frac{1}{2}d'\right)^2 \left(2 + \frac{1}{2}d'\right). \quad (3.51)$$

With some additional rearrangement, division by the volume of a unit sphere and recalling that  $d' = d_{\text{EUV}}$ , the fractional volume,  $\nu$ , is,

$$\nu = \frac{1}{16} (d_{\text{EUV}} - 2)^2 (d_{\text{EUV}} + 4). \quad (3.52)$$

The result of this is plotted in Figure 3.32 along with the data for examples of individual cloud calculations. The most useful aspect for the purposes of the clouds investigated by simulation later, is that for small  $d_{\text{EUV}}$ , the first order approximation of Equation (3.52) becomes the simple, linear,

$$\nu \approx 1 - \frac{3}{4}d_{\text{EUV}}. \quad (3.53)$$

This means that for small  $d_{\text{EUV}}$ , the mass loss through rapid evaporation is directly proportional to  $\frac{3}{4}d_{\text{EUV}}$ .  $d_{\text{EUV}}$  can therefore be described as a fundamentally physical parameter, describing the effect the ionising EUV radiation has relative to the cloud scale and mass, as well as its geometric configuration.

## 3.5 SETTING INITIAL CONDITIONS

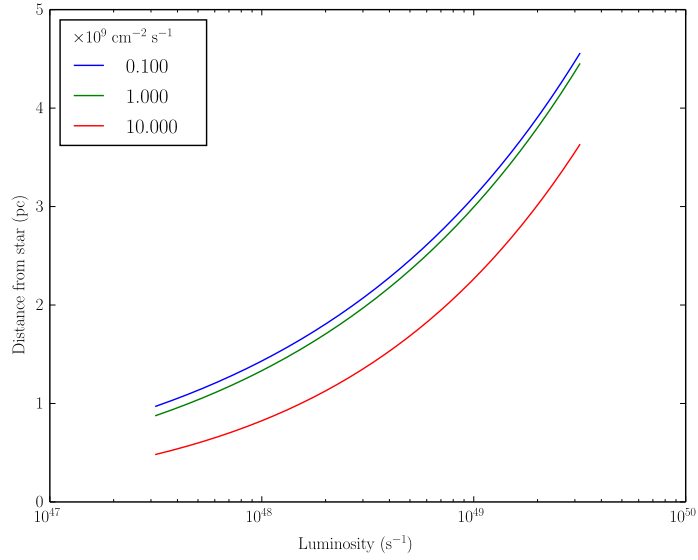
---

Shown in Figures 3.34a and 3.34b are the profiles of the distances with stellar luminosity at which certain specified surface fluxes would be observed, for an H II region expanding through a medium of constant density  $100 \text{ cm}^{-3}$ . The luminosity range was from stellar luminosities measured in hydrogen ionising photons per second calculated by Martins et al. (2005). Where, for O-stars of various luminosity classes, stellar temperatures of between 30 000 and 45 000 K provided a maximum luminosity range of around  $10^{47.5}$  to  $10^{49.5} \text{ s}^{-1}$ . Figure 3.34a displays this as absolute distances from the illuminating star; and Figure 3.34b as a fraction of the Strömgren radius as given in Equation (3.1).

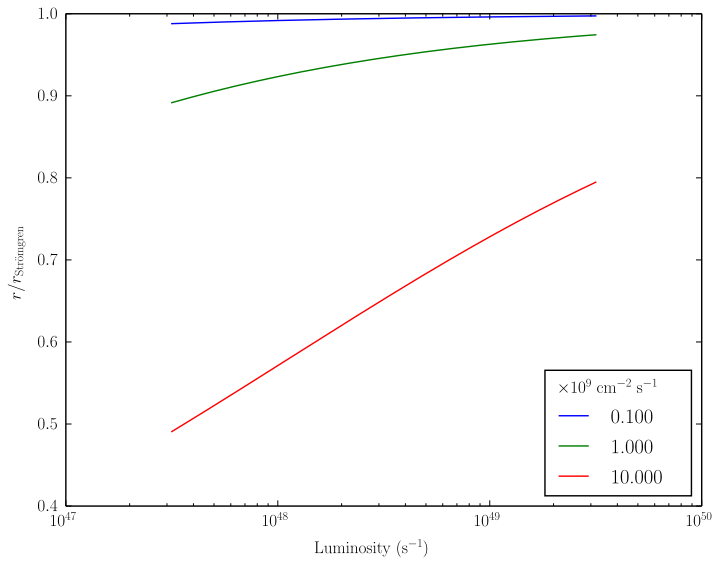
In both cases, the ranges for surface fluxes of the order of  $10^9 \text{ cm}^{-2} \text{ s}^{-1}$  provides sensible configurations. The range of distances is sensible in scale relative to observed structures, and not too close the Strömgren radius itself, where the front may already have transitioned to D-type.

These factors make the use of  $10^9 \text{ cm}^{-2} \text{ s}^{-1}$  a good basis for investigating the behaviour at the boundary of the H II region of an O-type star or small OB association.

In all cases, the recombination coefficient  $\alpha_B$  is set as  $2.7 \times 10^{-13} \text{ cm}^3 \text{ s}^{-1}$  (Lefloch and Lazareff, 1994), and the absorption cross-section,  $\sigma$  is set as  $6 \times 10^{-18} \text{ cm}^2$  (a wide range of values have been used in the past for this parameter, but see, for example Verner et al. (1996); in addition, there is some considerable leeway in which value is used for the numerical implementation as described in Kessel-Deynet and Burkert (2000)).



(a)



(b)

Figure 3.34: Profiles with stellar luminosities of the distances required for each specified flux of  $1 \times 10^8$ ,  $10^9$  and  $10^{10} \text{ cm}^{-2} \text{ s}^{-1}$ . (a) the distances themselves in parsec, (b) as a fraction of the Strömgen radius.

## CHAPTER 4

---

# THE EVOLUTION OF NORMAL PROLATE MOLECULAR CLOUDS AT HII BOUNDARIES

---

Content in this Chapter is based on, and in areas reproduced from, Kinnear et al. (2014). The aforementioned paper was produced during this PhD, and is listed in the declarations for this thesis.

In looking at the various geometric configurations of prolate clouds subject to EUV radiation, a logical starting point is a set up in which there is analytically advantageous symmetry. Such a configuration is a prolate ellipsoidal cloud of semi-major axis  $a$  and semi-minor axis  $b = a/\gamma$ , oriented such that the major-axis is perpendicular to the incident radiation. This geometry is illustrated in Figure 4.1, and represents the starting point for this investigation.

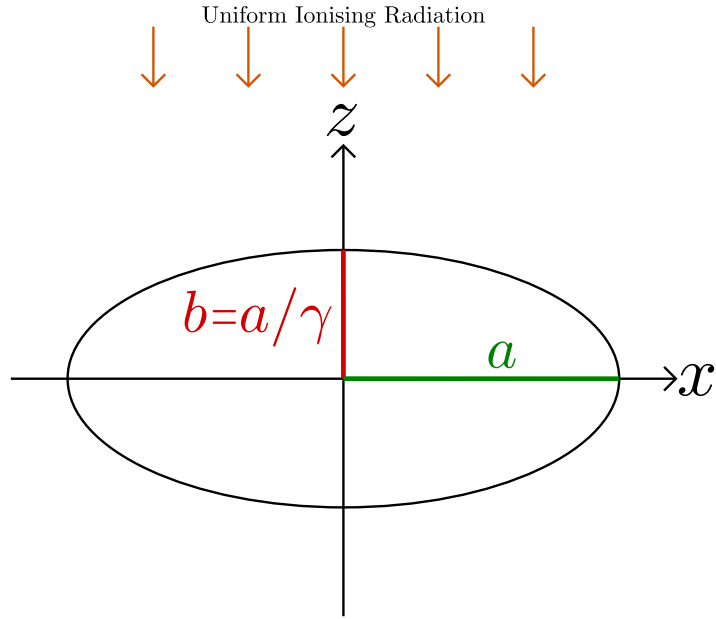


Figure 4.1: Annotated illustration of the geometry of the clouds investigated in this section; an isotropic interstellar background radiation field is also included, but not presented in the diagram.

## 4.1 INTRODUCTION

---

### 4.1.1 BACKGROUND

Most of the current RDI models adopt a spherical molecular cloud as the initial condition in simulations. However, recent observations on a large sample of isolated molecular cores have revealed that spherically symmetric molecular cloud cores are the exception rather than the rule (Jones et al., 2001; Myers et al., 1991; Curry and Stahler, 2001; Rathborne et al., 2009). Theoretical investigations have also found physical mechanisms which result in formation of prolate clouds in general astrophysical environments (Tassis, 2007; Boss, 2009; Cai and Taam, 2010). Shown in Figure 4.2 is the distribution of molecular clumps over the ratio  $\gamma$  of the semi-major ( $a$ ) to semi-minor ( $b$ ) axis, collated from a Galactic Ring survey of 6 124 objects, which gives a mean axial ratio  $\gamma = \frac{a}{b} = 1.6$  (Rathborne et al., 2009). It is worth noting that the data from which these ratios were calculated was determined using the FWHM of two axes in the observation. As such, clumps which are elongated but have their semi-major axis intercepting the observational plane by an angle are represented with a lower  $\gamma$  value than their actual ones. It can be expected that the ‘true’ ratios of these objects will be shifted to higher  $\gamma$  value range.

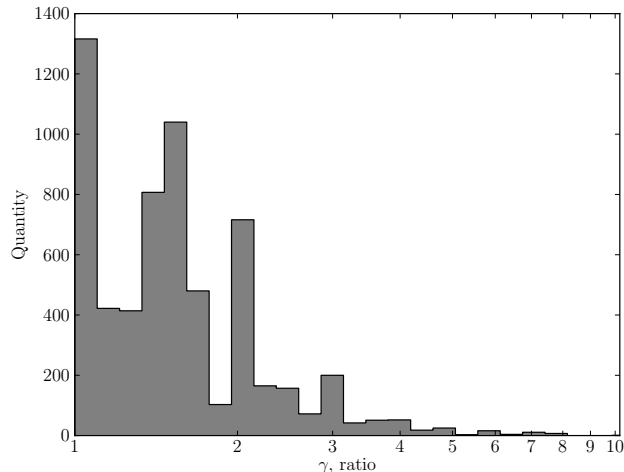


Figure 4.2: The distribution of molecular clumps over the semi-major to minor axial ratios  $\gamma$ . Statistics based on the data in a survey for 6 124 single molecular clumps (Rathborne et al., 2009).

#### 4.1.2 INITIAL STABILITY OF A PROLATE CLOUD

This chapter is concerned with the investigation of the dynamic evolution of a prolate cloud with its semi-major axis perpendicular to the incident direction of EUV radiation as shown in Figure 4.1. Dynamic evolution, in this context, constitutes the motion of material, material properties, and high density regions, up until the formation of the first, or first few, high density cores of  $\approx 10^{13} \text{ cm}^{-3}$ . The geometric parameters for the clouds will be notated as the semi-major axis,  $a$ , and the ratio of semi-major to semi-minor  $\gamma = a/b$ , rather than the semi-minor axis length itself.

As it is important to configure the initial cloud such that its collapse can be positively linked with the incident EUV radiation, it is necessary to ensure that the initial conditions of the cloud are stable against pure gravitational collapse. The Jeans' criterion (in terms of Jeans' number  $J$ ) for an isolated prolate cloud to be stable against its own gravity can be expressed as (Bastien, 1983),

$$J = \frac{\pi G \rho \mu b^2}{15 e R_g T} \ln \left( \frac{1+e}{1-e} \right) \leq 1, \quad (4.1)$$

where  $\rho$ ,  $b$ ,  $T$  and  $\mu$  are the mass density, the minor axis, the initial temperature and the mean molecular mass of the prolate cloud respectively,  $G$  and  $R_g$  the Gravitational Constant and Specific Gas Constant, and with the eccentricity  $e = \sqrt{1 - \frac{b^2}{a^2}} = \frac{\sqrt{\gamma^2 - 1}}{\gamma}$ .

Substituting  $\rho = (3M) / (4\pi ab^2)$  into Equation 4.1, the condition for the major axis

$a$  of an isolated non-collapsing prolate cloud is obtained,

$$\begin{aligned} a \geq a_{\text{crit}} &= \frac{\mu G M}{20 R_g T e} \ln \left( \frac{1+e}{1-e} \right) \\ &= 0.052 \frac{M^* \gamma}{T \sqrt{\gamma^2 - 1}} \ln \left( \frac{\gamma + \sqrt{\gamma^2 - 1}}{\gamma - \sqrt{\gamma^2 - 1}} \right) [\text{pc}], \end{aligned} \quad (4.2)$$

where  $M^*$  is the mass of the prolate cloud in units of solar masses, and  $a$  and  $a_{\text{crit}}$  have units of Parsecs. For a given molecular cloud of mass  $M^*$ , initial temperature  $T$  and ratio  $\gamma$ , the conceptual minimum value of semi-major axis length  $a_{\text{crit}}$  can be calculated, the major axis of an initially gravitationally stable cloud should therefore satisfy  $a > a_{\text{crit}}$ .

### 4.1.3 INITIAL CONDITIONS OF PROLATE CLOUDS

Table 4.1 describes the range of initial conditions for the simulated prolate clouds, the corresponding section numbers in which they appear as well as the objective of investigation for each. The initial conditions are described in terms of the mass ( $M$ ), density ( $n$ ), axial ratio ( $\gamma$ ), and EUV flux ( $F_0$ ), covering the range of defining characteristics of the clouds investigated.

## 4.2 CORE FINDING

---

A limitation of the code being used for this investigation is the omission of ‘sink particles’. SPH simulations are subject to what constitutes both an advantage and disadvantage with their effective adaptive spacial resolution. Increasing densities occur through SPH particles becoming closer together, with adaptive smoothing length, particles closer together represents smaller smoothing lengths, and hence increased spacial resolution. Unfortunately, when there is gravitational collapse, especially when chemistry is included, producing decreasing temperatures enhancing the collapse, particles will continue closing together. As the timestep of the simulation is based on the Courant-Friedrichs-Lewy (CFL) condition, the result of this is that the timesteps will become vanishingly small, preventing the simulation from advancing. This can be ‘catastrophic’, in that a rapidly increasing number of timesteps is required for decreasing amounts of time and, for all intents and purposes, the simulation has ended.

Sink particles were created as a remedy for this situation (Bate et al., 1995). Once a dense collection of particles obtained collective properties which exceeded the require-

Name	Mass ( $M_{\odot}$ )	Density ( $\text{cm}^{-3}$ )	Ratio	EUV Flux ( $\text{cm}^{-2} \text{s}^{-1}$ )	Varied Parameter	Section	Purpose
A, B, C	$M$	100	2	$10^9$	$100 \leq M \leq 200$	4.4	Observation of the evolution of high $d_{\text{env}}$ clouds of varied mass.
D1-3	200	$n$	2	$10^9$	$100 \leq n \leq 1,200$	4.4.3(a)	Observation of high mass clouds with varied density.
E1-3	200	100	2	$F$	$10^7 \leq F \leq 8 \times 10^9$	4.4.3(b)	Observation of high mass clouds with varied incident flux.
G1(1-19)	30	600	$\gamma$	$10^9$	$1 \leq \gamma \leq 8$	4.5.2	Observation of low mass clouds at medium initial density across varied ratios.
G2(1-19)	30	1,200	$\gamma$	$10^9$	$1 \leq \gamma \leq 8$	4.5.1	Observation of low mass clouds at high initial density across varied ratios.
G0	30	100	2	$10^9$		4.5.3	Observation of extending particular ratios to a low initial density (other ratios were produced, but only $\gamma = 2$ is presented).

Table 4.1: Summary of the parameters of all tests examined. After the name of the test series, the next four columns (Mass, Density, Ratio & EUV Flux) are the defining parameters of each simulation set. For all series, three of the four are fixed values, and the remaining parameter is represented by a variable, whose range is described in the Varied Parameter column. The final column indicates the main Section/Subsection in which the test series is discussed.

ments for its formation, a sink particle would be placed at their centre of mass, and the original particles removed from the simulation. The sink particle would possess all of the fundamental quantities of the ensemble of particles used in its creation, conservation of mass, momentum and energy. They are usually designed with the assumption that they already represent compact (compared to the SPH particles) objects, e.g. protostars or similar. They can accrete additional SPH particles, but otherwise only interact gravitationally with their surroundings, no longer representing a fluid element.

Sink particles are accompanied by their own drawbacks, including the extensive calibration necessary to ensure that their properties are consistent with the other accompanying physics. These can be improved upon and modified (Hubber et al., 2013) for consistency with comparable simulations, across resolutions, and in comparison with theory. However, implementation is still an extensive process and due to these difficulties, testing must always be very extensive in order to validate the implementation.

Whilst sink particles are not implemented in `RadCode II` and the simulations halt upon the formation of the initial highly condensed cores, it is useful to be able to identify objects/regions which could be classed as collapsing material or actual pre-protostars. For this purpose an algorithm and code was developed to search through particles to find localised density peaks and material associated with those positions. The code will be referred to as `corefinder`.

A ‘core’ in this context is defined as a region surrounding a local density maxima with a peak  $\text{H}_2$  number density greater than  $10^6 \text{ cm}^{-3}$ . This results in selection of ‘cores’ with a wide range of peak densities, from just over  $10^6 \text{ cm}^{-3}$  up to the code’s effective limit of  $\approx 10^{13} \text{ cm}^{-3}$ . This is less specific than the equivalent criteria to form sink particles. This is because the intent is to locate regions which are approaching collapse in addition to those actively undergoing collapse. Since the timestep issue ends the progress of the simulation prior to all potential cores having reached the point of formation, objects which would *not* be identified as ready to become an actual sink particle *can* be identified as local density maxima. With information on their context (peak density/surrounding mass/etc.), it can be determined in post processing what prospect, if any, each may have to collapse to actual cores.

Importantly, for this work, a determination of whether the core is gravitationally bound is not conducted. Implementation of criteria for selection based on the Virial Theorem was not performed, though has been considered for future analysis. The cores in this context are designed to represent high density regions only, as an alternative to a ‘mass above a threshold density’ metric with ability to provide some indication of probable core formation locations.

The end of a simulation is taken as the practical limit of the formation of the first, or first few, timestep converging cores with sufficient quantities of material at, or approaching,  $n = 10^8 \text{ cm}^{-3}$  for the timestepping to have ceased advancing. This will be referred to as ‘density triggered completion’ of the simulation.

#### 4.2.1 THE ALGORITHM

In the following, the main framework of the corefinding code is presented.

To begin with, all particles below a density threshold ( $n < n_{\text{thresh}}$ ) are discounted. Following this initial filter of particles, the cores are determined in the following procedures:

1. The code generates nearest neighbour lists for every particle using an Oct Tree method, such as that described in Section 2.3.1. A set of  $N_{\text{nc}}$  neighbours is selected, with this value configurable to adjust the qualities of cores identified. It was intended that the same value as  $N_{\text{neigh}}$  for the SPH code be used, however others are also investigated.
2. The particle with maximum density is selected and acts as the seed for the first core.
3. The code then searches outwards to select all of the nearest neighbour particles which have a density lower than  $n_{\text{current}} \times f_n$ . Where  $n_{\text{current}}$  is the density of the currently branching particle, and  $f_n$  is a fractional threshold for selection. This fractional threshold is intended to be set as just over 1, to provide a selection of marginally over-dense particles. For most of the work presented here, this was set as  $f_n = 1.01$  for a 1% over-density margin. From each of these neighbours, the selection process then attempts to search further outward for any lower density neighbours which have not already been selected. Each particle is added to a list for the current seed as they are selected. An additional selection criteria is that any connected particles will be automatically selected, regardless of relative number density, if they are above the Jeans’ density limit described by Bate and Burkert (1997),  $n_{\text{limit}}$  here. This is the density above which artificial fragmentation is expected to occur, and the selection process ensures that local density maxima separated by greater than this density are jointly selected as a single core.
4. The selection process continues until no particles remain which are: (a) lower number density than the last seed particle (plus the two exceptions); (b) not already selected by the current seed.

5. This procedure is then repeated from step 2. This time the new seed particle is selected as being the next maximum density particle which has **not** already been selected by a previous descent along nearest neighbour branches. This is done until no particles remain which can be selected, having been ruled out by one or more of the previously described criteria. Note that particles already selected and labelled by one seed may also be selected and labelled by another seed. Each particle builds up a list of which seeds have selected it.
6. Through this process, particles are selected in groups growing out from all localised density maxima. Following the selection of all possible candidate groups, mean properties for each group are determined (position, density, i.e., collective properties of any attribute possessed by the component particles).
7. An additional point of note regards particles which were selected and labelled from multiple seeds. In the current implementation, the properties of any particle which is part of more than one seed descent is equally weighted between those seeds. A more comprehensive process for deciding ‘ownership’ of each particle will be implemented in the near future.
8. Following the selection of all possible particles, some post-processing is performed to filter the core selections. This incorporates deallocating any core possessing fewer than a particular count  $N_{\text{unique}}$  of ‘uniquely selected’ particles (i.e. particles selected by only itself, not shared with any other cores), and/or fewer than a particular count  $N_{\text{total}}$  of particles for the entire core, including those shared with another core. As the mass per particle is constant, these criteria can also be considered as a minimum unique mass threshold for the core, and a minimum total mass threshold for the core.

This method may provide an advantage in determining non-spherical or highly asymmetrical cores, for which a radial selection or search may not be sufficient. It additionally permits determination of structure shapes which are of highly irregular geometries. These include filament and clump features as the approximate shape, size and extent of each core can be determined in the code.

Figure 4.3 presents a graphical illustration of the process for a 1D arrangement of particles. The following is the step-by-step explanation of the specific case illustrated.

- a) The initial layout of particles, with the first seed having been selected as the particle with the maximum density.

- b) Nearest neighbour particles are selected sequentially in a branching fashion. Note the branch presented as a bold line, the density gradient is positive, which would usually result in this branch not being permitted, however, since both particles are above  $n_{\text{limit}}$  the branch is forced. Note that the algorithm is tracing as far as it can down and to the left first, with leftmost particles furthest down the tree begin selected afterwards. This reflects the true algorithmic operation of the code, in which one particular path is traced all the way down, before backtracking and trying routes from further up.
- c) With all particles that can be selected based on the rules from the first seed. The new maximum is selected from the particles not already marked as belonging to a core.
- d) The descent for the second core is performed. Particles already possessed by the first core are permitted to be reselected.
- e) An unselected particle still remains, and so is selected as a progenitor for a third candidate core; most of its component particles are shared between all three cores.
- f) With no unselected particles remaining, the core select process finishes, and those which fail to fulfil remaining criteria are deselected. In this case, the third core (blue) only possess one unique particle, assuming that  $N_{\text{unique}} > 1$  this core is removed from the candidate list.

#### 4.2.2 CODE TESTING

Although there are no comparable codes available to provide a direct benchmark of results and performance, the sensitivity of the results obtained to variation in the free parameters for the selection criteria can be examined to determine the extent to which the code is self-consistent and insensitive to resolution. The parameters which characterise the behaviour of the algorithm are:

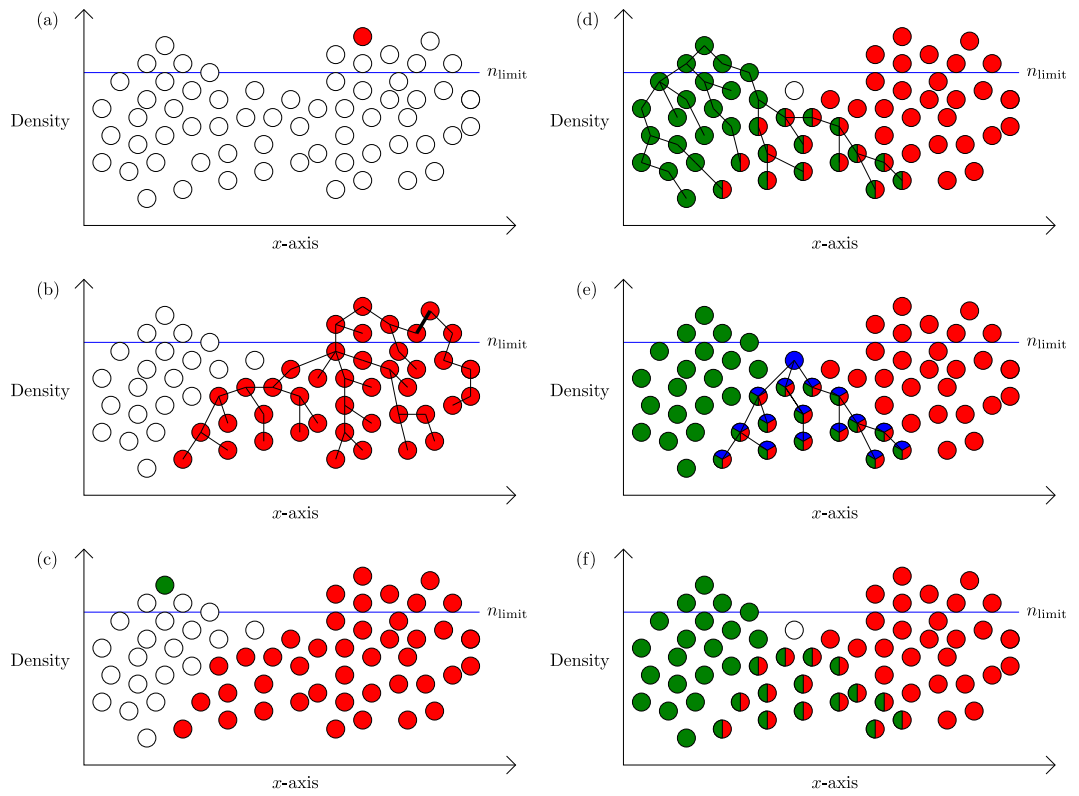


Figure 4.3: Illustration of the corefinding process for a 1D representation of SPH particles. Sequence of operations is from a) to f) in alphabetical order. Each particle is represented by a circle of particular  $x$ -coordinate and density.  $n_{\text{limit}}$  represents the density resolution threshold for artificial fragmentation.

$n_{\text{thresh}}$	The threshold above which particles are permitted to be selected (below it being discounted), and the lowest density for which a prospective seed can be selected. This includes the selection of particles, as well as the minimum core density peak; in other words, raising this value also reduces the total number of particles, and hence mass, available to be selected for cores which have a peak above the both threshold values.
$f_n$	The ‘over-density’ ratio, the fraction of the current branching particle above which neighbours can be selected.
$N_{\text{nc}}$	The number of neighbours to populate the nearest neighbour list with.
$N_{\text{unique}}$	The minimum number of uniquely selected particles (shared with no other core) a core is permitted to possess, below which it is discounted.
$N_{\text{total}}$	The minimum total number of particles which a core must possess, below which it is discounted.

Slight variation of these values should not substantially modify the statistics of the cores being identified. It is also important to note that some of these criteria are not equivalent to just selecting a subset of cores from a single run of the algorithm.

Presented in Figure 4.4 is the final timestep of a cloud from Section 4.5.1, with initial properties of:  $\gamma = 2$ ,  $n = 1\,200\text{ cm}^{-3}$  and  $M = 30 M_{\odot}$ , subjected to a EUV flux of  $2 \times 10^9\text{ cm}^{-2}$ . The projected images of the final snapshot of this simulation are presented in Figure 4.4.

This will be used as a sample cloud on which to examine the results of `corefinder` for several selections of the available parameters. Table 4.2 describes the variations in the parameters with which `corefinder` was run, and the basic results of each run of the program.

For each combination of set parameters, the resultant core properties  $N_c$  and  $M_c$  (number of cores, and the total mass of the cores, respectively), are presented along with subsets of those properties for only cores above set density thresholds.

The data from this algorithm are only meant to be representative, not deterministic. Given this, the results in Table 4.2 show good similarity for the ranges of parameters investigated. The total selected core masses in each case vary by a maximum of  $< 10\%$  for the selection of every core,  $\pm 2$  cores for high densities ( $n > 10^8\text{ cm}^{-3}$ ) and no more than averaging  $0.25 M_{\odot}$  per core for the extremely high density selection ( $n > 10^{11}\text{ cm}^{-3}$ ).

Of interest, restricting the code to requiring higher numbers of unique and total cores (higher  $N_{\text{unique}}$  and  $N_{\text{total}}$ ), *increases* the mass found in higher density cores, where it might be expected that the stricter criteria would reduce it. This is because ‘smaller’ cores which would otherwise be assumed to share the mass of the high peak

label	$n_{\text{thresh}}$ ( $\text{cm}^{-3}$ )	$f_n$	$N_{\text{nc}}$	$N_{\text{unique}}$	$N_{\text{total}}$	$N_c$ (all)	$M_c$	$N_c$ ( $n_{\text{peak}} > 10^8$ )	$M_c$	$N_c$ ( $n_{\text{peak}} > 10^{11}$ )	$M_c$
T1	$10^6$	1.01	45	20	30	152	23.6	12	3.60	2	0.75
T2	$10^6$	1.01	45	40	60	104	23.2	10	4.44	2	1.08
T3	$10^6$	1.01	45	100	200	56	22.3	8	5.50	2	1.54
T4	$10^6$	1.01	100	20	30	106	23.9	10	4.05	2	0.94
T5	$10^6$	1.05	45	20	30	99	23.8	10	4.25	2	1.02

Table 4.2: Summary of test conditions for evaluation of the corefinding algorithm parameters. To the left are the parameters as set, to the right are the results for several properties of obtained from running the algorithm on identical sample simulations.

density cores are discounted, and no mass is shared away from the few, definite, high density cores themselves.

Configuration T3 proved to find core properties which could be considered more useful, discounting smaller cores in favour of the few most massive and densest ones. It is of less importance to identify the larger number of lower density cores, as a great deal more uncertainty surrounds their continuing evolution. It was deemed suitable to use as the basis for analysis, though can be modified based on selection of only the higher mass cores, in addition to the other properties, for particular purposes in other sections.

### 4.3 AXIAL DENSITY PROFILE

In order to better characterise the distribution of high density material along the major-axis of the cloud, a method was desired to describe not just the distribution of mass, but that weighted by density (Nelson and Papaloizou, 1993; Nelson and Langer, 1999). When sampling along a single axis, distributions of mass (mass per unit length) can be deceptive. High values of mass per unit length cannot be assumed to represent compact material, as the distribution in the remaining two axes is not described. For an axial mass plot along the  $x$ -axis, a high value could be down to a particular mass clustered in a small portion of the  $y$ - and  $z$ - axes (a high local density), or extremely broadly along those axes (no high local densities). In determining to where material is converging and where star formation is most probable, it is preferable to indicate where high density is, not simply high mass per unit length.

One slight postscript to the statement that ‘mass per unit length is not preferable’, is any instance in which the extent along the remaining two axes is known or limited.

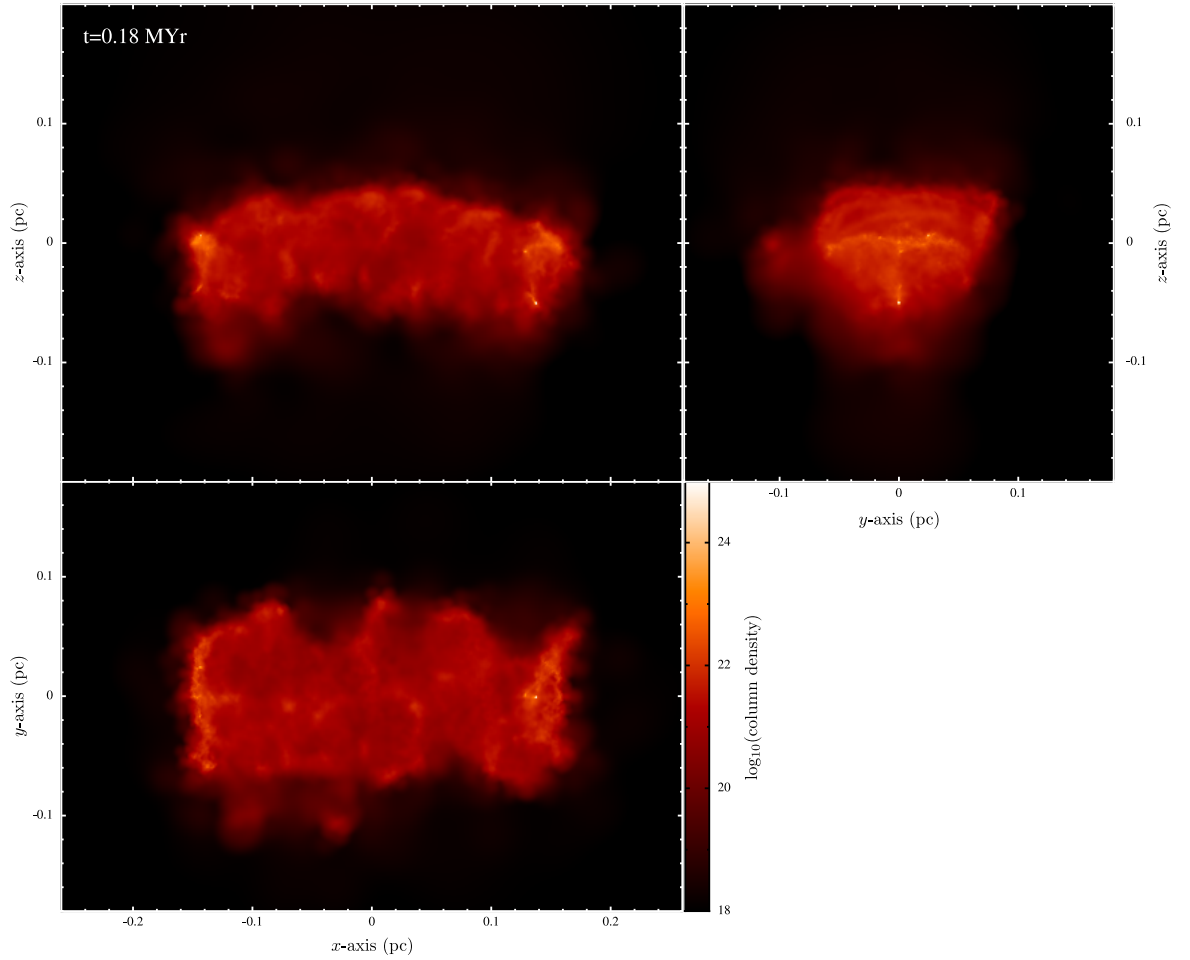


Figure 4.4: Each of three axial projections for a cloud with initial conditions  $\gamma = 2$ ,  $n = 1200 \text{ cm}^{-3}$  and  $M = 30 M_{\odot}$ . Column density is in  $\text{cm}^{-2}$ .

For initial conditions of an prolate molecular cloud, mass per unit length can provide information of the clustering of material. However, this is due to the constrained geometry and uniform density.

The method represents the desired cloud properties by binning the SPH particles along the cloud’s major axis, with each particle contributing its *density* towards the bin total, rather than mass. This represents an effective mass per unit length weighted by density (as each SPH particle is of the same mass). This will produce a ‘mean SPH particle density per unit length’ if it were divided by the width of the bin, though it is more convenient not to do so (the values remain related to the actual densities involved) leaving the values ‘mean SPH particle density per bin’. This is a clearly non-physical value, and does not represent any ‘real’ property of the simulated cloud, it is a purely statistical *impression* of high density material distribution.

### 4.3.1 BIN RESOLUTION

A key factor to consider in determining whether the binning method is suitable is whether each SPH particle can be counted as being *in* a particular bin. Being, as they are, a description of a distributed fluid packet, rather than a point, a choice for determining whether or not they can fall inside a bin is whether the majority of their smoothing kernel is inside it. This would prohibit cases in which the bins were thinner than a particle’s smoothing length, or some proportion of it.

This situation extends to create the issue that you have the clear limiting factor of, as the bin widths tend towards zero, the plot will be isolated individual spikes at the exact axial location of the SPH particles, with the height of each spike the density of the SPH particle. This would be the same (albeit without the vertical lines) as plotting the SPH particle densities with  $x$ -axis position. This is shown in Figure 4.5 and could be thought of as a suitable representation of the density distribution, however it prohibits the presentation of multiple results simultaneously.

Presented in Figure 4.6 are six different bin resolutions evaluating the same cloud. The cloud used for comparison is the same as in Section 4.2.2, with initial properties of:  $\gamma = 2$ ,  $n = 1\,200\text{ cm}^{-3}$  and  $M = 30 M_{\odot}$ , subjected to a EUV flux of  $2 \times 10^9\text{ cm}^{-2}$ . The axial binning evaluations were performed along the  $x$ -axis, always between plus and minus 0.78 pc, the initial semi-major axis of the cloud.

Values for the bin widths for these resolutions vary from 0.16 pc at 10 bins down to 0.0004 pc at 4000 bins. However, it is also important to consider that density and smoothing length are related by  $h \propto n^{-1/3}$ , and that, with a weighting factor based on density, only dense particles (therefore those with the smallest smoothing lengths) contribute to any noticeable degree. This means that even for bins widths larger than

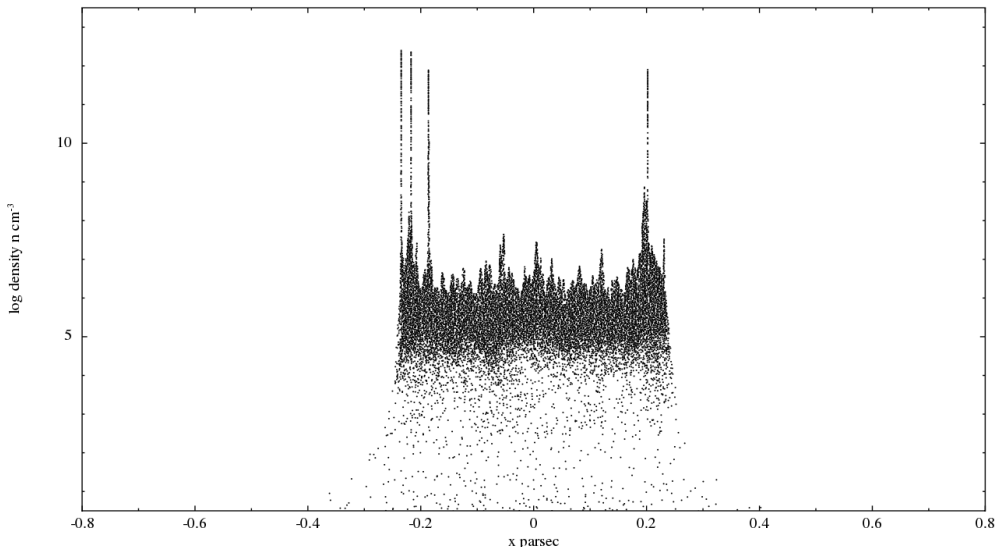


Figure 4.5: Raw particle density properties with position along  $x$ -axis for the cloud of  $\gamma = 2$ ,  $n = 1\,200\text{ cm}^{-3}$  and  $M = 30 M_{\odot}$ .

the smallest smoothing lengths, particles with smoothing lengths greater than the bin widths can simply be discarded with almost no difference to the resulting plot. This is only untrue in areas of the plot which are very sparsely populated (towards and beyond the edges of the cloud), or extremely high bin resolutions. A presentation of the same collection of resolutions, but with a filter applied to sample only those SPH particles whose smoothing length is less than the width of the bin ( $h < x_{\text{bin}}$ ) is in Figure 4.7. The qualitative shapes of the plots are the same for all resolutions bar 4000, in which only the high density core associated particles are able to be selected, leading to several isolated peaks and zero elsewhere. A direct comparison of the 150 bin resolution with and without the selection filter applied is shown in Figure 4.8.

A cursory analysis of the plots in Figure 4.6 illustrates that the underlying profile is obtained for all of the investigated resolutions, with varying degrees of detail. Characteristic values remain the same ( $\approx 10^{10}\text{ cm}^{-3}$  for the peaks and  $\approx 10^6\text{ cm}^{-3}$  for the bulk cloud), which would not be the case for a ‘mean density per unit length’ formulation.

An alternative is to produce the same style of plot but rather than calculate the mean density for each bin, use the maximum. This would produce a plot which would effectively be an outer boundary around the particles displayed in Figure 4.5. Figure 4.9 displays again the mean particle density per bin for 150 bins (Figure 4.6) along with the equivalent with maximum particle density per bin; superimposed over the top of the plot of raw SPH particle densities with  $x$ -position. The outer bound provided by the maxima bins are extremely sensitive to the densities of individual particles; the

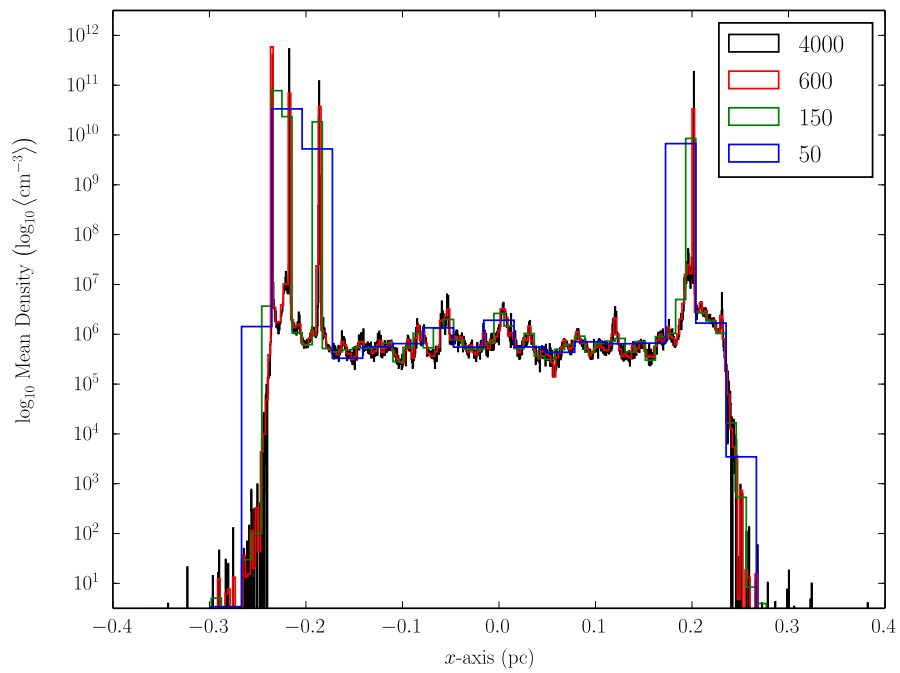


Figure 4.6: Comparison of varied bin resolution for axial density plots, the minimum, mean, median and maximum smoothing lengths for the cloud were:  $1.87 \times 10^{-5}$ , 0.060 1, 0.002 7 and 0.741 6 pc; where bin widths are  $\approx 0.016$ , 0.005, 0.001 and 0.000 2 pc for 50, 150, 600 and 4 000 respectively. Compare with column density plots for the same cloud in Figure 4.4.

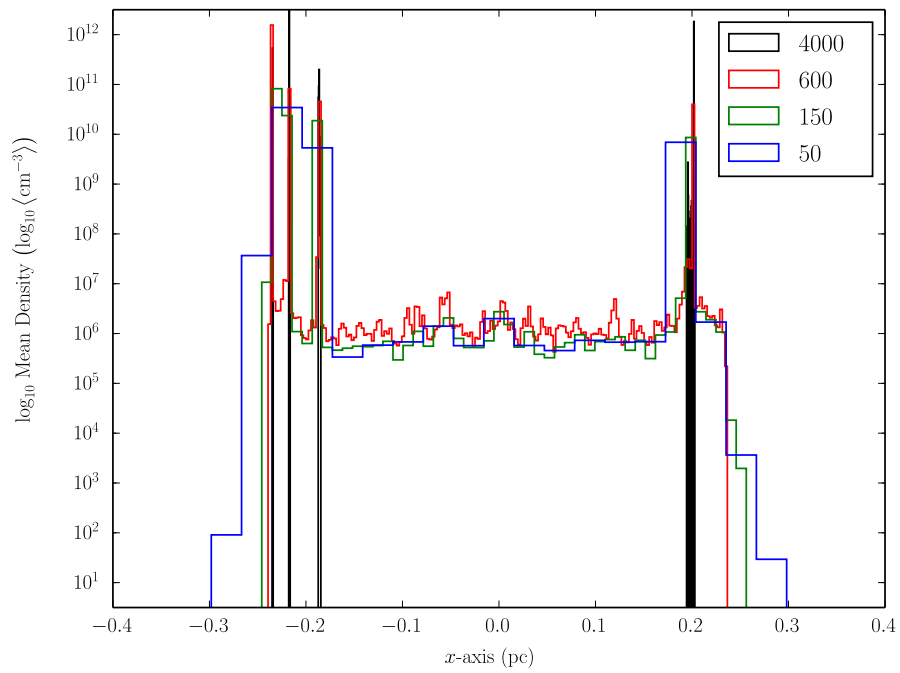


Figure 4.7: Equivalent of Figure 4.6 with a filter to only sample those SPH particles with  $h < x_{\text{bin}}$ . Problematic zero-weighted bins only occur at the high resolution configuration, the other profiles are qualitatively identical to those without the filter. See Figure 4.8 for a direct comparison.

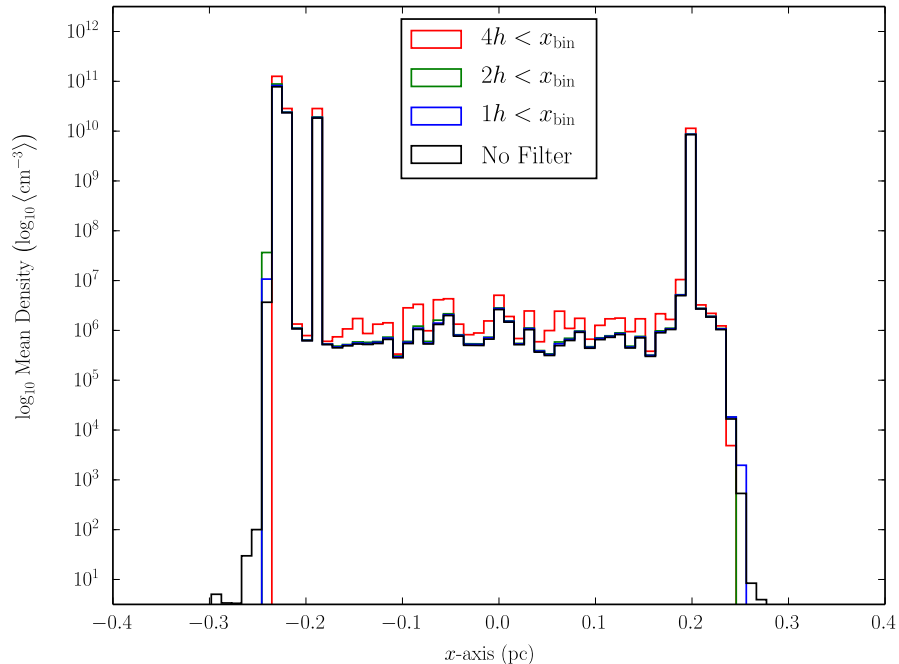


Figure 4.8: Direct comparison of the 150 bin resolution plots without and with the  $h < x_{\text{bin}}$  SPH particle filter applied.

mean bins smooth out this effect, and give a better idea of the significance of each apparent ‘peak’ as weighted by both the density and quantity of particles. The result, for the mean bin method, is a compromise between the sensitive taking of maxima, and a mass-per-unit-length plot which would show only the distribution of material, as opposed to whether or not it was compact, high density material.

## 4.4 EVOLUTION OF HIGH MASS PROLATE CLOUDS

Nelson and Langer (1997) investigated the formation of high density spindles from prolate ellipsoidal clouds subjected to isotropic Far-Ultraviolet (FUV) interstellar background radiation. Clouds of several masses were investigated, 100, 150 and 200  $M_{\odot}$ , all of initial axial ratio,  $\gamma = 2$ , and density  $n = 100 \text{ cm}^{-3}$ , with an FUV flux of one Habing unit (Habing, 1968). In order to observe how the evolution of the same set of clouds are altered when an EUV radiation field is introduced, this initial batch of tests is based on these pre-existing configurations and notated A, B and C for the 100, 150 and 200  $M_{\odot}$  clouds respectively. Table 4.3 describes the set of initial properties for these clouds in full.

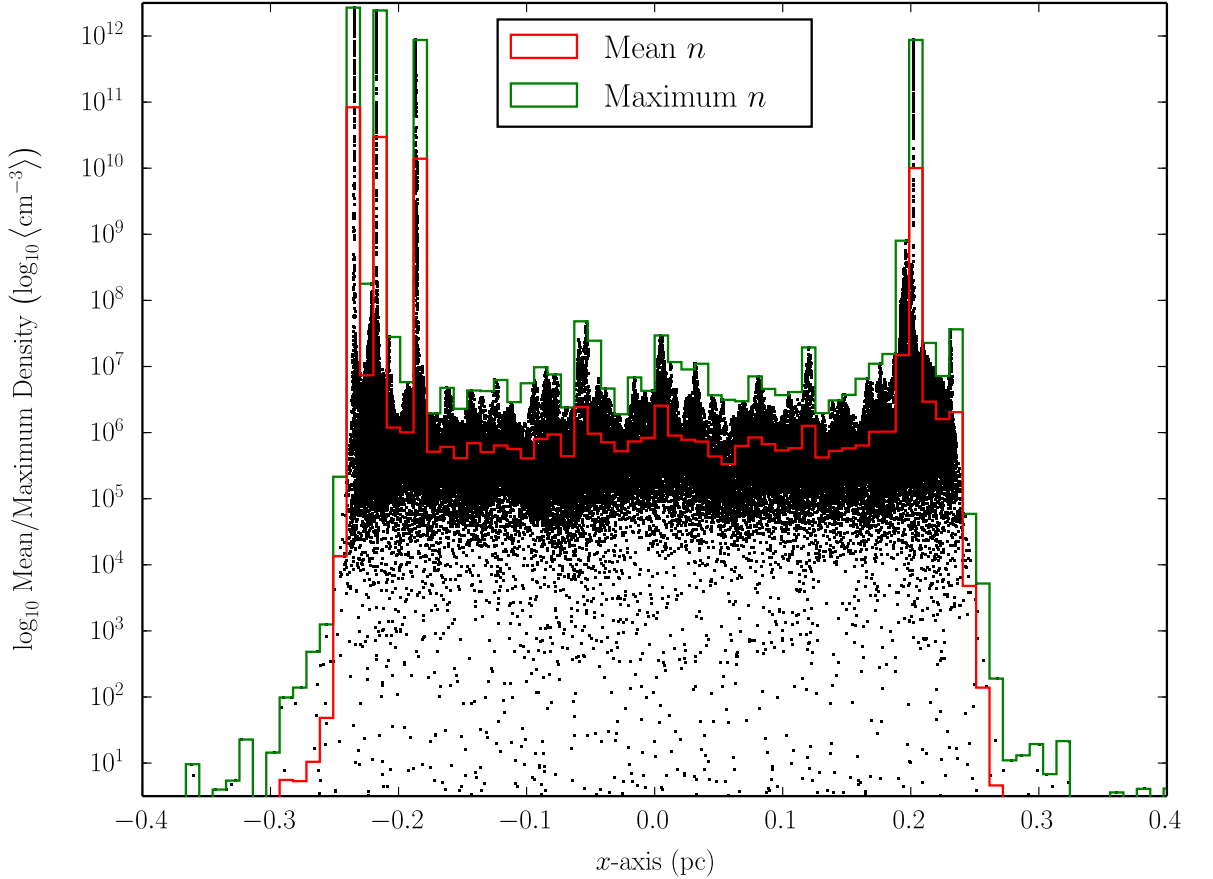


Figure 4.9: Comparison of the mean SPH particle density for each bin (red) and the maximum SPH particle density per bin (green) for the 150 bin resolution plots.

Name	Mass ( $M_{\odot}$ )	$a$ (pc)	$a_{\text{crit}}$ (pc)	$\frac{d_{\text{EUV}}}{10^2}$	Particles
A	100	2.68	1.58	12	100 000
B	150	3.07	2.37	10	150 000
C	200	3.38	3.16	9.5	200 000

Table 4.3: The parameters of the three prolate clouds of similar initial uniform density of  $100 \text{ cm}^{-3}$  and axial ratio  $\gamma = 2$ . They have particle mass resolution of  $10^{-3} M_{\odot}$  per SPH particle (the resolution requirement determined in Section 3.3.1). The columns, from left to right, are the name, mass, major axis length  $a$ , the critical major axis length and the ionising radiation penetration depth parameter (calculated with Equations 4.2 and 3.36).

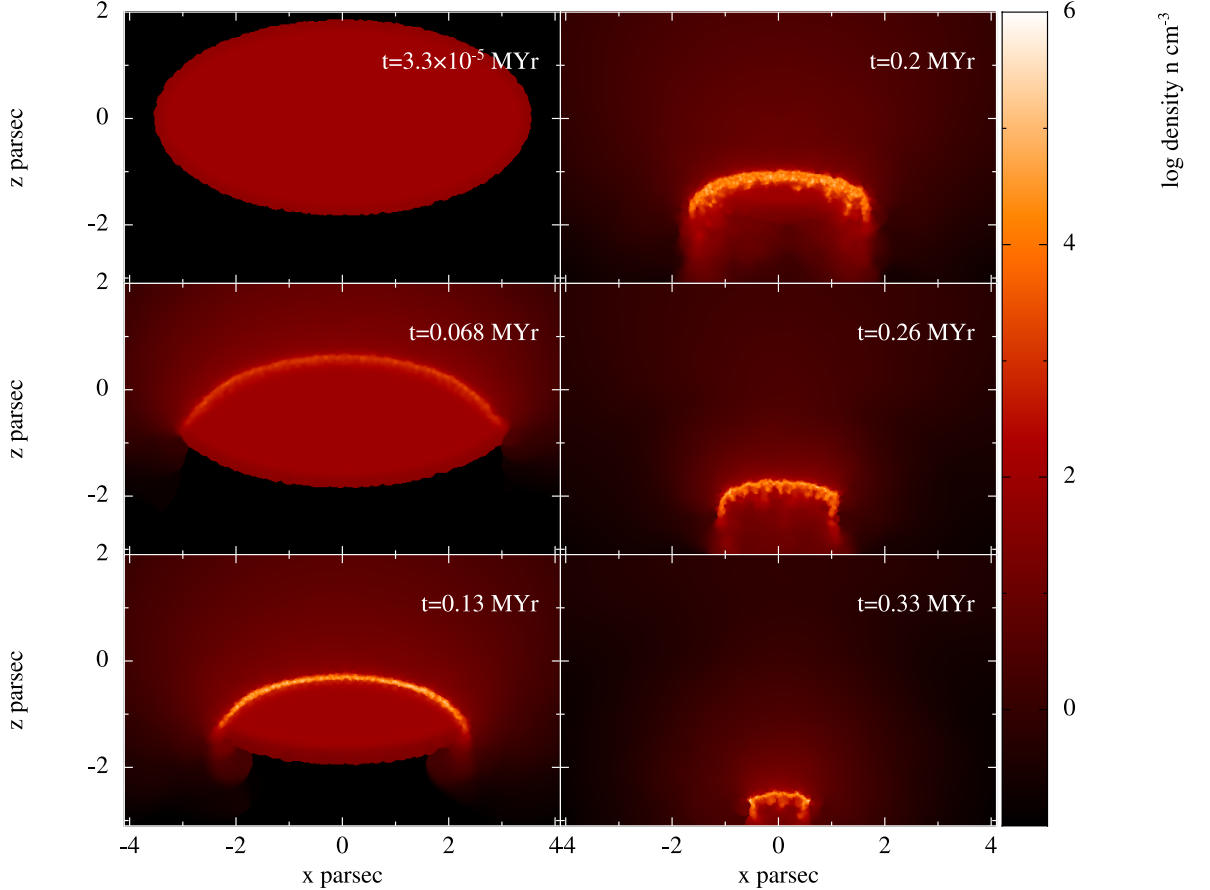


Figure 4.10: Sequence of the evolution of the mid-plane cross-sectional number density for Cloud C, of initial density  $100 \text{ cm}^{-3}$  and  $\gamma = 2.0$ ; subject to an isotropic interstellar background radiation and ionising radiation. Time sequence is top to bottom then left to right.

#### 4.4.1 BASIC EVOLUTIONARY FEATURES

All three clouds in this group of tests exhibit similar basic characteristics in their evolutions. Using cloud C as the exemplar model, it is possible to examine these in more detail. Figure 4.10 shows snapshots of the evolution of this cloud covering the initial conditions up to the formation of  $n_{\text{max}} \approx 10^{13} \text{ cm}^{-3}$  regions at  $t = 0.33 \text{ Myr}$ .

As time progresses from the start of the simulation, the ionisation heating induced shock propagates into the cloud through the upper half ellipsoidal surface (the star-facing side), which is much stronger than that surrounding the lower half ellipsoidal surface caused by FUV only. The shocked thin layer is very distinctive when  $t = 0.13 \text{ Myr}$ . During this time, the overall dimensions of the cloud greatly decreases due to the photo-evaporation. With the shock propagating into the neutral cloud, the condensed thin shell starts to fragment at  $t = 0.2 \text{ Myr}$  due to its gravitational instability. The density of the gas between the fragments is lower than that in the fragments and are pushed into

the cloud by the high pressure in the HII region, forming spike-like micro-structures. These micro-structures have higher density than the neutral interior of the cloud, but do not play significant role over the evolution of the whole system because of their very small volume. At 0.33 Myr, the remaining material has evolved to a clumpy linear structure of  $\approx 1$  pc in length, along which multiple condensed cores are embedded. The peak density increases from  $10^2 \text{ cm}^{-3}$  at the beginning of the simulation to  $\approx 10^{13} \text{ cm}^{-3}$  at  $t = 0.33$  Myr.

Using the axial density profile method of analysis described in Section 4.3, Figure 4.11 shows that profile for each of clouds A, B and C, along with the profile for the same clouds without exposure to EUV radiation for comparison (independently run simulations matching those in Nelson and Langer (1997)). The green line profiles in the two panels of this figure describe the axial density profile of cloud C at its final timestep of  $t = 0.33$  Myr (lower panel) and the version without EUV at its final timestep of  $t = 3.03$  Myr (upper panel). The most obvious feature of the comparison of these two profiles is that the EUV radiation for cloud C induces the formation of clearly separated density peaks, mostly connected by a lower density structure; whereas its FUV-only counterpart has all of its high density structure in a single, fragmented region concentrated at the centre of mass. It is important to remind that an apparent high density peak in axial density plots does not necessarily correspond to a single high density core; multiple cores may be present at different  $y$  and  $z$  positions within the same  $x$ -axis bin. Similarly, apparently continuous features (such as the broad plateau for the FUV-only versions of clouds A, B and C) do not necessarily represent continuous distributions of material with those densities. Multiple, high density peaks separated by distances of the order of, or smaller than, the bin widths are not resolved. This is exactly the case with the upper panel of Figure 4.11, where fragmentation of a spindle structure formed along the semi-major axis of the clouds has produced narrowly separated, high density cores along its length. This mode of collapse is that which was observed and noted by Nelson and Langer (1997).

Whilst the scale and extent of high density structure formation is substantially smaller in cloud C than its FUV-only counterpart, the structure and densities it does create are formed on a timespan of only  $1/20^{\text{th}}$  of the FUV-only case. The weaker collapse triggered by the FUV radiation is slower and, importantly, results in the evaporation and loss of far less material than when EUV affects a cloud. In this instance the FUV is also isotropic, with this symmetric collapse resulting in the containment and collection of material more efficiently (with respect to mass) than EUV.

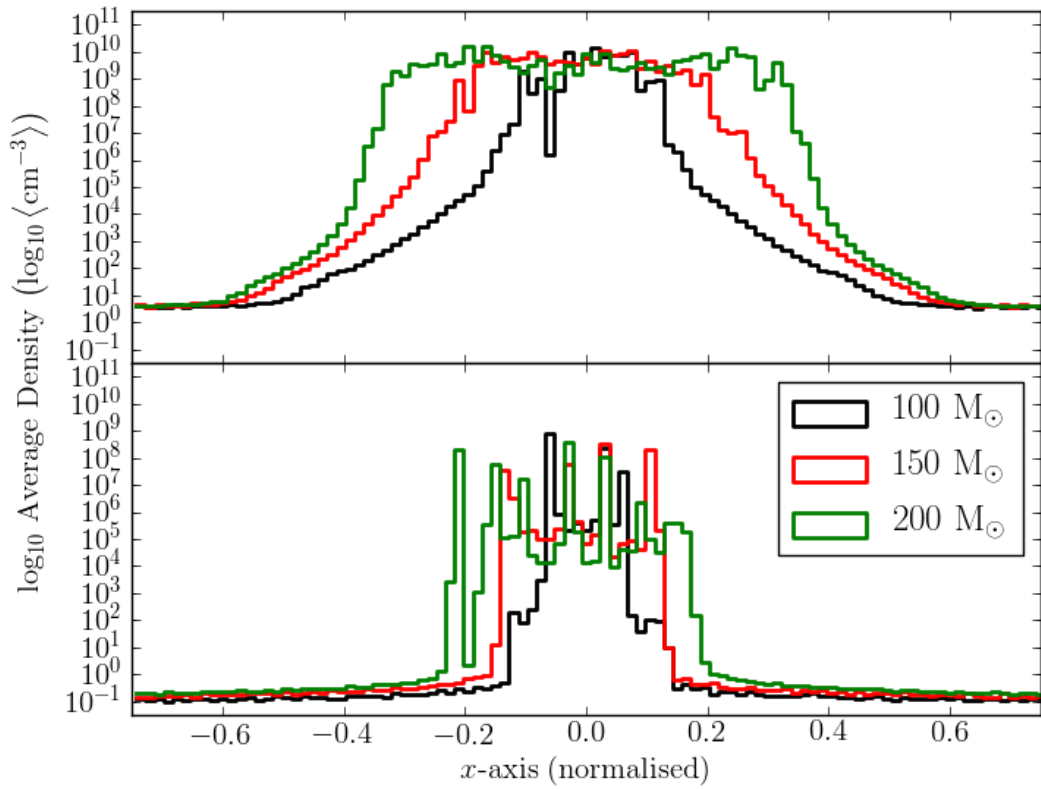


Figure 4.11: Mean hydrogen number density along the semi-major axis of three prolate clouds of initial density  $100 \text{ cm}^{-3}$  and varying masses. The upper panel displays the three clouds subject to an isotropic FUV radiation only; the lower panel shows the same three clouds subject to both FUV and EUV radiation fields. The time scales for the clouds in frame (a) are 3.10, 3.02 and 3.03 Myr for the clouds of  $100$ ,  $150$  and  $200 M_{\odot}$  respectively; and 0.33 Myr for *all* of the clouds in frame (b).

#### 4.4.2 COMMON AND DISSIMILAR EVOLUTIONARY FEATURES

The basic appearance of clouds A and B during their evolution is the same as that of cloud C, albeit at size scales varying according to their initial semi-major axes. Furthermore, all clouds evolve to their final collapse state at the same time of  $t = 0.33$  Myr.

It is apparent that the high density cores in all three simulated clouds including EUV radiation scatter over the final clumpy linear structure unlike their corresponding non-EUV simulations. In the FUV-only cases the high density material is more evenly distributed along the final spindle structure. Also apparent in Figure 4.11 is that more gas material remains in the linear structure in the simulation without EUV radiation than that with EUV radiation. This is because the EUV radiation flux is more than 20 times more energetic than the interstellar background FUV radiation, the consequent photoevaporation effect is stronger in a similar proportion. Furthermore, the number of distinctive peaks increases with the initial mass of the cloud. This is understandable as the major axis is longer in higher mass clouds to keep the same initial density, accompanied with an increase in mean mass per unit length. Fragmentation of a longer structure produces more individual fragments.

These highly condensed peaks can be considered to be potential sites for new star formation. The scattered distinctive high density cores over the remaining linear structure implies that EUV radiation may be able to trigger a chain of stars to form in the examined prolate clouds at an HII boundary in less than 0.5 Myr. In contrast, the same prolate clouds further away from a massive star are more likely to form a condensed filamentary structure under the effect of the FUV only radiation over a period of a few Myr.

#### 4.4.3 EFFECTS OF VARIED INITIAL DENSITY AND EUV FLUX

To obtain a broader view of the high mass cloud simulation in an extended parameter space, an additional set of simulations were conducted to observe the changes to the evolution of the  $200 M_{\odot}$  clouds subject to variation in density  $n$  (D series simulations) and incident EUV flux  $F_0$  (E series simulations). These tests, along with cloud C for reference, have their properties tabulated in Table 4.4. For each parameter,  $n$  and  $F_0$ , three additional simulations were run.

##### 4.4.3(a) D SERIES SIMULATIONS - VARIED INITIAL DENSITY

Presented in Figure 4.12 are the axial mean density distributions along the linear structures at the final timestep. The plot for cloud C is also included for comparison.

Name	Density ( $\text{cm}^{-3}$ )	$a$ (pc)	Flux ( $\text{cm}^{-2} \text{s}^{-1}$ )	$d_{\text{EUV}}$ ( $10^{-2}$ )	Time (Myr)
C	100	3.38	$10^9$	9.5	0.334
D1	400	2.13	$10^9$	0.93	0.327
D2	600	1.86	$10^9$	0.48	0.288
D3	1,200	1.48	$10^9$	0.15	0.233
E1	100	3.38	$10^7$	0.095	0.966
E2	100	3.38	$10^8$	0.95	0.776
E3	100	3.38	$8 \times 10^9$	76	0.268

Table 4.4: The parameters of the further exploration high mass prolate clouds. The columns, from left to right, are the name, density, major axis length  $a$ , incident EUV flux and the ionising radiation penetration depth parameter. Time indicates the final simulation time. Clouds D1-3 are the additional density-varied tests, and clouds E1-3 are the additional incident flux-varied tests.

It is interesting to see that with increasing initial density, the condensed cores gradually occur closer to the two foci, the two ends of the final filament structure. This is because the ionising radiation penetration depth parameter decreases with the increase of the initial density, the mode of the evolution of the cloud changes from ‘linear’ to ‘foci’ convergence. These modes of convergence can be described as the scenarios in which either the initial compressed shock causes superposition of sufficiently high densities that core formation occurs at regions where the shock surfaces are focused (‘focus’/‘foci’ convergence), or this does not directly result in sufficient densities, but the subsequent, turbulent, flattened ‘linear’ structure results in secondary high density regions through complex motion and cooling.

#### 4.4.3(b) E SERIES SIMULATIONS - VARIED INITIAL FLUX

The four panels in 4.13 illustrate the axial mean density distributions, in simulations with a cloud of the same initial conditions as cloud C, but different EUV radiation fluxes; notated as clouds E1-3 in 4.4. The distribution of the condensed cores gradually changes from the two-foci concentrated to scattered over the whole filament, with the increase of the EUV radiation flux, i.e., increase of  $d_{\text{EUV}}$ . The mode of the evolution of the cloud changes from foci to linear convergence.

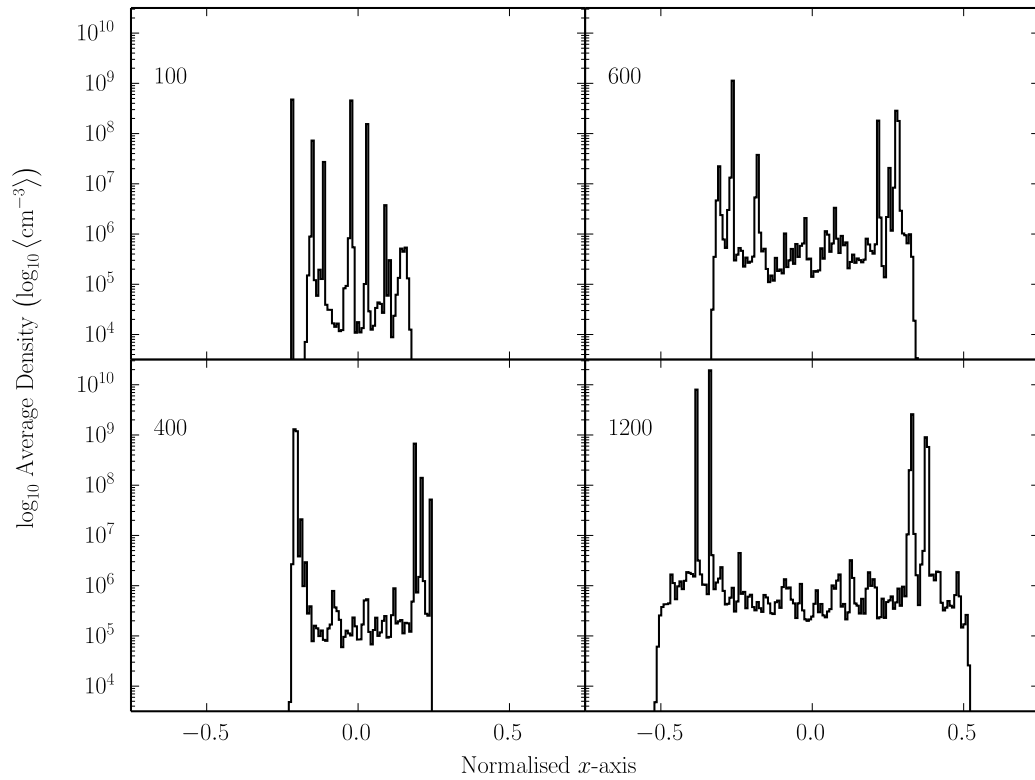


Figure 4.12: The axial mean number density profile at the final timesteps in four molecular clouds of same mass of  $200 M_{\odot}$ , and  $\gamma = 2$ , but different initial densities as shown in the top-left corner in each panel. The densities are in units of  $\text{cm}^{-3}$ . The times at which the simulations ended are shown in Table 4.4.

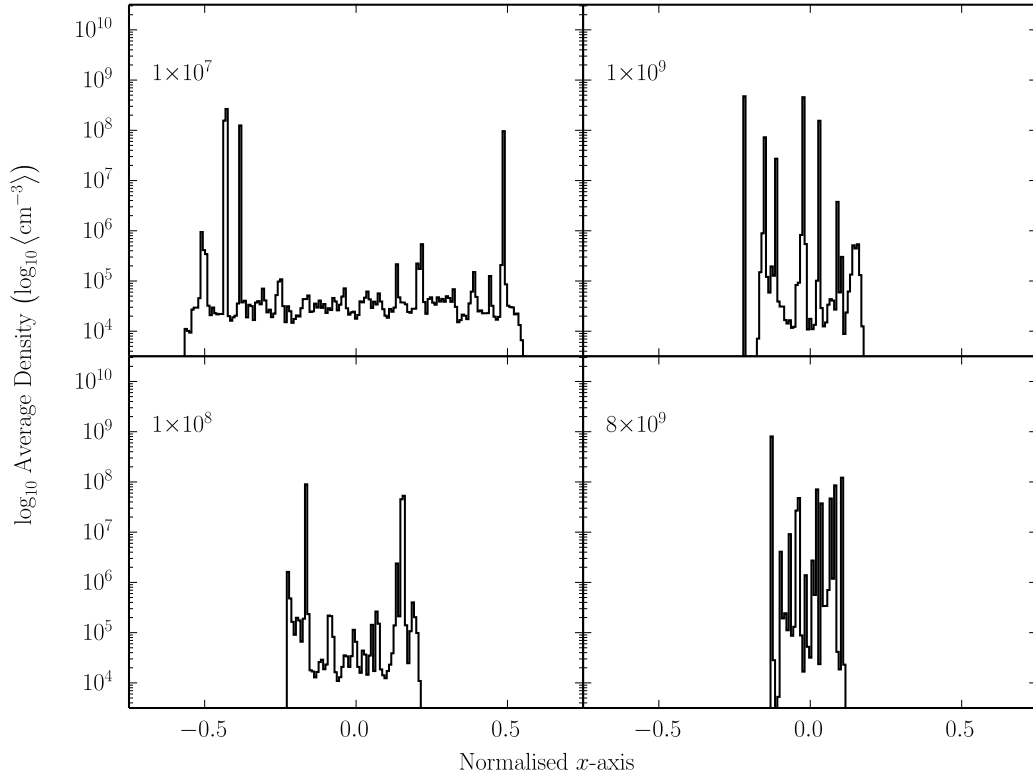


Figure 4.13: The axial mean number density profile at the final timesteps in four molecular clouds of same mass of  $200 M_{\odot}$ ,  $\gamma = 2$  and initial density of  $100 \text{ cm}^{-3}$ , but under the effect of different EUV radiation fluxes as shown in the top-left corner in each panel. The fluxes are in units of  $\text{cm}^{-2} \text{ s}^{-1}$ . The times at which the simulations ended are shown in Table 4.4.

## 4.5 EVOLUTION OF $30 M_{\odot}$ PROLATE CLOUDS

---

The prolate clouds in this section have masses  $M = 30 M_{\odot}$ , two initial densities of  $n = 600$  and  $1200 \text{ cm}^{-3}$ , and varied initial geometrical shapes defined by the axial ratio parameter  $1 \leq \gamma \leq 8$ . These are categorised into two groups, G1 and G2, as listed in Table 4.5. Their initial major axes are all larger than their  $a_{\text{crit}}$ , which means they are all stable against purely gravitational collapse. There are 19 clouds in each group and are numbered from 1 to 19. The identification for each cloud is notated as G1(No.) and G2(No.), e.g. the 5th cloud in the G2 series,  $\gamma = 2.0$ , is named as G2(5). Each of the simulations for the 38 clouds was run with  $10^5$  SPH particles, leading to a mass resolution of  $3 \times 10^{-4} M_{\odot}$  per SPH particle, meeting the mass resolution requirements imposed by the convergence testing in Section 3.3.1.

### 4.5.1 EFFECTS OF VARIED AXIAL RATIO AT $1200 \text{ cm}^{-3}$

The morphological evolutions of the clouds in the G2 group bear many similarities; in the same manner as Section 4.4.1, one cloud from G2 is taken as the exemplar to examine in detail, and with which to describe the common features of the evolutionary sequences of the G2 series as a whole. The cloud for this purpose is G2(5), initial axial ratio  $\gamma = 2$ , the same ratio as the high mass clouds.

The six panels in Figure 4.14 describe the evolution of the cross-sectional number density in the mid-plane ( $x - z$  and  $y = 0$ ) of G2(5). The morphological evolution appears to follow the general picture described by the RDI mechanism. A condensed gas layer at the upper ellipsoidal surface has formed within 0.11 Myr. The density inside the shocked layer increases as it propagates inwards. At  $t \approx 0.19$  Myr, the highly condensed layer fragments, creating a curved clumpy filamentary structure with condensed cores embedded. The corresponding overhead ( $x - y$ ) column density view of the evolution of the cloud displayed in Figure 4.15, further confirms the formation of the filamentary structure and its fragmentation. It can be seen that the filamentary structure forms as a high-density ‘spine’ aligned with the semi-major axis at  $t = 0.11$  Myr. The material in the two hemispheres is seen converging to the major x-axis, and material from negative  $y$  heads toward the positive  $y$  direction, and vice-versa. At  $t = 0.15$  Myr, this thin and long structure starts fragmentation. Some of the fragments disperse off the major axis, and a broadly zig-zag fragment-core structure is left at  $t = 0.19$  Myr.

The red dotted line in Figure 4.16 describes the axial mean density distribution at  $t = 0.19$  Myr. It shows distinctive high density peaks forming at the two ends of the fila-

No.	$\gamma$	$a_{\text{crit}}$	G1		G2	
			$a_{600}$	$d_{\text{EUV}}$	$a_{1200}$	$d_{\text{EUV}}$
1	1.00	0.052	0.623	0.713	0.494	0.225
2	1.25	0.060	0.722	0.770	0.573	0.242
3	1.50	0.067	0.816	0.817	0.648	0.257
4	1.75	0.073	0.904	0.860	0.718	0.271
5	2.00	0.079	0.988	0.900	0.784	0.283
6	2.25	0.084	1.069	0.935	0.849	0.294
7	2.50	0.039	1.147	0.969	0.910	0.305
8	2.75	0.093	1.222	1.001	0.970	0.315
9	3.00	0.097	1.295	1.030	1.028	0.324
10	3.25	0.101	1.366	1.057	1.084	0.333
11	3.50	0.104	1.435	1.084	1.139	0.341
12	3.75	0.107	1.503	1.109	1.193	0.349
13	4.00	0.110	1.569	1.133	1.245	0.357
14	4.50	0.116	1.697	1.179	1.347	0.371
15	5.00	0.121	1.820	1.221	1.445	0.384
16	5.50	0.126	1.940	1.260	1.540	0.397
17	6.00	0.130	2.056	1.297	1.632	0.408
18	7.00	0.138	2.278	1.366	1.808	0.430
19	8.00	0.145	2.490	1.428	1.977	0.450

Table 4.5: Parameters of two groups of molecular clouds of same mass but different initial densities of 600 and 1 200  $\text{cm}^{-3}$ . From left to right, columns 1-3 are the number identity, axial ratio and the critical semi major axis defined by Equation 4.2 for both G1 and G2 clouds. Columns 4-5 are the major axis and  $d_{\text{EUV}}$  defined by Equation 3.36 for the G1 clouds, and columns 6-7 are the same parameters for the G2 clouds. All of the semi-major axes and critical semi-major axes are in units of pc and  $d_{\text{EUV}}$  values as percentages.

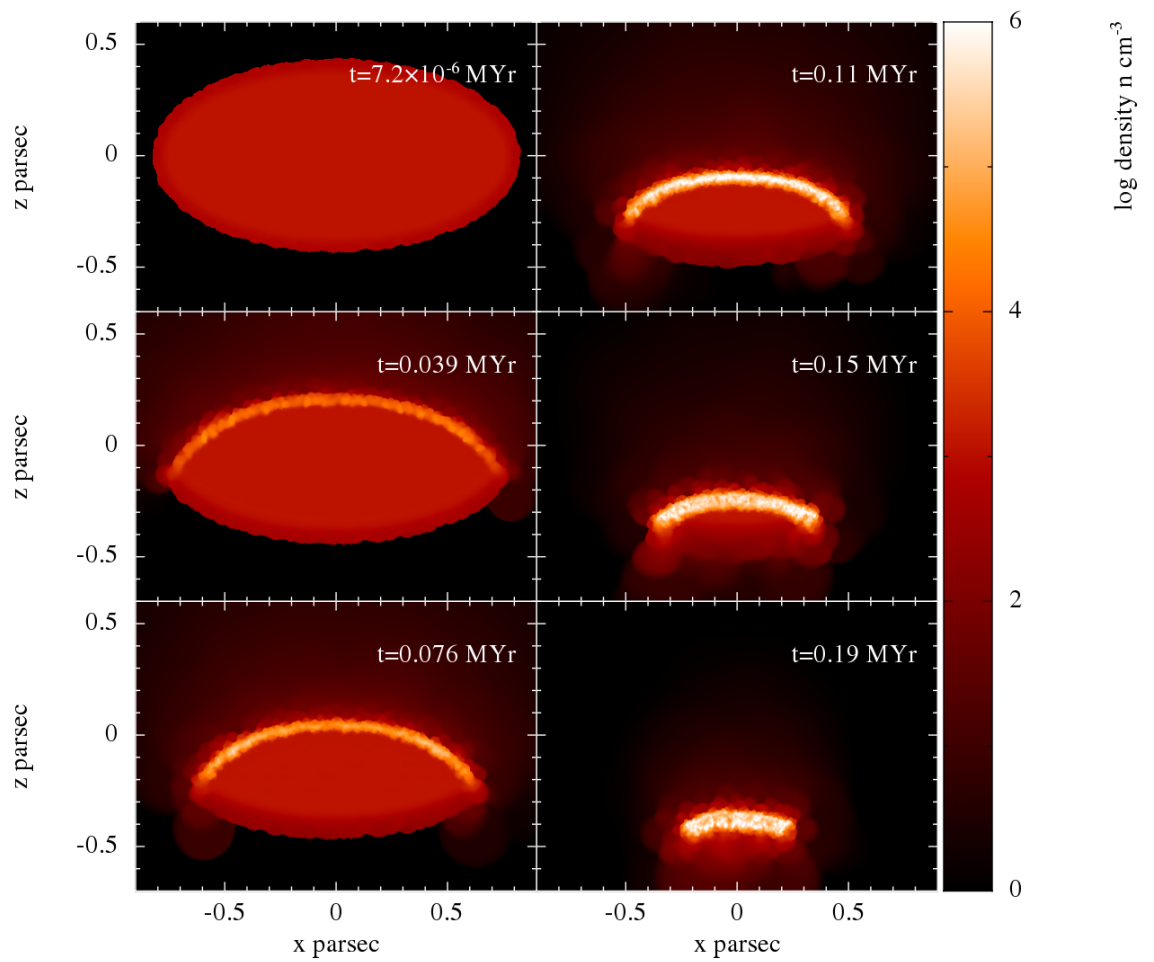


Figure 4.14: Evolution of the cross-sectional density in the mid-plane for the prolate cloud G2(5) over 0.19 Myr. Time is displayed in the upper right of each panel. The order of time evolution is top to bottom and then left to right.

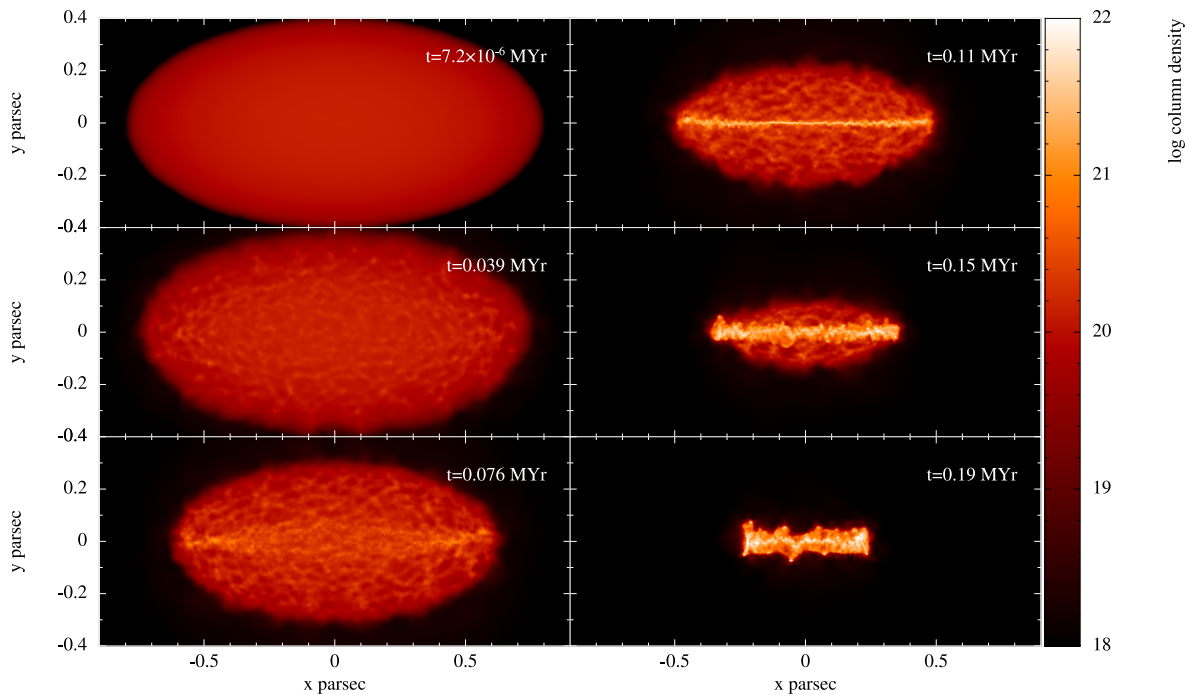


Figure 4.15: Evolution in the  $xy$ -plane projection (column density) of the prolate cloud G2(5). Time is displayed in the upper right of each panel. The development of a linear filament-like structure along the ‘spine’ of the cloud can be seen to have occurred by 0.11 Myr; its fragmentation into zig-zagging, thinner filaments visible at the final time, 0.19 Myr. Column density is in  $\text{cm}^{-2}$ .

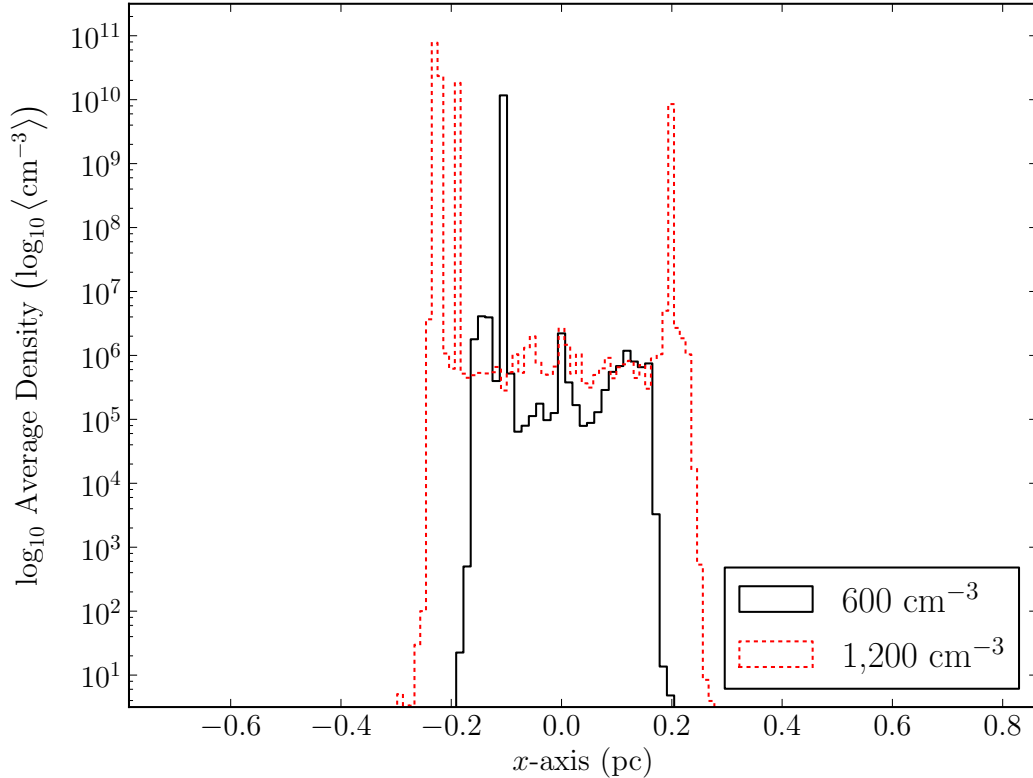


Figure 4.16: The axial mean number density profile for clouds G1(5) ( $600 \text{ cm}^{-3}$ ,  $\gamma = 2$ ) in solid black and G2(5) ( $1\,200 \text{ cm}^{-3}$ ,  $\gamma = 2$ ) in dashed red. G1(5) is at  $t = 0.22 \text{ Myr}$  and G2(5) at  $t = 0.19 \text{ Myr}$ .

mentary structure. The penetration depth parameter of cloud G2(5) is  $d_{\text{EUV}} = 0.283 \%$  as shown in Table 4.5, which means that EUV radiation induced shock dominates the evolution of G2(5) and enhances the self-gravity of the cloud G2(5) so that most of remaining condensed gas is driven toward the two foci of the cloud over its evolution (foci convergence).

Figure 4.17 displays the cross sectional density distribution in the mid-plane for nine representative clouds in the G2 group, at the end of the simulation. The curvature of the final morphology of the structure formed decreases with the increase of the initial axial ratio  $\gamma$ . An initially spherical cloud ( $\gamma = 1$ ) evolves to a type B BRC with a highly condensed core forming at its head in the shortest time of  $0.13 \text{ Myr}$ . Clouds of  $1 < \gamma \leq 1.5$  evolve to a type A BRC with a dense core forming at its head in a longer time, between  $0.13$  and  $0.17 \text{ Myr}$ . In the clouds of  $1.5 < \gamma \leq 3$ , a bright rimmed, curved and clumpy filament forms with cores embedded along the linear structure over increasing timescales, with increasing  $\gamma$ , up to  $0.21 \text{ Myr}$ . The time for core collapse for a cloud increases when the foci changes from one to two. However, in the clouds of initial

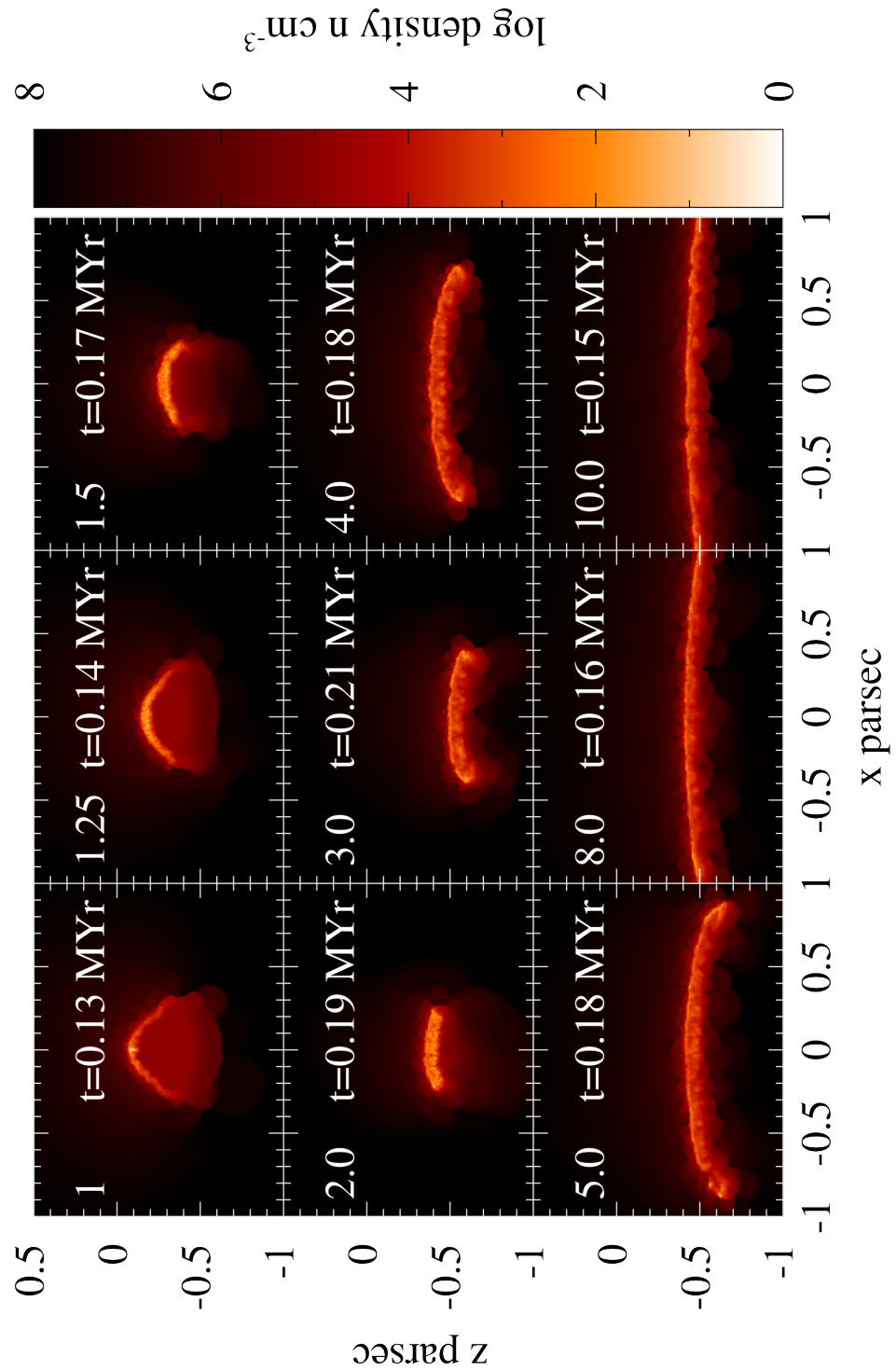


Figure 4.17: The cross-sectional density in the mid-plane for the 9 representative prolate clouds in the G2 series at their final time step. The number in the upper-left of each panel is the axial ratio  $\gamma$ , and the number in the upper right is the evolutionary time.

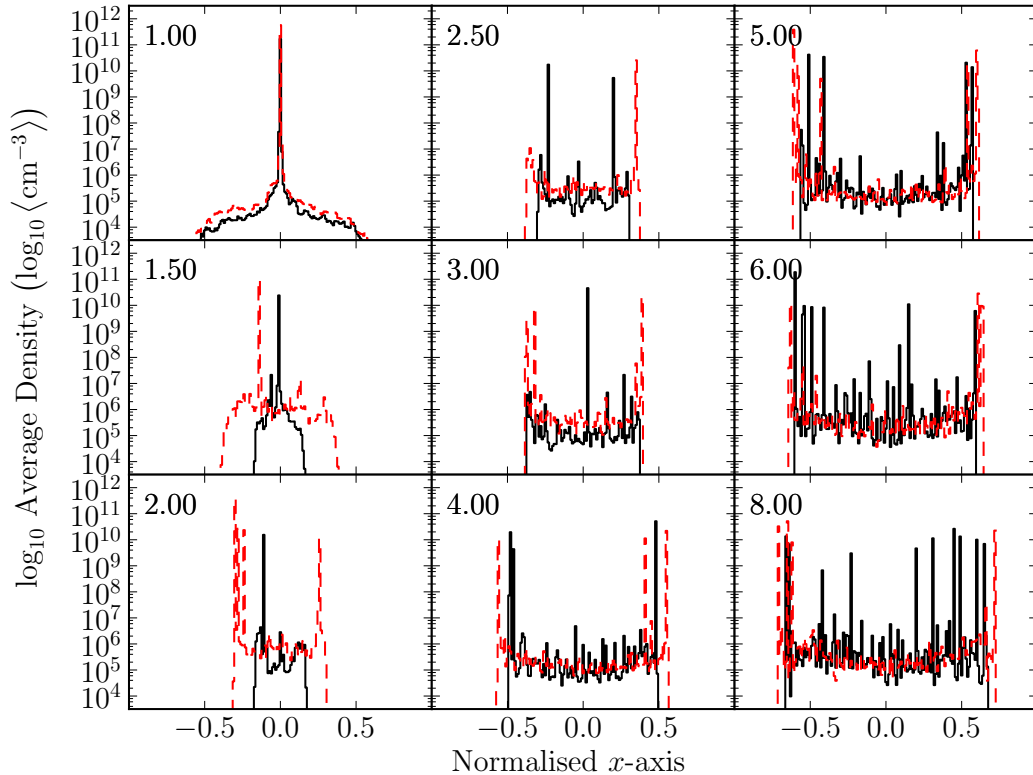


Figure 4.18: The axial mean density over  $x$ -axis (normalised to the initial cloud semi-major axis) for nine of the G1 (black solid line) and G2 (red dashed line) series clouds (indices 1, 3, 5, 7, 9, 13, 15, 17 and 19). The number in the upper left of each panel is the  $\gamma$  value of the clouds.

$3 < \gamma \leq 10$ , the core formation time decreases from 0.21 to 0.15 Myr with increasing  $\gamma$ . This may be because as the clouds with  $\gamma > 3$  become increasingly elongated, the converging gas material has ever shorted distances to reach their two foci. Therefore spherical and highly ellipsoidal clouds have shorter core formation times than those of the mid range of axial ratios (this can also be seen in Figure 4.22).

It is also possible to look at the axial mean density profiles of a set of clouds in the G2 group. The red dashed lines in Figure 4.18 reveal the location of the high density regions triggered by the EUV radiation flux for 9 representative clouds selected from the G2 group (the axial ratio for each is displayed in the upper left of the panel). An initially spherical cloud G2(1) converges to its gravitational centre to form a single dense peak as shown in the first panel. As axial ratio increases, high density cores begin to form at the two ends of the final structures. The G2 group clouds all have  $d_{\text{EUV}} < 0.5\%$  and therefore all collapse in the mode of foci convergence.

### 4.5.2 EFFECTS OF VARIED AXIAL RATIO AT $600 \text{ cm}^{-3}$

The clouds in the G1 series have an initial density of half that of the G2 group,  $600 \text{ cm}^{-3}$ . Their EUV radiation flux penetration parameters are in the range  $0.713\% \leq d_{\text{EUV}} < 1.428\%$ , higher than that of any cloud in the G2 group.

The morphological evolutions of G1 and G2 group clouds are similar. Clouds of  $\gamma$  equal or close to 1 form type B or type A BRCs with a single core at the peak of the structure. As  $\gamma$  increases, the clouds evolve into filamentary structures with cores embedded inside. For even higher axial ratios, warm but dense capillary structure appears ahead of the shocked layer as seen in Cloud C as well. The axial mean density profiles for 9 G1 group clouds are plotted as black solid lines in Figure 4.18, which cover the range of dynamic features of the G1 series.

As seen from Figure 4.18, the clouds of  $1 \leq \gamma < 2$  ( $0.713\% \leq d_{\text{EUV}} < 0.9\%$ ) in both groups are spherical or quasi-spherical and evolve to similar structures with a highly condensed core. One difference being that more gas material is evaporated from G1 group clouds than the G2 group clouds. This is shown by the narrower density profile when compared with the G2(1-4) clouds. The above feature can be explained by the higher values of  $d_{\text{EUV}}$  in G1 clouds, where more surface material is photoevaporated. However, the overall dynamical evolution of these clouds can still be categorised as shock dominant, as most of remaining material in the cloud converges to the gravitational centre of the BRCs.

Clouds of  $2 \leq \gamma < 6$  ( $0.90\% \leq d_{\text{EUV}} < 1.26\%$ ) in the G1 group not only develop highly condensed cores at one or both ends of the final filamentary structure, but also between the two foci. This is especially notable as the middle core in the cloud G1(9) of  $\gamma = 3$ , which has a much higher mean density than the ‘foci’ cores in the same cloud. The above feature suggests that the EUV radiation induced shock dominance decreases. As such, the gravitational convergence toward the two foci is gradually weakened and more gas collapses toward the major axis to form a filament, which then fragments into a few dense cores. It appears that their collapse modes are in a transition region between foci convergence and linear convergence.

The clouds with axial ratios  $6 \leq \gamma \leq 8$  ( $d_{\text{EUV}} > 1.26\%$ ) all collapse in the mode of linear convergence, and the condensed cores spread over the final filamentary structure. For example, in the cloud of  $\gamma = 8$  ( $d_{\text{EUV}} = 1.43\%$ ), convergence toward two foci has broken, the high density cores have similar mean peak density as the consequence of the fragmentation of the final filamentary structure.

Cloud name	$M$ ( $M_{\odot}$ )	$n$ ( $\text{cm}^{-3}$ )	$d_{\text{EUV}}$ (%)	Mode of convergence
G0	30	100	17.8	linear
G1(17-19)	30	600	1.30 - 1.43	linear
G1(5-16)	30	600	0.90 - 1.26	foci/linear
G1(1-4)	30	600	0.71 - 0.86	foci
G2(1-19)	30	1200	0.23 - 0.45	foci

Table 4.6: A summary of the evolutionary destiny of the molecular clouds of mass  $30 M_{\odot}$ .

### 4.5.3 EFFECTS OF VARIED AXIAL RATIO AT LOWER DENSITIES

To confirm the correlation observed between  $d_{\text{EUV}}$  and the evolutionary destiny of a cloud, two additional sets of simulations were run with prolate clouds of  $30 M_{\odot}$ , but of lower initial densities, 300 and  $100 \text{ cm}^{-3}$ . Each group has four different clouds of  $\gamma = 1.5, 2.0, 2.5$  and  $4.0$ . With these initial conditions, the  $300 \text{ cm}^{-3}$  clouds have ionising depth parameters of  $2.6\% \leq d_{\text{EUV}} \leq 3.6\%$ , and the clouds of  $100 \text{ cm}^{-3}$ ,  $16\% \leq d_{\text{EUV}} \leq 22\%$ . In total 8 simulations were run with the same mass resolution as used in the G1 and G2 series simulations.

The morphological evolution and the axial mean density profiles are qualitatively similar to that of the highly ellipsoidal clouds in the G1 simulations, so similar plots to Figure 4.16 and Figure 4.17 are not presented. None of these clouds collapse in the mode of foci convergence. A representative simulation from the set of 8 is selected to compare its mode of convergence with that of the G2(5) and G1(5) clouds illustrated in Sections 4.5.1 and 4.5.2 respectively. The cloud selected has an initial density of  $100 \text{ cm}^{-3}$ ,  $\gamma = 2$  and  $d_{\text{EUV}} = 17.8\%$ , and is notated as cloud G0.

Figure 4.19 shows a comparison of the axial mean density profile over the *normalised*  $x$ -axis for three molecular clouds of  $\gamma = 2$ ,  $M = 30 M_{\odot}$ , and initial densities of 100 (black line for G0), 600 (red for G1(5)) and 1200 (green for G2(5))  $\text{cm}^{-3}$ . It is clearly seen again that the mode of collapse in the three clouds changes from linear convergence in G0, to the foci-linear mixture in cloud G1(5), then to foci convergence in G2(5), with  $d_{\text{EUV}}$  decreasing from 17.8% to 0.28%.

Table 4.6 presents a summary on the evolutionary destiny of all the investigated clouds in this series, related to the diagnostic parameter  $d_{\text{EUV}}$ .

### 4.5.4 LOCATION AND DISTRIBUTION OF CORES

From the above investigation, it is known that high density cores formed in clouds of lower  $d_{\text{EUV}}$  ( $\leq 1.25\%$ ) tend to locate around the two ends (foci) of the final filamentary

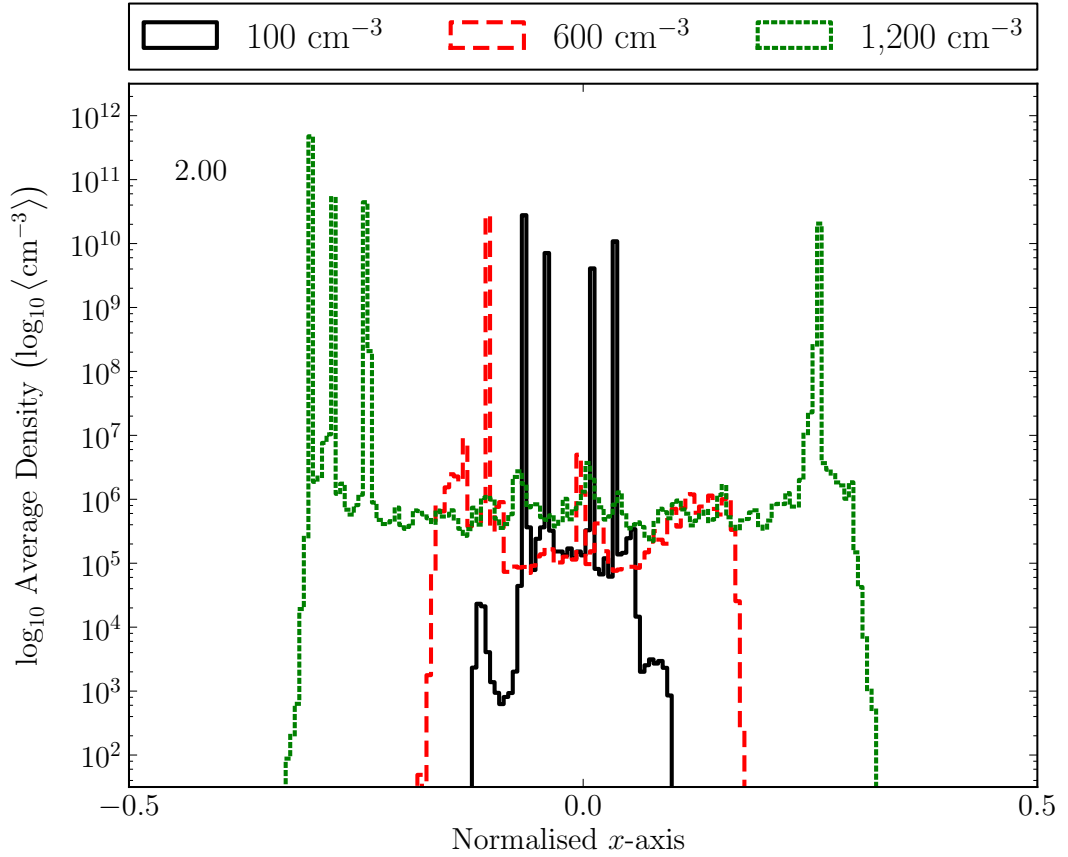


Figure 4.19: The axial mean number density distribution for molecular clouds of  $30 M_{\odot}$  and  $\gamma = 2$  but different initial densities. The legend boxes describe the line styles and colours for the densities of the featured clouds, G0 ( $100 \text{ cm}^{-3}$ ), G1(5) ( $600 \text{ cm}^{-3}$ ) and G2(5) ( $1\,200 \text{ cm}^{-3}$ ). The evolutionary times of the clouds featured are 0.25, 0.22 and 0.19 Myr for G0, G1(5) and G2(5), respectively.

structure. The detailed location profiles of condensed cores along the  $x$ -axis using the core finding program described in Section 4.2 are now investigated. For this objective, only cores with a peak density ( $n_c$ ) higher than  $10^8 \text{ cm}^{-3}$  are of interest, which can be taken as the potential seeds for new stars to form (Nelson and Langer, 1997).

Plotted in Figure 4.20 are the distributions of condensed cores in G1 and G2 clouds of different  $\gamma$ . The short horizontal lines specify the initial extent of the semi-major axis along the  $x$ -direction for clouds of the  $\gamma$  and initial density specified in the plot. The derived data of cores from the corefinding process has been further filtered by the peak density,  $n_c$ , ( $\geq 10^8 \text{ cm}^{-3}$  in all cases described here) and a minimum mass threshold  $m_c$ . The two panels on the left have a selection of  $m_c \geq 0.06 M_\odot$ , and the two on the right of  $m_c \geq 0.2 M_\odot$ . The  $x$ -displacement parameter is the modulus of the  $x$ -axis position of the peak of the core,  $|x_c|$ . Within each panel, two peak density regimes are distinguished by circles with white fill, indicating a density of  $10^8 \leq n_c \leq 10^{12} \text{ cm}^{-3}$ , and black filled circles for  $n_c > 10^{12} \text{ cm}^{-3}$ , being cores of extremely high density. It is seen from each panel in Figure 4.20, that extremely high density cores only form in the clouds of lower  $\gamma$  values and appear at the focus points.

In the two panels on the left, where  $m_c \geq 0.06 M_\odot$ , the upper of these is for the G2 series of clouds, and the lower for the G1 series. With increasing  $\gamma$ , high density cores form mainly around the foci of the ellipsoidal cloud in G2, but appear scattered over the whole cloud length in some of the G1 clouds.

The results for the higher core mass criteria ( $m_c > 0.2 M_\odot$ ) are the two panels on the right. It is seen that the high mass cores in all clouds of the G2 series are located at the centre or foci along the  $x$ -axis. The picture is not so simple in G1 clouds. In clouds of  $\gamma \leq 2$ , high mass cores appear close to the centre point  $x = 0 \text{ pc}$ . Some clouds of  $\gamma > 2$  have the high mass cores at two foci and closer to the middle of the  $x$ -axis as well. Some more ellipsoidal clouds have high mass core(s) either at/around the foci or spread between the foci. A few of the higher  $\gamma$  clouds in G1 have no core(s) with mass higher than the threshold  $0.2 M_\odot$ .

The general picture that is revealed is that the clouds in the G2 and the low  $\gamma$  clouds in the G1 groups have almost all of their cores located around their foci. Clouds of higher  $\gamma$  values in G1 have their condensed cores spread along the  $x$ -axis. The different core distributions between these clouds can be explained by the lower  $d_{\text{EUV}}$  in the G2 and low- $\gamma$  G1 clouds, compared to the high  $\gamma$  G1 clouds.

#### 4.5.5 TOTAL MASS AND FORMATION TIMES OF CORES

In order to evaluate the efficiency of EUV radiation triggered potential star formation in the different prolate clouds of the G1 and G2 groups, it is sensible to investigate

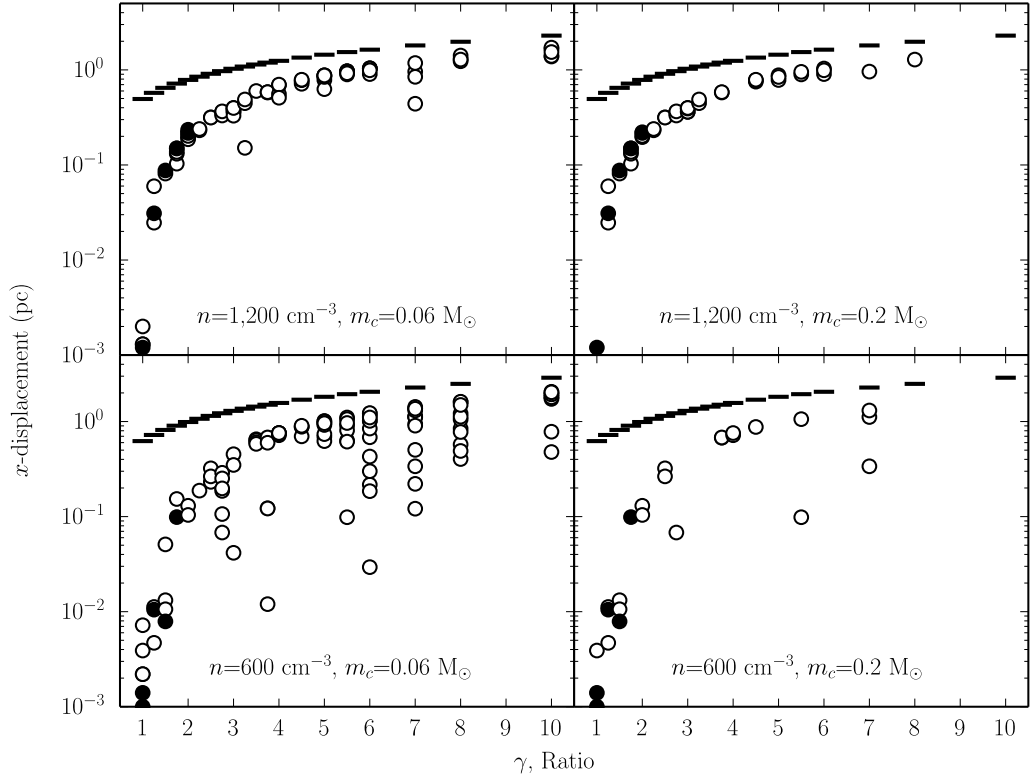


Figure 4.20:  $x$ -displacement locations ( $|x_c|$ ) of condensed cores formed in the G1 and G2 cloud series with different criteria on the threshold of core mass  $m_c$ .  $n$  is the initial density of the clouds whose cores are sampled in the corresponding panel. The short horizontal line for each  $\gamma$  examined denotes the initial semi-major axis of the cloud. The white circles indicate cores of density  $10^8 \leq n_c \leq 10^{12} \text{ cm}^{-3}$  and the black circles core densities of  $n_c \geq 10^{12} \text{ cm}^{-3}$ .

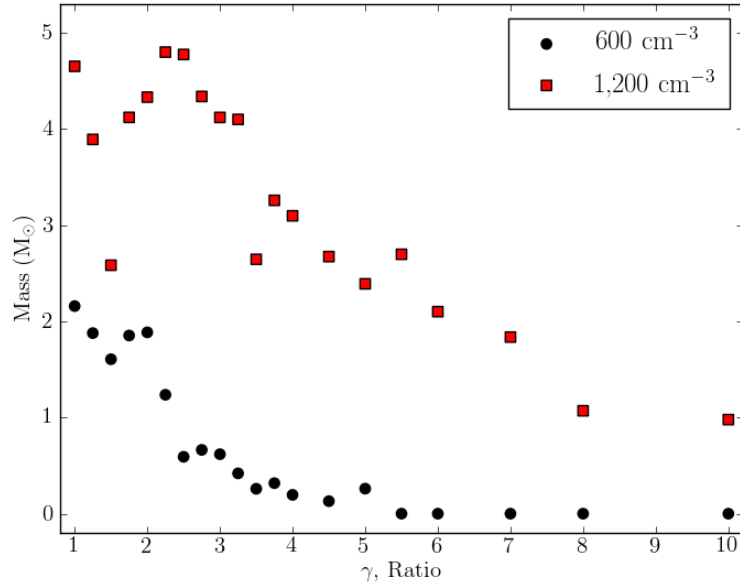


Figure 4.21: The total mass  $m_{\text{tot}}$  of all cores with selection criteria of  $n_c \geq 10^6 \text{ cm}^{-3}$  and  $m_c = 0.06 M_{\odot}$  at the end of the simulated evolution for all G1 and G2 clouds.

the total mass of dense cores and the time for high density core formation in clouds of different  $\gamma$  in both groups.

Plotted in Figure 4.21 is the variation of the total mass of high density cores in a cloud,  $m_{\text{tot}}$ , with  $\gamma$  for both groups. It is clearly seen that for each pair of G1 and G2 clouds of the same  $\gamma$ ,  $m_{\text{tot}}$  for the G2 cloud is more than double that of the G1 cloud. G1 group clouds have higher  $d_{\text{EUV}}$  and therefore lose more material through photoevaporation. The range of  $m_{\text{tot}}$  is 1 to  $4.85 M_{\odot}$  in the G2 series and  $0.05$  to  $2.2 M_{\odot}$  in the G1 series.

However the variation of  $m_{\text{tot}}$  over  $\gamma$  in each individual group is non-monotonic. Taking G2 group as an example, the spherical cloud has highest degree of convergence, so it has the maximum total core mass. When  $1 < \gamma \leq 1.5$ , although the cloud becomes an ellipsoid, the two foci are still very close to each other that their effect on gathering gas toward them is similar to one focus cloud. This can be confirmed by the single high density peak in the corresponding axial mean density distribution (in red lines) in Figure 4.18. The final structure still keep the morphology of a single BRC as shown in Figure 4.14. When  $\gamma$  increases to 1.5, the overall gravitational convergence toward the centre of mass decreases, so the total core mass  $m_{\text{tot}}$  of the high density core decreases with  $\gamma$ , to the value of  $2.6 M_{\odot}$ .

When  $1.75 \leq \gamma \leq 2.25$ , the distance between the two foci in a cloud increases to

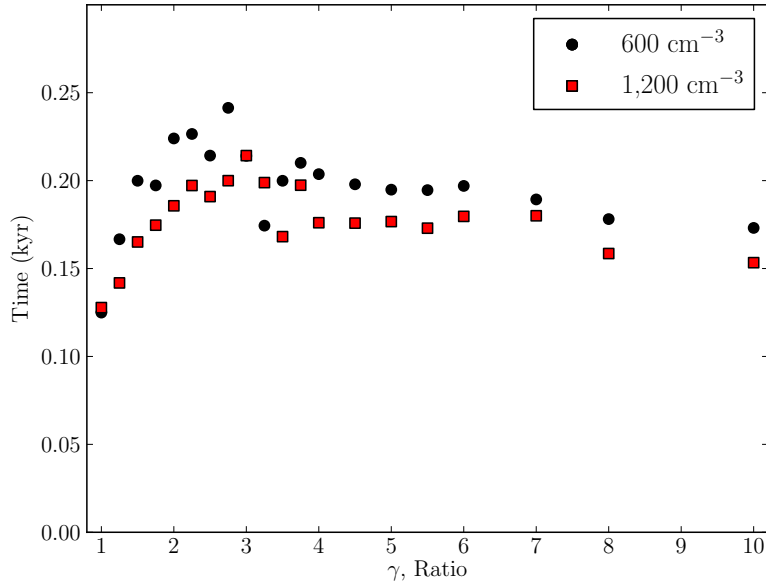


Figure 4.22: The earliest core formation time for all clouds in the G1 and G2 series.

such a degree that two foci convergence becomes obvious, as shown in the corresponding panels (in red lines) in Figure 4.18, the morphology of the final cloud is no longer a single BRC but a linear structure as shown in Figure 4.14. Now there are two gravitational converging centres to accrete gas, so the total core mass shows a sharp increase to  $4.2 M_{\odot}$  at  $\gamma = 1.75$ , then slightly increases with  $\gamma$  up to  $4.85 M_{\odot}$  at  $\gamma = 2.25$ .

As  $\gamma$  increases further, the initial cloud becomes highly elongated, the initial mass per unit length along the major axis becomes extremely low and the gas available to be accreted by the two foci similarly decreases. Therefore  $m_{\text{tot}}$  decreases with  $\gamma$  as shown in Figure 4.21.

Figure 4.22 shows the variation of the characteristic high density core formation time,  $t_{\text{core}}$ , over  $\gamma$  for the two groups of clouds. An overall picture is that the core formation time is shorter in all (but two) of the G2 clouds than in its  $\gamma$  counterpart for G1. This can be surmised to be due to the evolution of each of the G2 clouds being more shock dominated than each for G1. The variation in initial cloud density ( $600$  and  $1\,200 \text{ cm}^{-3}$ ) is small compared to the final densities (of order  $10^{12} \text{ cm}^{-3}$ ), meaning that the increase in starting density alone for the G2 clouds relative to the G1 clouds is unlikely to account for the reduction in formation time.

In both series, spherical clouds take the shortest time to be RDI shocked into form condensed cores, at  $t \approx 0.125 \text{ Myr}$ . Beyond  $\gamma = 1$ , the core formation time increases. This is determined to be because, as the single focus splits towards two foci, collection

of material, and subsequent gravitational collapse becomes slower. The clouds in the G2 set are taken as an example to look at the variation of  $t_{\text{core}}$  over  $\gamma$ .  $t_{\text{core}}$  increases from 0.125 to 0.22 Myr in clouds of  $1 < \gamma \leq 3$ . For clouds with axial ratio  $\gamma > 3$ , the shocked gas has a decreasing distance to travel along the smaller semi-minor axes to collapse toward the foci, resulting in a decreasing time required for collection of material and core formation. The variation of  $t_{\text{core}}$  with  $\gamma$  in G1 clouds is observed to follow a similar pattern.

## 4.6 CORRELATION WITH OBSERVATIONS

---

Many of the fragment-core structures found at HII boundaries have their linear axes perpendicular to the direction of the host star(s). A few examples of such structures are presented in Figure 4.23. The morphology of these structures is very similar to that within the simulations which are presented here. Object A in the left panel of Figure 4.23 (a 60  $\mu\text{m}$  Herschel image of M16) is a typical linear structure with two condensed ends, whose morphological image is similar to the simulated structures from G2 clouds. Objects B and C in the same panel, as well as the other linear structures in the upper and lower right panels in Figure 4.23, have similar morphological structures to clouds A, B, C and several clouds in the G1 series. Therefore, it is reasonable to suggest that these fragment-core structures are the outcomes of the interplay between the EUV radiation from nearby stars and its initial prolate molecular cloud.

## 4.7 LINK WITH OTHER MODELLING WORK

---

The fragment-core structures found along HII boundaries and the perfect HII bubble structure (Whitworth et al., 1994; Deharveng et al., 2009, 2012) were taken as the result of the ‘Collect and Collapse’ (C & C) mechanism (Elmegreen and Lada, 1977; Dale et al., 2007) in previous theoretical modelling work. By setting a star in the centre of a uniform spherical cloud, C & C simulation can result in a perfect ‘Bubble’-like HII region with a fragment-core inner boundary.

Recently, Walch et al. (2012) performed SPH simulations based on the RDI model, by replacing the uniform density spherical cloud used in C & C model with a fractal molecular cloud. Their simulations revealed the formation of a similar HII bubble structure with a wide spread network of fragment-core structure.

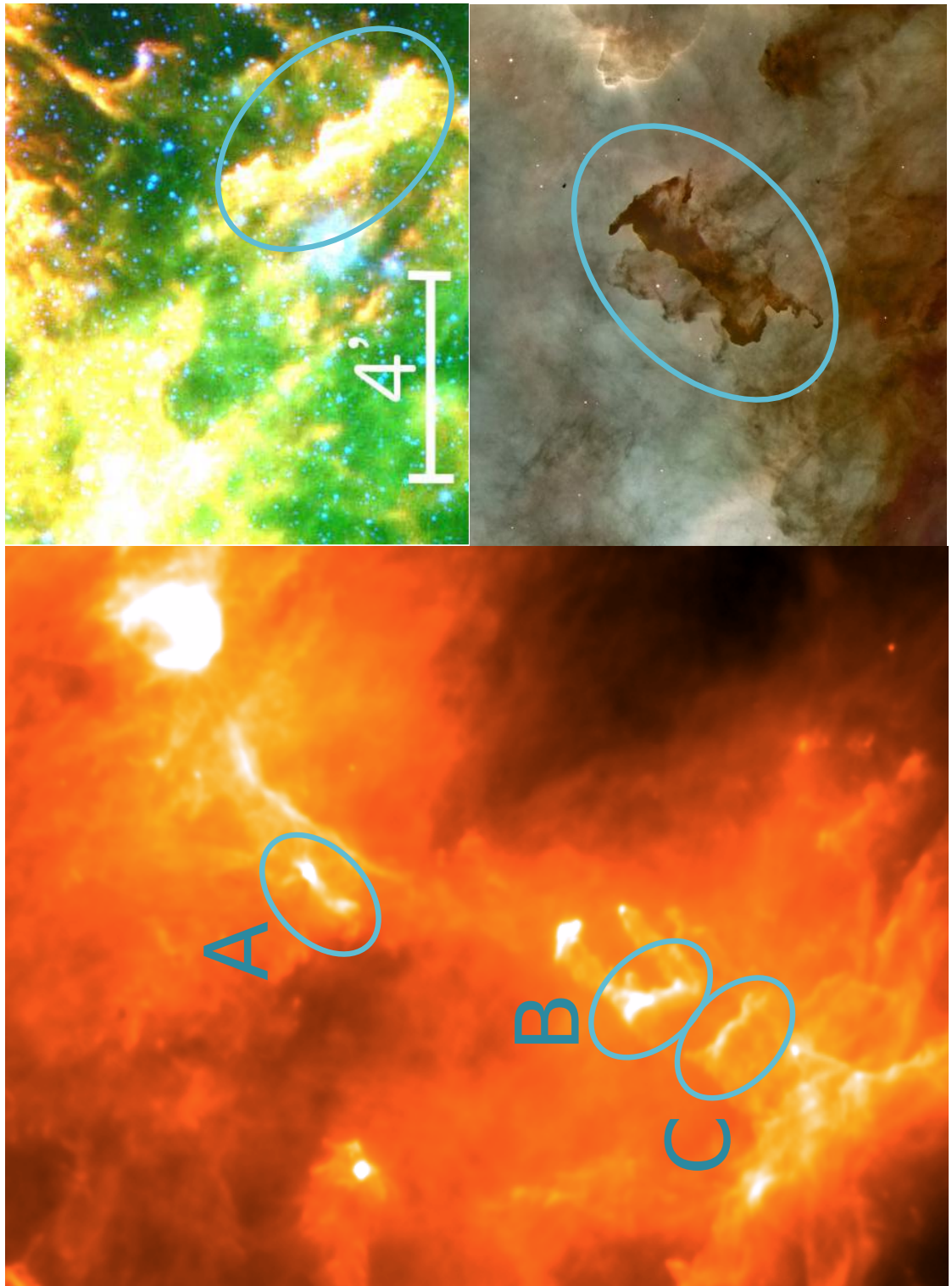


Figure 4.23: Fragment-core structures taken from various sources. On the left is the segment of the Herschel image of M16 at  $60\ \mu\text{m}$ . In the upper right panel is a section of a Spitzer pseudo-colour image of part of IC1848E (Chauhan et al., 2011). The lower right panel shows a segment of a fragment-core structure in a Hubble image of Carina Nebula in neutral hydrogen, taken from the Hubble website.

These simulations show that the fragment-core structure sporadically located along an HII boundary could also be the consequence of RDI on a pre-existing uniform prolate cloud with its semi-major axis perpendicular to the ionising radiation flux.

The RDI and C & C mechanisms are equivalent in terms of the physical interaction process between ionisation radiation and a molecular cloud, but they are different in terms of the initial conditions of the molecular cloud used and the relative position of the star to the molecular cloud. A uniform spherical cloud with ionising star in its centre is used in C & C model, a fractal and spherical molecular cloud with stars at its centre is used in Walch's RDI model, and a pre-existing prolate cloud with ionising stars at its one side is used in the RDI model here. The details resolved from different models could explain the variety in the structures of HII regions observed.

The structural differences can be argued to be the variation in initial conditions between ionisation fluxes embedded within perfectly uniform environments (C & C bubbles); environments with a medium degree of inhomogeneity (Walch et al., 2012); up to a very high degree of inhomogeneity, in which separated structures exist, providing small isolated molecular clouds with a high density ratio to their surroundings. The latter of these incorporates this research where, instead of the entire environment being the subject, the clouds could be considered individual isolated elements of a larger structure.

## 4.8 CONCLUSIONS

---

- I. Simulation results on three high mass prolate clouds reveal that a plane-parallel EUV radiation field can trigger formation of distinctive fragment-core structures, in comparison with the formation of a high density spindle when no EUV radiation is present.
- II. Further investigation on both the high and low mass clouds finds the embedded cores can either spread over the final linear structure or accumulate around the two foci of the cloud, dependent on the initial conditions and radiation fluxes. A dimensionless parameter of the EUV radiation flux penetration depth  $d_{\text{EUV}}$  can be used as an indicator to the evolutionary destiny of the clouds investigated. In clouds of  $d_{\text{EUV}} \leq 0.86\%$ , the collapse of a cloud is through foci convergence. The high density cores mainly locate around the two ends (two gravitational foci) of the linear structure with potential to form two well separated stars or two groups of stars. In clouds of  $0.86\% < d_{\text{EUV}} \leq 1.26\%$ , the mode of the cloud collapse is a

mixture of foci and linear convergence. The high density cores are found at one or two ends of the linear structure, while some cores with slightly lower density are also found between the two foci. In clouds of  $d_{\text{EUV}} > 1.26\%$ , the cloud collapses in the mode of linear convergence, when the high density cores spread over the whole linear structure with potential to form a chain of stars.

- III. Data analysis on the total core mass and core formation time in the two groups of low mass clouds (the G1 group with initial density of  $600 \text{ cm}^{-3}$ , G2 with that of  $1200 \text{ cm}^{-3}$ ) finds that:
- i. the total core mass  $m_{\text{tot}}$  in each of the G2 clouds is more than double that in each corresponding G1 cloud.
  - ii. in clouds of the same initial density,  $m_{\text{tot}}$  decreases with  $\gamma$  in clouds where there is only one or quasi-one gravitation centre, then a sharp increase for where there are two well separated foci, finally decreasing with  $\gamma$  again after  $\gamma > 2.25$ .
  - iii. the characteristic core formation time  $t_{\text{core}}$  is shorter in 95% of the G2 clouds than that in the corresponding cloud in the G1 series. It increases with  $\gamma$  when  $\gamma \leq 3$ , then becomes a quasi-constant at  $\gamma > 3$  in both cloud groups.
  - iv. the spherical cloud has the highest  $m_{\text{tot}}$  and shortest  $t_{\text{core}}$  in both groups of clouds, which implies that EUV radiation triggered star formation in spherical cloud is most efficient for the perpendicular cloud scenario.
- IV. On an extremely general level, it is observed that high EUV fluxes (high  $d_{\text{EUV}}$ ) disrupts clouds, whereas low fluxes (low  $d_{\text{EUV}}$ ) gives higher potential for star formation, agreeing with other statements to the same effect (Bisbas et al., 2011a).
- V. As the high density cores are the potential sites for future star formation, it can be concluded that, for prolate clouds with their major-axis perpendicular to the same incident EUV radiation:
- i. in clouds of the same axial ratio, EUV radiation triggered star formation would be more efficient in the cloud with higher initial density.
  - ii. in a group of clouds with same initial density, EUV radiation triggered star formation is more effective in clouds of intermediate axial ratio  $1.75 \leq \gamma < 3$ .
- VI. The sporadic core-fragment structures found in multiple HII boundaries may be taken as the result of RDI in pre-existing prolate clouds, such as investigated here.

# CHAPTER 5

---

## THE EVOLUTION OF INCLINED PROLATE MOLECULAR CLOUDS AT HII BOUNDARIES

---

### 5.1 INTRODUCTION

---

The previous chapter examined prolate clouds exclusively oriented such that there was a high degree of symmetry. All clouds began with their semi-major axes normal to the incident radiation. This scenario can be extended to incorporate off-axis incident radiation. This is implemented by rotating a prolate ellipsoidal cloud of semi-major axis  $a$  and semi-minor axis  $b = a/\gamma$  through an angle  $\varphi$ , being the angle between the semi-major axis, and an axis normal to the incident radiation. This configuration is illustrated in Figure 5.1, and represents the starting point for this investigation.

Although mirrored symmetry still exists about the  $x - z$  plane, unlike the previous chapter the symmetry about the  $y - z$  plane has been removed, and can be expected to result in more substantial complex and dynamical effects in the cloud evolution.



### 5.1.1 BACKGROUND

Modelling the RDI mechanism with a spherical molecular cloud as an initial condition, exposure to plane-parallel Extreme Ultraviolet (EUV) ionizing radiation, produces formation of standard type A, B and C BRCs and illustrates their formation process. The resultant BRCs follow the existing symmetry of their initial conditions, axially aligned to the direction of the incident radiation, with rotational symmetry around that structure axis (Bertoldi, 1989; Lefloch and Lazareff, 1994; Kessel-Deynet and Burkert, 2003; Miao et al., 2006, 2009; Gritschneider et al., 2009b; Miao et al., 2010; Bisbas et al., 2011b).

However, there is sufficient evidence to suggest that these results are not representative of the most common circumstances in HII regions. Investigation of the structures at HII boundaries shows that,

- i. some BRCs do not present with a cometary morphology, rather a ‘fragment-core’ linear structure perpendicular to the incident radiation axis (see, for example Chauhan et al. (2011))
- ii. most BRCs nominally classed as A, B or C type BRCs are not symmetric about the incident radiation direction, possessing structural axes at inclinations to it, and asymmetric structure around that axis (Thompson et al., 2004; Morgan et al., 2004). As shown in Figure 5.2, there is a distribution in inclination between the general structural axis and the incident radiation axis, based on the observation data of groups of BRCs in about 10 emission nebulae (Osterbrock, 1957)
- iii. in observed asymmetric BRCs, the head or tip of the BRC is not the exclusive location of identified multiple star or sequential star formation; being also present in compressed layers along the star facing sides of the BRCs (Fukuda et al., 2013; Mäkelä and Haikala, 2013; Sicilia-Aguilar et al., 2014; Panwar et al., 2014).

This observational evidence would suggest that RDI modelling from spherical initial conditions, or even symmetric conditions (up to and including the mirror symmetry of Chapter 4), are not sufficient to accommodate the variety of potential morphologies and physical features which should be expected.

Observations on the physical properties of molecular clouds have revealed that spherical clouds are rare cases (Gammie et al., 2003; Doty et al., 2005; Rathborne et al., 2009) and there are many physical processes which lead to formation of prolate molecular clouds (Gong and Ostriker, 2011; Gholipour and Nejad-Asghar, 2013). To investigate the mechanism for the development of structures of various morphologies

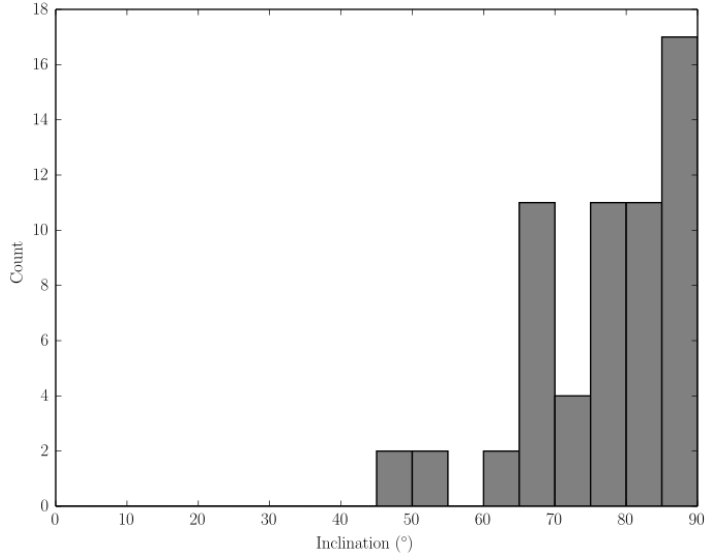


Figure 5.2: The distribution of the inclination angle  $\varphi$ , which is defined as the angle between the major axis and the  $x$  axis as shown in Figure 5.1, of the BRCs in about 10 emission nebulae (Osterbrock, 1957).

other than the conventional symmetrical A, B and C type BRCs at HII boundaries, using an initially non-spherical cloud in RDI modelling seems the most feasible choice.

For an ellipsoidal geometry cloud, a parameter  $\varphi$  can be defined, being the inclination between the plane normal to the incident radiation direction and the semi-major axis of the cloud. This expands upon the existing geometric parameter  $\gamma = \frac{a}{b}$ , the ratio of the semi-minor and semi-major axes, introduced for Chapter 4. Illustrated in Figure 5.1 is the configuration of these parameters, along with several to be described and utilised later in the Chapter. By expanding the parameter space in this way, one can expect that the variety of the morphological structures derived from RDI simulations must be greatly increased.

### 5.1.2 INITIAL CONDITIONS

The initial conditions are subject to the same criteria as those in Section 4.1.2 for stability against gravitational collapse, i.e. that the semi-major axis is equal to, or exceeds the value defined in Section 4.1.2 for other given parameters of the cloud.

The geometric shape of a prolate cloud in the simulations is described by a pair of initial parameters  $(a, \gamma)$  with an orientation to the plane of the plane-parallel ionization radiation flux being  $0^\circ \leq \varphi \leq 90^\circ$ , as shown in Figure 5.1. The ionization flux onto the surface of the cloud on the star side is plane-parallel to the  $z$  axis.

Letting  $r$  be the distance of any point on the surface of a prolate cloud in the  $xz$  plane from the origin, and  $\theta$  the angle between  $r$  and the  $x$  axis, the equation of an

inclined ellipsoid is,

$$r = \frac{a}{\sqrt{\cos^2(\theta - \varphi) + \gamma^2 \sin^2(\theta - \varphi)}}. \quad (5.1)$$

Several locations of interest are notated in Figure 5.1. The maximum  $x$  coordinate ( $x_{\max}$ ), the  $x$  projection of the semi-major axis ( $x_a$ ) and the  $x$  position of the apex ( $x_p$ ), in this Figure are, respectively,

$$x_{\max} = a \sqrt{\cos^2 \varphi + \frac{\sin^2 \varphi}{\gamma^2}}, \quad (5.2)$$

$$x_a = a \cos \varphi, \quad (5.3)$$

$$x_p = \left( \frac{a \sin \varphi}{\sqrt{1 + \gamma^2 \tan^2 \varphi}} \right) \left( \gamma - \frac{1}{\gamma} \right). \quad (5.4)$$

As an important indicator to the dynamical evolution of a prolate cloud with an inclination angle  $\varphi$ , the effective illuminated area by the EUV radiation is,

$$A = \frac{\pi a x_{\max}}{\gamma} = \frac{\pi a^2}{\gamma} \sqrt{\cos^2 \varphi + \frac{\sin^2 \varphi}{\gamma^2}}, \quad (5.5)$$

which is a decreasing function with  $\varphi$ , has a maximum  $\pi ab = \pi a^2/\gamma$  at  $\varphi = 0^\circ$  (perpendicular to the radiation direction) and a minimum  $\pi b^2 = \pi a^2/\gamma^2$  at  $\varphi = 90^\circ$  (parallel to the radiation direction).

### 5.1.3 IONISATION PENETRATION DEPTH PARAMETER $d_{\text{EUV}}$

In Section 4.1.2 the ionisation penetration depth parameter,  $d_{\text{EUV}}$ , was used to characterise the EUV radiation state for each cloud. In that case it was defined as the ratio of the true (physical) ionisation penetration depth to the scale depth (in the direction of the ionising radiation) of the cloud. This scale length was easily defined as simply being the semi-minor axis,  $b$ , or  $a/\gamma$ . The case for an inclined ellipsoidal cloud is more complex; the scale length is similarly defined as half the maximum path length through the cloud, resulting in a more complex expression for the overall value of  $d_{\text{EUV}}$ , shown in Equation (3.38) and repeated here for convenience,

$$d_{\text{EUV}} = \frac{F_0 \gamma}{n^2 a \alpha_B} \sqrt{\cos^2 \varphi + \frac{\sin^2 \varphi}{\gamma^2}}. \quad (5.6)$$

Series name	$n$ cm <sup>-3</sup>	$\gamma$	$\varphi$ °	$F_0$ ×10 <sup>9</sup> cm <sup>-2</sup> s <sup>-1</sup>
G1200	1200	1-10	0-90	1
density & flux	100-1200	2	60	1 & 2
irregular	400	2-3.5	60-85	2

Table 5.1: Summary of the parameter spaces investigated for the separate series of cloud groups.  $n$  is initial density,  $\gamma$  the axial ratio,  $\varphi$  the inclination angle and  $F_0$  the incident flux.

#### 5.1.4 INVESTIGATED PARAMETER SPACE

To illustrate the range of effects caused by the inclined geometries, variation in the parameters is built up from examination of a limited case, with increasing complexity added in steps.

- The first evaluations are made of the cloud G1200(5) from the Chapter 4 dataset described in Table 4.1. This cloud is initially investigated with a rotation of  $\varphi = 45^\circ$ .
- The same cloud is then examined at a range of angles  $0^\circ \leq \varphi \leq 90^\circ$  at  $15^\circ$  increments.
- The effects of axial ratio,  $\gamma$ , variation for an inclined cloud is then examined with  $1 \leq \gamma \leq 8$  at  $\varphi = 45^\circ$ .
- The parameter range is further expanded by investigating an increased range of  $d_{\text{EUV}}$  values, by varying both density ( $100 \text{ cm}^{-3} \leq n \leq 1200 \text{ cm}^{-3}$ ) and incident flux ( $F_1 = 1 \times 10^9 \text{ cm}^{-2} \text{ s}^{-1}$  and  $F_2 = 2 \times 10^9 \text{ cm}^{-2} \text{ s}^{-1}$ ).
- The final set of results evaluated is a range of high- $d_{\text{EUV}}$  combinations of  $F = F_2$ ,  $2 \leq \gamma \leq 3.5$  and  $60^\circ \leq \varphi \leq 85^\circ$  which create irregular morphologies, including some which present with ‘Horse-head’-like features.

The simulations conducted fall into three data series, with the ranges of values presented in Table 5.1.

## 5.2 EVOLUTION OF CLOUD G1200(5) WITH $\varphi = 45^\circ$

The cloud examined here is the fifth one in the G1200 set from Chapter 4; notated G1200(5). It has an initial shape defined by  $\gamma = 2.0$ , its major axis (0.784 pc) is

$\approx 10$  times of its critical major axis (0.079 pc) derived with Section 4.1.2, this makes it substantially super-critical, and over-stable against collapse; it would be expected to dissipate over fluid-dynamic timescales. It has  $d_{\text{EUV}} = 0.224\%$ ; below 1% which, if similar patterns to the  $\varphi = 0^\circ$  investigation are present should indicate that it is likely to undergo foci-convergent collapse.

In Figure 5.3 the evolution of the cloud can be seen spread across six timesteps through the simulation, running to 0.13 Myr. For the same evolution, Figure 5.4 illustrates the axial density distribution of the cloud, which has been shown in Section 4.3 to be an efficient method to reveal the regions of high density core formation. This method is decreasingly useful as a tool of analysis for clouds lacking a convenient axis of symmetry, however.

Both Figure 5.3 and Figure 5.4 provide qualitative views of the build-up of dense material on the upper surface of the cloud and the formation of the high-density core(s) beneath the apex, which will become a running theme in describing the mechanism of the core formation in these triggered scenarios.

From these figures is it apparent that by 28 kyr after the beginning of the simulation along with activation of the radiation flux, a shock has been established by the ionization heating across the upper surface. This shock starts compressing the cloud surface on the star-facing side creating a thin layer of mean density  $\approx 3 \times 10^3 \text{ cm}^{-3}$ . The density at  $x = 0.49 \text{ pc}$  is slightly higher than the axial mean density, which reflects the very early stage of the focusing of the density front and condensed core formation around the apex of the cloud.

During  $t = 0.028$  to 0.11 Myr, the shock continues propagating into the cloud. The density in the thin shocked layer increases further and the structure of the ‘head’ (near the apex of the starting cloud) becomes more distinctive. The ‘body’ (non-head) mean axial density and the central density of the head increase to  $10^4$  and  $10^5 \text{ cm}^{-3}$  respectively by 0.054 Myr, and to  $2 \times 10^4$  and  $10^6 \text{ cm}^{-3}$  respectively by 0.08 Myr. At  $t = 0.11$  Myr, the density in the shocked layer increases dramatically in the vicinity of the apex of the cloud (at  $x \approx 0.32 \text{ pc}$ ). This density jumps from  $\approx 8 \times 10^4 \text{ cm}^{-3}$  along the ‘body’ to  $\approx 8 \times 10^5 \text{ cm}^{-3}$  at  $x = 0.24 \text{ pc}$ , then to the maximum  $4 \times 10^6 \text{ cm}^{-3}$  at the apex.

Figure 5.5 displays a magnified view at the head of the cloud during its late stage evolution. It is interesting to note the substructure which becomes evident by 0.11 Myr (the left panel), which has a filament-like appearance aligned with the EUV radiation direction (though the specific alignment may be coincidental). The sub-structure size is only  $\approx 0.03 \text{ pc}$  long and coincides with the location of the apex of the cloud and the formation of the high density cores.

$\varphi(^{\circ})$	0	15	30	45	60	75	90
$d_{\text{EUV}}(\%)$	0.283	0.276	0.255	0.224	0.187	0.155	0.141

Table 5.2: Values for  $d_{\text{EUV}}$  of molecular cloud G1200(5) with  $0^{\circ} \leq \varphi \leq 90^{\circ}$  for the cloud G1200(5).  $d_{\text{EUV}}$  defined by Equation (3.38).

The gas contained in both the shocked surface layer and in the filament becomes further compressed by  $t = 0.13$  Myr. At this stage the mean density in the shocked layer and in the dense filament/sub-structure are  $10^5$  to  $10^6$  and  $> 10^9 \text{ cm}^{-3}$  respectively. The right panel of Figure 5.5 further reveals the formation of two high density cores in close proximity. These dual cores may be the result of fragmentation of the filament-like structure observed at 0.11 Myr. Unfortunately the output time resolution of the simulation is not sufficient to resolve the breakup of the filament itself. Given that examination of any single feature within a single sample is of limited applicability, it wasn't deemed a good use of resources to resolve the structure and its behaviour further here, but closer examination could be made in future projects.

Overall, the cloud G1200(5) with an initial inclination angle of  $\varphi = 45^{\circ}$  evolves to an asymmetrical type B BRC, with two RDI triggered high density cores embedded at its head, very close to the apex of the BRC. As with previous examinations, the cores can be deemed to be the potential sites for new star formation. By this time the apex of the cloud has travelled down from  $z = 0.61$  pc to  $z = 0.035$  pc, a net recoil velocity of  $\langle v_z \rangle = 4.3 \text{ km s}^{-1}$ , due to the rocket effect caused by the evaporating gas from the star-facing surface irradiated by the ionizing radiation (Oort and Spitzer, 1955).

### 5.3 EVOLUTION OF CLOUD G1200(5) WITH $0^{\circ} \leq \varphi \leq 90^{\circ}$

---

To investigate the evolutionary dependence on the inclination, the cloud G1200(5) is simulated with a range of inclinations  $0^{\circ} \leq \varphi \leq 90^{\circ}$ . This was done in a  $15^{\circ}$  interval sequence for 7 total simulations. The values of  $d_{\text{EUV}}$  for these seven clouds are listed in Table 5.2, from which it can be seen that the ionizing penetration depth decreases with  $\varphi$ , and is very shallow, with values  $\ll 1\%$ . As a result, all of these clouds are in the RDI shock-dominated regime and focus convergent triggered collapse is expected.

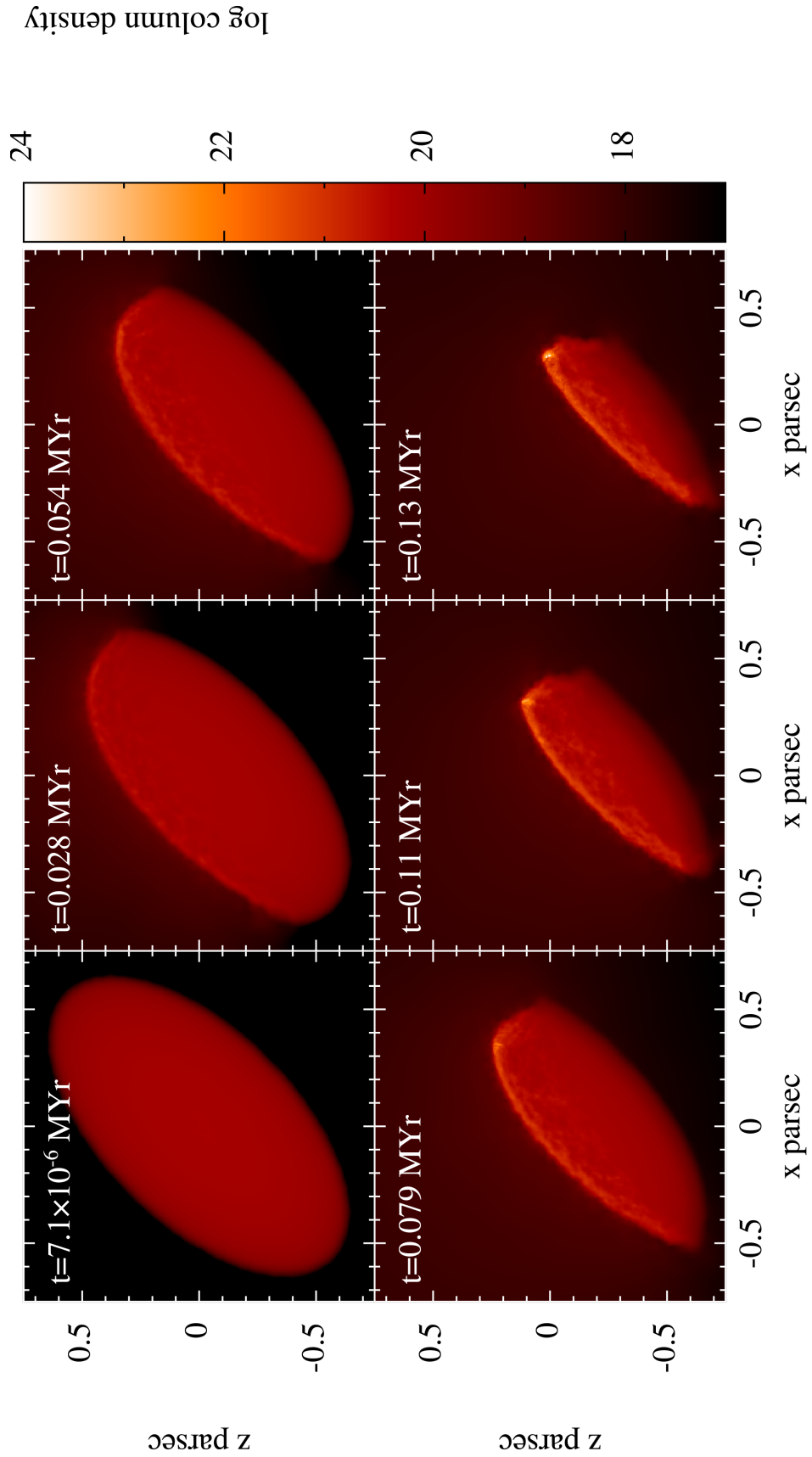


Figure 5.3: Sequential evolution of the column number density for Cloud G1200(5) with the incline angle  $\varphi = 45^\circ$ . Time sequence is left to right, then top to bottom then left to right. Column density is in  $\text{cm}^{-2}$ .

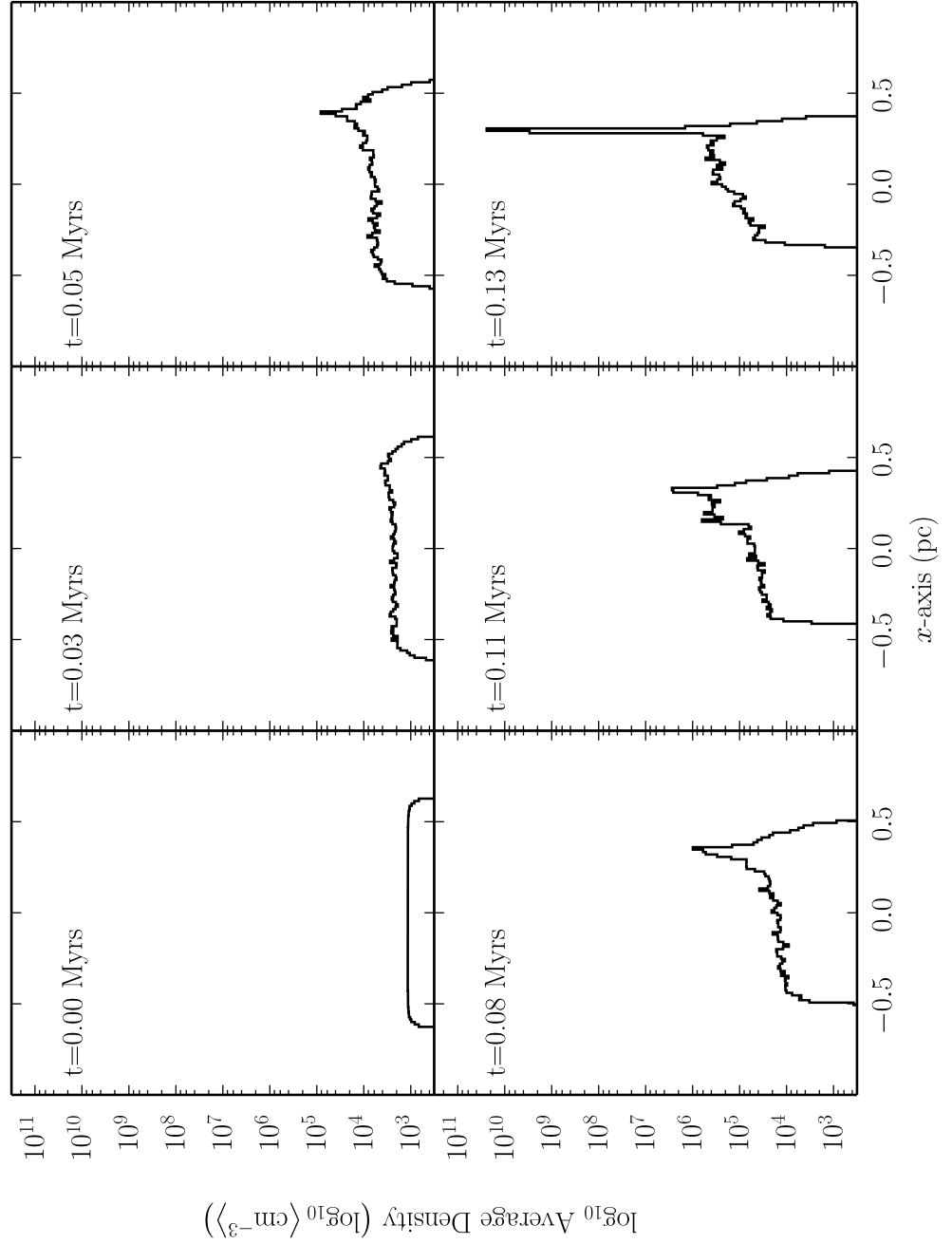


Figure 5.4: Axial mean density distribution along the  $x$  axis of the cloud G1200(5) corresponding to the column density evolutionary snapshots in Figure 5.3.

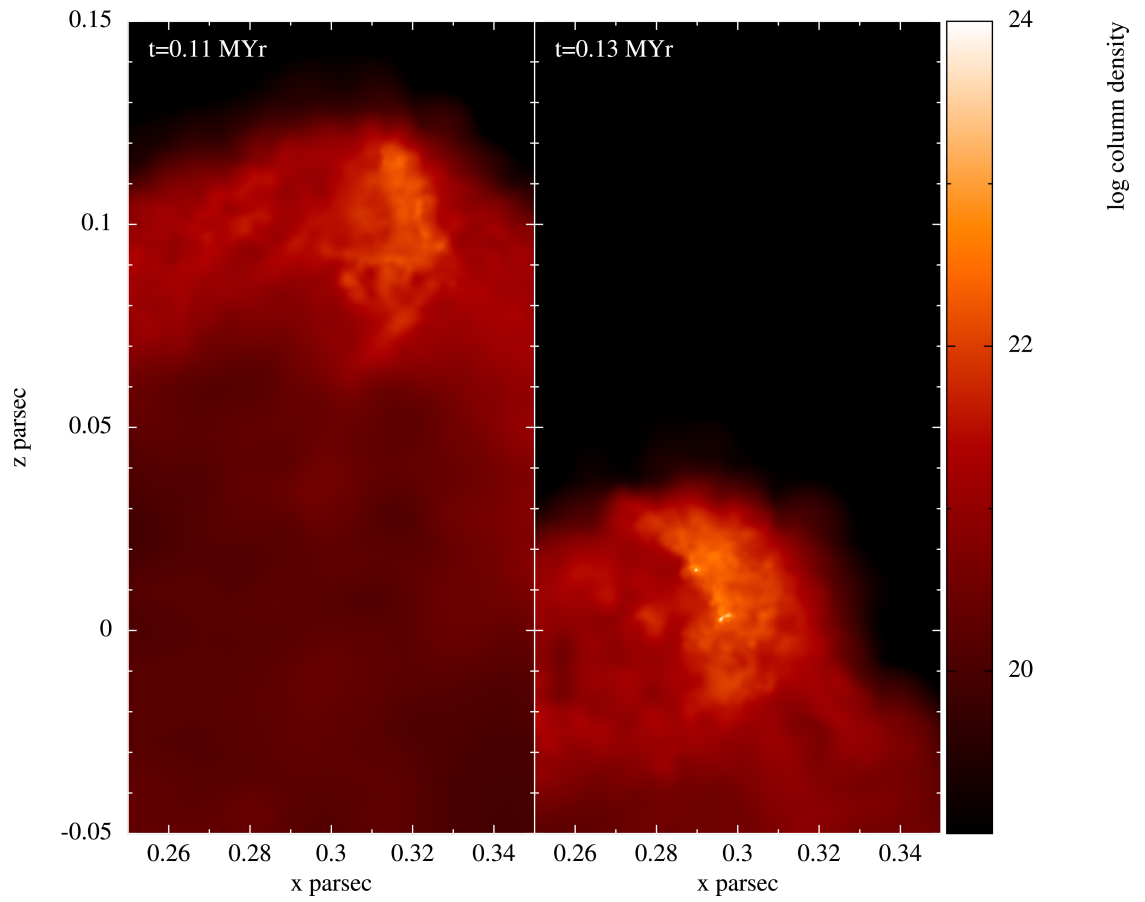


Figure 5.5: Magnification of the column density profiles time  $t = 0.11$  (left) and  $0.13$  Myr (right) at the head of the cloud G1200(5) with  $\varphi = 45^\circ$ . Column density is in  $\text{cm}^{-2}$ .

### 5.3.1 MORPHOLOGICAL VARIATION WITH $\varphi$

The evolutionary sequences of the clouds at varying  $\varphi$  are qualitatively similar to that with  $\varphi = 45^\circ$ . They all begin with the formation of a condensed layer on the star facing surface of the cloud, a shock directed inwards normal to the surfaces and highly condensed core(s) usually below the apex of the cloud, or at least at the location(s) at which density fronts converge. The final morphologies themselves depend on the initial inclination angle of the cloud but, as the general evolutionary sequence is so similar, they are not discussed individually, instead focusing on the comparison of the differences in their final morphologies and the physical properties of any high density core(s). In Figure 5.6, the final snapshots of column density of cloud G1200(5) from 6 different simulations with  $\varphi = 0, 15, 30, 60, 75$  and  $90^\circ$ , are presented. The equivalent for  $\varphi = 45^\circ$  can be found as the final panel of Figure 5.3.

When the inclination angle  $\varphi$  is small ( $\leq 30^\circ$ ),  $x_a \approx x_{\max}$ , the EUV radiation mainly illuminates the surface of the front semi-ellipsoid. The effect of the RDI is to drive a pseudo-plane-parallel shock propagating into the cloud, and the prolate cloud evolves to a filamentary structure with a condensed surface layer on the star side and highly condensed core(s) at the apex (when  $\varphi \neq 0^\circ$ ) or at either the apex or the two ends (when  $\varphi = 0^\circ$ ). The latter of these having been illustrated and examined in detail in Section 4.5.1.

When  $45^\circ \leq \varphi < 90^\circ$ , the EUV radiation illuminates more of the cloud beyond the  $x_a$  position on the cloud. As a result the shock induced by RDI creates a condensed and curved surface layer with a location beneath the apex ( $x_p$ ) as a convergence point of compressed curving surface layers from opposing sides of the apex. In fact the convergence is from all directions, in 3D, with short path lengths from the ‘near’ and ‘far’ upper portions of the cloud as illustrated in Figure 5.1. The region around the apex is also the site for the formation of high density core(s).

These clouds evolve to asymmetrical BRCs of different morphologies. Comparing the three final morphologies of the simulations at  $45, 60$  and  $75^\circ$  in Figures 5.3 and 5.6, it can be seen that as the inclination angle increases, the final structure of the asymmetrical BRC becomes increasingly extended both in the head and tail.

When  $\varphi = 90^\circ$ , the cloud G1200(5) develops into a symmetrical type B/C BRC but with a wide tail structure, with the widest part defined by the initial semi-minor axis. This would be likely to evaporate and contract with continued evolution, with the outermost edge of the tail being vertically thin and subsequently exposed to the incident radiation. The morphology developed is different from that of standard type B/C BRC structure, which has a much narrower width in its tail, if one assumes that the progenitor cloud was initially spherical (Lefloch and Lazareff, 1994; Kessel-Deynet

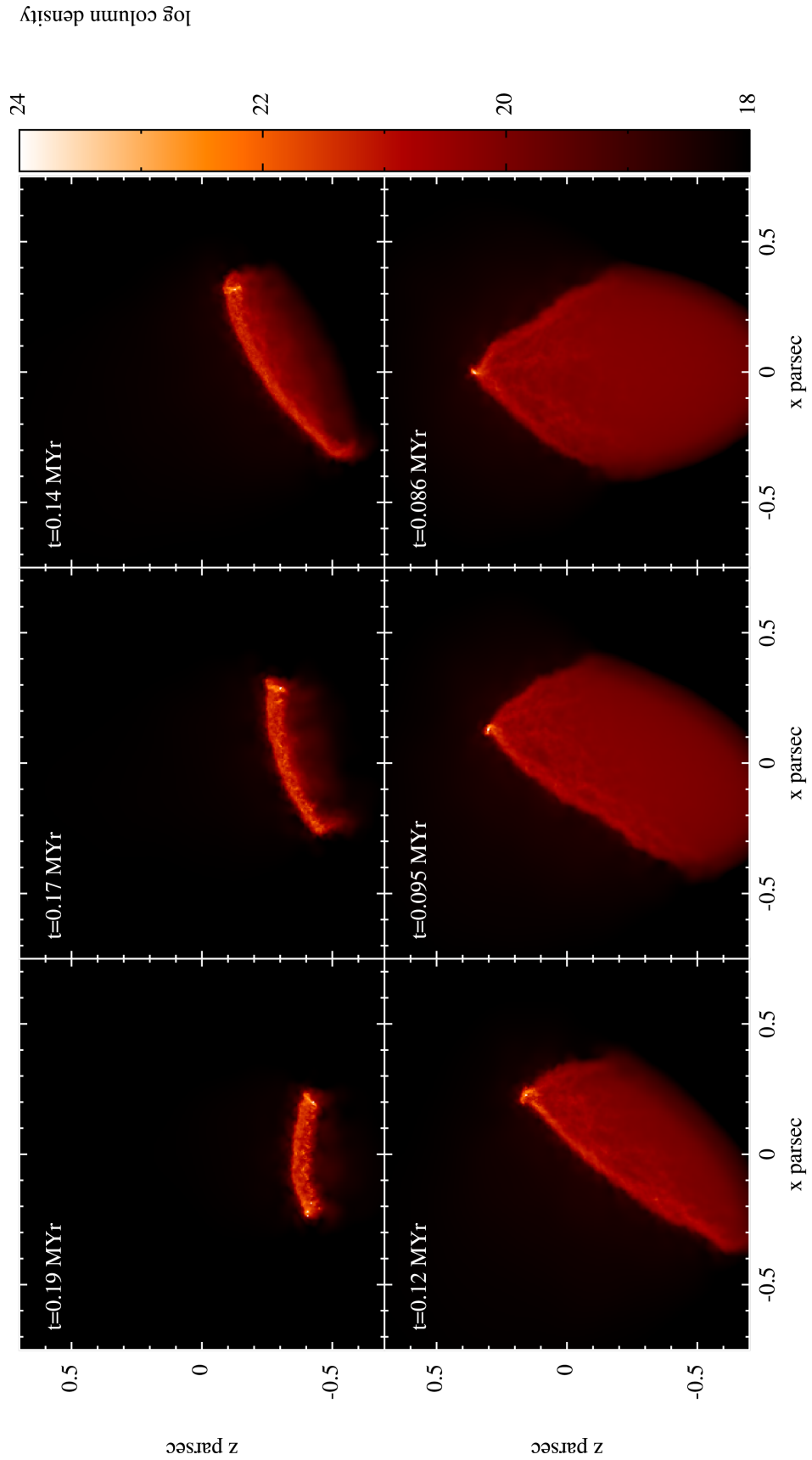


Figure 5.6: The final snapshot of the column density from six simulations of G1200(5) with different initial inclination angles; left to right, top row then bottom row are: 0, 15, 30, 60, 75 and 90°. Column density is in  $\text{cm}^{-2}$ .

and Burkert, 2003; Miao et al., 2006, 2009). Observations have also reported several type B/C BRCs with wide tail morphological structures, e.g. SFO74 (Thompson et al., 2004; Kusune et al., 2014).

In summary, a variety of non-standard morphological structures can be obtained by changing the inclination of cloud G1200(5). At low inclination, linear fragment-core structures form, at middle inclinations, asymmetric type B and C structures, and approaching  $90^\circ$  inclinations these return to symmetrical type B and C structures.

### 5.3.2 THE LOCATION OF HIGH DENSITY CORES

Figure 5.7 illustrates the distribution of the  $x$ -displacements of the condensed cores formed in the 7 simulations of different initial inclination angle  $\varphi$ . A point to note is that, where cores form in very close proximity, their positions cannot be distinguished on the scale used, regardless of the size choice of the marker. As a result, some markers effectively indicate the position of two or more cores; though the exact quantity is less important to convey with the figure than their distribution. It can be seen that when  $\varphi > 0^\circ$ , core(s) always form at the side of positive  $x$  axis and the change of the  $x$  displacement with  $\varphi$  follows the trend of  $x_p$  with  $\varphi$ . This illustrates an extremely high preference for high density core(s) to form around the apex  $x_p$  in each simulation.

It is possible to observe lower mass and density cores with a distribution at and around the apex. These lower mass and density cores occupy a wider spread of the  $x$ -axis, but are distributed per the net density pattern illustrated by Figure 5.4 with the population and size peaking at the highest density region under the apex. This is to be expected with increased availability of material for their formation.

### 5.3.3 THE EARLY TRIGGERED CORE MASSES AND FORMATION TIMESCALES

In order to examine the effect of varying inclination angle on the core properties of RDI triggered high density core formation, the angle dependence of the core formation time and the accumulated core mass is investigated. Figure 5.8 shows the evolution of the maximum density in the 7 simulations with different inclination angles. In general, the evolution of  $n_{\max}$  in each simulation passes through three different phases: quasi-linear, quasi-stable and steeply rising, although the time of each phase varies with inclination angle  $\varphi$ . These phases appear to correspond to the different stages of RDI triggered high density core formation. Beginning with initial compression by an RDI induced shock, mass accumulates to form the condensed region, which finally collapses to form high density core(s). The time for a simulation to reach the highest density (high

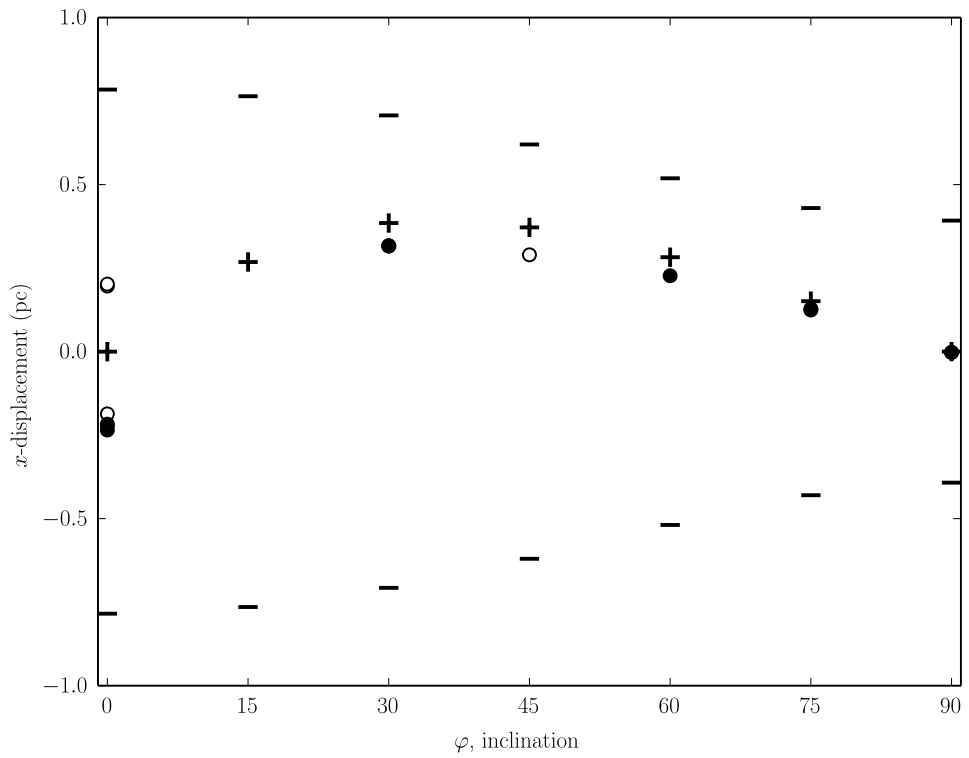


Figure 5.7: The  $x$  displacement of the cores formed in G1200(5) with different initial inclination angles. The short ‘-’ indicates  $x_{\max}$ , ‘+’  $x_p$ , ‘o’ for the cores with  $10^8 \leq n_{\text{peak}} \leq 10^{12} \text{ cm}^{-3}$ , and ‘•’ for the extremely high density cores with  $n_{\text{peak}} > 10^{12} \text{ cm}^{-3}$ .

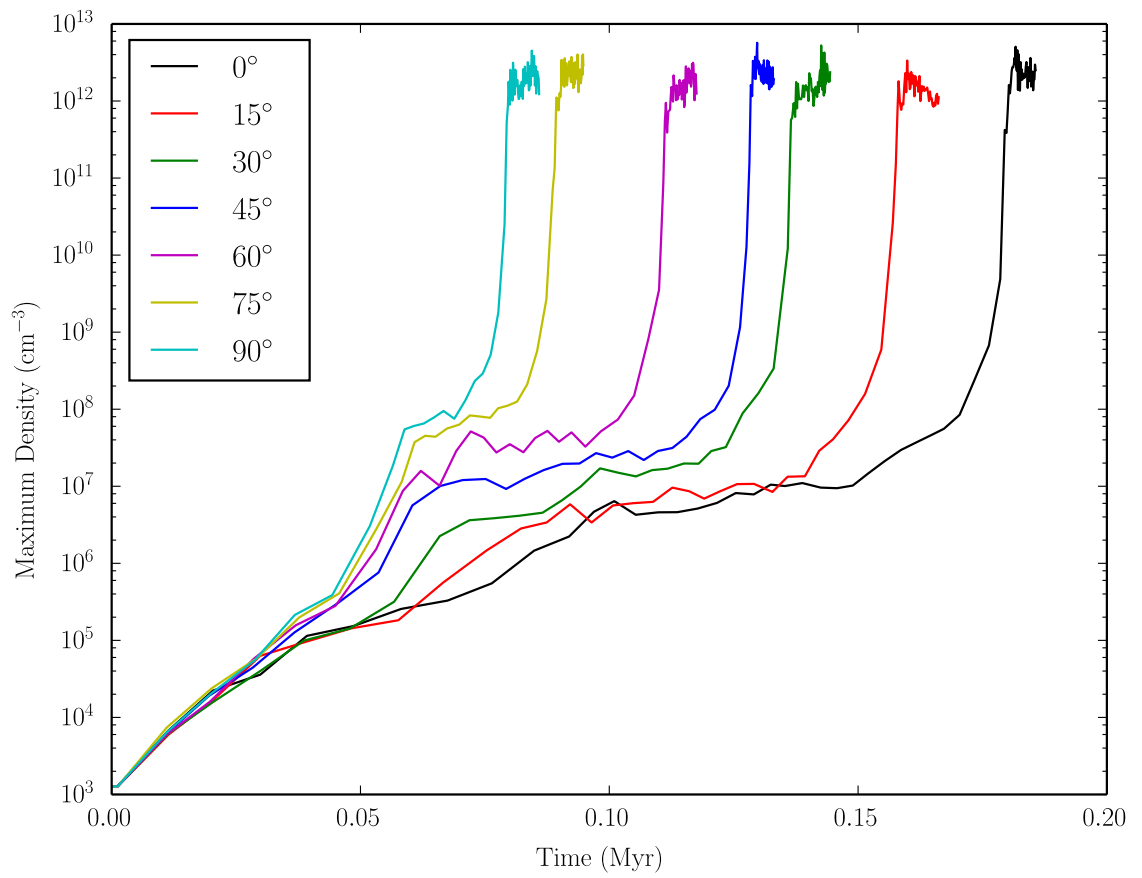


Figure 5.8: The evolution of maximum density of the core(s) in the cloud G1200(5) with different initial inclination angles.

density core formation) decreases with inclination angle, from 0.19 down to 0.086 Myr for simulations with  $\varphi = 0$  and  $90^\circ$  respectively. This is a result of the curvature of the EUV radiation illuminated surface around the apex of the prolate cloud increasing with  $\varphi$ . This enhances the accumulation of mass towards a geometric focus underneath the curved surface as a ‘lens’ effect. This decreases the path length to the focus, and so also the time for accumulating mass around it and triggering gravitational instability of the condensed region. Whilst this results in rapid core formation, the volume of mass swept by the EUV radiation induced shock *decreases* with  $\varphi$ , which results in a direct decrease in the amount of available mass to be accreted into the cores formed at the head of the BRC. Therefore it can be expected that the total mass of the early triggered cores should decrease with  $\varphi$ .

The relation between the total high density core mass and inclination angle  $\varphi$  is shown in Figure 5.9, which reveals that the total high density ( $n \geq 10^6 \text{ cm}^{-3}$ ) core mass is about  $4.1 M_\odot$ , in simulation of  $\varphi = 0^\circ$ , then decreases with  $\varphi$ , becoming  $0.4 M_\odot$  at  $\varphi = 90^\circ$ . This is consistent with the above expectation. However the total mass of the extremely high density core(s) ( $n > 10^8 \text{ cm}^{-3}$ ) doesn’t show an obvious similar relation with  $\varphi$  to the mass of high density core(s).

This may be for several reasons. Firstly, as the simulation is curtailed before the end of all of the dynamic processes, extremely high density cores may be on the cusp of formation, but have not yet had the opportunity. Secondly, a large degree of random variation is expected with such gravitational instability-based collapse. Accumulating mass in compact high density regions can be fairly consistent, but the collapse of these regions or parts of these regions to extremely high densities through gravitational instability is chaotic and varies strongly with the exact configuration of the dynamics. This is in accordance with the investigation into the uncertainties and variations within the simulations conducted as part of Section 3.3.

From the above result, as a cloud is rotated from  $\varphi = 0$  to  $90^\circ$ , the morphology of the cloud varies from fragment-core filamentary structures to varied asymmetrical BRCs, then to standard symmetrical BRCs as  $\varphi$  approaches  $90^\circ$ . At high  $\varphi$ , RDI triggered star formation occurs earlier with lower masses at high densities. However, for the sampling performed, such a pattern is not obvious for the extremely high density core formation, which appears to be chaotic within the limitations of the simulation timescales.

In order to better understand the dynamical circumstances from which the varied potential-star formation characteristics arise, the  $x - z$  density projection views in combination with known behaviours of the shock front can be examined in concert. This is performed for some of those simulations exhibited so far and additional data in

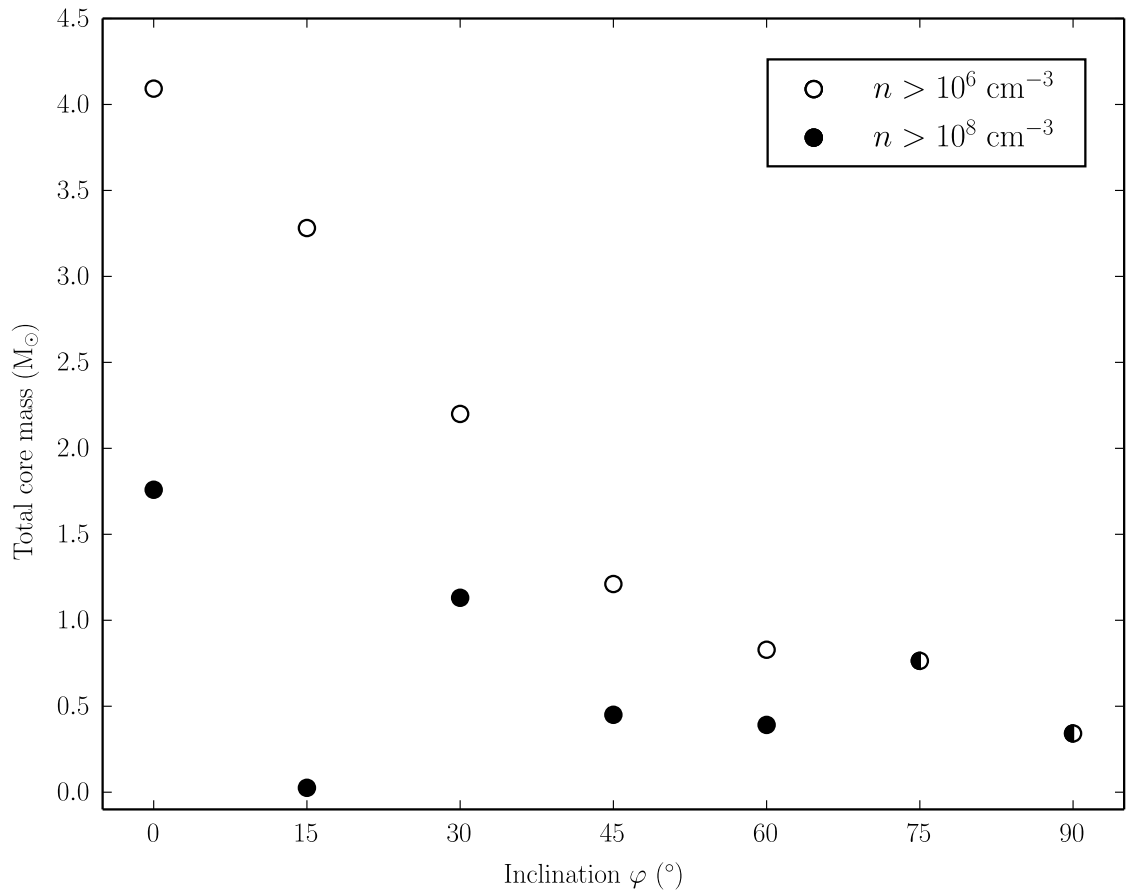


Figure 5.9: The variation of the total core mass of the cloud G1200(5) over different initial inclination angles. The symbols and their represented properties of cores are shown in the legend box.

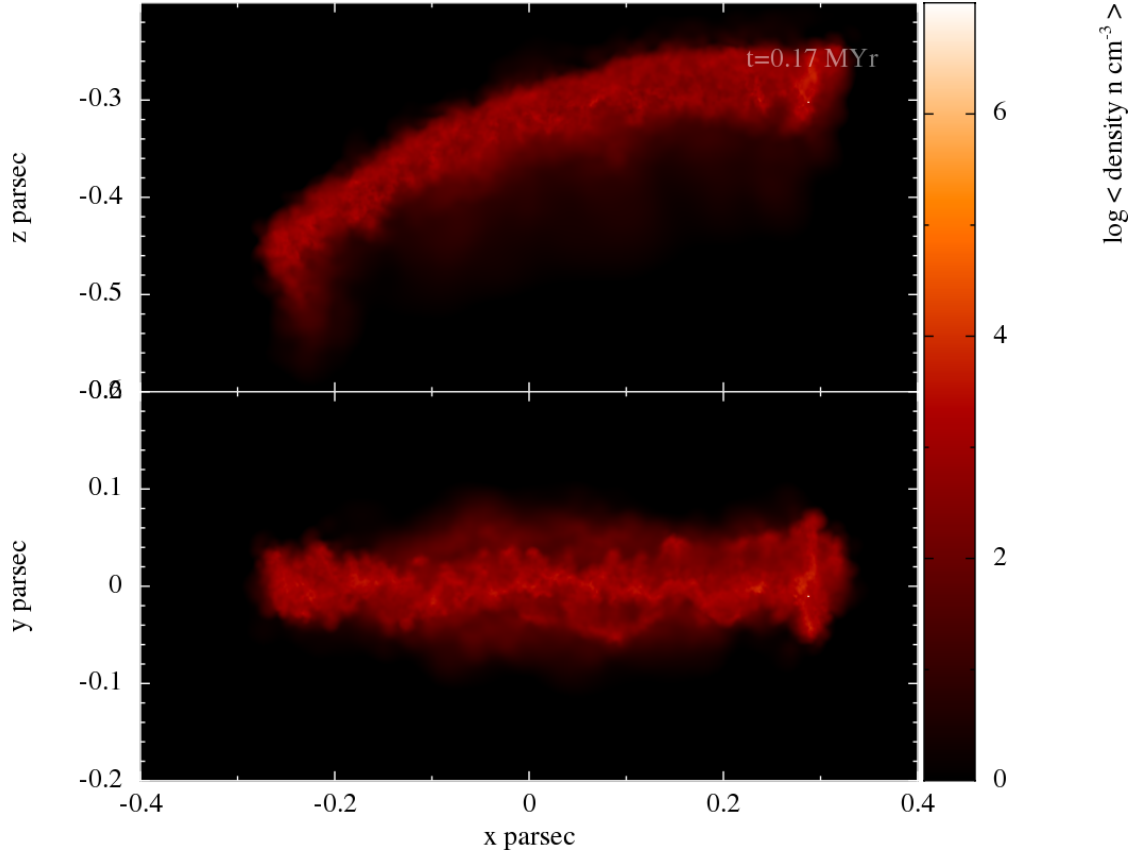


Figure 5.10:  $x - z$  (top) and  $x - y$  (bottom) column density projections for the cloud of  $n = 1200 \text{ cm}^{-3}$ ,  $\gamma = 2$  and  $\phi = 15^\circ$ . Column density is in  $\text{cm}^{-2}$ .

the subsequent Section.

### 5.3.4 PROJECTED VIEWS

Figures 5.10 and 5.11 illustrate the  $x - z$  and  $x - y$  projections of clouds at inclinations of  $\phi = 15$  and  $60^\circ$  for the  $n = 1200 \text{ cm}^{-3}$ ,  $\gamma = 2$  configuration. The ‘pinch’ effect at the tip of the cloud is visible, as is some degree of the elongation of the head along the  $y$ -axis caused by the shorter path along the ‘short’ axis of the ellipsoid than the ‘long’ axis.

This effect is even clearer in Figures 5.12 and 5.13, illustrating the same as previously but for the lower density of  $n = 600 \text{ cm}^{-3}$ . In this circumstance, the inwards driving waves undergo superposition and, failing to form high density cores or cancel out momentum in either direction due to collisions, continue in their original direction past the point at which they converged.

A substantial amount of dynamic interaction happens during this coalescing phase, and leaves the material in a turbulent state, with dynamic instability creating localised regions of higher and lower density. These are drawn out along the direction of travel,

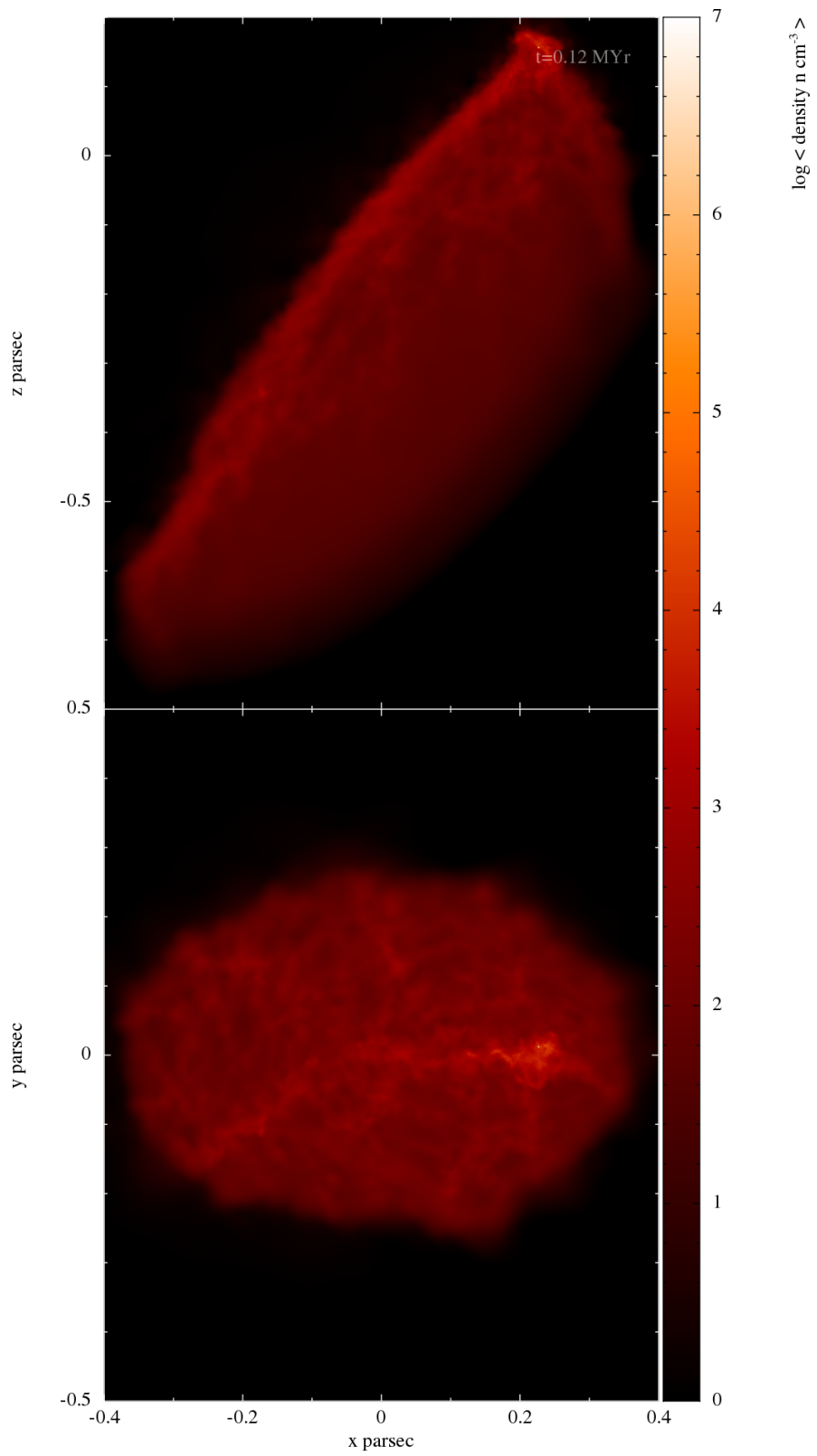


Figure 5.11:  $x - z$  (top) and  $x - y$  (bottom) column density projections for the cloud of  $n = 1200 \text{ cm}^{-3}$ ,  $\gamma = 2$  and  $\phi = 60^\circ$ . Column density is in  $\text{cm}^{-2}$ .

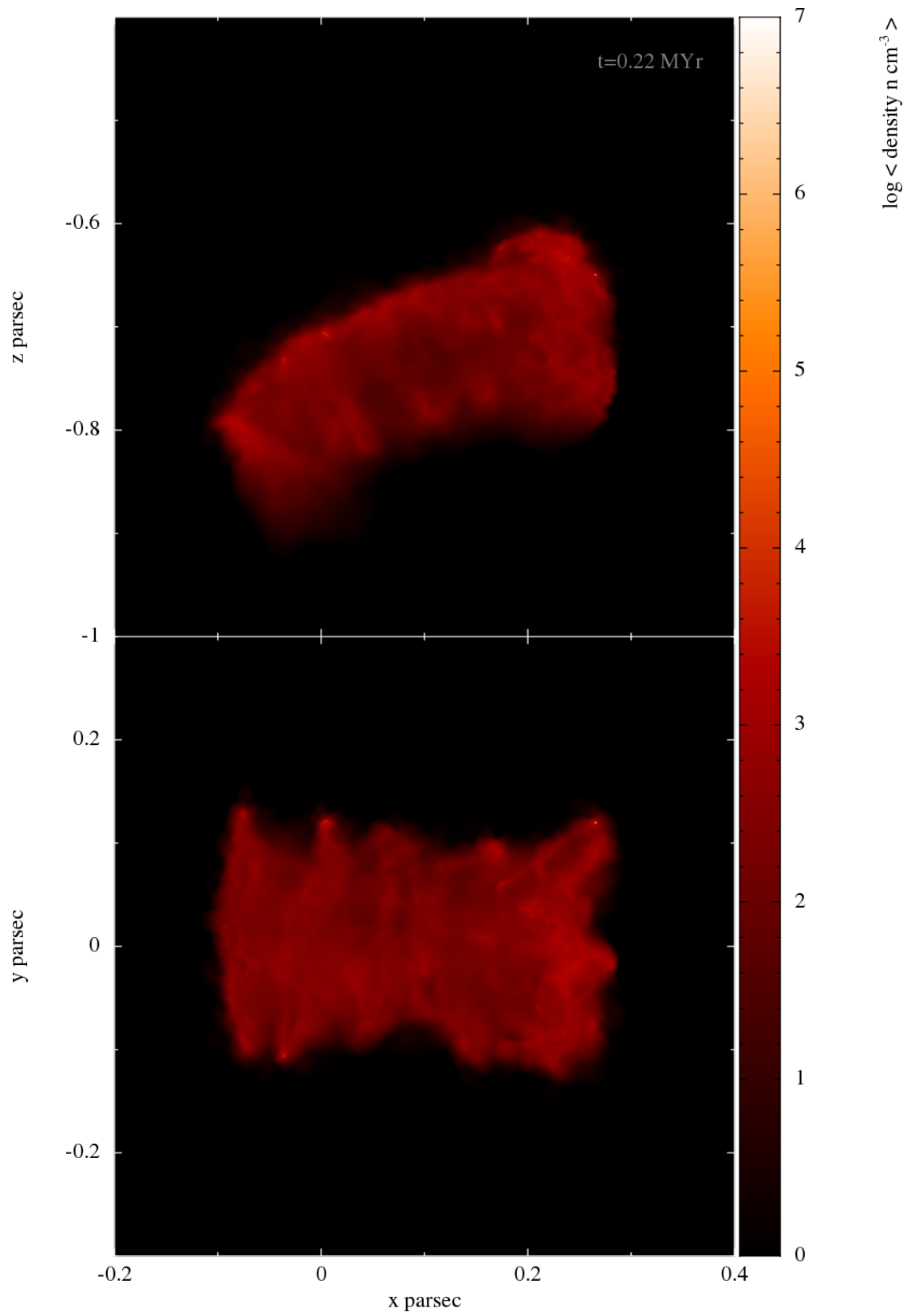


Figure 5.12:  $x - z$  (top) and  $x - y$  (bottom) column density projections for the cloud of  $n = 600 \text{ cm}^{-3}$ ,  $\gamma = 2$  and  $\phi = 15^\circ$ . Column density is in  $\text{cm}^{-2}$ .

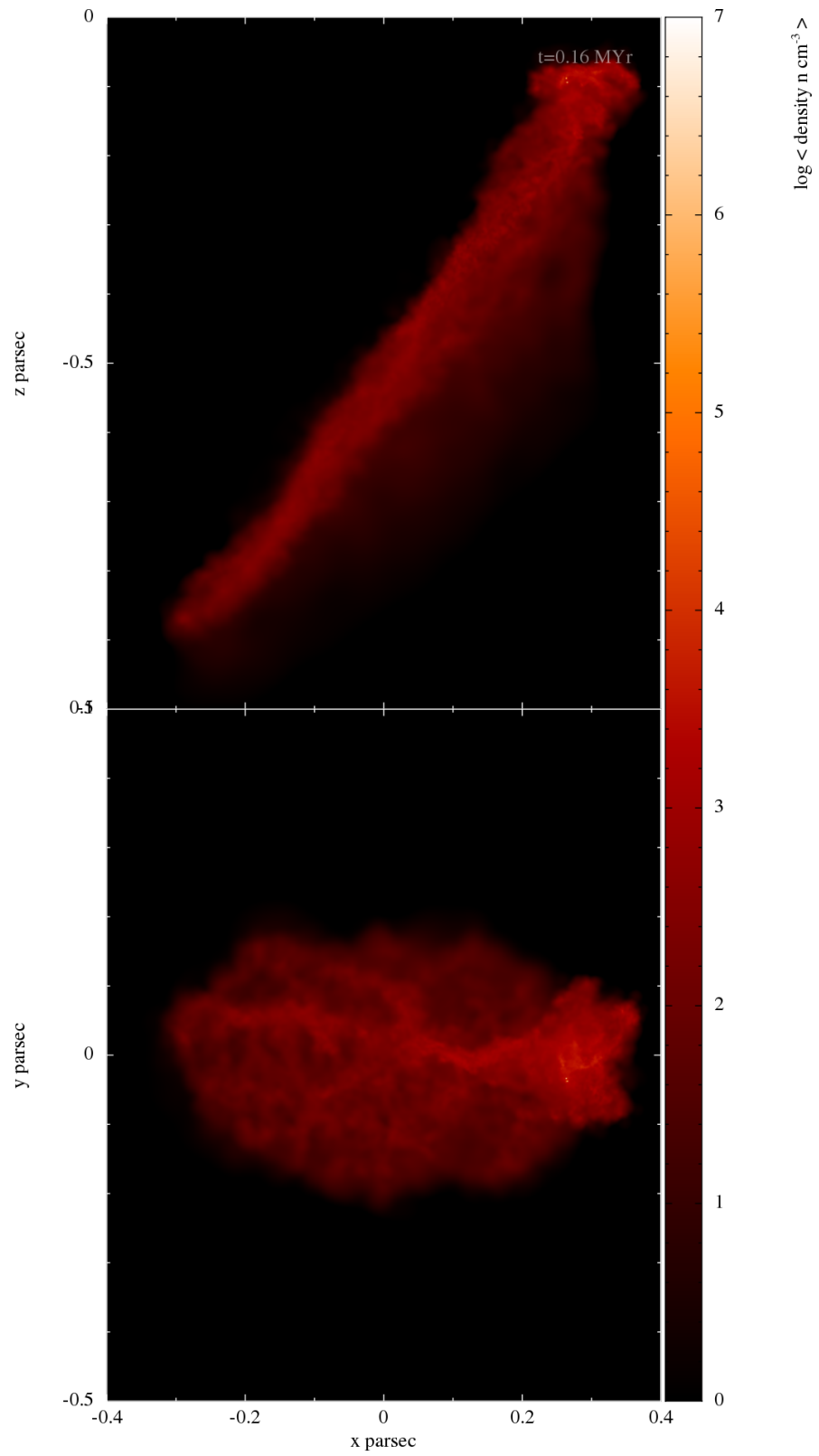


Figure 5.13:  $x - z$  (top) and  $x - y$  (bottom) column density projections for the cloud of  $n = 600 \text{ cm}^{-3}$ ,  $\gamma = 2$  and  $\phi = 60^\circ$ . Column density is in  $\text{cm}^{-2}$ .

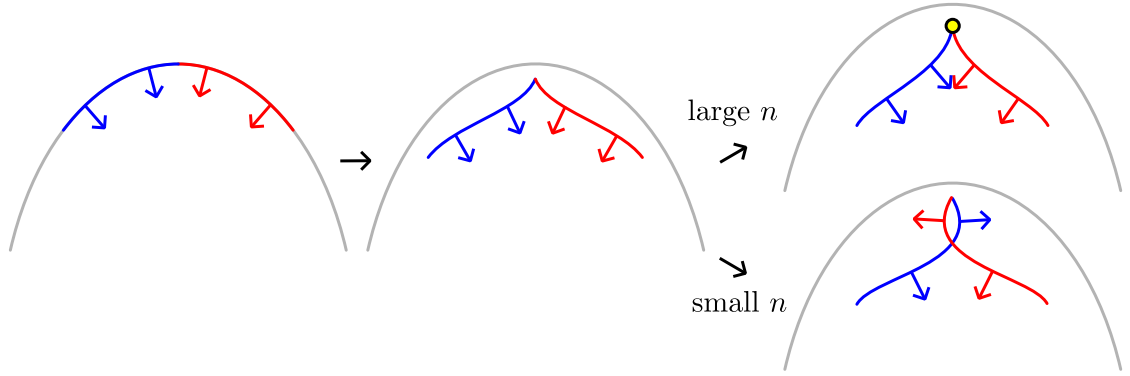


Figure 5.14: Diagrammatic illustration of the observed front convergence and density enhancement. Time advances from left to right, with the blue and red lines representing the initial positive and negative axis surface material (respectively). Yellow circle indicates a position of core formation.

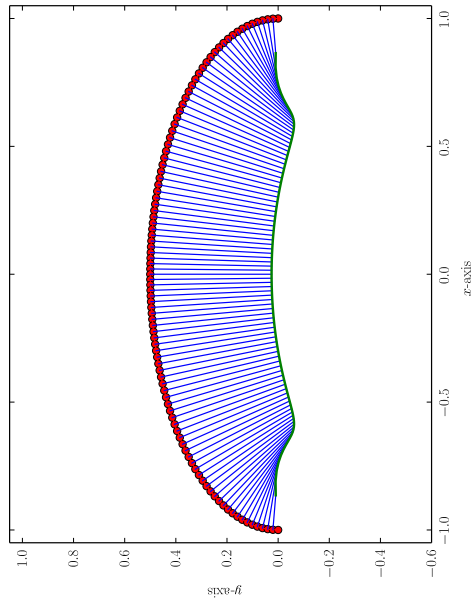
leading to the ‘rib’-like structures visible in some of the clouds.

### 5.3.5 SHOCK FRONT CONVERGENCE ANALYSIS

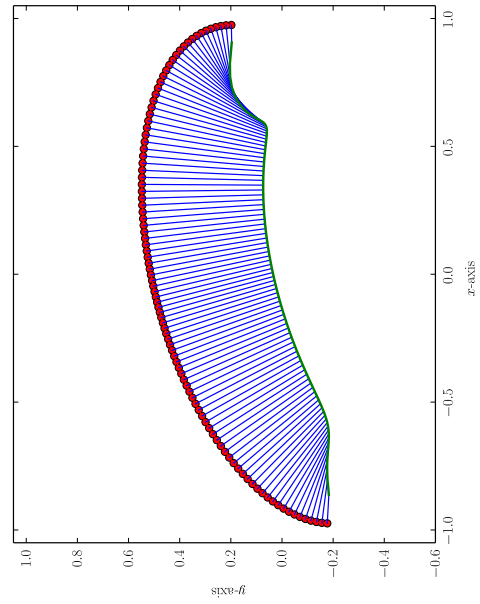
It is important to construct a conceptual schematic of the behaviour exhibited by these clouds with converging shock front surfaces. This can be used to estimate the behaviour of clouds with similar properties in a more general context.

Figure 5.14 is a diagrammatic representation of one plane of front convergence. Time progresses from left to right and shows the triggered motion of the shock normal to the surface of the cloud, which results in higher densities in regions where the fronts from multiple points converge on one another. For sufficiently high densities, this results in cancelling out of the motions of the fronts (resulting in a net zero lateral velocity  $v_x$ ) and build up of density which can lead to core formation. For low densities, the fronts are not halted by coalescing, and continue to propagate in their original directions. This results in a lateral ‘spreading’ of the front material. Within this region, the material has been highly disrupted by the coalesced phase and has randomly distributed regions of high and low density, drawn out as filamentary-like structures. Some of these high density filaments appear to subsequently collapse to form cores. This latter mode of formation is the linear-convergence mode described in Chapter 4, and generalised here to asymmetry in multiple axes.

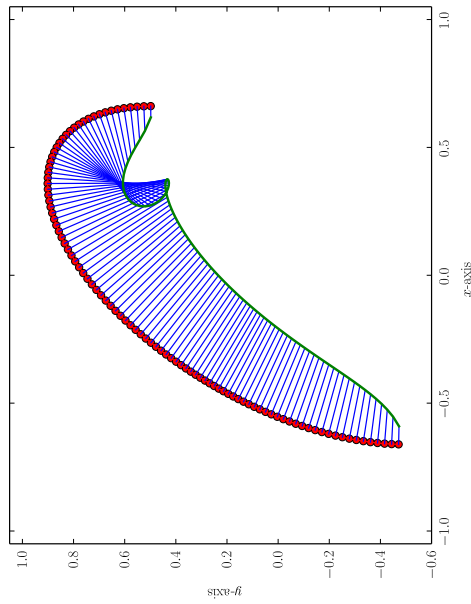
Figure 5.15 shows a highly simplified representation of the radiation triggered motion of the shock front in clouds of different  $\varphi$ . The projected blue lines from each surface element location (the red circles, distributed in equal intervals across the upper cloud surface) are the normals to each element, scaled to a length proportional to the approximate velocity  $\left(v_s \approx \sqrt{\frac{F_{\text{Lyman}}}{n}}\right)$  (Bertoldi, 1989) for that element (with the effec-



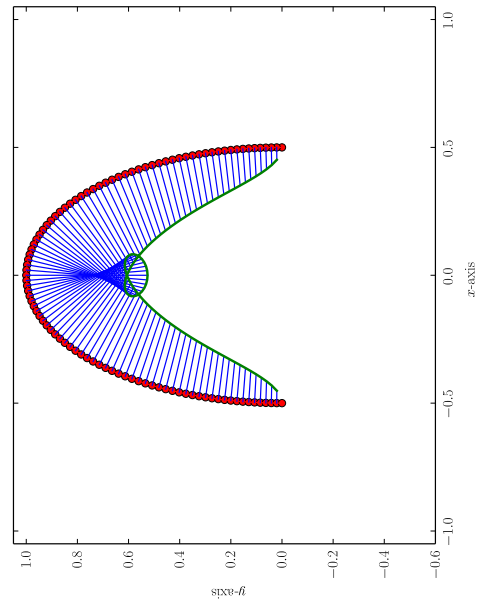
(a)  $\varphi = 0^\circ$



(b)  $\varphi = 15^\circ$



(c)  $\varphi = 60^\circ$



(d)  $\varphi = 90^\circ$

Figure 5.15: Simplistic representation of motion of the shock front normal to positions along the upper surface of a  $\gamma = 2$  cloud for several inclinations. Red dots represent initial surface elements, with blue lines indicating normals to those elements with a length proportional to the square root of the flux at each element ( $\propto v$ ) and the solid green line connecting the final positions after the pseudo-motion.

tive flux taken as  $\sin(\theta)$  with  $\theta$  the angle between the surface element and the direction of the incident radiation). For  $\varphi = 60^\circ$  in Figure 5.15c, the more-or-less parallel motion along the length of the flatter portion of the cloud is observed to form the ‘spine’ structure combined with the narrowing of the sides through the shorter axis lateral convergence of the fronts. The interesting portion of this plane occurs either side of the apex of the initial cloud. The lines can be seen to cross along a focal region, but not specifically an exact focal point. This mirrors what is observed in the simulations, in which a region reaches higher density, and core formation is ‘randomly’ located within that general volume.

Cross-over of the lines can be seen below the apex, too. Which also is in agreement with observed simulation results where, as described above, insufficient densities for an effective ‘collision’ of material to occur result in passage of material to the opposing side of its origin in a similar pattern to that shown by the projected lines. This becomes especially clear in the high  $d_{\text{EUV}}$  conditions examined in the subsequent sections.

The overall pattern observed through these illustrations, corresponding to observed patterns in the simulations, follows several regimes of behaviour. For  $\varphi = 0^\circ$  (Figure 5.15a), a large, flat front is combined with two focal regions. As the inclination increases (Figure 5.15a,  $\varphi = 15^\circ$ ) the convergence produced from the ‘lower’ end of the cloud becomes less significant, and increasing focusing occurs at the ‘upper’ end of the cloud. At higher inclinations (Figure 5.15c,  $\varphi = 60^\circ$ ), as already described, the focusing is very pronounced and virtually no significant focusing occurs along the ‘spine’ or low end of the cloud. The most extreme inclination (Figure 5.15d,  $\varphi = 90^\circ$ ) returns to a symmetric pattern, with very close focusing near the apex.

In all of these scenarios, for high density (low  $d_{\text{EUV}}$ ), regions convergence would be expected to be host to core formation. For low density (high  $d_{\text{EUV}}$ ), these regions become turbulent and the fronts pass one another, dragging disrupted material out behind them and leading the the fragment-core type structures described originally in Chapter 4.

## 5.4 EVOLUTION OF G1200 CLOUD SERIES AT $1 \leq \gamma \leq 8$

---

The initial shape of the clouds investigated here is defined by the ratio of the major to minor axis which are in the range of  $1 \leq \gamma \leq 8$ . When the initial density and total mass are constants, the major axis changes with  $\gamma$ . The inclination angle is kept at  $45^\circ$ . The ionization radiation penetration depth ranges from 0.225 to 0.320% as listed in Table 5.3.

G1200				
No.	$\gamma$	$a_{\text{crit}}$ (pc)	$a_{1200}$ (pc)	$d_{\text{EUV}}$ (%)
1	1.00	0.052	0.494	0.225
2	1.25	0.060	0.573	0.218
3	1.50	0.067	0.648	0.219
4	1.75	0.073	0.718	0.221
5	2.00	0.079	0.784	0.224
6	2.25	0.084	0.849	0.228
7	2.50	0.039	0.910	0.232
8	2.75	0.093	0.970	0.237
9	3.00	0.097	1.028	0.241
10	3.25	0.101	1.084	0.246
11	3.50	0.104	1.139	0.250
12	3.75	0.107	1.193	0.256
13	4.00	0.110	1.245	0.260
14	4.50	0.116	1.347	0.268
15	5.00	0.121	1.445	0.277
16	5.50	0.126	1.540	0.285
17	6.00	0.130	1.632	0.292
18	7.00	0.138	1.808	0.307
19	8.00	0.145	1.977	0.320

Table 5.3: Parameters of molecular clouds of G1200 series with an inclination angle  $\varphi = 45^\circ$ . From left to right, columns 1-3 are the number identity, axial ratio and the critical semi major axis defined by Section 4.1.2. Columns 4-5 are the major axis and  $d_{\text{EUV}}$  defined by Equation (3.38). All of the semi-major axes and critical semi-major axes are in units of pc and the penetration depth is in %.

### 5.4.1 MORPHOLOGY OF FINAL STRUCTURES

The dynamical evolution of these clouds is also qualitatively similar to that discussed in Section 5.2. Focus here is on the analysis of the effect of the initial shape of a cloud on the final morphology, the location(s) of the condensed core(s) and the total core masses. Figure 5.16 presents six simulation result of cloud G1200 with different initial major to minor axis ratio  $\gamma = 1.0, 1.5, 2.0, 2.5, 3.0$  and  $5.0$ , selected from simulation results for 19 different initial clouds, described in Table 5.3. With increasing  $\gamma$ , the final morphology changes from a standard (symmetrical) type A ( $\gamma = 1.0$ ), to an asymmetric type A BRC ( $\gamma = 1.5$ ), then to an asymmetric type B BRC ( $\gamma = 2.0$ ), next to evolve to an asymmetrical type C BRC ( $\gamma = 2.5$ ). With further increase ( $\gamma \geq 3.0$ ) only a spine-like filamentary structure can form.

In these six simulations, high density cores form at the head of the structure except in the case of  $\gamma = 2.5$ , where the highly condensed core is embedded in the small ‘nose’ structure just outside the head. It is interesting to notice that the morphological structure of SFO46 (CG1) from observations (Harju et al., 1990; Haikala et al., 2010; Mäkelä and Haikala, 2013) bears a similar feature to that of  $\gamma = 2.5$ . The discussion for the formation mechanism of this morphology is left to the Section 5.5, where the regions of the parameter space which exhibit such features, and the formation mechanism, is examined in more detail.

The qualitative similarities between any single simulation result and observation is of limited value. The subjective nature of such comparisons leaves the method open to problems in agreement over whether features do correspond. Nonetheless it can provide a useful starting point for refining parameter regimes and illustrating that the results can still be shown to be consistent with what is observed. It is not intended to compare the detailed physical structures between simulation and observation on SFO46, but only to point out the link between the interesting features from these simulations to such observations. Further simulations could potentially provide greater ability to describe such comparisons in more detail, both qualitatively and quantitatively.

### 5.4.2 DISPLACEMENT OF THE HIGH DENSITY CORES

Figure 5.17 displays the  $x$ -displacement of condensed core(s) with changing geometry, based on the simulation results of 19 clouds with varying  $\gamma$ .

As  $\gamma$  increases,  $x_p$  moves further in the  $+x$  direction. The  $x$ -displacements of the condensed cores closely echo this pattern. They are positioned, in almost every case, in close proximity to the location of the apex of the cloud. A very clear trend of the core formation occurring at or around the apex for all ratios is exhibited.

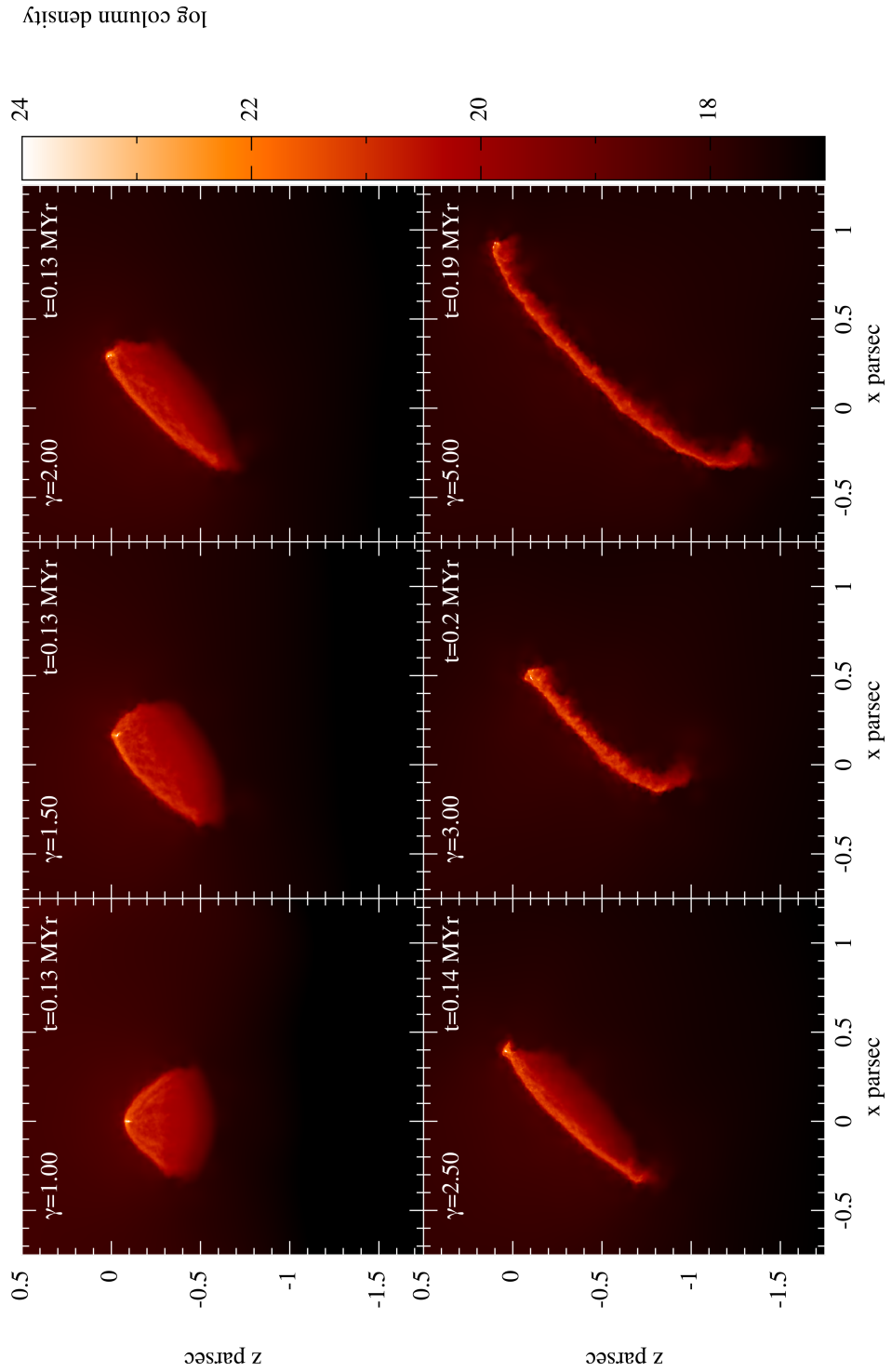


Figure 5.16: The final snapshots of the column density from six simulations of G1200 with  $\gamma$  equal to the values shown in the top-left corner of each panel. The inclination angle is  $45^\circ$  for all of the initial clouds. Column density is in  $\text{cm}^{-2}$ .

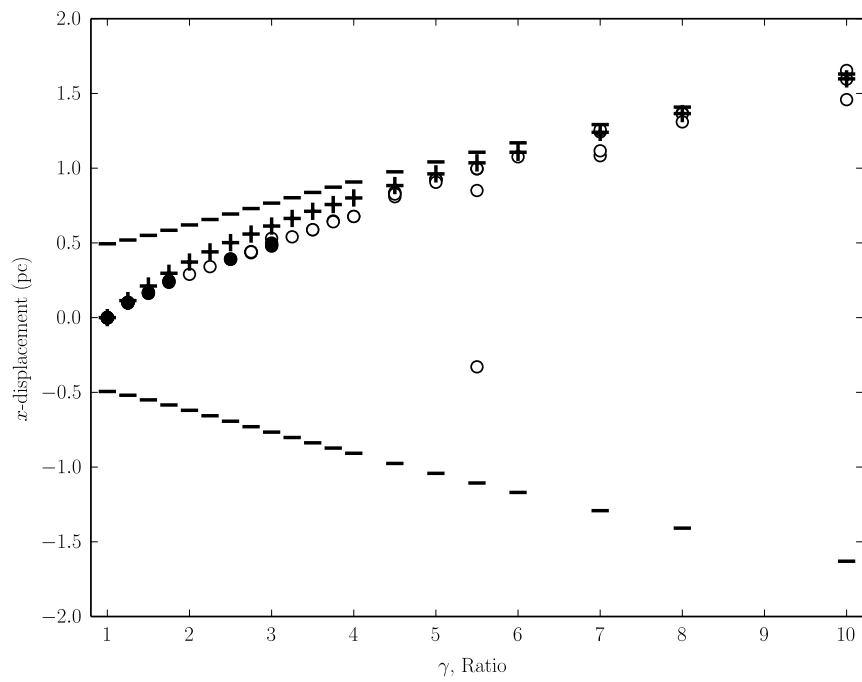


Figure 5.17: The  $x$  displacement of condensed core in G1200 series with an inclination of  $\varphi = 45^\circ$  for varied  $\gamma$ . The short ‘-’ indicates  $x_{\max}$ , ‘+’  $x_p$ , ‘o’ for the cores with  $10^8 \leq n_{\text{peak}} \leq 10^{12} \text{ cm}^{-3}$ , and ‘•’ for the extremely high density cores with  $n_{\text{peak}} > 10^{12} \text{ cm}^{-3}$ .

This is especially true for the displayed high-density and extremely high density cores. However, a similar trend is also exhibited with the overall mass distribution of the cloud, displaying patterns similar to Figure 5.4 for most ratios.

Shown in Figure 5.18 are the  $x$ -displacement plots for cores at other cloud inclinations (per panel) for each set of ratios. Visible in this series is the gradual transition from the two-point foci described in detail for the  $\varphi = 0^\circ$  clouds previously to the single focus beneath the apex as the inclination increases. These effects are clearer at medium axial ratios, near-spherical clouds being similar, and highly elongated clouds exhibiting more sporadic core formation.

### 5.4.3 THE TOTAL CORE MASS

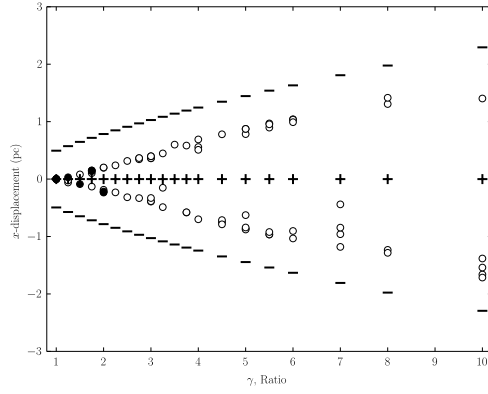
The trend of total mass of both the high density core(s) (empty circles) and extremely high density cores (solid black circles) is a decrease with  $\gamma$ . This is illustrated in Figure 5.19. The total mass of high density cores has an approximate pattern of maximum mass of  $2 M_\odot$  at  $\gamma \approx 2.25$  (with an outlier as high as almost  $3 M_\odot$  at  $\gamma = 2.75$ ) and a minimum of  $0.6 M_\odot$  at  $\gamma = 8$  (with an unusually low outlier value of only around  $0.2 M_\odot$  for  $\gamma = 6.0$ ). Clouds with lower ellipticity appear to have a higher probability of collecting greater mass in the final cores. This can be expected as the initial mass per unit length along the major axis decreases with  $\gamma$ . As a result, the amount of mass able to collapse toward the apex region decreases, which is similar to the case when  $\varphi = 0^\circ$  described in Section 4.5.1. When  $\varphi \neq 0^\circ$ , due to the wide range of variation in the final morphologies of the clouds, the amplitude of the fluctuation is similarly increased.

From the same figure, the mass of extremely condensed cores (solid black circles) in the clouds can also be seen to decrease with  $\gamma$  in a similar pattern to the high density cores. The mass of these cores corresponds to the precursor mass for possible protostars forming later in the evolution of the cloud, having a maximum of  $\approx 1.6$  and a minimum of  $\approx 0.2 M_\odot$ .

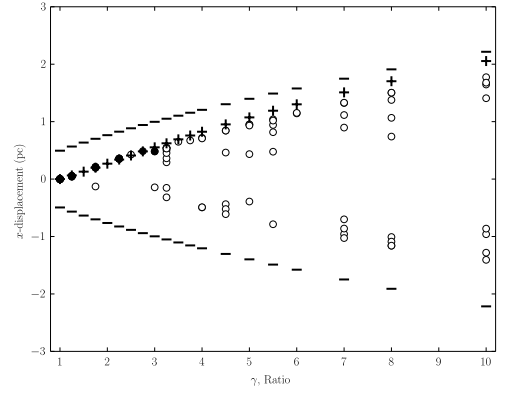
## 5.5 EVOLUTION OF CLOUDS WITH VARIED DENSITY AND IONISING FLUX

---

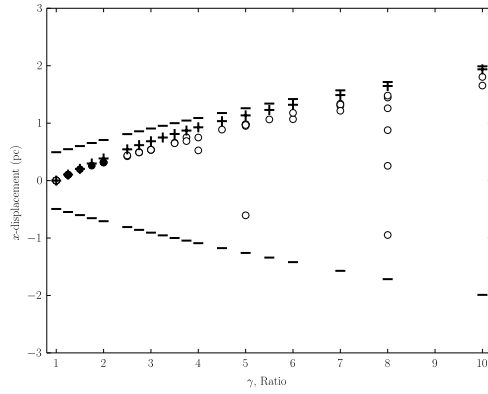
To further examine the consistency of the  $d_{\text{EUV}}$  parameter in characterising a wider variety of cloud parameters; it is of interest to expand the parameter space further to determine whether  $d_{\text{EUV}}$  itself truly describes the evolution environment, or whether



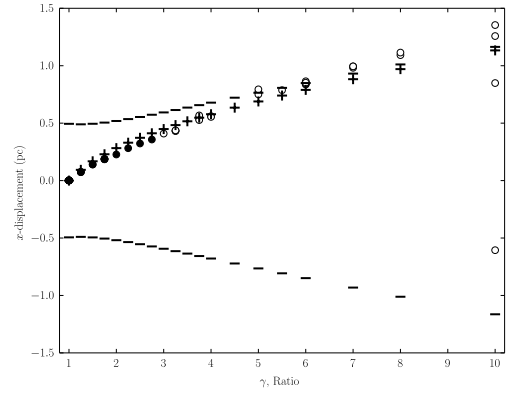
(a)  $\varphi = 0^\circ$



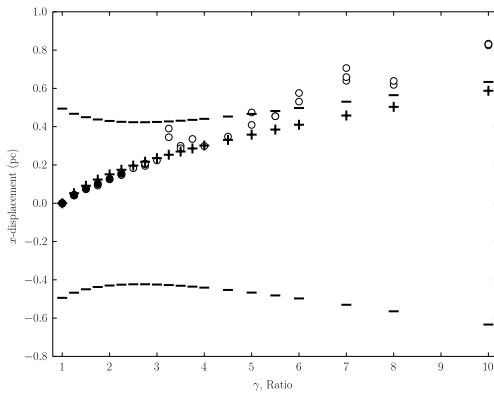
(b)  $\varphi = 15^\circ$



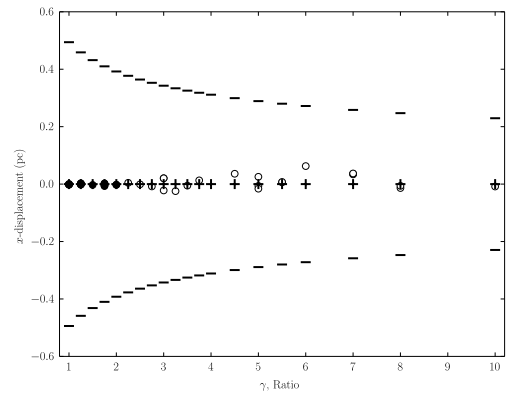
(c)  $\varphi = 30^\circ$



(d)  $\varphi = 60^\circ$



(e)  $\varphi = 75^\circ$



(f)  $\varphi = 90^\circ$

Figure 5.18: The  $x$  displacements of the cores formed in G1200 for each of multiple inclinations and axial ratios, the same for  $\varphi = 45^\circ$  can be found as Figure 5.17. The short ‘-’ indicates  $x_{\max}$ , ‘+’  $x_p$ , ‘o’ for the cores with  $10^8 \leq n_{\text{peak}} \leq 10^{12} \text{ cm}^{-3}$ , and ‘●’ for the extremely high density cores with  $n_{\text{peak}} > 10^{12} \text{ cm}^{-3}$ .

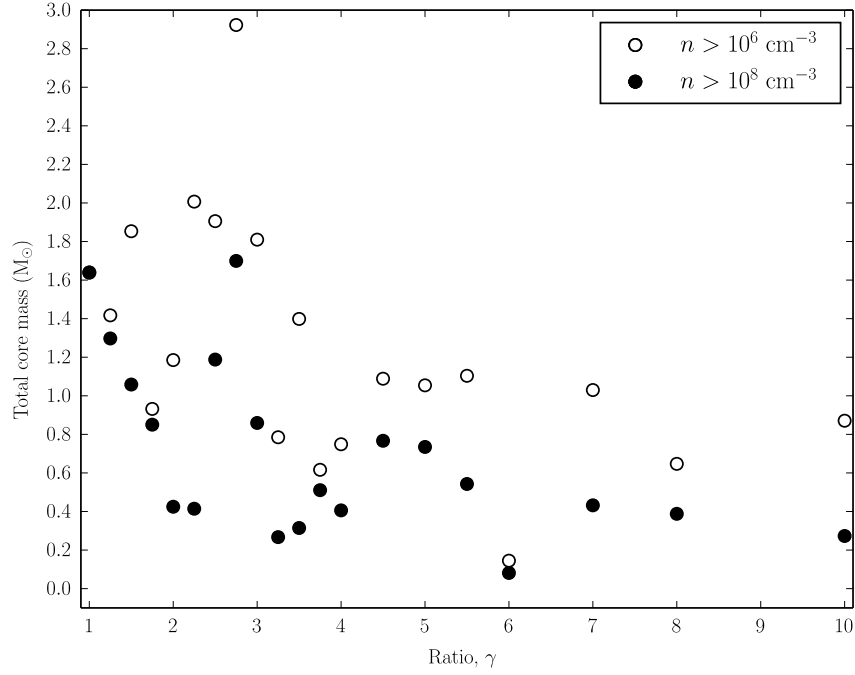


Figure 5.19: Total mass of condensed cores in cloud G1200 series at an inclination of  $45^\circ$  for varied axial ratio  $\gamma$ .

Index	$n$ $\text{cm}^{-3}$	$a$ parsec	$d_{\text{EUV}}(F_1)$ %	$d_{\text{EUV}}(F_2)$ %
G100	100	1.797	11.779	23.558
G200	200	1.427	3.708	7.416
G400	400	1.132	1.17	2.34
G600	600	0.989	0.594	1.188
G700	700	0.940	0.460	0.920
G800	800	0.899	0.368	0.736
G1000	1000	0.834	0.254	0.508
G1200	1200	0.784	0.187	0.374

Table 5.4: Parameters of molecular clouds of mass  $30 M_{\odot}$ , inclination angle  $\varphi = 60^\circ$ ,  $\gamma = 2$ , and  $a_{\text{crit}} = 0.079 \text{ pc}$ . From left to right, columns are the cloud index, initial number density, the major axis and  $d_{\text{EUV}}$  defined by Section 4.1.2, with different ionization fluxes  $F_1$  and  $F_2$  being  $1 \times 10^9$  and  $2 \times 10^9 \text{ cm}^{-2} \text{ s}^{-1}$  respectively.

this varies based on degenerate combinations of the parameters from which it is defined. This is performed by varying the densities and incident ionisation fluxes to create a series of 16 simulations with a wide and overlapping range of  $d_{\text{EUV}}$ .

A sequence of 8 different initial densities are chosen, being 100, 200, 400, 600, 700, 800, 1 000 and 1 200  $\text{cm}^{-3}$ . Two different ionization fluxes of  $F_1 = 1 \times 10^9$  and  $F_2 = 2 \times 10^9 \text{ cm}^{-2} \text{ s}^{-1}$  are applied for a total of 16 simulations; these are listed in full along with their semi-major axes and values of  $d_{\text{EUV}}$  in Table 5.4.

An inclination angle of  $60^\circ$  and  $\gamma = 2.0$  is used for all cases. This is as a result of the simulation of G1200(5) exhibiting the formation of the ‘nose’ structure in the vicinity of these geometries. This may provide a clue of how the ‘nose’ structure develops and changes with the initial properties of a cloud. The corresponding parameters of the clouds are listed in Table 5.4. The change in EUV radiation penetration depth over the initial density ( $100 \leq n \leq 1\,200 \text{ cm}^{-3}$ ) is almost two orders of magnitude, a much more dramatic variation than from changing either of  $\gamma$  or  $\varphi$  alone.

### 5.5.1 AN OVERVIEW OF THE FINAL MORPHOLOGICAL STRUCTURES

Figure 5.20 displays the final snapshots of the column density of the 8 simulations with ionization flux of  $F_1$ . The morphology of the final structure of a cloud changes from an asymmetrical type C BRC to a filamentary structure and then to an irregular structure, as the initial density is decreased from 1 200 to 100  $\text{cm}^{-3}$ , which leads to an increase of  $d_{\text{EUV}}$  from 0.187 to 11.779 %.

As shown in the top row panels, an asymmetrical type C BRC is developed in G1200, G1000, G800, and G700, with  $d_{\text{EUV}}$  of 0.187, 0.254, 0.368 and 0.460 % respectively. Although they all bear an asymmetric type C BRC morphology, the minor axis becomes narrower with increasing  $d_{\text{EUV}}$ , which results in more cloud material being photo-evaporated from their star facing surfaces. When the initial density  $n = 600 \text{ cm}^{-3}$  ( $d_{\text{EUV}} = 0.594 \%$ ), the prolate cloud evolves into a filamentary structure, as shown in the first panel in the bottom row of Figure 5.20. Clouds of initial densities of 400, 200 and 100  $\text{cm}^{-3}$  ( $d_{\text{EUV}} = 1.17, 3.708$  and  $11.779 \%$  respectively) are all seen to form irregular structures.

The final morphological structures from the simulations using the higher ionization flux  $F_2$  are presented in Figure 5.21. Similar morphological structure sequences to those seen in Figure 5.20 are observed. An asymmetrical type C BRC is formed from G1200, G1000 and G800, a filamentary structure from G700, and irregular structures in G600, G400, G200 and G100. The only difference is that the morphological transition point shifts to a cloud of higher initial density compared to the  $F_1$  simulations.

The first transition from type C BRC to filamentary morphology occurs around

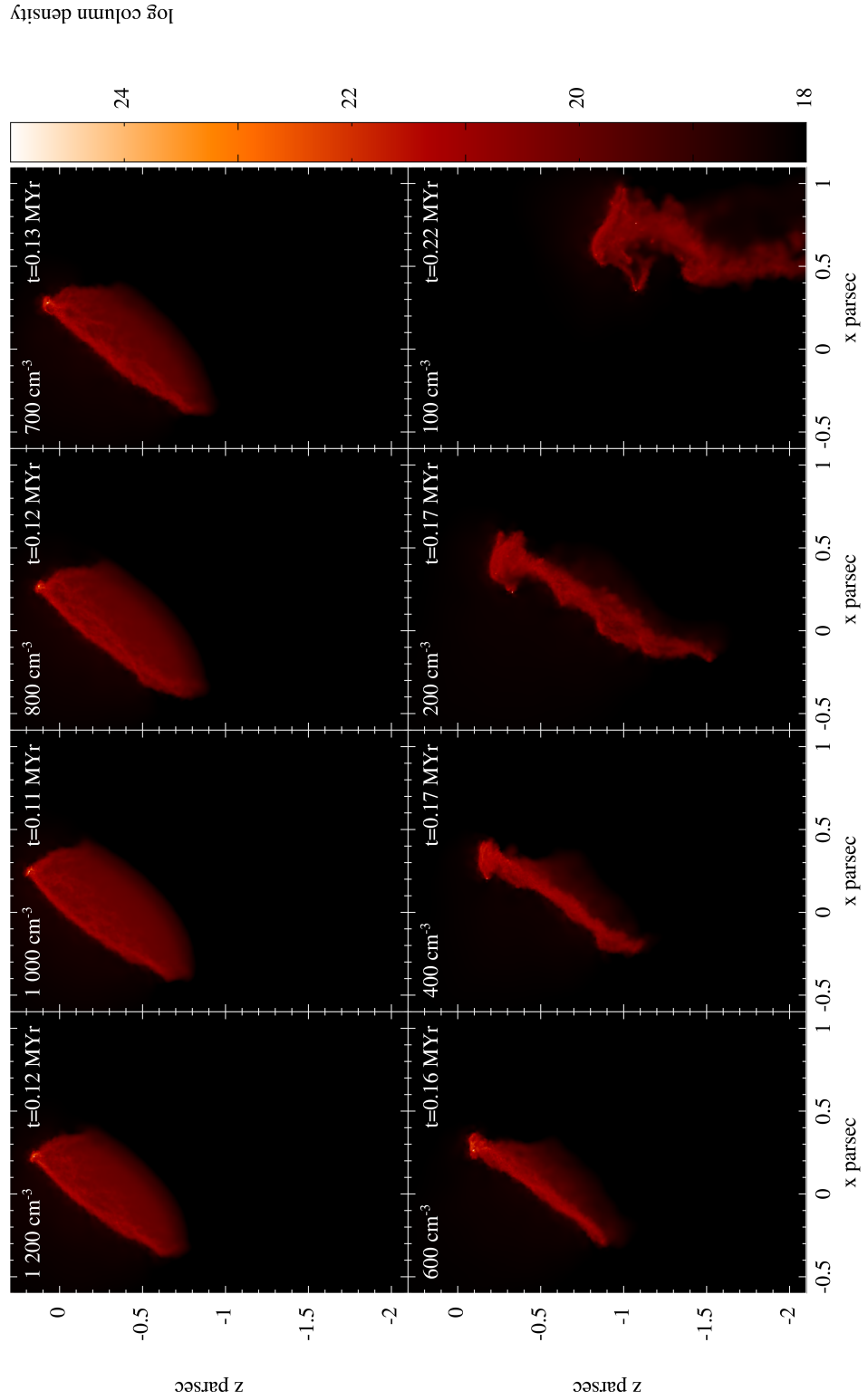


Figure 5.20: The final snapshot of the column density of clouds of initial mass of  $30 M_{\odot}$ ,  $\gamma = 2.0$  and  $\varphi = 60^{\circ}$  but different initial densities as shown in the top-left corner of each panel. The ionization flux  $F_1 = 1 \times 10^9 \text{ cm}^{-2} \text{ s}^{-1}$ . Column density is in  $\text{cm}^{-2}$ .

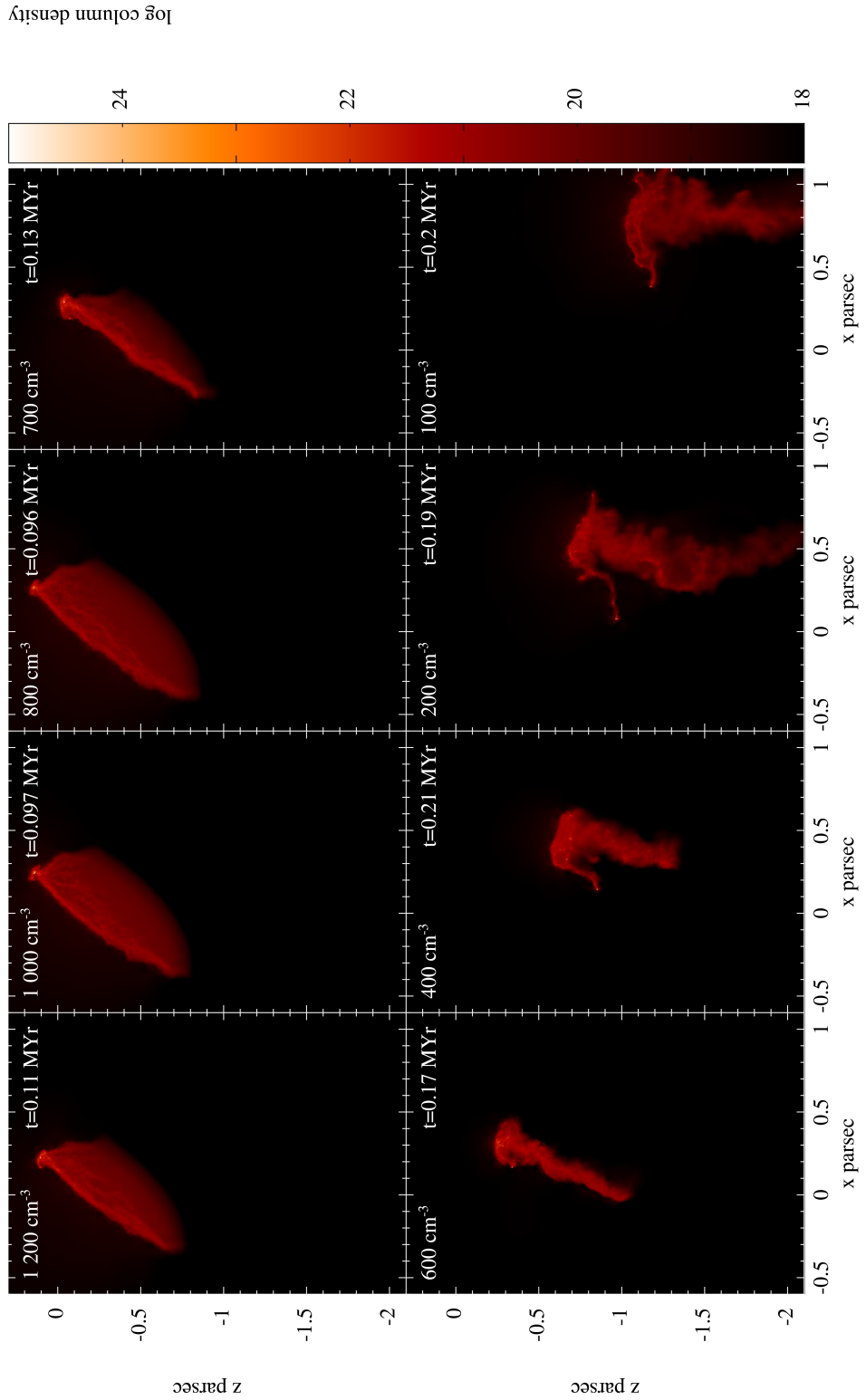


Figure 5.21: The final snapshot of the column density of the same 8 clouds as in Figure 5.20 (initial mass of  $30 M_{\odot}$ ,  $\gamma = 2.0$  and  $\varphi = 60^{\circ}$ ) but with increased incident flux of  $F_2 = 2 \times 10^9 \text{ cm}^{-2} \text{ s}^{-1}$ . Column density is in  $\text{cm}^{-2}$ .

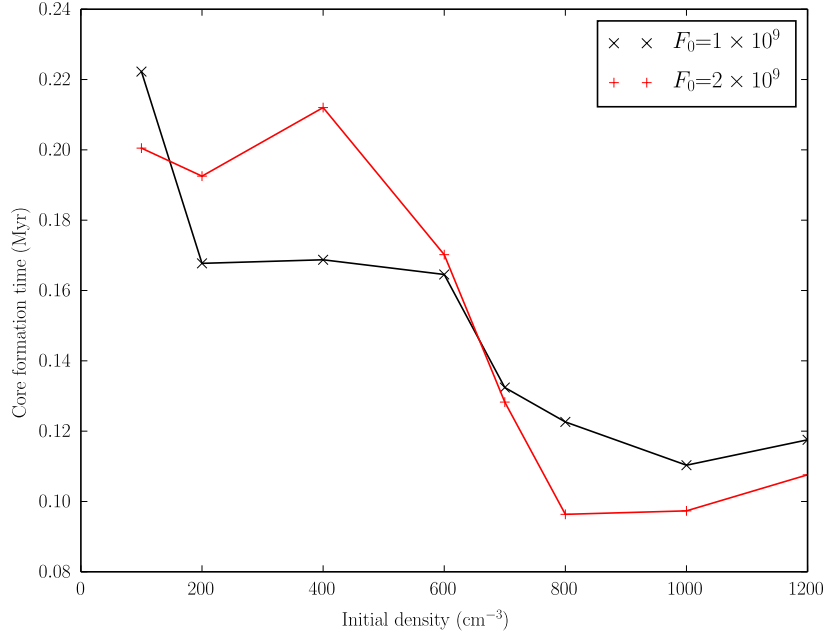


Figure 5.22: The core formation time of the  $F_1$  and  $F_2$  group clouds vs. their initial densities.

G600( $F_1$ ) and G700( $F_2$ ), and the second transition from filamentary to irregular morphology is around G400( $F_1$ ) and G600( $F_2$ ). These appear to correspond to similar  $d_{\text{EUV}}$  in each case, for both fluxes. The former transition occurs at  $d_{\text{EUV}} \approx 0.8$  and the latter at  $d_{\text{EUV}} \approx 1.1$ . This indicates that  $d_{\text{EUV}}$  remains a characteristic parameter for the dynamical evolution of a cloud for the parameter space so far investigated.

Figures 5.22 and 5.23 present the core formation time and the total mass of the RDI triggered condensed cores vs. the initial density of the clouds of the above two groups of simulated clouds, with black lines for  $F_1$  group and red for  $F_2$ . It is shown that the core formation time in both group clouds decreases with the initial density of a cloud. This is because of the stronger initial gravitational bonding in the high density cloud. For the same reason, the total mass of the condensed cores follow an increasing trend with the initial density of the cloud. However the effect of the strength of the EUV radiation flux on the timescales and masses of triggered core formation vs. initial density is two fold. When the initial density is below  $600 \text{ cm}^{-3}$  the clouds illuminated by the higher flux ( $F_2$ ) take a longer time to form condensed cores, and collect slightly more mass in their condensed cores than in the clouds illuminated by the lower flux ( $F_1$ ). This trend is reversed when the initial density is higher than  $600 \text{ cm}^{-3}$ . In other words, clouds illuminated by higher flux take a shorter time to form condensed core and collect less mass into their condensed cores than the clouds illuminated by lower

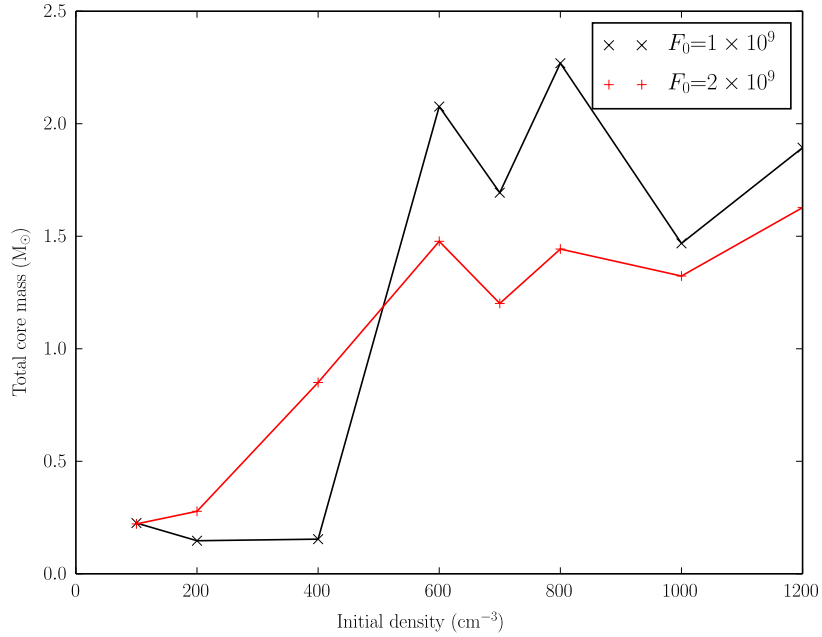


Figure 5.23: The total mass of the cores formed in  $F_1$  and  $F_2$  group clouds vs. their initial densities.

flux.

Overall, the information delivered in the above two figures suggests that the effectiveness of RDI triggered star formation, measured as a combination of formation speed and masses of the early cores, is much higher (shorter core formation time and higher total core mass) in molecular clouds of shorter  $d_{\text{EUV}}$  (corresponding to higher initial density) in both  $F_1$  and  $F_2$  group clouds.

In these sets of simulations, when  $d_{\text{EUV}} \geq 1.0\%$ , the deep penetration of the EUV radiation into the cloud causes irregular structure formation. A closer look at the above two morphological variation sequences tells that with increasing  $d_{\text{EUV}}$ , the tiny ‘nose’ structure around the apex of the asymmetrical type C BRC gradually grows and becomes an irregular ‘horse-head’ structure. In order to understand how the ‘nose’ and ‘horse-head’ structures form, further investigation into the evolutionary process of one of the above clouds which presents a clear horse-head-like morphology is conducted.

### 5.5.2 GROWING FROM ‘NOSE’ TO ‘HORSE-HEAD’ STRUCTURE

Cloud G400( $F_2$ ) is chosen to analyse the evolution of irregular structures due to its own distinctive ‘horse-head’ morphology. Figure 5.24 shows a six-snapshot column density evolutionary sequence of cloud G400( $F_2$ ), which shows a growing process from a small ‘nose’ to a ‘horse-head’ morphological structure. The corresponding RDI induced shock

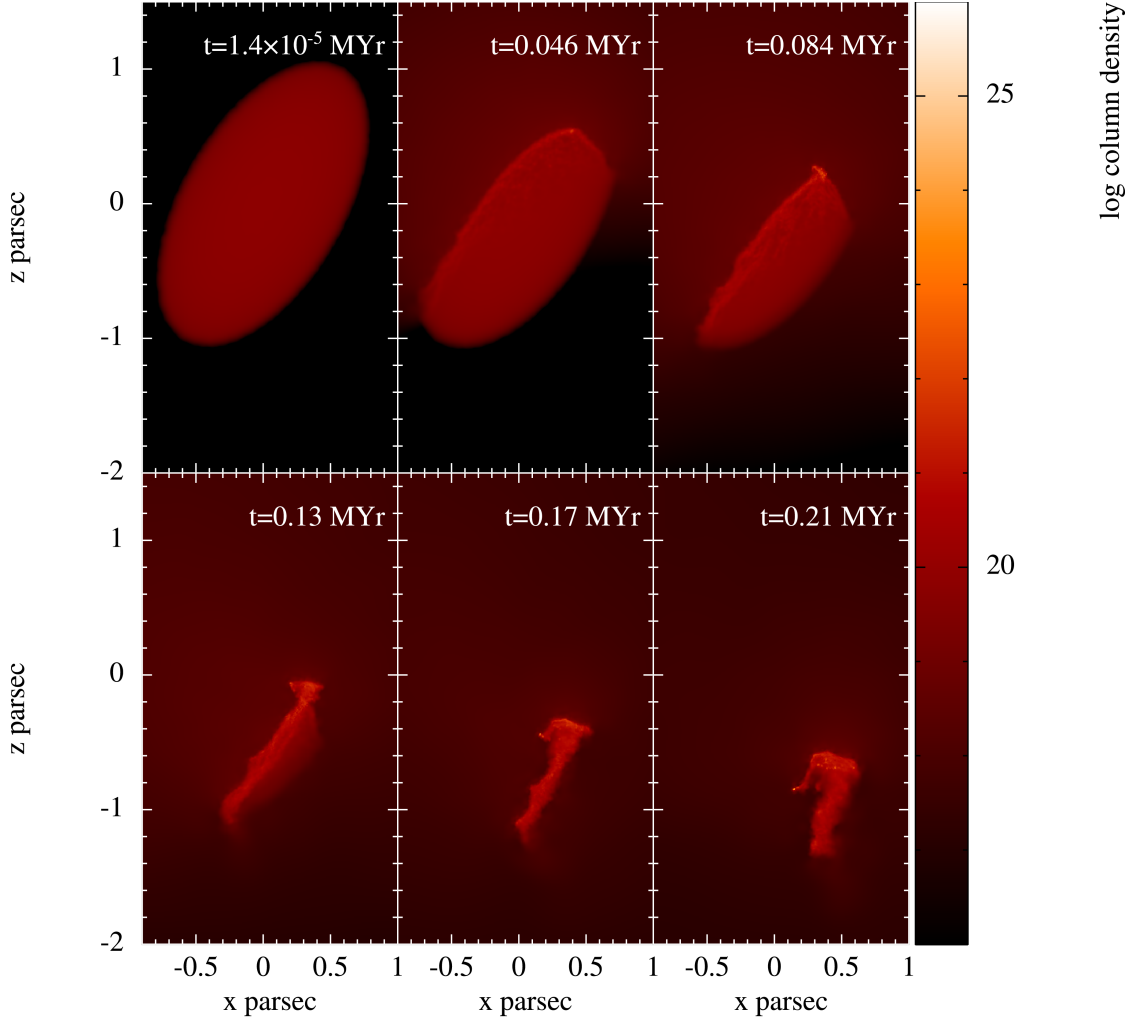


Figure 5.24: The column density evolution of a cloud G400( $F_2$ ), with an inclination angle of  $60^\circ$ . This Figure pairs with Figure 5.25, with the same frame times per panel, though note that the colour scale in this figure is specifically column density, whilst the other is cross-sectional density. Column density is in  $\text{cm}^{-2}$ .

velocity profiles for each of the snapshots are plotted in Figure 5.25, which reveals the kinematic mechanism for the morphology formation in G400( $F_2$ ).

In Figure 5.24, a shocked layer has visibly formed by  $t = 0.046$  Myr, which surrounds most of the surface of the front semi-ellipsoid and a small part of the top surface of the back semi-ellipsoid. The maximum magnitude of the shock velocity  $v_s = 12 \text{ km s}^{-1}$ , calculated as the peak velocity of non-ionized gas within the condensed shock front. Most of the shocked layer surrounding the front semi-ellipsoid propagates into the cloud smoothly toward  $(+x, -z)$  direction. Very close to the apex, the shock velocity of the front semi-ellipsoid is toward the direction of  $(x, -z)$ , and that of the back semi-ellipsoid is  $(-x, -z)$ , the gas material from the two sides of the apex converge beneath the apex to make a small ‘nose’ structure by  $t = 0.084$  Myr, as shown in the top-right

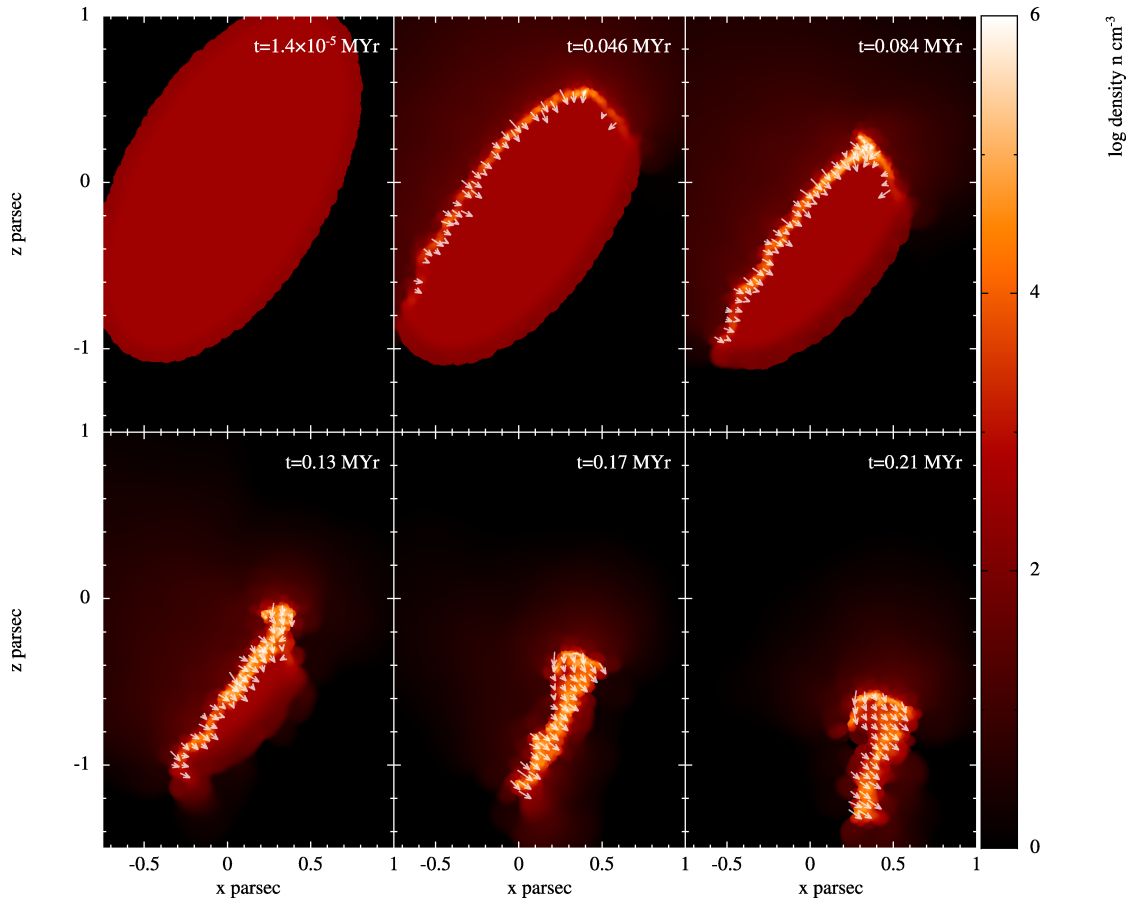


Figure 5.25: The evolution of the RDI induced shock velocity of cloud G400( $F_2$ ) overlapped in the corresponding cross-section density snapshot. The magnitude of the velocity is between  $2$  and  $12 \text{ km s}^{-1}$ . This Figure pairs with Figure 5.24, with the same frame times per panel, though note that the colour scale in this figure is specifically cross-sectional density, whilst the other is column density.

panels Figures 5.24 and 5.25.

While a small ‘nose’ structure forms at the point of  $(x, z) \approx (0.2, 0.2)$  pc and with  $v_x \approx 0$ , below the nose structure, the RDI induced shock keeps pushing the surface layer of the front semi-ellipsoid moves toward the  $(+x, -z)$  direction at the shock velocity. This makes the below-nose region of the BRC gradually produce a displacement along  $x$  direction relative to the nose. The nose becomes a short horizontal fragment by  $t = 0.13$  Myr, in which the direction of the RDI induced shock velocity is mainly along  $z$  direction. The short horizontal fragment gradually forms a ‘hook’ by  $t = 0.17$  Myr as shown in the lower middle panels of Figures 5.24 and 5.25. Further propagation of the shocked layer below the hook toward  $(+x, -z)$  direction makes the ‘hook’ structure grow to look like a ‘horse-head’ as shown in the last panels in the above two figures. The final ‘horse-head’ structure bears some resemblance to the well known Horsehead Nebula.

It is seen from the above analysis that the appearance of a ‘horse-head’ morphology in this instance is a consequence of growing a small ‘nose’ structure. The ‘nose’ structure forms if the gas around the apex of an ellipsoidal cloud converge beneath that apex due to a strong RDI induced shock effect, as described above. This requires that the cloud should have a reasonably high inclination angle, i.e.,  $\varphi > 45^\circ$  in these simulations. However the formation of a ‘nose’ structure does not necessarily lead to a ‘horse-head’ structure. For example, a small ‘nose’ formation is seen from the final morphologies of G700-1200 in the  $F_1$  series and G800-1200 in the  $F_2$  series. Whether the ‘nose’ can grow into a ‘horse-head’ also depends on the initial ionization penetration depth, i.e.,  $d_{\text{EUV}} > 1.0\%$ . The latter is to guarantee a higher enough shock velocity  $\left(v_s \approx \sqrt{\frac{F_{\text{Lyman}}}{n}}\right)$  (Bertoldi, 1989), which can push the majority of the gas which starts at lower  $z$  than the nose toward the  $(+x, -z)$  direction to ‘overtake’ it.

### 5.5.3 DEVELOPMENT OF OTHER IRREGULAR MORPHOLOGIES

Further simulations were conducted, to explore if there are other structures which form different irregular morphologies to a ‘horse-head’ as a consequence of the variation of initial conditions of the cloud and ionization flux. A series of 16 simulations with G400( $F_2$ ) of different  $\gamma = 2.0, 2.5, 3.0$  and  $3.5$ , and  $\varphi = 60, 70, 80$  and  $85^\circ$  were conducted. For all 16 clouds,  $d_{\text{EUV}} > 1.0\%$ .

The first column panels in Figure 5.26 present the final morphologies of G400( $F_2$ ) of  $\gamma = 2$  and four different initial inclination angles, which show that when the initial angle  $\varphi$  increases from  $60^\circ$ , the ‘horse-head’ in the final structure becomes longer in the  $z$  direction. The connection point between the ‘horse-head’ and the section below

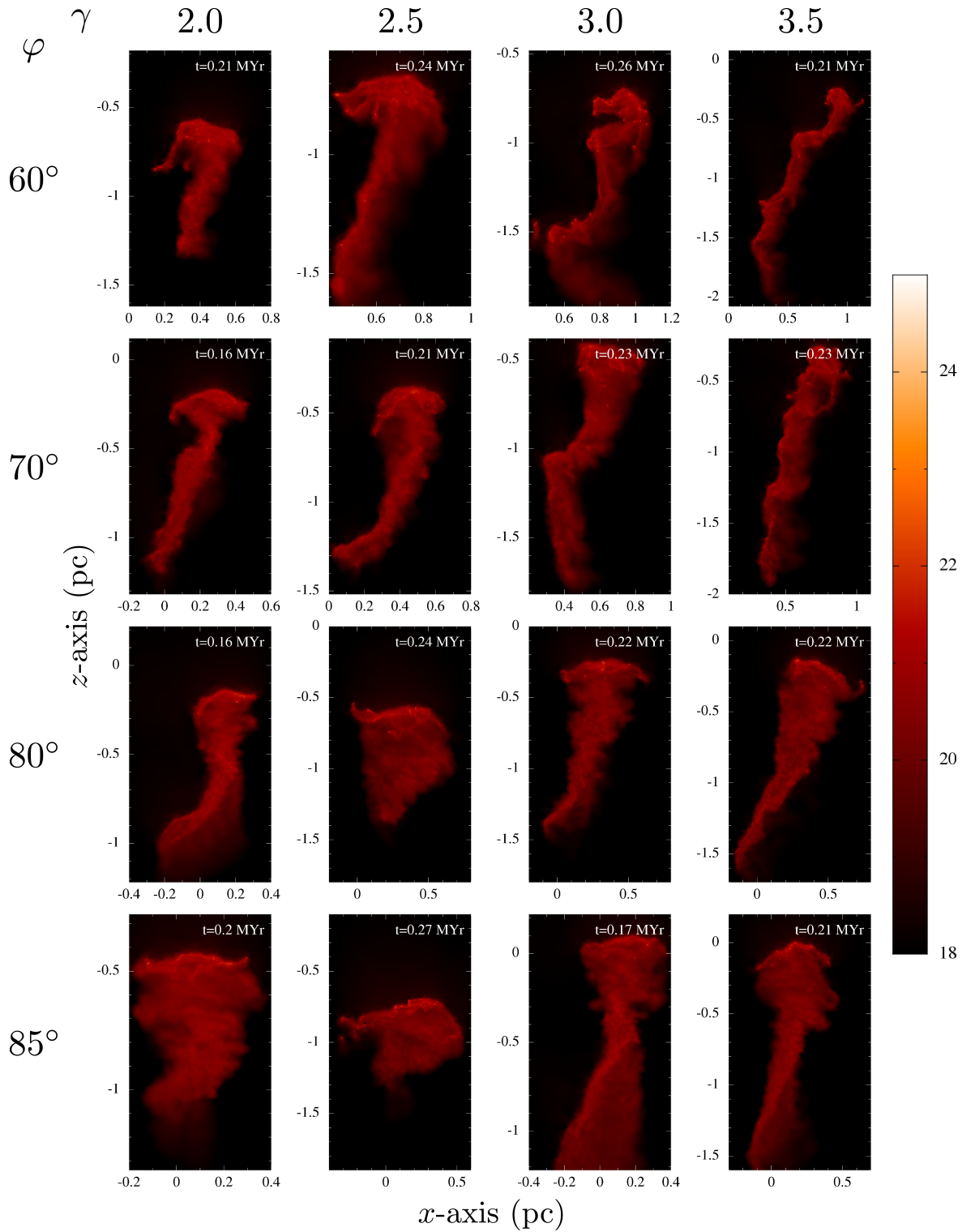


Figure 5.26: The final morphologies of the clouds G400( $F_2$ ) of different initial geometry and inclination angle. The axis scales vary between panels, because of the different initial scale of the major- and minor axes for the clouds depicted.

moves downward with  $\varphi$ . At  $85^\circ$ , the whole morphology is a broadly ‘elephant trunk’ like structure. This appears to be because the ‘nose’ structure formed in the first tens of kyr of the evolution is increasingly stretched along the  $z$  axis with increasing  $\varphi$ . The first row panels in Figure 5.26 describe the morphology change of cloud G400( $F_2$ ) with inclination angle  $\varphi = 60^\circ$  and varied  $\gamma$ . When the initial prolate cloud becomes more elliptical, in addition to a ‘horse-head’ structure, the RDI induced shock also triggers linear gravitational instability along the major axis in some clouds.

The 16 panels in Figure 5.26 present 16 different final morphologies which appear in the clouds of the initial  $(\gamma, \varphi)$  as stated above. It can be easily concluded that the larger the inclination angle, the longer the ‘horse-head’ sub-structure; and that the more elliptical the cloud initially, the thinner the final morphology is. Although, as in previous instances, their structural details differ across the range of  $\gamma$ .

The variety of morphologies which result from a wider range of combinations of the initial parameter space  $(F_{\text{Lyman}}, n, \gamma, \varphi)$  for high  $d_{\text{EUV}}$  ( $d_{\text{EUV}} > 1\%$ ) is extensive. Further instances of these variations are not shown, as their individual features fall within the broader descriptions of those already shown and add little specific detail.

As a minor point of interest, were the clouds in Figure 5.26 to exist and be observed, I have little doubt that the cloud created from the parameters  $\gamma = 3$ ,  $\varphi = 60^\circ$  (top row, third from the left) would be named the ‘Seahorse Nebula’!

## 5.6 CONCLUSIONS

---

The simulation results presented here indicate that various morphological structures found at HII regions can be generated from uniform-density ellipsoidal molecular clouds, subjected to EUV radiation at various inclinations to the cloud structure. It also reinforces the validity of the  $d_{\text{EUV}}$  parameter as a reasonable descriptor of the evolutionary direction which will be taken by a given cloud.

- I. The cloud of  $n = 1200 \text{ cm}^{-3}$ ,  $\gamma = 2$  and  $\varphi = 45^\circ$  is observed to evolve to a asymmetric BRC with embedded cores at the head of the structure. This occurs through initial creation of a shock forming a contracting dense shell across the upper surface. This propagates inwards, collecting material and causing high density collapse at the head, where the shock becomes most converged beneath the apex of the initial cloud.
- II. Rotating this cloud to the range of inclinations  $0^\circ \leq \varphi \leq 90^\circ$ , varied geometry BRCs are formed. For  $\varphi$  increasing from  $0^\circ$  these are observed to transition from

horizontal filamentary/fragment-core structure, to asymmetrical BRCs and back to symmetrical B/C BRCs as  $\varphi$  reaches  $90^\circ$ .

The increasing inclination leads to decreasing path lengths from the portion of the surface near the apex to a point of convergence between the shock fronts. This leads to decreasing core formation times for increasing  $\varphi$ . These decreasing path lengths also result in lower quantities of material being ‘swept up’ by the converging fronts, leading to generally lower total core masses for high inclinations.

For other parameters being fixed, core formation is faster in high inclination clouds than low inclination, but results in lower mass included in cores. For the density and ratio investigated ( $n = 1\,200\text{ cm}^{-3}$ ,  $\gamma = 2$ ) very low inclination clouds  $\varphi \approx 0^\circ$  result in the fragment core morphology with two main high density converged regions.

- III. Examining varied aspect ratios  $1 \leq \gamma \leq 8$  for a fixed inclination  $\varphi = 45^\circ$  demonstrates that structures of symmetrical BRC, asymmetrical BRC and filamentary form are created with increasing  $\gamma$ . Total core mass decreases with increasing aspect ratio, due to a combination of decreased mass-per-unit-length of the higher  $\gamma$  clouds, and the same focusing effect for a sharper apex observed previously.
- IV. The final morphology is sensitive to initial density, and specifically  $d_{\text{EUV}}$ , observed when varying density from 100 to  $1\,200\text{ cm}^{-3}$ . When fixing  $\gamma = 2$  and  $\varphi = 60^\circ$ , for decreasing density, the structures are seen to change from asymmetric type C BRCs, to filamentary structures similar to the high  $\gamma$  clouds to irregular structures just as the ‘horse-head’-like morphology. Throughout, the more regular BRC-like structures (with  $d_{\text{EUV}} < 1\%$ ) are found to have larger total core masses than those of irregular structures (with  $d_{\text{EUV}} > 1\%$ ).
- V. For widened  $d_{\text{EUV}}$  ranges using an alternative radiation flux of  $F_2 = 2 \times 10^9\text{ cm}^{-2}\text{ s}^{-1}$ , two key transitions in  $d_{\text{EUV}}$ -space are observed. For  $d_{\text{EUV}} \lesssim 0.8$  a type B/C BRC structure forms, for  $0.8 \lesssim d_{\text{EUV}} \lesssim 1.1$  filamentary structures form, and  $d_{\text{EUV}} \gtrsim 1.1$  irregular structures begin to form.

In summary, based on this systematic investigation on the evolution of molecular clouds (or clumps) at an HII boundary, it is possible to suggest a unified formation mechanism for the varied morphological structures seen in the published images of HII regions: Giant molecular clouds (GMCs) are clumpy and the numerous clumps are of different shapes, from spherical to highly elliptical, and with their major axes not exhibiting a strong preference for any particular alignment within their environment. When a star or a cluster of stars forms inside a GMC, the interaction between the

ionizing radiation with the surrounding molecular clumps of different shapes and orientations creates structures of various morphologies. The spherical and prolate clumps aligned with the radiation flux form standard type BRCs, the inclined prolate clumps with a shallow ionizing radiation penetration depth form asymmetrical BRCs or an inclined linear structures; the inclined prolate clumps with a deep radiation penetration depth form a variety of irregular structures, with the well known ‘horse-head’ structure being only one of them.

# CHAPTER 6

---

## CONCLUSIONS AND FUTURE WORK

---

### 6.1 CONCLUSIONS

---

The intention of this thesis was to examine the evolution of varied geometry clouds ( $\gamma$ ), of varied densities ( $n$ ) at varied angles of inclination ( $\varphi$ ) to several values of incident ionising radiation flux ( $F_0$ ). The available parameter space based on these key variables was explored to construct a picture of the formation of observed structures at H II region boundaries. A self-consistent scenario has been developed and examined based on a large number of simulations carried out, the findings of which are illustrated in the following points:

- I. With initial conditions of uniform prolate molecular clouds, a wide variety of structural features observed at the boundaries of H II regions can be replicated.
- II. The parameter  $d_{\text{EUV}}$  (defined as the ratio of the penetration depth of the ionising radiation to the longest path through the cloud) effectively describes the general pattern of evolution for a cloud.
- III. Low  $d_{\text{EUV}}$  ( $d_{\text{EUV}} \lesssim 0.8\%$ ) clouds are generally focus/foci convergent, and form symmetric or asymmetric B or C type BRCs depending on orientation. At medium  $d_{\text{EUV}}$  ( $0.8\% \lesssim d_{\text{EUV}} \lesssim 1.1\%$ ) there is a mixture of modes and filamentary or

fragment-core structures may form. At high  $d_{\text{EUV}}$  ( $1.1\% \lesssim d_{\text{EUV}} \lesssim 10\%$ ) only fragment-core and irregular structures form, with the clouds being increasingly dominated by photoevaporation. At extremely high  $d_{\text{EUV}}$  ( $d_{\text{EUV}} \gtrsim 10\%$ ) cores cannot form and the cloud will photoevaporate.

- IV. Simple initial conditions of uniform density prolate molecular clouds are good candidates to form structures including symmetric and asymmetric standard BRCs, sporadic fragment-core structures, irregular structures and filamentary structures under the effect of ionising radiation.
- V. These initial conditions represent idealised, somewhat-isolated, density enhancements within larger molecular clouds. Formation of similar shapes can be attributed to a number of prior formation mechanisms currently being investigated, such as turbulent motion and fractal arrangement. The ellipsoidal geometry is also supported by observation, which indicate a large proportion of early clouds with  $\gamma \neq 1$ .

## 6.2 FUTURE WORK

---

Although this work has revealed several likely patterns of evolution for molecular clouds there are still questions directly related to the investigation which remain unanswered, or expansions to the work which were slightly outside of the intended scope. The following is an overview of several such topics which could form extensions to the work already presented, or arise from questions determined by the results already found.

### 6.2.1 SYNTHETIC OBSERVATIONS

There is a great deal more work that can be done investigating the similarities and dissimilarities between simulated and observed objects (Goodman, 2011; Haworth et al., 2012). In particular, with the velocity profiles available from the simulations which describe the most interesting aspects of the front motion, investigation into observed velocity profiles in more detail could be performed (Haworth et al., 2015).

As fascinating as details provided by computational simulations in and of themselves can be, it is vital to be able to find methods to compare them on common ground to observations. This can be done in multiple ways, some have become fairly commonly used, and some are beginning to be developed in more detail. One such method is the production of ‘synthetic observations’. In this method, the data from simulations are

processed in a way directly analogous to actual observations, with the relevant limitations and bounds. Observations are invariably limited to two-dimensional projections, detailed line-of-sight distances being virtually impossible for the scenarios observed. This is sometimes coupled, through spectrometry, with line-of-sight velocity maps to produce 3D data cubes, but this still does not provide a true three dimensional image in the way that simulations are frequently analysed.

As an alternative, it is possible to ‘observe’ the relevant emissions from the simulation at some projected direction and distance. These maps can be produced in useful analytical observed lines such as  $H\alpha$  and the carbon monoxide isotopic lines ( $^{12}\text{C}^{16}\text{O}$ ,  $^{13}\text{C}^{16}\text{O}$  &  $^{12}\text{C}^{18}\text{O}$ ). The former is widely used, due to hydrogen abundance and ability to observe it easily. It does not provide details for dense cloud regions, however, as it is produced by atomic hydrogen. Molecular hydrogen, at cold temperatures ( $\approx 10\text{ K}$ ), has no emissions which are observable. In the stead of observing it directly, tracers must be used; emissions from materials which have a known, or estimated, ratio with molecular hydrogen. One of these sets are the aforementioned carbon monoxide lines. They are advantageous as, though affected by self shielding and so will attenuate, they still have a high penetration depth through clouds of mostly hydrogen and dust grains. This means they can be used to examine fairly deep into a cloud, aided by slightly varying penetrations of the different isotopic forms.

As the code used here explicitly tracks carbon monoxide abundance as part of the chemical evolution, highly detailed maps would be possible. These are useful at providing line-of-sight velocity maps, as the distribution in spectral space is easily observed through spectroscopy and translated into radial velocity distributions. This can be calculated from the simulations by using the net gas velocity of a particle, the temperature and, from the former, an estimate of the excited state distribution, to produce artificial contributions to emission. Along a given line of sight (working from the far side of the cloud towards the observer), these can then be summed, and attenuated, between particles along the line of sight. The end result would be a detailed spectra, directly comparable with those obtained from observation.

### 6.2.2 SEQUENTIAL STAR FORMATION IN BRC ASSOCIATIONS

One major limitation of the current simulations is that they are only able to simulate up to the initial creation of protostellar cores. This prevents the tracking of the further evolution of any particular core(s) or the formation of any others. A computational technique which circumvents this is the ‘sink particle’ concept (Bate et al., 1995). In this extension to the model, clusters of SPH particles representing collapsing gas are removed from the simulation, and replaced with one of these sink particles. The sink

particle represents a non-fluid element, acting instead as a condensed object, onto which other SPH particles can accrete.

Implementation of sink particles permits a simulation to continue evolving beyond the convention density-limited timestep. In turn, this enables more complex and prolonged behaviours to be examined. One of particular interest is sequential star formation (Matsuyanagi et al., 2006; Chauhan et al., 2009; Fukuda et al., 2013). In which stages of star formation, propagating away from the central illuminating source in an HII region, is observed to occur. This has been observed in a number of circumstances, and it would be of great interest to determine whether the simulations presented here would exhibit the same effect, given sufficient further time.

### 6.2.3 SEMI-ANALYTICAL MODEL

Presented in Section 5.3.5 is the description of the qualitative interpretation of the shock front motion from an non-spherical upper surface. In particular Figure 5.15 depicts the simple surface-normal velocity vectors, quite reasonably appearing to give an approximation of the behaviour observed in the actual simulations. This could be developed further, in a similar manner to Bertoldi (1989) to produce a numerical, semi-analytical toy model of an arbitrarily configured upper cloud surface.

### 6.2.4 NON-UNIFORM INITIAL CONDITIONS

One of the most artificial aspects of the current initial conditions setup is that the cloud is a uniform density. Whilst this should not substantially affect the behaviour of the shock front (its motion should be at least qualitatively the same), modifying the scenario to something more ‘realistic’ is still a potential path for investigation.

As referenced in several previous sections, there is substantial evidence to support clouds being clumpy at a wide range of length scales (Larson, 1981; Shu et al., 1987; Williams et al., 1994, 2000). This is compounded by the expectation of turbulent motion at various length scales, as part of other investigations (Klessen et al., 2000; Federrath et al., 2010).

One option would be to simulate a continuous medium, rather than just the cloud. This would entail adding in material for the very low density ( $< 10 \text{ cm}^{-3}$ ) ambient medium, which could then increase smoothly up to the position of the cloud (density enhancement) itself. It is then a question of determining what profile the structure should have, given that there is no isolated non-spherical pressure supported density profile solution.

This is not necessarily an issue, as further work could be performed investigating

the extent to which such objects are likely to be transient, only temporarily existing in the observed configuration. With further detail on the dynamics likely to produce this, initial conditions, including velocity profiles, could be produced as a result.

### 6.2.5 ALTERNATIVE GEOMETRIES

Several analyses suggest that the ‘true’ effective initial shape of the manner of cloud / clump initial conditions examined here are tri-axial rather than prolate (Jones et al., 2001; Gammie et al., 2003; Li et al., 2004). Investigating tri-axial initial conditions is a trivial change to facilitate, but requires a vastly increased parameter space to investigate adequately. Whilst the parameters can make use of the theoretical probability distribution modelling of the aforementioned research, this still requires an order of magnitude increase in required simulations to examine in even as much detail as the simple prolate axial ratio (with inclination) investigation presented here. This is made worse by the potential requirement of a second inclination angle variable, due to the further lack of symmetry. Nonetheless, this represents a viable route to investigate with a sensibly planned map of simulations.

The results of such an investigation would likely inform as to the reliability of the theoretical axial distributions, along with production of a more representative range of final morphologies.

---

## BIBLIOGRAPHY

---

- A. Abergel, D. Teyssier, J. P. Bernard, F. Boulanger, A. Coulais, D. Fosse, E. Falgarone, M. Gerin, M. Perault, J.-L. Puget, L. Nordh, G. Olofsson, M. Hultgren, A. A. Kaas, P. André, S. Bontemps, M. M. Casali, C. J. Cesarsky, E. Copet, J. Davies, T. Montmerle, P. Persi, and F. Sibille. ISOCAM and molecular observations of the edge of the Horsehead nebula. *A&A*, 410:577–585, November 2003. doi: 10.1051/0004-6361:20030878.
- A. W. Appel. An Efficient Program for Many-Body Simulation. *SIAM Journal on Scientific and Statistical Computing*, vol. 6, no. 1, January 1985, p. 85-103., 6: 85–103, January 1985.
- P. J. Armitage. Dynamics of Protoplanetary Disks. *ARA&A*, 49:195–236, September 2011. doi: 10.1146/annurev-astro-081710-102521.
- J. Barnes and P. Hut. A hierarchical  $O(N \log N)$  force-calculation algorithm. *Nature*, 324:446–449, December 1986. doi: 10.1038/324446a0.
- P. Bastien. Gravitational collapse and fragmentation of isothermal, non-rotating, cylindrical clouds. *A&A*, 119:109–116, March 1983.
- M. R. Bate and A. Burkert. Resolution requirements for smoothed particle hydrodynamics calculations with self-gravity. *MNRAS*, 288:1060–1072, July 1997.
- M. R. Bate, I. A. Bonnell, and N. M. Price. Modelling accretion in protobinary systems. *MNRAS*, 277:362–376, November 1995.
- E. A. Bergin, W. D. Langer, and P. F. Goldsmith. Gas-phase chemistry in dense interstellar clouds including grain surface molecular depletion and desorption. *ApJ*, 441:222–243, March 1995. doi: 10.1086/175351.

- F. Bertoldi. The photoevaporation of interstellar clouds. I - Radiation-driven implosion. *ApJ*, 346:735–755, November 1989. doi: 10.1086/168055.
- F. Bertoldi and C. F. McKee. The photoevaporation of interstellar clouds. II - Equilibrium cometary clouds. *ApJ*, 354:529–548, May 1990. doi: 10.1086/168713.
- T. G. Bisbas, A. P. Whitworth, R. Wünsch, D. A. Hubber, and S. Walch. Radiation Driven Implosion and Triggered Star Formation. In J. Alves, B. G. Elmegreen, J. M. Girart, and V. Trimble, editors, *Computational Star Formation*, volume 270 of *IAU Symposium*, pages 263–266, April 2011a. doi: 10.1017/S1743921311000482.
- T. G. Bisbas, R. Wünsch, A. P. Whitworth, D. A. Hubber, and S. Walch. Radiation-driven Implosion and Triggered Star Formation. *ApJ*, 736:142, August 2011b. doi: 10.1088/0004-637X/736/2/142.
- L. Blitz. Giant molecular clouds. In E. H. Levy and J. I. Lunine, editors, *Protostars and Planets III*, pages 125–161, 1993.
- B. J. Bok and E. F. Reilly. Small Dark Nebulae. *ApJ*, 105:255, March 1947. doi: 10.1086/144901.
- W. B. Bonnor. Boyle’s Law and gravitational instability. *MNRAS*, 116:351, 1956.
- A. P. Boss. Collapse and Fragmentation of Molecular Cloud Cores. X. Magnetic Braking of Prolate and Oblate Cores. *ApJ*, 697:1940–1945, June 2009. doi: 10.1088/0004-637X/697/2/1940.
- W. B. Burton. The morphology of hydrogen and of other tracers in the Galaxy. *ARA&A*, 14:275–306, 1976. doi: 10.1146/annurev.aa.14.090176.001423.
- M. J. Cai and R. E. Taam. The Equilibrium Structure of Prolate Magnetized Molecular Cores. *ApJ*, 709:L79–L82, January 2010. doi: 10.1088/2041-8205/709/1/L79.
- A. G. W. Cameron and J. W. Truran. The supernova trigger for formation of the solar system. *Icarus*, 30:447–461, March 1977. doi: 10.1016/0019-1035(77)90101-4.
- J. Cantó, A. Raga, W. Steffen, and P. R. Shapiro. Shadows behind Neutral Clumps in Photoionized Regions. *ApJ*, 502:695–707, August 1998. doi: 10.1086/305946.
- N. Chauhan, A. K. Pandey, K. Ogura, D. K. Ojha, B. C. Bhatt, S. K. Ghosh, and P. S. Rawat. Triggered star formation and evolution of T-Tauri stars in and around bright-rimmed clouds. *MNRAS*, 396:964–983, June 2009. doi: 10.1111/j.1365-2966.2009.14756.x.

- N. Chauhan, A. K. Pandey, K. Ogura, J. Jose, D. K. Ojha, M. R. Samal, and H. Mito. Star formation in bright-rimmed clouds and clusters associated with the W5 E H II region. *MNRAS*, 415:1202–1219, August 2011. doi: 10.1111/j.1365-2966.2011.18742.x.
- R. Courant, K. Friedrichs, and H. Lewy. Über die partiellen Differenzgleichungen der mathematischen Physik. *Mathematische Annalen*, 100:32–74, 1928. doi: 10.1007/BF01448839.
- C. L. Curry and S. W. Stahler. The Structure and Evolution of Magnetized Cloud Cores in a Zero-Density Background. *ApJ*, 555:160–177, July 2001. doi: 10.1086/321475.
- J. E. Dale, I. A. Bonnell, C. J. Clarke, and M. R. Bate. Photoionizing feedback in star cluster formation. *MNRAS*, 358:291–304, March 2005. doi: 10.1111/j.1365-2966.2005.08806.x.
- J. E. Dale, I. A. Bonnell, and A. P. Whitworth. Ionization-induced star formation - I. The collect-and-collapse model. *MNRAS*, 375:1291–1298, March 2007. doi: 10.1111/j.1365-2966.2006.11368.x.
- L. Deharveng and M. Maucherat. Optical study of the Carina Nebula. *A&A*, 41:27–36, June 1975.
- L. Deharveng, A. Zavagno, and J. Caplan. Triggered massive-star formation on the borders of Galactic H II regions. I. A search for “collect and collapse” candidates. *A&A*, 433:565–577, April 2005. doi: 10.1051/0004-6361:20041946.
- L. Deharveng, A. Zavagno, F. Schuller, J. Caplan, M. Pomarès, and C. De Breuck. Star formation around RCW 120, the perfect bubble. *A&A*, 496:177–190, March 2009. doi: 10.1051/0004-6361/200811337.
- L. Deharveng, F. Schuller, L. D. Anderson, A. Zavagno, F. Wyrowski, K. M. Menten, L. Bronfman, L. Testi, C. M. Walmsley, and M. Wienen. A gallery of bubbles. The nature of the bubbles observed by Spitzer and what ATLASGAL tells us about the surrounding neutral material. *A&A*, 523:A6, November 2010. doi: 10.1051/0004-6361/201014422.
- L. Deharveng, A. Zavagno, L. D. Anderson, F. Motte, A. Abergel, P. André, S. Bon-temps, G. Leleu, H. Roussel, and D. Russeil. Interstellar matter and star formation in W5-E. A Herschel view. *A&A*, 546:A74, October 2012. doi: 10.1051/0004-6361/201219131.

- S. Diehl, G. Rockefeller, C. L. Fryer, D. Riethmiller, and T. S. Statler. Generating Optimal Initial Conditions for Smooth Particle Hydrodynamics Simulations. *ArXiv e-prints*, November 2012.
- C. L. Dobbs and J. E. Pringle. The exciting lives of giant molecular clouds. *MNRAS*, 432:653–667, June 2013. doi: 10.1093/mnras/stt508.
- S. D. Doty, S. E. Everett, Y. L. Shirley, N. J. Evans, and M. L. Palotti. Constraining the structure of the non-spherical pre-protostellar core L1544. *MNRAS*, 359:228–236, May 2005. doi: 10.1111/j.1365-2966.2005.08893.x.
- J. E. Dyson and D. A. Williams. *The physics of the interstellar medium*. CRC Press, 1997.
- R. Ebert. Zur Instabilität kugelsymmetrischer Gasverteilungen. Mit 2 Textabbildungen. *ZAp*, 42:263, 1957.
- A. S. Eddington. On the radiative equilibrium of the stars. *MNRAS*, 77:16–35, November 1916.
- B. G. Elmegreen. Star Formation from Galaxies to Globules. *ApJ*, 577:206–220, September 2002. doi: 10.1086/342177.
- B. G. Elmegreen and C. J. Lada. Sequential formation of subgroups in OB associations. *ApJ*, 214:725–741, June 1977. doi: 10.1086/155302.
- B. G. Elmegreen and J. Scalo. Interstellar Turbulence I: Observations and Processes. *ARA&A*, 42:211–273, September 2004. doi: 10.1146/annurev.astro.41.011802.094859.
- A. E. Evrard. Beyond N-body - 3D cosmological gas dynamics. *MNRAS*, 235:911–934, December 1988.
- C. Federrath, R. Banerjee, P. C. Clark, and R. S. Klessen. Modeling Collapse and Accretion in Turbulent Gas Clouds: Implementation and Comparison of Sink Particles in AMR and SPH. *ApJ*, 713:269–290, April 2010. doi: 10.1088/0004-637X/713/1/269.
- P. N. Foster and A. P. Boss. Triggering Star Formation with Stellar Ejecta. *ApJ*, 468:784, September 1996. doi: 10.1086/177735.
- N. Fukuda, J. Miao, K. Sugitani, K. Kawahara, M. Watanabe, M. Nakano, and A. J. Pickles. Triggered Star Formation in a Bright-rimmed Cloud (BRC 5) of IC 1805. *ApJ*, 773:132, August 2013. doi: 10.1088/0004-637X/773/2/132.

- D. A. Fulk and D. W. Quinn. An Analysis of 1-D Smoothed Particle Hydrodynamics Kernels. *Journal of Computational Physics*, 126:165–180, June 1996. doi: 10.1006/jcph.1996.0128.
- C. F. Gammie, Y.-T. Lin, J. M. Stone, and E. C. Ostriker. Analysis of Clumps in Molecular Cloud Models: Mass Spectrum, Shapes, Alignment, and Rotation. *ApJ*, 592:203–216, July 2003. doi: 10.1086/375635.
- M. Gholipour and M. Nejad-Asghar. The transformation of molecular cloud cores from spherical to prolate shape via surface heating. *MNRAS*, 429:3166–3173, March 2013. doi: 10.1093/mnras/sts575.
- R. A. Gingold and J. J. Monaghan. Smoothed particle hydrodynamics - Theory and application to non-spherical stars. *MNRAS*, 181:375–389, November 1977.
- S. C. O. Glover and P. C. Clark. Is molecular gas necessary for star formation? *MNRAS*, 421:9–19, March 2012. doi: 10.1111/j.1365-2966.2011.19648.x.
- P. F. Goldsmith and W. D. Langer. Molecular cooling and thermal balance of dense interstellar clouds. *ApJ*, 222:881–895, June 1978. doi: 10.1086/156206.
- H. Gong and E. C. Ostriker. Dense Core Formation in Supersonic Turbulent Converging Flows. *ApJ*, 729:120, March 2011. doi: 10.1088/0004-637X/729/2/120.
- A. A. Goodman. A Guide to Comparisons of Star Formation Simulations with Observations. In J. Alves, B. G. Elmegreen, J. M. Girart, and V. Trimble, editors, *Computational Star Formation*, volume 270 of *IAU Symposium*, pages 511–519, April 2011. doi: 10.1017/S1743921311000901.
- U. Gorti and D. Hollenbach. Photoevaporation of Clumps in Photodissociation Regions. *ApJ*, 573:215–237, July 2002. doi: 10.1086/340556.
- M. Gritschneder, T. Naab, A. Burkert, S. Walch, F. Heitsch, and M. Wetzstein. iVINE - Ionization in the parallel TREE/SPH code VINE: first results on the observed age-spread around O-stars. *MNRAS*, 393:21–31, February 2009a. doi: 10.1111/j.1365-2966.2008.14185.x.
- M. Gritschneder, T. Naab, S. Walch, A. Burkert, and F. Heitsch. Driving Turbulence and Triggering Star Formation by Ionizing Radiation. *ApJL*, 694:L26–L30, March 2009b. doi: 10.1088/0004-637X/694/1/L26.

- M. Gritschneider, D. N. C. Lin, S. D. Murray, Q.-Z. Yin, and M.-N. Gong. The Supernova Triggered Formation and Enrichment of Our Solar System. *ApJ*, 745: 22, January 2012. doi: 10.1088/0004-637X/745/1/22.
- H. J. Habing. The interstellar radiation density between 912 Å and 2400 Å. *Bull. Astron. Inst. Netherlands*, 19:421, January 1968.
- L. K. Haikala, M. M. Mäkelä, and P. Väisänen. Star formation in Cometary Globule 1: the second generation. *A&A*, 522:A106, November 2010. doi: 10.1051/0004-6361/201014524.
- J. Harju, M. Sahu, C. Henkel, T. L. Wilson, K. C. Sahu, and S. R. Pottasch. Molecular gas in cometary globules - CG 1. *A&A*, 233:197–206, July 1990.
- T. J. Haworth and T. J. Harries. Radiation hydrodynamics of triggered star formation: the effect of the diffuse radiation field. *MNRAS*, 420:562–578, February 2012. doi: 10.1111/j.1365-2966.2011.20062.x.
- T. J. Haworth, T. J. Harries, and D. M. Acreman. Testing diagnostics of triggered star formation. *MNRAS*, 426:203–217, October 2012. doi: 10.1111/j.1365-2966.2012.21838.x.
- T. J. Haworth, E. J. Tasker, Y. Fukui, K. Torii, J. E. Dale, K. Shima, K. Takahira, A. Habe, and K. Hasegawa. Isolating signatures of major cloud-cloud collisions using position-velocity diagrams. *MNRAS*, 450:10–20, June 2015. doi: 10.1093/mnras/stv639.
- M. Hayashi, S. Suzuki, T. Omodaka, and T. Hasegawa. The bright-rimmed molecular cloud around S140 IRS. I - CS (J = 1-0) observations. *ApJ*, 288:170–174, January 1985. doi: 10.1086/162776.
- M. Hayashi, Y. Itoh, and Y. Oasa. Near-Infrared Survey of Bright Rimmed Clouds. *PASJ*, 64:96, October 2012. doi: 10.1093/pasj/64.5.96.
- P. Hennebelle and B. Commerçon. Theories of the massive star formation: a (short) review. *ArXiv e-prints*, September 2012.
- L. Hernquist and N. Katz. TREESPH - A unification of SPH with the hierarchical tree method. *ApJS*, 70:419–446, June 1989. doi: 10.1086/191344.
- D. A. Hubber, C. P. Batty, A. McLeod, and A. P. Whitworth. SEREN - a new SPH code for star and planet formation simulations. Algorithms and tests. *A&A*, 529: A27, May 2011. doi: 10.1051/0004-6361/201014949.

- D. A. Hubber, S. Walch, and A. P. Whitworth. An improved sink particle algorithm for SPH simulations. *MNRAS*, 430:3261–3275, April 2013. doi: 10.1093/mnras/stt128.
- D. G. Hummer and M. J. Seaton. The ionization structure of planetary nebulae, I. Pure hydrogen nebulae. *MNRAS*, 125:437, 1963.
- J. D. Hunter. Matplotlib: A 2d graphics environment. *Computing In Science & Engineering*, 9(3):90–95, 2007.
- Inkscape Team. Inkscape 0.48.5, 2014. URL <http://www.inkscape.org/>.
- J. H. Jeans. The Stability of a Spherical Nebula. *Royal Society of London Philosophical Transactions Series A*, 199:1–53, 1902. doi: 10.1098/rsta.1902.0012.
- C. E. Jones, S. Basu, and J. Dubinski. Intrinsic Shapes of Molecular Cloud Cores. *ApJ*, 551:387–393, April 2001. doi: 10.1086/320093.
- J. L. Karr, A. Noriega-Crespo, and P. G. Martin. A Multiwavelength Study of IC 63 and IC 59. *AJ*, 129:954–968, February 2005. doi: 10.1086/426912.
- O. Kessel-Deynet and A. Burkert. Ionizing radiation in smoothed particle hydrodynamics. *MNRAS*, 315:713–721, July 2000. doi: 10.1046/j.1365-8711.2000.03451.x.
- O. Kessel-Deynet and A. Burkert. Radiation-driven implosion of molecular cloud cores. *MNRAS*, 338:545–554, January 2003. doi: 10.1046/j.1365-8711.2003.05737.x.
- T. M. Kinnear, J. Miao, G. J. White, and S. Goodwin. Evolution of prolate molecular clouds at H II boundaries - I. Formation of fragment-core structures. *MNRAS*, 444:1221–1235, October 2014. doi: 10.1093/mnras/stu1510.
- T. M. Kinnear, J. Miao, G. J. White, K. Sugitani, and S. Goodwin. Evolution of prolate molecular clouds at H II boundaries - II. Formation of BRCs of asymmetrical morphology. *MNRAS*, 450:1017–1031, June 2015. doi: 10.1093/mnras/stv637.
- R. S. Klessen, F. Heitsch, and M.-M. Mac Low. Gravitational Collapse in Turbulent Molecular Clouds. I. Gasdynamical Turbulence. *ApJ*, 535:887–906, June 2000. doi: 10.1086/308891.
- P. Kroupa. On the variation of the initial mass function. *MNRAS*, 322:231–246, April 2001. doi: 10.1046/j.1365-8711.2001.04022.x.
- M. R. Krumholz. Star Formation in Molecular Clouds. In E. Telles, R. Dupke, and D. Lazzaro, editors, *American Institute of Physics Conference Series*, volume 1386

- of *American Institute of Physics Conference Series*, pages 9–57, September 2011. doi: 10.1063/1.3636038.
- T. Kusune, K. Sugitani, J. Miao, M. Tamura, Y. Sato, J. Kwon, M. Watanabe, S. Nishiyama, T. Nagayama, and S. Sato. Near-IR Imaging Polarimetry toward a Bright-Rimmed Cloud: Magnetic Field in SFO 74. *ArXiv e-prints*, November 2014.
- C. J. Lada and J. H. Black. CO observations of the bright-rimmed cloud B35. *ApJ*, 203:L75–L79, January 1976. doi: 10.1086/182023.
- R. B. Larson. Numerical calculations of the dynamics of collapsing proto-star. *MNRAS*, 145:271, 1969.
- R. B. Larson. Turbulence and star formation in molecular clouds. *MNRAS*, 194: 809–826, March 1981.
- R. B. Larson and S. Starrfield. On the formation of massive stars and the upper limit of stellar masses. *A&A*, 13:190–197, July 1971.
- B. Lefloch and B. Lazareff. Cometary globules. 1: Formation, evolution and morphology. *A&A*, 289:559–578, September 1994.
- B. Lefloch and B. Lazareff. Cometary globules. II. Observational tests of radiation-driven implosion: the case of CG7S. *A&A*, 301:522–+, September 1995.
- B. Lefloch, B. Lazareff, and A. Castets. Cometary globules. III. Triggered star formation in IC 1848. *A&A*, 324:249–262, August 1997.
- P. S. Li, M. L. Norman, M.-M. Mac Low, and F. Heitsch. The Formation of Self-Gravitating Cores in Turbulent Magnetized Clouds. *ApJ*, 605:800–818, April 2004. doi: 10.1086/382652.
- S. Li, A. Frank, and E. G. Blackman. Triggered star formation and its consequences. *MNRAS*, 444:2884–2892, November 2014. doi: 10.1093/mnras/stu1571.
- J. E. Liu and D. A. Liu. *Smoothed Particle Hydrodynamics: a meshfree particle method*. World Scientific Publishing Co Pte Ltd (12 Feb. 2003), 2003.
- S. Lizano and F. H. Shu. Molecular cloud cores and bimodal star formation. *ApJ*, 342: 834–854, July 1989. doi: 10.1086/167640.
- L. B. Lucy. A numerical approach to the testing of the fission hypothesis. *AJ*, 82: 1013–1024, December 1977. doi: 10.1086/112164.

- M. M. Mäkelä and L. K. Haikala. Star formation, structure, and formation mechanism of cometary globules: near-infrared observations of CG 1 and CG 2. *A&A*, 550:A83, February 2013. doi: 10.1051/0004-6361/201220027.
- F. Marinacci, R. Pakmor, and V. Springel. The formation of disc galaxies in high-resolution moving-mesh cosmological simulations. *MNRAS*, 437:1750–1775, January 2014. doi: 10.1093/mnras/stt2003.
- F. Martins, D. Schaerer, and D. J. Hillier. A new calibration of stellar parameters of Galactic O stars. *A&A*, 436:1049–1065, June 2005. doi: 10.1051/0004-6361:20042386.
- I. Matsuyanagi, Y. Itoh, K. Sugitani, Y. Oasa, T. Mukai, and M. Tamura. Sequential Formation of Low-Mass Stars in the BRC 14 Region. *PASJ*, 58:L29–L34, August 2006. doi: 10.1093/pasj/58.4.L29.
- C. F. McKee and E. C. Ostriker. Theory of Star Formation. *ARA&A*, 45:565–687, September 2007. doi: 10.1146/annurev.astro.45.051806.110602.
- C. F. McKee and J. C. Tan. Massive star formation in 100,000 years from turbulent and pressurized molecular clouds. *Nature*, 416:59–61, March 2002.
- C. F. McKee, E. G. Zweibel, A. A. Goodman, and C. Heiles. Magnetic Fields in Star-Forming Regions - Theory. In E. H. Levy and J. I. Lunine, editors, *Protostars and Planets III*, page 327, 1993.
- J. Miao, G. J. White, R. Nelson, M. Thompson, and L. Morgan. Triggered star formation in bright-rimmed clouds: the Eagle nebula revisited. *MNRAS*, 369:143–155, June 2006. doi: 10.1111/j.1365-2966.2006.10260.x.
- J. Miao, G. J. White, M. A. Thompson, and R. P. Nelson. An Investigation on the Morphological Evolution of Bright-Rimmed Clouds. *ApJ*, 692:382–401, February 2009. doi: 10.1088/0004-637X/692/1/382.
- J. Miao, K. Sugitani, G. J. White, and R. P. Nelson. An Investigation of the Type M Morphological Structure of IC59: A New Model for Bright Rim Clouds? *ApJ*, 717: 658–665, July 2010. doi: 10.1088/0004-637X/717/2/658.
- D. Mihalas. *Stellar atmospheres /2nd edition/*. 1978.
- S. M. Miyama, C. Hayashi, and S. Narita. Criteria for collapse and fragmentation of rotating, isothermal clouds. *ApJ*, 279:621–632, April 1984. doi: 10.1086/161926.

- J. J. Monaghan. Smoothed particle hydrodynamics. *ARA&A*, 30:543–574, 1992. doi: 10.1146/annurev.aa.30.090192.002551.
- J. J. Monaghan. SPH and Riemann Solvers. *Journal of Computational Physics*, 136: 298–307, September 1997. doi: 10.1006/jcph.1997.5732.
- J. J. Monaghan and R. A. Gingold. Shock Simulation by the Particle Method SPH. *Journal of Computational Physics*, 52:374–389, November 1983. doi: 10.1016/0021-9991(83)90036-0.
- J. J. Monaghan and J. C. Lattanzio. A refined particle method for astrophysical problems. *A&A*, 149:135–143, August 1985.
- J. J. Monaghan and J. C. Lattanzio. A simulation of the collapse and fragmentation of cooling molecular clouds. *ApJ*, 375:177–189, July 1991. doi: 10.1086/170179.
- L. K. Morgan, M. A. Thompson, J. S. Urquhart, G. J. White, and J. Miao. A radio and mid-infrared survey of northern bright-rimmed clouds. *A&A*, 426:535–545, November 2004. doi: 10.1051/0004-6361:20040226.
- L. K. Morgan, M. A. Thompson, J. S. Urquhart, and G. J. White. A SCUBA survey of bright-rimmed clouds. *A&A*, 477:557–571, January 2008. doi: 10.1051/0004-6361:20078104.
- J. P. Morris and J. J. Monaghan. A Switch to Reduce SPH Viscosity. *Journal of Computational Physics*, 136:41–50, September 1997. doi: 10.1006/jcph.1997.5690.
- P. C. Myers, G. A. Fuller, A. A. Goodman, and P. J. Benson. Dense cores in dark clouds. VI - Shapes. *ApJ*, 376:561–572, August 1991. doi: 10.1086/170305.
- R. P. Nelson. Collapse and fragmentation of rotating, prolate clouds. *MNRAS*, 298: 657–676, August 1998. doi: 10.1046/j.1365-8711.1998.01533.x.
- R. P. Nelson and W. D. Langer. The Dynamics of Low-Mass Molecular Clouds in External Radiation Fields. *ApJ*, 482:796–+, June 1997. doi: 10.1086/304167.
- R. P. Nelson and W. D. Langer. On the Stability and Evolution of Isolated BOK Globules. *ApJ*, 524:923–946, October 1999. doi: 10.1086/307823.
- R. P. Nelson and J. C. B. Papaloizou. Three-Dimensional Hydrodynamic Simulations of Collapsing Prolate Clouds. *MNRAS*, 265:905–+, December 1993.
- R. P. Nelson and J. C. B. Papaloizou. Variable Smoothing Lengths and Energy Conservation in Smoothed Particle Hydrodynamics. *MNRAS*, 270:1, September 1994.

- M. L. Norman, J. R. Wilson, and R. T. Barton. A new calculation on rotating protostar collapse. *ApJ*, 239:968–981, August 1980. doi: 10.1086/158185.
- J. M. Oliveira. *Star Formation in the Eagle Nebula*, page 599. December 2008.
- J. H. Oort and L. Spitzer, Jr. Acceleration of Interstellar Clouds by O-Type Stars. *ApJ*, 121:6, January 1955. doi: 10.1086/145958.
- D. E. Osterbrock. Comet-Tail Structures in Emission Nebulae. *ApJ*, 125:622, May 1957. doi: 10.1086/146336.
- N. Panwar, W. P. Chen, A. K. Pandey, M. R. Samal, K. Ogura, D. K. Ojha, J. Jose, and B. C. Bhatt. Young Stellar Population of the Bright-Rimmed Clouds BRC 5, BRC 7 and BRC 39. *ArXiv e-prints*, June 2014.
- M. Pomarès, A. Zavagno, L. Deharveng, M. Cunningham, P. Jones, S. Kurtz, D. Russeil, J. Caplan, and F. Comerón. Triggered star formation on the borders of the Galactic Hii region RCW 82. *A&A*, 494:987–1003, February 2009. doi: 10.1051/0004-6361:200811050.
- D. J. Price. splash: An Interactive Visualisation Tool for Smoothed Particle Hydrodynamics Simulations. *Publications of the Astronomical Society of Australia*, 24: 159–173, October 2007. doi: 10.1071/AS07022.
- D. J. Price. Smoothed Particle Magnetohydrodynamics - IV. Using the vector potential. *MNRAS*, 401:1475–1499, January 2010. doi: 10.1111/j.1365-2966.2009.15763.x.
- D. J. Price. Smoothed particle hydrodynamics and magnetohydrodynamics. *Journal of Computational Physics*, 231:759–794, February 2012. doi: 10.1016/j.jcp.2010.12.011.
- D. J. Price and J. J. Monaghan. Smoothed Particle Magnetohydrodynamics - I. Algorithm and tests in one dimension. *MNRAS*, 348:123–138, February 2004a. doi: 10.1111/j.1365-2966.2004.07345.x.
- D. J. Price and J. J. Monaghan. Smoothed Particle Magnetohydrodynamics - II. Variational principles and variable smoothing-length terms. *MNRAS*, 348:139–152, February 2004b. doi: 10.1111/j.1365-2966.2004.07346.x.
- D. J. Price and J. J. Monaghan. Smoothed Particle Magnetohydrodynamics - III. Multidimensional tests and the  $\nabla \cdot B = 0$  constraint. *MNRAS*, 364:384–406, December 2005. doi: 10.1111/j.1365-2966.2005.09576.x.

- K. Radhakrishnan and A. C. Hindmarsh. Description and use of LSODE, the Livermore Solver for Ordinary Differential Equations. *Lawrence Livermore National Laboratory Report*, 1993.
- A. C. Raga, E. M. de Gouveia Dal Pino, A. Noriega-Crespo, P. D. Mininni, and P. F. Velázquez. Jet/cloud collision, 3D gasdynamic simulations of HH 110. *A&A*, 392: 267–276, September 2002. doi: 10.1051/0004-6361:20020851.
- J. M. Rathborne, A. M. Johnson, J. M. Jackson, R. Y. Shah, and R. Simon. Molecular Clouds and Clumps in the Boston University-Five College Radio Astronomy Observatory Galactic Ring Survey. *ApJS*, 182:131–142, May 2009. doi: 10.1088/0067-0049/182/1/131.
- B. Reipurth. Star formation in BOK globules and low-mass clouds. I - The cometary globules in the GUM Nebula. *A&A*, 117:183–198, January 1983.
- Rosetta Code, 2015. Rosetta code fortran heapsort algorithm. <http://rosettacode.org/wiki/Heapsort#Fortran>. Accessed: 2015-05-28; used via GNU FDL.
- Guido Rossum. Python reference manual. Technical report, Amsterdam, The Netherlands, The Netherlands, 1995.
- M. T. Sandford, II, R. W. Whitaker, and R. I. Klein. Radiation-driven implosions in molecular clouds. *ApJ*, 260:183–201, September 1982. doi: 10.1086/160245.
- J. Scalo and B. G. Elmegreen. Interstellar Turbulence II: Implications and Effects. *ARA&A*, 42:275–316, September 2004. doi: 10.1146/annurev.astro.42.120403.143327.
- N. I. Shakura and R. A. Sunyaev. Black holes in binary systems. Observational appearance. *A&A*, 24:337–355, 1973.
- F. H. Shu. *The physics of astrophysics, Vol. I: Radiation*. 1991a.
- F. H. Shu. *Physics of Astrophysics, Vol. II: Gas Dynamics*. University Science Books, 1991b.
- F. H. Shu, F. C. Adams, and S. Lizano. Star formation in molecular clouds - Observation and theory. *ARA&A*, 25:23–81, 1987. doi: 10.1146/annurev.aa.25.090187.000323.
- A. Sicilia-Aguilar, V. Roccatagliata, K. Getman, T. Henning, B. Merín, C. Eiroa, P. Rivière-Marichalar, and T. Currie. A Herschel view of IC1396 A: Unveiling

- the different sequences of star formation. *A&A*, 562:A131, February 2014. doi: 10.1051/0004-6361/201322609.
- L. Spitzer. *Physical processes in the interstellar medium*. 1978.
- V. Springel. The cosmological simulation code GADGET-2. *MNRAS*, 364:1105–1134, December 2005. doi: 10.1111/j.1365-2966.2005.09655.x.
- V. Springel. Smoothed Particle Hydrodynamics in Astrophysics. *ARA&A*, 48:391–430, September 2010. doi: 10.1146/annurev-astro-081309-130914.
- V. Springel, N. Yoshida, and S. D. M. White. GADGET: a code for collisionless and gasdynamical cosmological simulations. *New A*, 6:79–117, April 2001. doi: 10.1016/S1384-1076(01)00042-2.
- V. Springel, S. D. M. White, A. Jenkins, C. S. Frenk, N. Yoshida, L. Gao, J. Navarro, R. Thacker, D. Croton, J. Helly, J. A. Peacock, S. Cole, P. Thomas, H. Couchman, A. Evrard, J. Colberg, and F. Pearce. Simulations of the formation, evolution and clustering of galaxies and quasars. *Nature*, 435:629–636, June 2005. doi: 10.1038/nature03597.
- D. Stamatellos, S. Goodwin, and D. Ward-Thompson. The Labyrinth of Star Formation. *Astrophysics and Space Science Proceedings*, 36, 2014. doi: 10.1007/978-3-319-03041-8.
- A. A. Stark and L. Blitz. On the masses of giant molecular cloud complexes. *ApJ*, 225:L15–L19, October 1978. doi: 10.1086/182783.
- A. Sternberg, T. L. Hoffmann, and A. W. A. Pauldrach. Ionizing Photon Emission Rates from O- and Early B-Type Stars and Clusters. *ApJ*, 599:1333–1343, December 2003. doi: 10.1086/379506.
- B. Strömgren. The Physical State of Interstellar Hydrogen. *ApJ*, 89:526, May 1939. doi: 10.1086/144074.
- K. Sugitani and K. Ogura. A catalog of bright-rimmed clouds with IRAS point sources: Candidates for star formation by radiation-driven implosion. 2: The southern hemisphere. *ApJS*, 92:163–172, May 1994. doi: 10.1086/191964.
- K. Sugitani, Y. Fukui, and K. Ogura. A catalog of bright-rimmed clouds with IRAS point sources: Candidates for star formation by radiation-driven implosion. I - The Northern Hemisphere. *ApJS*, 77:59–66, September 1991. doi: 10.1086/191597.

- J. C. Tan, S. N. Shaske, and S. Van Loo. Molecular Clouds: Internal Properties, Turbulence, Star Formation and Feedback. In T. Wong and J. Ott, editors, *IAU Symposium*, volume 292 of *IAU Symposium*, pages 19–28, March 2013. doi: 10.1017/S1743921313000173.
- K. Tassis. The shapes of molecular cloud cores in Orion. *MNRAS*, 379:L50–L54, July 2007. doi: 10.1111/j.1745-3933.2007.00332.x.
- S. Terebey, F. H. Shu, and P. Cassen. The collapse of the cores of slowly rotating isothermal clouds. *ApJ*, 286:529–551, November 1984. doi: 10.1086/162628.
- M. A. Thompson, J. S. Urquhart, and G. J. White. A Compact Array imaging survey of southern bright-rimmed clouds. *A&A*, 415:627–642, February 2004. doi: 10.1051/0004-6361:20031681.
- H. Trac and U.-L. Pen. A Primer on Eulerian Computational Fluid Dynamics for Astrophysics. *PASP*, 115:303–321, March 2003. doi: 10.1086/367747.
- P. Tremblin, E. Audit, V. Minier, and N. Schneider. 3D simulations of pillar formation around HII regions: the importance of shock curvature. *A&A*, 538:A31, February 2012. doi: 10.1051/0004-6361/201118031.
- J. S. Urquhart, M. A. Thompson, L. K. Morgan, and G. J. White. Radio continuum and molecular line observations of four bright-rimmed clouds. *A&A*, 450:625–643, May 2006. doi: 10.1051/0004-6361:20053417.
- Stéfan van der Walt, Chris S. Colbert, and Gaël Varoquaux. The numpy array: A structure for efficient numerical computation. *Computing in Science & Engineering*, 13(2):22–30, 2011. doi: <http://dx.doi.org/10.1109/MCSE.2011.37>. URL <http://scitation.aip.org/content/aip/journal/cise/13/2/10.1109/MCSE.2011.37>.
- E. F. van Dishoeck and J. H. Black. The photodissociation and chemistry of interstellar CO. *ApJ*, 334:771–802, November 1988. doi: 10.1086/166877.
- E. F. van Dishoeck and G. A. Blake. Chemical Evolution of Star-Forming Regions. *ARA&A*, 36:317–368, 1998. doi: 10.1146/annurev.astro.36.1.317.
- D. A. Verner, G. J. Ferland, K. T. Korista, and D. G. Yakovlev. Atomic Data for Astrophysics. II. New Analytic FITS for Photoionization Cross Sections of Atoms and Ions. *ApJ*, 465:487, July 1996. doi: 10.1086/177435.

- S. K. Walch, A. P. Whitworth, T. Bisbas, R. Wunsch, and D. Hubber. Dispersal of molecular clouds by ionizing radiation. *MNRAS*, 427:625–636, November 2012. doi: 10.1111/j.1365-2966.2012.21767.x.
- M. Wenger, F. Ochsenbein, D. Egret, P. Dubois, F. Bonnarel, S. Borde, F. Genova, G. Jasniewicz, S. Laloë, S. Lesteven, and R. Monier. The SIMBAD astronomical database. The CDS reference database for astronomical objects. *A&AS*, 143:9–22, April 2000. doi: 10.1051/aas:2000332.
- M. Wetzstein, A. F. Nelson, T. Naab, and A. Burkert. Vine-A Numerical Code for Simulating Astrophysical Systems Using Particles. I. Description of the Physics and the Numerical Methods. *ApJS*, 184:298–325, October 2009. doi: 10.1088/0067-0049/184/2/298.
- A. Whitworth. The erosion and dispersal of massive molecular clouds by young stars. *MNRAS*, 186:59–67, January 1979.
- A. P. Whitworth, A. S. Bhattal, S. J. Chapman, M. J. Disney, and J. A. Turner. The Preferential Formation of High-Mass Stars in Shocked Interstellar Gas Layers. *MNRAS*, 268:291, May 1994.
- J. P. Williams and C. F. McKee. The Galactic Distribution of OB Associations in Molecular Clouds. *ApJ*, 476:166–183, February 1997.
- J. P. Williams, E. J. de Geus, and L. Blitz. Determining structure in molecular clouds. *ApJ*, 428:693–712, June 1994. doi: 10.1086/174279.
- J. P. Williams, L. Blitz, and C. F. McKee. The Structure and Evolution of Molecular Clouds: from Clumps to Cores to the IMF. *Protostars and Planets IV*, page 97, May 2000.
- M. G. Wolfire, D. Hollenbach, C. F. McKee, A. G. G. M. Tielens, and E. L. O. Bakes. The neutral atomic phases of the interstellar medium. *ApJ*, 443:152–168, April 1995. doi: 10.1086/175510.
- T. Wong and L. Blitz. The Relationship between Gas Content and Star Formation in Molecule-rich Spiral Galaxies. *ApJ*, 569:157–183, April 2002. doi: 10.1086/339287.
- J. L. Yun and D. P. Clemens. Star formation in small globules - Bart BOK was correct. *ApJ*, 365:L73–L76, December 1990. doi: 10.1086/185891.
- A. Zavagno, L. Deharveng, F. Comerón, J. Brand, F. Massi, J. Caplan, and D. Russeil. Triggered massive-star formation on the borders of Galactic H II regions. II. Evidence

for the collect and collapse process around RCW 79. *A&A*, 446:171–184, January 2006. doi: 10.1051/0004-6361:20053952.

H. Zinnecker and H. W. Yorke. Toward Understanding Massive Star Formation. *ARA&A*, 45:481–563, September 2007. doi: 10.1146/annurev.astro.44.051905.092549.

---

## ABOUT THE AUTHOR

---

Timothy Michael Kinnear was born on an otherwise inauspicious day in March of 1987<sup>1</sup> at a hospital in Croyden to his mother and father, Natalie and Michael Kinnear (respectively). Timothy began growing up in Thornton Heath during which time he became accompanied by an increasing number of sisters, born in 1989, 1991 and 1993; Sophie, Amy and Hayley (also respectively).

In 1994 the Kinnear family moved to Crawley Down, a village situated unsurprisingly near Crawley, in West Sussex. Here he briefly attended Crawley Down Infants School, finding integration initially difficult, due to a combination of the complex socio-political environment common to all infant schools, and being shy. He then proceeded to Crawley Down Church of England Junior school, followed by Imberhorne School in East Grinstead. For GCSEs he is indebted to all of the staff at The Link. During this time, the millennium<sup>2</sup> passed and the world didn't end, as a present reader may have noticed. For A-levels, he attended Hazelwick School sixth form in Crawley.

Having been exceedingly keen, and notionally capable, at maths, physics and computing, he selected the University of Warwick and Physics as his Higher Education/degree combination. Enjoying this, but finding himself inordinately more fond of coursework than exams, he completed a Bachelor's of Science in Physics after three years, and set to continue with a Research Master's in Science with (then Doctor, now Professor) Boris Gänsicke for the year following that. Set, now, on pursuing an astronomical<sup>3</sup> career (in topic, if not in profile and fame), he began a Philosophical Doctorate with Dr. Jingqi Miao at the University of Kent.

---

<sup>1</sup>The 28th. Though, with regards to the day's auspices, it was also the day on which the actor Patrick Troughton, known for his role as The Doctor in the television serial *Doctor Who*, passed away. It is left to the reader to decide whether this has the serious implication that Timothy may be a subsequent incarnation of said Timelord.

<sup>2</sup>The dawn of the year 2001, not 2000 as was popularly celebrated.

<sup>3</sup>Technically 'astrophysical', though the subsequent comment regarding his career profile would be less effective with that wording.

To borrow the description of Douglas Adams' *Hitchhiker's Guide to the Galaxy*, his PhD was a trilogy in five parts; taking the better part<sup>4</sup> of five years<sup>5</sup> rather than the intended three. During this time, however, in addition to working through various problems and setbacks with his research (which *were/were not* overcome<sup>6</sup>), he fit in copious amounts of additional<sup>7</sup> work, especially involving teaching as well as writing a course book for a programming module. With the university having reminded him that being a PhD candidate was not an indefinite occupation, this document was finished and submitted for your pleasure, dear reader. Timothy hopes that you enjoy, or have enjoyed, reading it.

Furthermore, if you are from 'the future', Timothy hopes that his work proved to be of use to all humankind, and contributed to defeating the inevitable (if contemporary science-fiction is any judge<sup>8</sup>) invasion of Earth by aliens. His more practical hope is that it was of use for at least one, or perhaps two, other scientists working in the same field. With a love of the scientific process, that can be enough.

---

<sup>4</sup>All.

<sup>5</sup>Also a lie, it took slightly longer, but that would prevent the HHGTTG comparison.

<sup>6</sup>Examiner should delete as appropriate.

<sup>7</sup>Unnecessary.

<sup>8</sup>It isn't.